Activity, Selectivity and Stability of Colloidal Silver Catalysts for Electrochemical CO₂ Reduction Reaction

Inaugural dissertation

of the Faculty of Science,

University of Bern

Presented by

Huifang Hu (胡慧芳)

from China

Supervisor of the doctoral thesis:

Prof. Dr. Peter Broekmann

Department of Chemistry, Biochemistry and Pharmaceutical Sciences

Activity, Selectivity and Stability of Colloidal Silver Catalysts for Electrochemical CO₂ Reduction Reaction

Inaugural dissertation

of the Faculty of Science,

University of Bern

Presented by

Huifang Hu (胡慧芳)

from China

Supervisor of the doctoral thesis:

Prof. Dr. Peter Broekmann

Department of Chemistry, Biochemistry and Pharmaceutical Sciences

Activity, Selectivity and Stability of Colloidal Silver Catalysts for Electrochemical CO₂ Reduction Reaction

Inaugural dissertation

of the Faculty of Science,

University of Bern

Presented by

Huifang Hu (胡慧芳)

from China

Supervisor of the doctoral thesis :

Prof. Dr. Peter Broekmann

Department of Chemistry, Biochemistry and Pharmaceutical Sciences

Accepted by the Faculty of Science.

Bern, February 24ᵗʰ, 2023   The Dean

Prof. Dr. Marco Herwegh

Abstract

Electrochemical CO_2 reduction reaction (denoted hereinafter CO_2RR) using renewable electric power from carbon-free sources shows high potential to transform CO_2 into value-added commodity chemicals, such as carbon monoxide and formic acid. The ultimate goal of research activities in this field is to achieve a commercial scale of CO_2 conversion, which requires not only the development of effective catalysts but relies also on the design of appropriate electrochemical reactors to reach the high target product partial current density with long-term operation stability. There are still challenges towards industrial application, such as CO_2 mass transport limitations, and severe system stability issues due to flooding, and precipitation phenomena occurring in the gas diffusion electrodes (GDEs) during operation.

Colloidal catalysts are typically prepared by reducing metal precursors in the presence of capping agents which are used to control the size distribution of the colloidal particles, their shape and composition. These well-defined colloidal catalysts have already showed excellent electrocatalytic performance for CO_2RR. However, most of research has prioritized the activity and selectivity of catalysts, while the stability received less attention, especially in the presence of surfactants. In addition, the studies on the residual capping agents that may block the active site from colloidal synthesis processes are few for CO_2RR.

For this PhD project, various colloidal Ag catalysts with different sizes, morphologies and capping agents were employed for electrochemical CO_2RR. The capping agents (i.e. polyvinylpyrrolidone, PVP) were demonstrated to severely affect the CO_2RR performance on Ag catalysts due to its coverage of active site. Electrochemical looping has been proved herein to be a suitable and effective method for surfactant removal in particular when using H-type electrolysis cells where the catalysts are exposed to a liquid electrolyte solution; this leads the Ag catalysts to perform close 100% of faradaic efficiency for CO. More importantly, the excess capping agents (e.g. PVP) not only changed the degradation pathway of Ag catalysts but they also reduced the stability of gas-fed electrolyzer systems. Ag catalysts with distinct sizes, morphologies and capping agents showed dissimilar degradation pathways for CO_2RR when using these gas-fed flow cells. However, the loss of CO_2RR performance could be in many cases regained after removing

precipitate formed on the GDEs. It is further demonstrated herein that cracks often appearing as defects in the gas-diffusion layers (GDLs) and the removal of excess PVP from the catalyst inks could effectively mitigate flooding phenomena and prolong the life-time of the electrolyzer systems.

In conclusion, to advance electrochemical CO_2RR towards commercial scale, durability is currently more reliant upon the reactor and GDE design rather than the catalyst itself in this stage. The influence of capping agents, especially the excess surfactant, should not be neglected.

Contents

List of figures

List of tables

List of abbreviations

AEMs	anion exchange membranes
Ag NCs	silver nanocubes
Ag NPs	silver nanoparticles
Ag NWs	silver nanowires
BPEI	branched polyethylenimine
BPMs	bipolar membranes
CE	counter electrode
CEMs	cation exchange membranes
CFL	carbon fibers layer
CO_2RR	CO_2 reduction reaction
CTAB	cetyltrimethylammonium bromide
DFT	density functional theory
ec-looping	electrochemical looping
EDX	energy dispersive-X-ray
E_{vertex}	vertex potential
FE	faradaic efficiency
GDE	gas diffusion electrode
GDL	gas diffusion layer
HER	hydrogen evolution reaction
ICP-MS	inductively coupled plasma mass spectrometry
IL-SEM	identical location scanning electron microscopy
IPCC	the Intergovernmental Panel on Climate Change
MPL	microporous layer
MPS	macroporous support
OAm	oleylamine
OER	oxygen evolution reaction
PCD	partial current density
PEG	polyethylene glycol
PTFE	polytetrafluoroethylen

PVP   polyvinylpyrrolidone

PVA   polyvinyl alcohol

RE   reference electrode

RHE   reversible hydrogen electrode

SCE   saturated calomel electrode

SHE   standard hydrogen electrode

WE   working electrode

XPS   X-ray photoelectron spectroscopy

1 Theoretical background

1.1 Climate change and rising CO_2 status

Unnatural climate change has been observed. Extreme natural disasters, such as wildfires, hurricanes, floods and droughts, have happened more frequently and caused greater damage. Global annual temperature has increased at an average rate of 0.08 °C per decade since 1880 and the rise has accelerated since the Industrial Revolution [1]. Sea level rise has continued due to global warming; the global sea level reached a new high record in 2020, which was 91.3 mm (3.6 inches) higher than the record in 1993 [2]. Some of these changes, such as continued sea level rise, are irreversible and could last hundreds of years.

The rising concentration of greenhouse gases such as water vapor (H_2O), carbon dioxide (CO_2), methane (CH_4), and nitrous oxide (N_2O) in the atmosphere leads to sever changes of the global climate. The greenhouse gases particularly impact on Earth's climate through the absorption of infrared radiation. Approximately 30% of solar radiation is reflected back to space by clouds and the Earth's surface. Approximately 20% of solar radiation is absorbed by the atmosphere. The Earth's surface absorbs the rest 50% of the solar radiation. The remaining solar radiation in Earth's surface is then emitted with infrared wavelengths. The majority of this infrared radiation emission is absorbed by greenhouse gases and remitted in all directions such as to other greenhouse gases molecules, back to Earth's surface and towards space. The trapped heat by greenhouse gases warms the Earth's surface. This cycle known as greenhouse effect, is natural and in principle beneficial for maintaining temperatures that sustain life. The increased concentration of atmospheric greenhouse gases negatively alters, however, the balance of Earth's incoming and outgoing radiation, which forces the climate to change.

CO_2, the most released greenhouse gas, contributes significantly to the enhanced greenhouse effect and climate changes due to its long atmospheric lifetime (hundreds of years). For this reason, CO_2 is of great concern and studied thoroughly. The most renowned observatory for measurements of anthropogenic CO_2 concentration is the Mauna Loa Observatory in Hawaii. The measurements of CO_2 concentration started in 1958 by Charles David Keeling and are presented in a plot referred to as the Keeling Curve (presented in Fig 1.1) [3]. The graph shows the continuous rising of CO_2

concentration in the atmosphere. Global emissions of CO_2 have increased by almost 50% since 1990. More than 50% of CO_2 was emitted from combustion of fossil fuels since 1950s [4].
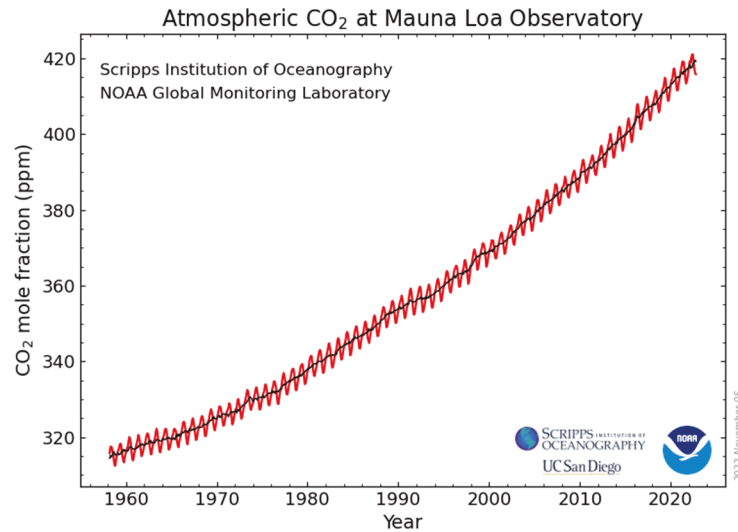
Fig 1.1 Keeling Curve-Trend in atmospheric carbon dioxide concentration [3]. Reprinted from ref. [3].

There are several international organizations that proposed suggestions to retard the climate changes. The United Nations Environments Programme and the World Meteorological Organization established the Intergovernmental Panel on Climate Change (IPCC) to provide science assessments related to climate changes in 1988. The Paris Agreement adopted by 196 members in 2015 aims to limit global warming to well below 2 °C, ideally to 1.5 °C, compared to pre-industrial levels [5]. The Sustainable Development Goals, which were adopted by all United Nations Member States in 2015, include goals concerning climate action and affordable and clean energy.

1.2 CO₂ capture, storage and utilization

A range of strategies and concepts are explored to reduce or avoid releasing CO_2 emissions. The capture of CO_2, from the primary industrial sources of CO_2 include power plants, oil refineries, and steel industries, is an important and viable CO_2 emission reduction technology (shown in Fig 1.2 [6]). The CO_2 capture involves absorption, adsorption, and separation technologies [7]. There are basically three routes of CO_2 capture: post-combustion, pre-conversion and oxy-fuel combustion [6], as summarized in Fig 1.2. The post-combustion capture process captures and

separates CO_2 from waste gas streams after the conversion of the carbon source to CO_2. Monoethanolamine, assumed to capture 90% of the CO_2 in the system, is commonly used in the post-combustion capture system [8]. The pre-conversion capture process refers to capturing CO_2 generated as an undesired co-product of an intermediate reaction of a conversion process [6]. The oxy-fuel combustion can be used only in the industries involving combustion.
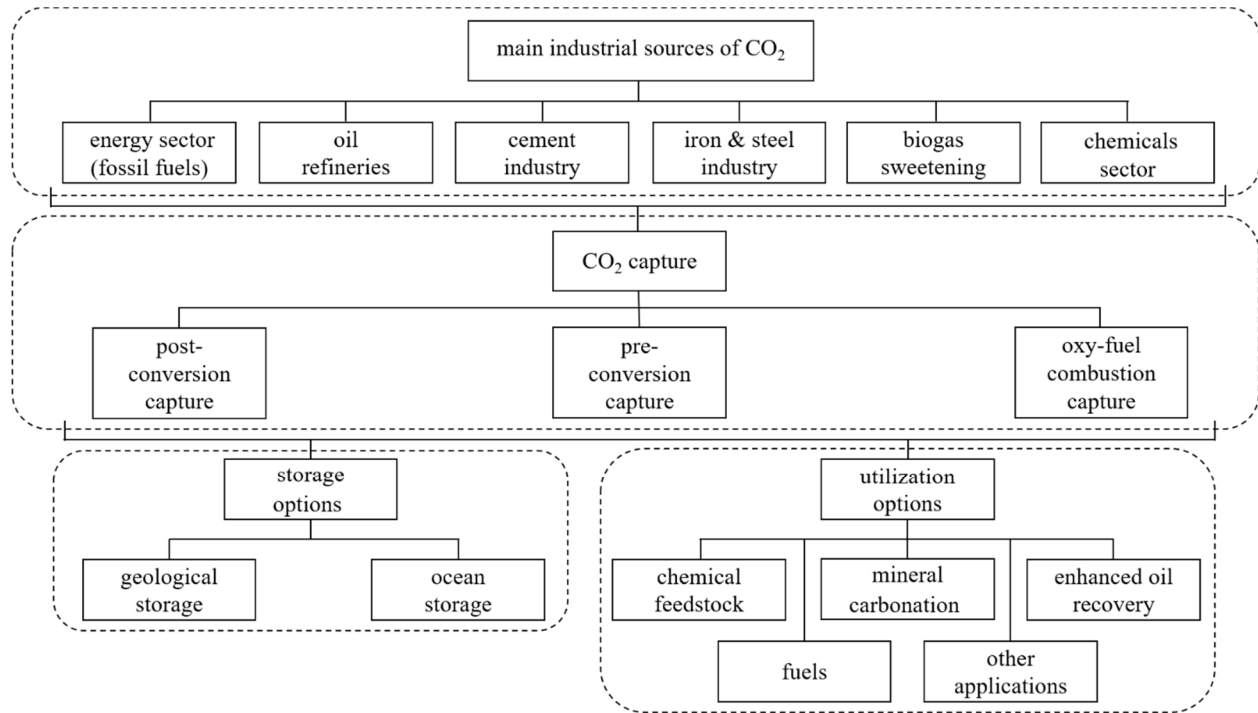
Fig 1.2 Different carbon capture, storage and utilization options [6]. Adapted from ref. [6].

CO_2 storage strategy includes CO_2 capturing and compression, followed by pumping to geological reservoirs and ocean for long-term storage [9]. However, there are challenges, such as the possible leaks depending on the permeability of the geological structure, non-profit requiring large capital investment of CO_2 storage, and limitation of storage capacity in some regions [8-10].

In contrast to CO_2 storage, CO_2 utilization is more profitable and attracts great interest in recent years. The captured CO_2 can be utilized directly in food and drink industry as a carbonating agent, packaging gas, and preservative [11-13]. In addition, it can be used for enhanced oil recovery by decreasing viscosity of oil and increasing the extraction yields [14-15]. Mineral carbonation and

biofuels from microalgae are other options to fix CO_2 [9,16]. Furthermore, CO_2 can also be converted into valuable products such as chemicals [17] and fuels [18] via carboxylation or reduction. Various concepts of chemical CO_2 conversion have been investigated recently [19]. Most chemical conversions are based on classical heterogeneous catalysis, typically employing solid catalysts and gaseous reactants. For example, methanol synthesis from CO_2 occurs by using hydrogenation catalyst at high temperatures (> 413 K) and high pressures (> 1 MPa) [20].

Among CO_2 conversion technologies, electrochemical CO_2 reduction reaction (CO_2RR) is especially noteworthy. This approach is promising not only because the electrolysis converts CO_2 directly into value-added chemical feedstock but also it uses renewable electric power generated from various carbon-free sources such as solar, wind, hydroelectric, tidal and hydrothermal processes (shown in Fig 1.3). There are two primary ways for electrochemical CO_2RR: (i) the electrochemical reduction of CO_2 with other organic substrates to produce some target compounds (electrochemical synthesis) and (ii) direct electrochemical reduction of CO_2 to some value-added products, such as CO, ethylene, alcohols, and formic acid [21]. This PhD project focuses on the direct electrochemical CO_2 conversion.
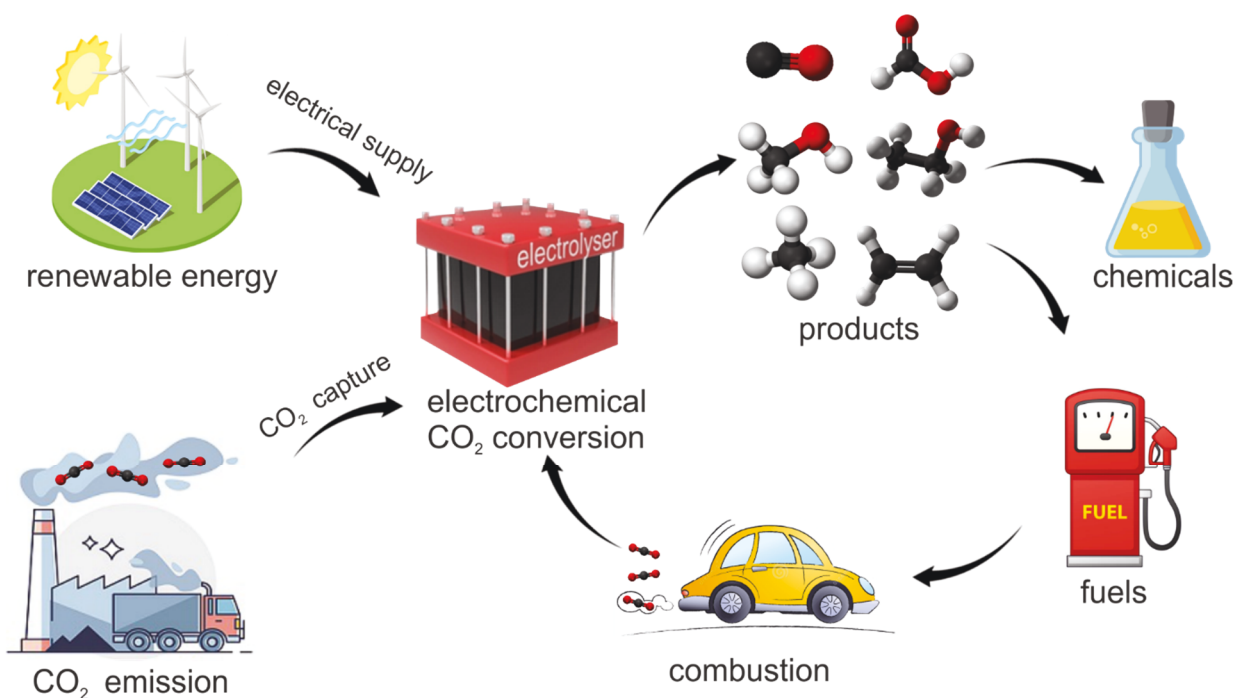
Fig 1.3 Schematic representation of CO_2 electroreduction using renewable electric energies

1.3 Thermodynamics and kinetics for electrochemical CO_2 reduction

CO_2 is a linear molecule (O=C=O) in which two oxygen atoms are each covalently double bonded to a single carbon atom. The equivalent carbon‑oxygen bond length is 116.3 pm, which is much shorter than that of C-O single bond. An average C=O bond energy (745 kJ/mol) is much higher than O=O bond energy (495 kJ/mol) and C=C bond energy (614 kJ/mol) [21]. The Gibbs free energy of formation of CO_2 is -394.0 kJ/mol. Therefore, CO_2 is incredibly stable. A substantial input of energy, optimized reaction conditions and active catalysts are necessary for any chemical conversion of CO_2 to a carbonaceous fuel or other commodity chemicals.

An electrochemical reaction always includes two half reactions: the oxidation of reactants (loss of electrons) occurs at an anode and the reactant reduction (gain of electrons) occurs at a cathode. In the case of electrochemical CO_2RR, CO_2 reduction occurs at the cathode, while the anode reaction is typically the oxygen evolution reaction (OER).

1.3.1 Thermodynamics

A chemical conversion is driven by the differences in the Gibbs free energy between the reactants and the products of chemical transformation (under standard conditions: 298.15 K, 1 bar), as determined by the Gibbs-Helmholtz relationship.

$$\Delta G^0 = \Delta H^0 - T\Delta S^0 \tag{1}$$

ΔH^0 refers to the enthalpy changes at standard conditions, T is the system temperature and ΔS^0 represents the entropy changes at standard conditions. In electrochemical reactions, this equation transforms for a reversible reaction at constant temperature and pressure to:

$$\Delta G^0 = -nFE^0 \tag{2}$$

where n represents the number of transferred electrons, F is the Faraday's constant (96485.33 C/mol), and E^0 is the standard state potential that refers standard electromotive force as well. E^0 means the minimum potential required for CO_2RR. When the sign of ΔG^0 is negative, the reaction occurs spontaneously.

Table 1 Selected standard electrode potentials for half-cell reactions related CO_2RR at 1.0 atm and 298.15 K [21-23].

Products	Reactions	n	E^0 / V vs SHE
carbon monoxide	$CO_2 + 2H^+ + 2e^- \rightarrow CO + H_2O$	2	-0.106
	$CO_2 + 2H_2O + 2e^- \rightarrow CO + 2OH^-$	2	-0.934
formic acid	$CO_2 + 2H^+ + 2e^- \rightarrow HCOOH$	2	-0.250
methane	$CO_2 + 8H^+ + 8e^- \rightarrow CH_4 + 2H_2O$	8	0.169
ethylene	$2CO_2 + 12H^+ + 12e^- \rightarrow CH_2CH_2 + 4H_2O$	12	0.064
	$2CO_2 + 8H_2O + 12e^- \rightarrow CH_2CH_2 + 12OH^-$	12	-0.764
ethanol	$2CO_2 + 12H^+ + 12e^- \rightarrow CH_3CH_2OH + 3H_2O$	12	0.084
methanol	$CO_2 + 6H^+ + 6e^- \rightarrow CH_3OH + H_2O$	6	0.016
	$CO_2 + 5H_2O + 6e^- \rightarrow CH_3OH + 6OH^-$	6	-0.812
propanol	$3CO_2 + 18H^+ + 18e^- \rightarrow C_3H_7OH + 5H_2O$	18	0.09
hydrogen	$2H^+ + 2e^- \rightarrow H_2$	2	0
	$2H_2O + 2e^- \rightarrow H_2 + 2OH^-$	2	-0.830
CO_2 radical anion	$CO_2 + e^- \rightarrow * CO_2^-$	1	-1.9
oxygen (anode reaction)	$2H_2O \rightarrow O_2 + 4H^+ + 4e^-$	4	1.23

From thermodynamics, Gibbs free energy is related to the concentrations of reactants and products (reaction quotient, Q) as follows.

$$\Delta G = \Delta G^0 + RT \ln Q \tag{3}$$

The relationship between the electrode potential and the standard-state potential can be obtained, which is known as Nernst equation, shown in equation (4).

$$E = E^0 - \frac{RT}{nF} \ln \frac{C_r}{C_o} \tag{4}$$

E^0 is the standard state potential, R is the universal gas constant, n is the number of transferred electrons, and $\frac{C_r}{C_o}$ is the bulk concentration of reduced and oxidized species. The Nernst equation provides a bridge between electrode potential and the concentrations of participants in the

electrode process and characterize the equilibrium for the electrode reaction. If a system follows the Nernst equation or an equation derived from it, the electrode reaction is often considered thermodynamically or electrochemically reversible [24].

The standard potential can be calculated from Gibbs free energy. Some of the half-cell reactions related to CO_2RR, the associated standard electrode potentials E^0 (V vs SHE, standard hydrogen electrode), and the number of transferred electrons are summarized in Table 1.

1.3.2 Kinetics

The standard potentials listed in Table 1 only indicate the thermodynamic tendencies of reactions; they do not take into consideration of the role of kinetics. CO_2RR is not achieved at applied potentials predicted from thermodynamics. Instead, much higher electron energies (more negative potentials) must be applied to initiate the reaction at a measureable rate. The rate constant for a heterogeneous electron-transfer reaction is a function of applied potential, which is a constant at a given temperature. The deviation of the electrode potential from its equilibrium value is termed as overpotential [24]. The lower the overpotential is, the more active the catalyst is.

The electrode reaction overpotential consists of three main components: ohmic overpotential, concentration overpotential, and activation overpotential [21,25-27]. The ohmic losses are from conduction of ions in the bulk electrolytes and ion transport across the membrane. The ohmic losses are greater at high current density. The activation overpotential is the overpotential from anodic and cathodic kinetic activation; it strongly depends on the electrode catalytic characteristics. The activation overpotential can be reduced by obtaining a catalyst with a faster oxidation/reduction rate constant for CO_2RR [21]. The concentration overpotential is required to maintain concentration gradients near the electrode for sustained electrochemical reactions and is caused by the slow diffusion of reactant or products. For CO_2RR, the mass transport includes diffusion of CO_2 and forming products (e.g. CO formed at the cathode and O_2 produced at the anode). The overall reaction rate can be limited by the CO_2 mass transport to the electrode surface. Other additional overpotentials can be minimized by material modification and altering the cell design. Moreover, the electrolysis condition (such as pressure and temperature) affect the overpotential as well. Therefore, it is highly desired to develop superior catalysts and optimize cell

design and operation conditions to lower the total energy applied to the conversion system via decreasing the overpotential.

CO$_2$RR on the electrode surface consists of several steps: mass transfer of the reactants, surface reactions, interfacial charge transfer, and products involving bulk and surface diffusion [21]. The first step of CO$_2$RR is one-electron reduction of CO$_2$ to radical anion *CO$_2^-$ (* means absorption state) has been suggested to be a common critical limiting step with a standard potential of -1.9 V vs SHE as shown in Table 1 [23]. This step causes the geometry of linear CO$_2$ molecule to become a bent *CO$_2^-$ radical ion, which in turn leads to increased overpotential of CO$_2$RR. Stabilization of the *CO$_2^-$ radical ion intermediate at a catalyst surface may lead to decreasing CO$_2$RR overpotentials. In addition, CO$_2$RR proceeds in aqueous media in the potential range of a parasitic hydrogen evolution reaction (HER) [28-29]. Therefore, the designed catalysts should display high selectivity for CO$_2$RR and suppress HER.

1.4 Classification of catalysts for electrochemical CO$_2$ reduction reaction

Catalysts are essential to decrease the overpotential of electrochemical CO$_2$RR. Selectivity, activity, and stability are three important requirements for a CO$_2$RR catalyst. The selectivity is expressed in faradaic efficiency (FE) which is the fraction of faradaic charge consumed to produce a targeted product. The activity corresponds to the rate of conversion and is usually described as a decrease of overpotential. Instead, the activity towards a given product, referred as partial current density, is extracted from the total current density. Only the charges converted to given product are counted for the calculation of the partial current density. The stability of catalysts is the least studied aspect, although it is one of the most important factors for the commercial applications. The factors impacting the stability of catalysts include the deposition of metal impurities in the electrolyte [28], the formation of graphitic carbon from CO$_2$ reduction intermediates [30], and the degradation of the catalysts [31].

Table 2 Catalyst classification according to Hori et al. [32]. Adapted with permission from *Electrochim. Acta*, 1994, 39 (11), 1833-1839 [32]. Copyright 1994 Elsevier.

Catalysts	Potentia / V vs NHE	Current density / mA cm^{-2}	Faradaic efficiency / %						
			CH$_4$	C$_2$H$_4$	EtOH	PrOH	CO	HCOO$^-$	H$_2$
Pb	-1.63	-5.0	0.0	0.0	0.0	0.0	0.0	97.4	5.0
Hg	-1.51	-0.5	0.0	0.0	0.0	0.0	0.0	99.5	0.0
In	-1.55	-5.0	0.0	0.0	0.0	0.0	2.1	94.9	3.3
Sn	-1.48	-5.0	0.0	0.0	0.0	0.0	7.1	88.4	4.6
Cd	-1.63	-5.0	1.3	0.0	0.0	0.0	13.9	78.4	9.4
Tl	-1.60	-5.0	0.0	0.0	0.0	0.0	0.0	95.1	6.2
Au	-1.14	-5.0	0.0	0.0	0.0	0.0	87.1	0.7	10.2
Ag	-1.37	-5.0	0.0	0.0	0.0	0.0	81.5	0.8	12.4
Zn	-1.54	-5.0	0.0	0.0	0.0	0.0	79.4	6.1	9.9
Pd	-1.20	-5.0	2.9	0.0	0.0	0.0	28.3	2.8	26.2
Ga	-1.24	-5.0	0.0	0.0	0.0	0.0	23.2	0.0	79.0
Ni	-1.48	5.0	1.8	0.1	0.0	0.0	0.0	1.4	88.9
Fe	-0.91	-5.0	0.0	0.0	0.0	0.0	0.0	0.0	94.9
Pt	-1.07	-5.0	0.0	0.0	0.0	0.0	0.0	0.1	95.7
Ti	-1.60	-5.0	0.0	0.0	0.0	0.0	0.0	0.0	99.7
Cu	-1.44	5.0	33.3	25.5	5.7	3.0	1.3	9.4	20.5

The activity and selectivity of CO$_2$RR greatly depend on the type of the heterogeneous catalysts. Extensive research has been dedicated to design the catalysts with high activity, selectivity, and stability for CO$_2$RR [33-37]. Y. Hori et al classified metallic catalysts into four groups according

to the product distribution of CO_2RR during electrolysis at the current density of -5.0 mA/cm^2 in 0.1 M $KHCO_3$ solution at ambient condition (shown in Table 2) [32]: (1) Pb, Hg, In, Sn, Cd, and Tl bind strongly $^*CO_2^-$ and can transform CO_2 to $HCOO^-$; (2) Au, Ag, Zn, Pd, and Ga produce CO mainly; (3) Cu is the only catalyst yielding hydrocarbons and oxygenates; (4) this group includes Ni, Fe, Pt, and Ti that are not active for CO_2RR and mainly produce H_2 in HER.

1.5 Mass transport

The performance of CO_2RR is kinetically limited at low current densities, whereas mass transport limitation becomes the key factor at high current densities. Most CO_2RR studies have been carried out in aqueous solution. CO_2 molecules firstly dissolve in an electrolyte solution and then diffuse through the liquid to the cathode-electrolyte interface. The solubility of CO_2 in aqueous media is about 30 mM in water at 1 atm at ambient temperature, which is low. Under this circumstance, the highest partial current density of target product is typically far lower than 100 mA/cm^2, which does not meet criteria for a commercially viable process [38]. Various solutions have been proposed to improve the mass transport of CO_2. The solubility of CO_2 in aqueous electrolyte can be increased by using pressurized CO_2 in the reaction cell. The solubility of CO_2 in organic solutions (e.g. methanol, acetonitrile) is typically higher than that in common aqueous systems, and the HER can be hindered in the organic solution due to the low proton availability [39]. Ionic liquid is another alternative electrolyte for increasing the solubility of CO_2. Ionic liquids provide increased solubility of CO_2 and serve as co-catalysts for CO_2RR stabilizing radical-anion $^*CO_2^-$ at the electrode surface and decreasing overpotential of the reaction [40]. So-called gas diffusion electrodes (GDEs) employing a porous catalysts layer along with diffusion media to facilitate reactant transport and distribution can also help to overcome the CO_2 mass transport problem [41]. The alternative to solve the mass limitation of CO_2 is the direct flow of CO_2 to the catalyst surface achieving by application of GDE in the flow cell. Flow cells are discussed in more details in section 1.7.1.

1.6 Possible target products from CO_2 reduction reaction

Electrochemical CO_2RR is a multiple proton- and electron-transfer reaction that converts CO_2 into value-added products. Table 3 lists the cost of major CO_2RR products from CO_2-electrolysis cell

and the well-established commercial chemical synthesis [42]. Compared to the production prices from the conventional production routes, CO_2-electrolysis are not competitive for all of the possible reaction products. The conversion of CO_2 into CH_4, C_2H_4, and CH_3OH by electrochemical CO_2RR appears much higher in cost than the current market prices shown in Table 3. From an economic perspective, the generation of CO and formate from CO_2 electrolysis seems to be most promising. The cost of transforming CO_2 to CO is 0.27-0.54 \$/kg, which is lower than the current market price (0.65 \$/kg). Moreover, the production volume for CO is large at 210000 Mt per year. Formate production ranges from 0.17 \$/kg to 0.34 \$/kg, which is 2-4 times lower than the current market price (0.8-1.2 \$/kg). However, the annual market production (0.8 Mt) is much smaller compared to the demand of CO.

Table 3 Costs of H_2, CH_4, C_2H_4, CO, $HCOO^-$ and CH_3OH from commercial synthesis and CO_2 electrolysis [42]. Reprinted from ref. [42].

Product	Produced by	Current market price / \$ kg^{-1}	Current production volume / Mt y^{-1}	Production price by electrolysis / \$ kg^{-1}	Production volume per electrolysis unit / Mt y^{-1}
H_2	Steam reforming, partial oxidation of methane or gasification	2-4	65	4	0.0003
CH_4	methanogenesis or hydrogenation of CO_2	<0.08	2400	2-4	0.0007
C_2H_4	pyrolysis or vapocracking	0.8-1.5	141	1.6-3.2	0.0009
CO	Boudouard reaction	0.65	210000	0.27-0.54	0.005
$HCOO^-$/ $HCOOH$	hydrolysis form methyl formate and formamide or by-product of acetic acid production	0.8-1.2	0.8	0.17-0.34	0.008
CH_3OH	from natural gas, coal, biomass, waste	0.4-0.6	100	0.7-1.4	0.002

CO has a wide range of applications in a metal fabrication, steel production, and pharmaceutical manufacturing. In addition, CO combines with H_2 (syngas) serves as an important chemical precursor for a number of industrial processes via Fischer-Tropsch [43-44]. The Fischer-Tropsch process converts CO and hydrogen into liquid hydrocarbons such as synthetic lubrication and synthetic fuel (shown in Fig 1.4). However, Fischer-Tropsch reactions require high temperature and pressure in the presence of the catalysts. The effort to convert chemical feedbacks from CO_2 electrolysis with less chemical infrastructure has done by Haas and co-workers [45]. The system

coupled a CO_2 electrolyzer by using photovoltaic electricity and a fermentation module to convert syngas from CO_2RR to butanol and hexanol. It reaches nearly 100% FE conversion of CO_2 and H_2O to CO and H_2, and nearly 100% transformation of CO and H_2 to desired alcohols [45].
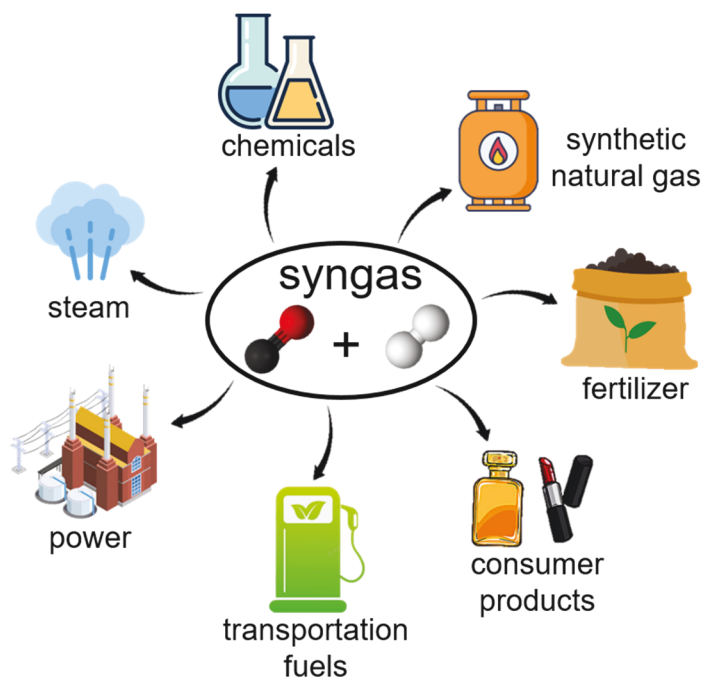
Fig 1.4 Main uses of syngas [46]. Adapted with permission from *React. Chem. Eng.*, 2021, 6 (6), 954-976. [46]. Copyright 2021 Royal Society of Chemistry.

The possible reaction pathway of CO_2 conversion into CO on Ag that was the main catalyst material in this PhD project is shown in Fig 1.5. It is proposed as a two-electron and two-proton reaction [47]. The first step is formation of the bent structure of intermediate $^*CO_2^-$ by a single electron transformation, which is crucial step mentioned in the section of 1.3.2. Subsequently, a proton transfers to $^*CO_2^-$ resulting the formation of $^*COOH$. Another coupled electron-proton transfers to $^*COOH$ and drives on the hydroxyl group in $^*COOH$ to yield a water molecule, leaving $^*CO$ on the catalyst surface. $^*CO$ desorbs from the electrode surface as a main product due to the moderate binding of intermediates on Ag catalysts [47].
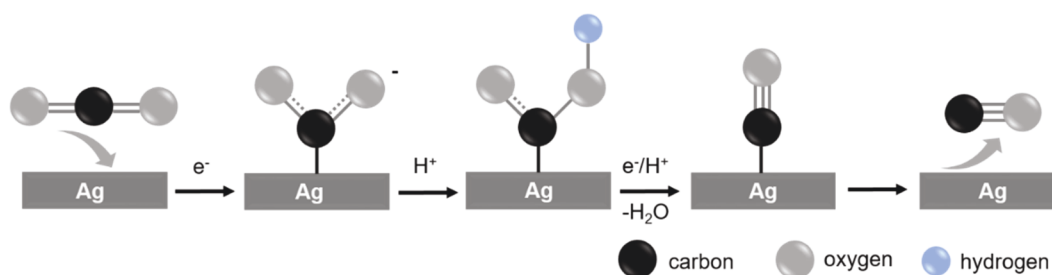
Fig 1.5 Reaction pathway of CO_2 conversion into CO on Ag catalysts [48]. Adapted with permission from *ACS Catal.*, 2020, 10 (15), 8503-8514 [48]. Copyright 2020 American Chemical Society.

1.7 Electrolyzer for electrochemical CO_2 reduction

The electrolysis cell is the fundamental hardware device for performing CO_2 electroreduction. There are mainly two types of configurations available: H-type cell and flow cell. Many researchers have sought to design and optimize the reactors to achieve high current densities for long durations.

1.7.1 Electrochemical cell designs

The classic H-type cell has been commonly used for lab-scale electrochemical CO_2RR because the configuration is low cost, easy to operate, and fast to screen for the catalysts. Its schematic is presented in Fig 1.6. The H-type cell includes two compartments separated by a cation/anion exchange membrane. The electrochemical reactions typically employ a system with three electrodes. The working electrode (WE) is cathode where CO_2RR occurs, while the counter electrode (CE) is anode where the OER processes. The third electrode referred as reference electrode (RE) is used to control and measure the working electrode potential. The commonly used RE include the saturated calomel electrode (SCE), SHE, and the silver/silver chloride electrode (Ag/AgCl). In case of CO_2RR, the measured potentials are converted to the reversible hydrogen electrode (RHE) usually for the sake of comparability. The H-type cell is filled with an electrolyte solution. CO_2 gas is bubbled through the solution to saturate it with dissolved CO_2 molecules. High selectivity of CO_2RR has been obtained in this cell; Liu et al tested colloidal silver nanowires (Ag NWs) in H-type cell, and achieved maximum values of 99.3% for the FE of CO [49]. Ag nanoparticles (Ag NPs) prepared by dip-coating and thermal annealing method in air showed over 90% of CO selectivity under a current density of ~21 mA/cm^2 [50]. However, as stated in section

1.5, the solubility and diffusion of CO_2 in electrolyte solution is quite low under ambient conditions [38]. In this case, the achievable partial current density of desired product is far below than 100 mA/cm^2. The commercial applications for CO_2 electrolysis require high current densities (> 200 mA/cm^2) and long-term operation (> 8000 h or 1 year) with high selectivity and low overpotential, which was highlighted in a gross margin model developed by Kenis and co-workers [51].
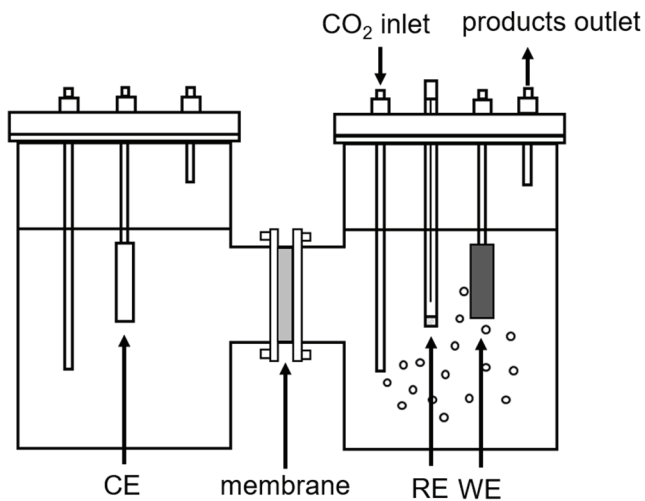
Fig 1.6 Schematic of the H-type cell used in this work

To overcome the mass-transport limitation of the H-type reactor configuration, flow cells have been developed. The reactants are continuously circulated to and away from the electrodes, and the products are transported away from the electrodes. This configuration can be realized at a laboratory scale as well as an industrial scale. This approach has already proved to be highly effective in fuel cells and water electrolyzers [52]. The flow cells employed for CO_2 electrolysis have two primary architectures: microfluidic reactors and membrane-based flow cells [38]. The microfluidic cell (shown in Fig 1.7 (a)), described by Kenis and co-workers [53-54], uses a thin layer (<1 mm) electrolyte flow channel to separate the anode and the cathode. The CO_2 gas diffuses through the GDE and reacts at the electrode-electrolyte interface. This configuration can operate without a membrane. The diffusion of reactants and products is controlled by laminar flow conditions. This system could reach high current densities for CO_2RR through precise control of pH and water management [53-54]. However, it is challenging to scale up this reactor because of the pressure of the microfluidic architecture. The most widely used flow reactor is membrane-

based flow cell, which introduces a polymer electrolyte membrane to separate the anodic component and the cathodic component and attenuate the crossover of products. Zero-gap membrane configuration (shown in Fig 1.7(b)) is one of the prevalent flow cell presented in the literature. There is no space between the catalysts on the electrode and the membrane in the zero-gap membrane based flow cell. Three different membranes have been deployed in this configuration: cation/proton exchange membranes (CEMs) [55], anion exchange membranes (AEMs) [56-57], and bipolar membranes (BPMs) [58]. The CEMs promote the cation includes H^+ from the anode to the cathode. The cathode is required to suppress HER; however, the transport of protons to the cathode favors HER instead of CO_2RR. Therefore, CEMs may not be the most suitable membranes for CO_2RR. BPMs facilitate the dissociation of water into their ionic counterparts under reverse bias, forcing OH^- and H^+ to the anode and the cathode, respectively [38]. The advantages of BPMs are maintaining the constant pH on the electrode and minimizing the crossover of products. The disadvantage of this membrane is the function of BPMs consuming large potential, which reduces the overall energy efficiency of the cell.
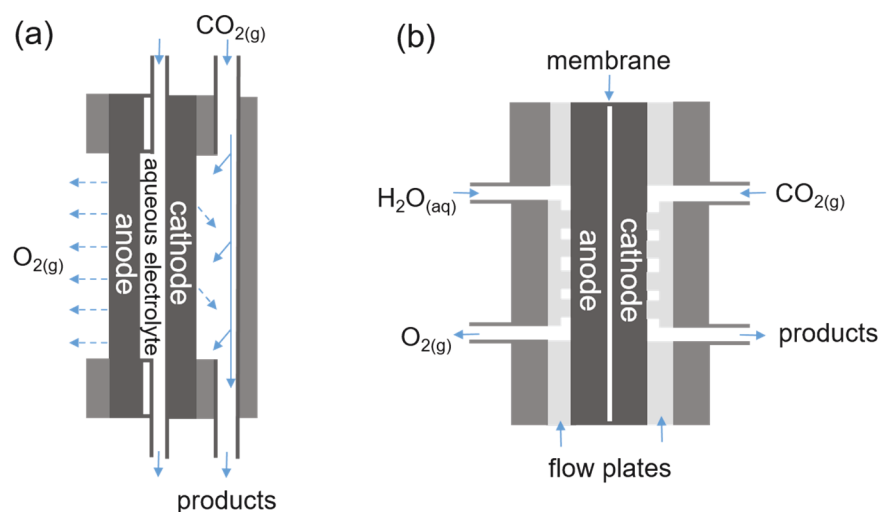
Fig 1.7 Schematic of (a) microfluidic reactor and (b) zero-gap membrane-based flow cell [38]. Reprinted with permission from *Acc. Chem. Res.*, 2018, 51 (4), 910-918 [38]. Copyright 2018 American Chemical Society.

Many of the best performing membrane-based CO_2 flow cells utilize AEMs. AEMs were employed in this project as well. AEMs facilitates the transport of anions (e.g., OH^-, CO_3^{2-}, and

HCO_3^-) from the cathode to the anode compartment. The flow cell equipped with AEMs have been demonstrated high current densities with high CO and hydrocarbon selectivity [59-62]. However, most of the devices exhibit limited durability with performance loss after a few hours of operation [63-64]. The loss of CO_2RR performance may be related to the cathode flooding, (bi)carbonate salt formation in the cathode, and catalyst failure [65]. The flooding refers to water penetrating the cathode and blocking the CO_2 diffusion pathway to active sites of the catalysts. Flooding may happen after a decrease in hydrophobicity of GDE and the break-down of hydrophobic ionomers and/or polytetrafluoroethylene (PTFE) binders in catalyst layer. Flooding may result from the movement of water accompanied with the migration of cations, especially at high concentration of electrolyte and the high potentials [66]. The (bi)carbonate salt formation is caused by the increased local pH at the cathode [67]. During CO_2 electrolysis, CO_2RR and HER consume protons from water molecules and form OH^- ions as a by-product. The OH^- ions react with CO_2 and form HCO_3^- and CO_3^{2-}, significantly reducing the CO_2 availability. The mobility of HCO_3^- and CO_3^{2-} are lower than that of OH^-, and the accumulation of the ions will hinder the membrane ion transport [68]. Furthermore, the accumulation of (bi)carbonate ions with the cross-over of cation ions (e.g. K^+) from the anolyte lead to the precipitation of (bi)carbonate salt on the GDE. The (bi)carbonate salt hampers the CO_2 diffusion and decreases the CO_2RR performance. Another possible reason for decreased CO_2RR performance is catalyst failure referring to degradation of catalysts that lowers the selectivity and rate of CO_2 reduction. The catalyst failure is discussed in section of 1.8.2.

Efforts have been made to improve the cell performance including optimizing GDE material and structure [41,69], reactor design [65], and operating conditions [70-71]. The porous solid electrolyte reactor was designed to use a sulfonated polymer electrolyte buffer layer between cathode and anode [72]. The carbonate ions formed at the cathode were converted back to CO_2 in the solid electrolyte, and recaptured CO_2 was fed back to the CO_2 input stream. By this way, the high CO_2 conversion efficiency and long-term operation were obtained. Xu et al. switched the applied voltages between an operational potential and a lower regeneration potentials to avoid the salt formation and gained 236 h duration with 80% selectivity of C_2 products and 138 mA/cm^2 of C_2 partial current density [70]. The direct injection of water into gas channels has been demonstrated to prevent salt crystallization in a zero-gap flow cell [71].

1.7.2 Gas diffusion electrode

The GDE design plays a critical role on CO_2 reduction flow cell. It presents a porous material with high surface area and comprises an electrocatalyst layer deposited on a porous gas diffusion layer (GDL). It reduces the CO_2 diffusion pathway to the surface of the catalyst through a liquid phase: from ~50 μm in H-type cells (an approximate thickness of diffusion layer) to ~50 nm using GDEs, which allows for high current densities [63]. The most common GDE for CO_2 electrolysis consists of a microporous layer (MPL, typically compressed carbon powder) and macroporous support (MPS, typically carbon fibers layer (CFL)). The MPS provides mechanical stability and electrical contact for the GDEs as well as distribution of CO_2 gas through its macro-scale pores [73]. The structure and composition of MPL and MPS influence the transport of reactants and products through electrolyzers, which affects the transport of chemical species to and from the catalyst and thus the CO_2RR electrolyzer performance [69]. The hydrophobicity is required for prevention of GDE flooding and often enhanced by coating with a fluorinated polymer, such as PTFE. The loading of PTFE in each GDE layer should be optimized to achieve desired hydrophobicity, good GDL electrical conductivity, and sufficient gas permeability [69]. Kim et al demonstrated that the GDE containing 10% PTFE in MPS and 20% PTFE in MPL with a thickness of 190 μm for MPS exhibited the highest partial current density of CO on Ag catalyst compared to higher or low concentration of PTFE in MPS and MPL [74]. The porosity and thickness of GDE are also crucial for CO_2RR electrolysis because they affect CO_2 and water transport, (bi)carbonate formation and local pH [69]. Even though several GDLs have been developed for fuel cells and electrolyzers, most of them are not suitable for long-term CO_2 electroreduction operation, especially at high current density and the processes involving liquid products [75]. To improve the stability of GDL, functionalization of carbon-based GDLs with hydrophobic compounds was applied [76]. Another approach to increase the stability is to use non-carbon-based GDLs, such as porous PTFE [59,62].

1.8 Colloidal catalysts

1.8.1 Synthesis of colloidal catalysts

The physicochemical properties of catalysts are strongly influenced by their size, shape and composition; structural and compositional design provides an effective strategy to boost their performances and broaden their applications. Effort has been devoted to developing stable electrocatalysts that can reduce CO_2 with high efficiency and selectivity towards one specific

product. Traditional synthetic routes usually lead to forming low surface energy facets, which usually have low catalytic activities [77]. Compared to traditional methods, colloidal protocol is one of the most powerful wet-chemistry techniques to achieve the nanocatalysts with narrow size distribution, well-defined shape, and precise composition through the appropriate reaction conditions. A typical colloidal approach involves the reduction or decomposition of metal precursors in the presence of surfactants/capping agents in either aqueous or organic media [78]. Nanomaterial structures that can be obtained through colloidal synthesis, range from sphere, cube, wire, and triangular plate to more complex structures, such as rhombic dodecahedra, and core–shell heterostructures [78-79]. To rationally tailor the nanocatalysts to desired shape and size, many reaction parameters need to be considered during the synthesis. Reaction temperature, reaction time, ratio of reactants (e.g., metal ion precursor and reducing agent), injection speed of chemicals, atmosphere, and reactor volume need to be considered. However, the action of the so-called surfactants and capping agents is especially important. The binding affinities of capping agents are varied on the crystal facets. The preferential capping can effectively hinder the growth of a certain surface facet, thus crucially affecting the nucleation and growth kinetics of nanomaterials for controlling the nanocrystal structure [80]. Most of the capping agents are organic molecules or polymers, such as polyvinylpyrrolidone (PVP), polyvinyl alcohol (PVA), oleylamine (OAm), oleic acid, branched polyethylenimine (BPEI), polyethylene glycol (PEG), and cetyltrimethylammonium bromide (CTAB).

The capping agents may functionalize as a byproduct liberated during the synthesis. For example, decomposition of metal carbonyl compounds during a synthesis liberates CO binding strongly to many metal surfaces [81-82]. The adsorption of CO can hinder the reaction rate on certain facets resulting in anisotropic growth. More importantly, the capping agents can stabilize the high-energy surface of the nanoparticles and protect them from overgrowth and aggregation. They can also affect the reduction kinetics by forming complexes with original metal precursors and control the growth of nanocatalyst via the selective adsorption on particular crystallographic planes facets [83]. Through its chemical interaction with a metal surface, the presence of a capping agent can change the order of free energies for different crystallographic planes, and thus their relative growth rates to surfaces with different surface orientations [79]. For example, PVP can serve as capping agents of which oxygen atoms bind most strongly to the {100} facets of Ag [84].

Citrate ion binds most strongly to {111} facets for Pd favoring the formation of decahedrons, icosahedrons, and octahedrons [85]. After the synthesis, the capping agents play a vital role to protect the nanomaterials from aggregation and decomposition.

1.8.2 Colloidal catalysts for CO_2 electroreduction

Catalysts are essential for CO_2 electrolysis, as they decrease the activation barrier (overpotential) and direct the electrolytic reaction towards the desired target product. Nanomaterials produced via colloidal synthesis have shown potential for industrial CO_2 reduction applications due to easy scaling-up of their production and simplicity of their deposition on GDEs. The selectivity and rate of electrochemical CO_2 conversion can be governed by controlling size, shape, and compositions of colloid nanocatalysts. Furthermore, nanocatalysts synthesized by colloidal means represent a material platform to correlate the catalytic performance with its structure and composition, which is of significant importance in advancing the knowledge of the structural and compositional reaction sensitivities and the degradation pathways of catalysts for electrochemical CO_2 conversion [86-87].

As catalyst size reduces towards the nanoscale, the surface-to-volume (or mass) ratio increases, and size effect becomes more pronounced [88]. The small nanomaterials with high density of low-coordinated atoms show high surface energy. The colloidal nanocatalysts with different size may reveal distinct performances for CO_2 reduction; the performance can be adjusted by controlling the structure and size of nanomaterials [39]. For example, the ultrathin Ag NWs prepared with diameters smaller than 25 nm synthesized through polyol method obtained nearly 100% of FE for CO and lower overpotentials compared to the thicker Ag NWs with diameters of 100 nm in an H-type configuration with 0.1 M $KHCO_3$ [49]. Pd nanoparticles with narrow size distribution (ranging from 2.4 to 10.3 nm) were prepared using $NaBH_4$ and sodium citrate as a reductant and a stabilizing agent. The FE for CO production vary at -0.89 V vs RHE from 5.8% over 10.3 nm nanoparticles to 91.2% over 3.7 nm nanoparticles in an H-type cell filled with 0.1 M $KHCO_3$; this is due to the changing ratio of corner, edge, and terrace sites [89].

Previous studies have shown that the nanocatalyst morphology influences CO_2RR performance. The adjustment of catalyst morphology causes the changes in particular exposed facets and the

surface area of the materials, which in turn affects the number of available active sites. Some researchers have demonstrated that colloidal nanomaterials, with optimal facet and edge site, may tune electrocatalytic activity and selectivity for CO_2RR through precise shape-control synthesis. Gregorio and co-workers employed the colloidal Cu nanocrystals of different shapes (i.e., sphere, cube of (100) facets, and octahedra of (111) facets) at commercial scale current densities in a gas-fed flow cell. They observed that Cu sphere nanocatalysts are not selective toward any specific product, Cu cube nanocatalysts are highly selective toward ethylene, and Cu octahedral nanocatalysts are selective toward methane [90]. The triangular silver nanoplates reveal significantly improved FE of CO, enhanced current density, an ultralow overpotential, and considerable durability (7 days) compared to similarly sized Ag nanoparticles and bulk Ag, which is due to both the optimum edge-to-corner ratio and the predominant Ag(100) facet in the triangular silver nanoplates [91].

Besides the tuning of size and morphology, tuning composition of nanocatalysts via colloidal approach has also attracted attention. Considering Ag has high catalytic performance as well as lower price and richer reserves compared with Au, the alloys based on Ag have been widely reported in CO_2 conversion. For example, the bimetallic Ag-Cu nano-dimers of tunable Cu domain size (Ag_1-$Cu_{0.4}$, Ag_1-$Cu_{1.1}$, and Ag_1-$Cu_{3.2}$) were prepared by pre-synthesizing Ag NPs as nucleation seed for the growth of the Cu domain through colloidal chemistry. The Ag_1-$Cu_{1.1}$ nano-dimers show a 3.4-fold enhanced FE and a 2-fold improved partial current density of C_2H_4 at -1.1 V vs RHE in a CO_2-saturated 0.1 M $KHCO_3$ solution compared with the Cu NPs of similar size and shape, which is attributed to design multicomponent catalysts efficiently [92].

Most studies have focused on exploring the selectivity and the activity of colloidal electrocatalysts. The durable electrochemical performance is an equally important characteristic of catalysts as the high activity and selectivity for commercial applications of CO_2RR. Nevertheless, the structural alterations of the catalysts have received much less attention than activity/selectivity issues. Understanding the degradation pathway occurring during operation and developing mitigation strategies of structural alteration may improve catalyst design, facilitating the translation of fundamental knowledge to technological application. The degradation mechanism of the catalysts during CO_2 electroreduction includes agglomeration, corrosion,

Ostwald ripening, detachment, and chemical poisoning [31]. The degradation may change the surface area and number of active sites. Thus, it affects the selectivity and activity of catalysts [93].

1.8.3 Surfactant effects for CO_2 electroreduction

The colloidal synthesis of nanocatalysts with precise control of size, morphology, and composition have been successful used for catalytic applications in electrochemical reactions (e.g. CO_2RR and OER). Capping agents are usually required in colloidal synthesis. After the synthesis process, capping agents or their decomposition products presumably remain in the catalyst suspension. They can be divided into two types: ligands adsorbed on the catalyst surface and free ligands (excess capping agents) in the suspension (shown in Fig 1.8). Understanding how these surfactants affect electrolytic performance is important for optimizing the utilization of colloidal catalysts for electrochemical applications. It has been proved that surfactants influence the catalytic performance through steric and electronic effects [94-95]. Surfactants sterically contain a particular conformation for an adsorbed intermediate or block certain reactants from reaching the catalytically active sites, affecting the activity and selectivity [96]. The electronic effects refer to that ligands tuning the electronic structure of a catalyst surface by modulating the electron density, e.g. via Lewis acid-based interactions [96].
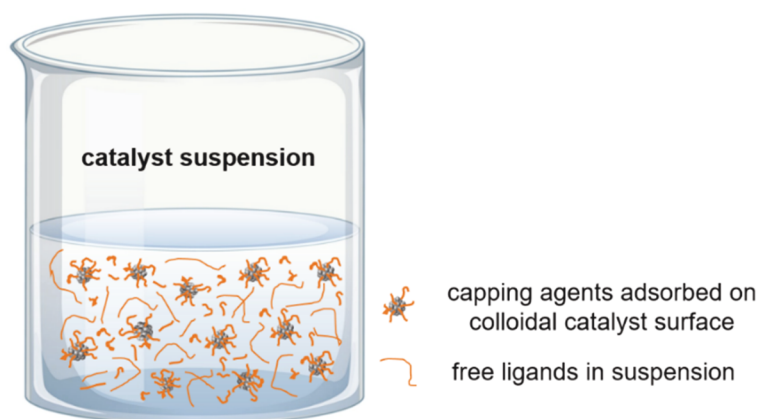
Fig 1.8 Schematic of capping agents adsorbed on the catalyst surface and free ligands in the catalyst suspension.

The local environment plays an important role in driving CO_2 reduction and suppressing the HER. The local environment for CO_2RR is the interfacial region of the electrode/electrolyte in an

H-type cell and the electrode/gas/water triple-phase boundary on the GDE in a flow cell reactor. This microenvironment can be modulated by surfactants on colloidal nanomaterials. The surfactant can change permeable selectivity, tune cation adsorption and interfacial solvation, participate in chemical activation, and template active site selection [96]. An increasing number of studies have been reported to improve CO_2RR by the tenability of molecules on nanocatalysts surface. Kim and co-workers applied OAm, oleic acid, and dodecanethiol to prepare Ag NPs modified with amine, carboxyl, and thiol groups, respectively [97]. The amine functional group on Ag nanoparticles shows highest FE for CO production, while the thiol group favors HER. The density functional theory (DFT) calculation supports the results: the attaching amine molecules destabilize the hydrogen binding, while the thiol molecules show strong hydrogen binding [97]. From Breugelmans's group, the bimetallic Cu-Ag core-shell nanoparticles were produced with three different surface modes: (i) capped with OAm, (ii) capped with monoisopropylamine, and (iii) surfactant-free with reducing borohydride agent respectively and these nanoparticles were applied on GDEs in flow reactor [98]. Cu-Ag capped with OAm gives a lower overpotential for hydrocarbon production, whereas Cu-Ag capped with monoisopropylamine and surfactant-free favor syngas production; this can be associated with gradual increases in the electrical conductivity and active surface area after each surface treatment [98].

Capping agents attached on the catalyst surface may block the active sites and reduce the activity of catalyst. For example, capping agent PVP prefers to adsorb on Ag(100) facet, which is highly active for CO_2RR [79]. The remaining capping agents also add complexity to the system, such as uncertain coverage density of capping molecules, noncovalent interaction between capping molecules and reactants, and charge transfer at the organic−metal interface [99]. Therefore, it is crucial to activate the colloidal catalysts by removing the capping agents.

Some methods have been developed to clean the catalyst surface, such as chemical washing [100], thermal treatment [101], plasma treatment [102], ozone treatment [103] and photonic curing [104]. Chemical washing procedures involve: (1) repeatedly washing catalysts with chemical solvent and collecting catalysts by centrifugation or precipitation and (2) displacing long-chain hydrocarbons on catalysts surfaces with small molecules, which are easy to dispose [100]. It is difficult to separate small unsupported catalysts from the solvent with regular centrifugation. In

practice, the poor/good solvent mixtures are employed (e.g., acetone/water for PVP removal and ethanol/hexane for oleylamine removal) [99]. Chemical treatment is flexible, but it consumes a large quantity of chemicals, which contradicts to green chemistry principles. Thermal treatment is also used to decompose the ligands; however, it may cause sintering [101]. Photonic curing has been demonstrated as an effective method to activate and stabilize the copper nanowires for the electrochemical reduction of CO_2 in our previous work [104]. Electrochemical cleaning is also useful in dealing with the capping agents. For example, electrochemical potential cycling was carried out between 0 and 1.0 V vs RHE to remove PVP and OAm/oleic acid on Pt nanocubes in 0.5 M NaOH and 0.5 M H_2SO_4, respectively. The electrochemical treatment shows it is more effective to remove capping agents in alkaline solution than acidic solution [105]. It is noted that harsh treatment may cause undesired morphological changes (e.g., agglomeration) that reduce the activity of catalysts, while the gentle approaches to surfactant cleaning may leave residues that still block the active sites [99]. Furthermore, readsorption of capping agents and poison from the decomposition of ligands compounds should not be ignored [93].

1.9 Thesis outline

Electrochemical CO_2RR has shown promise in converting CO_2 to value-added chemical feedstock, which combines with renewable power supply. Among the products of CO_2 electroreduction, carbon monoxide attracts high attention due to its relative low cost from CO_2 electrolysis and high market demand. Ag is an excellent catalyst for electrochemical CO_2-to-CO conversion. The structure of the nanocatalysts plays an important role for CO_2RR performance. The nanomaterials with well-defined sizes and shapes can been obtained through colloidal approaches controlled via capping agents. Most of the research have explored the selectivity, activity, and stability of colloidal catalysts. However, there are a few studies related to the influences of capping agents from the colloidal synthesis, especially free ligands in the catalyst suspension. This dissertation presents a study of activity, selectivity, and stability of colloidal Ag nanocatalysts capped with different capping agents for electrochemical CO_2 reduction in the H-type cell (shown in Publications 5.1, 5.9, and 5.10) and the gas-fed zero-gap flow cell (shown in Publications 5.2, 5.3, 5.4, 5.5, 5.6, 5.7, and 5.8). It aims to correlate the capping agents with nanocatalysts for CO_2RR performance and further promote Ag nanocatalysts on electrochemical CO_2RR at commercial scale (e.g., electrolysis stability with high product partial current density).

The colloidal Ag catalysts (Ag NWs and Ag nanocubes, Ag NCs) were synthesized through a polyol process with PVP as capping agents to control the size distribution and the shape. PVP adsorbs on the surface of Ag catalysts that blocks the active sites and reduces the selectivity and activity of the catalysts for CO_2RR, even after chemical washing by acetone/water. Electrochemical method was applied to remove the capping agents in the H-type cell as shown in section 2.1 and Publications 5.1 and 5.10.

To achieve industrially relevant CO_2 conversion rate, the CO_2 electrolysis was investigated in a gas-fed zero-gap flow cell. The influence of capping agents, including ligands adsorbed on Ag catalyst surface and free ligands in the Ag catalyst ink, was studied (section 2.2 and 2.3). The commercial PVP-capped Ag NPs with the initial sizes of 10, 40, and 100 nm were used in the flow cell to study the structural alterations during the CO_2RR as shown in Publication 5.2. The effects of different ligands (i.e., BPEI, PVP, PEG, and citrate) on Ag NPs were discussed in Publication 5.6. The influence of excess capping agents (i.e., free ligands in the ink) on the stability of the flow cell and on the Ag degradation pathway was included in Publications 5.3 and 5.6, respectively.

In addition, a novel analytic method based on the combination of inductively coupled plasma mass spectrometry (ICP-MS) and energy dispersive-X-ray (EDX) spectroscopy was introduced to help visualize and quantify flooding phenomena in the flow cell (shown in Publication 5.7). Some parameters (e.g., the cracks on GDEs) influencing the stability of the gas-fed zero-gap electrolyzer have been investigated in Publication 5.8. Furthermore, the limitation of identical location scanning electron microscopy (IL-SEM) in the presence of capping agents was investigated in Publication 5.9.

2 Results and discussion

2.1 Selectivity and activity of colloidal Ag catalysts in H-type cell

As stated in previous sections 1.4 and 1.8.2, Ag catalysts with well-defined size distribution and faceting display excellent selectivity and activity for CO_2RR. In some cases, however, the CO_2RR performance of colloidal Ag catalysts is hindered by the capping agents (e.g., PVP) used in the process of synthesis. There are various methods to remove the capping agents, such as chemical washing, thermal treatment, plasma treatment, ozone treatment and photonic curing [77,99]. Here the selectivity and activity of Ag NWs and Ag NCs capped with PVP were studied, and electrochemical means were applied to activate the colloidal Ag nanocatalysts.

Ag NWs were synthesized by the PVP assisted-polyol process. After washing with water/acetone, some PVP still adsorb on the surface of Ag NWs, which blocks the active site of catalysts and promotes HER. The CO_2RR itself was utilized to activate the Ag NWs catalysts in an H-type cell. The electrochemical activation denoted hereinafter *electrochemical looping* (ec-looping) refers to a sequence of potentiostatic CO_2 electrolysis. The electrolysis started at a fixed potential (E_{start}) of -0.6 V vs RHE to a variable more negative vertex potential (E_{vertex}) in a stepwise manner ranging from -0.9 V vs RHE to -1.3 V vs RHE. The loop is closed through the backward run of electrolysis and ended at the starting potential. The electrolysis time for each applied potential was 20, 40, and 60 min. It is identified as the most effective treatment for the removal of capping agents applying electrochemical looping to vertex potential of -1.3 V vs RHE with the individual 40 min-long electrolysis for each potential, which achieves over 80% of FEs for CO, as shown in Fig 2.1 (a). After pretreatment by electrochemical looping, the true potential-dependent product distribution was presented in Fig 2.1 (b). The CO faradic efficiencies are close to 100% after the successful removal of PVP, which is much higher than the ones for the as-prepared catalysts. The removal of PVP was confirmed by X-ray photoelectron spectroscopic (XPS) inspection in Fig 2.1 (e). When extending the E_{vertex} from -0.9 V vs RHE to -1.3 V vs RHE, the elemental concentrations for nitrogen originating from the PVP capping agent decrease. This observation is full agreement with the corresponding increase of the CO selectivity.

25
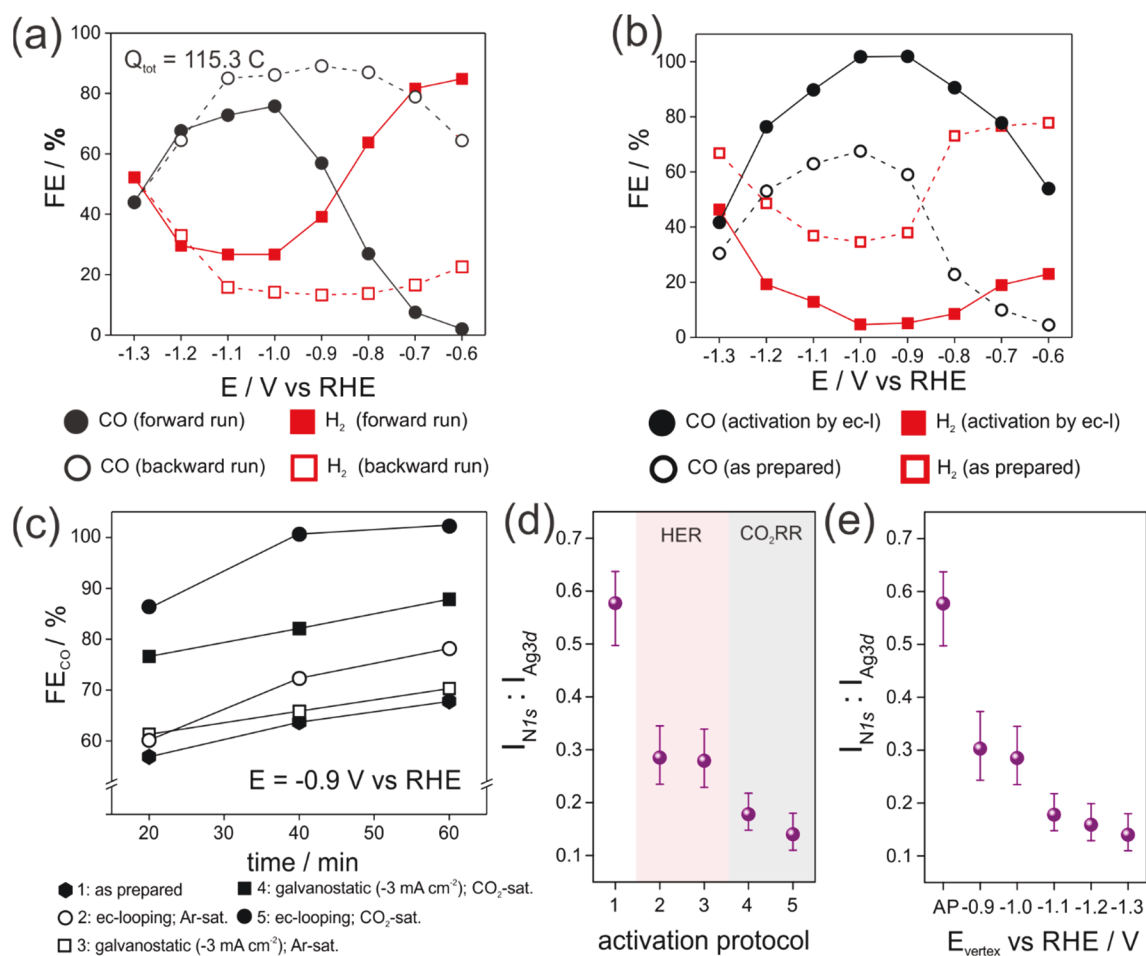
Fig 2.1 (a) Product distribution in the forward and backward runs of the electrochemical looping experiments (40 min duration at each potential) employed on Ag NWs catalysts in CO_2-saturated 0.5 M $KHCO_3$. (b) The CO_2RR product distribution for 1 h lasting electrolysis experiments on as-prepared Ag NWs catalysts and those pretreated by an electrochemical looping (E_{vertex} = -1.3 V vs RHE, 40 min duration at each potential). (c) Faradic efficiencies of CO at potential of -0.9 V vs RHE for 1 h electrolysis after different activation protocols. The integrated intensity of N1s emissions normalized to the corresponding integrated intensity of the Ag3d emission (d) of different protocols corresponding to (c) and (e) after the ec-looping treatment with different E_{vertex}. Adapted with permission from *ACS Catal.*, 2020, 10 (15), 8503-8514 [48]. Copyright 2020 American Chemical Society.

In addition, ec-looping in Ar-saturated electrolyte and in CO_2- and Ar- saturated electrolyte with galvanostatic electrolysis were tested. The selectivity of CO has been further improved after the ec-looping in CO_2 electrolysis than in HER, as shown in Fig 2.1 (c), which corresponds to the

removal of PVP in Fig 2.1 (d). It demonstrates that the CO formed during the CO_2 electrolysis is vital for removing the capping agents efficiently. More details can be found in Publication 5.1.

The similar hysteresis was observed in PVP-capped Ag NCs. However, Ag NCs show some degradation after the electrochemical activation. It is due to lower thermodynamic stability of Ag NCs compared with Ag NWs [106]. More details are described in Publication 5.10.
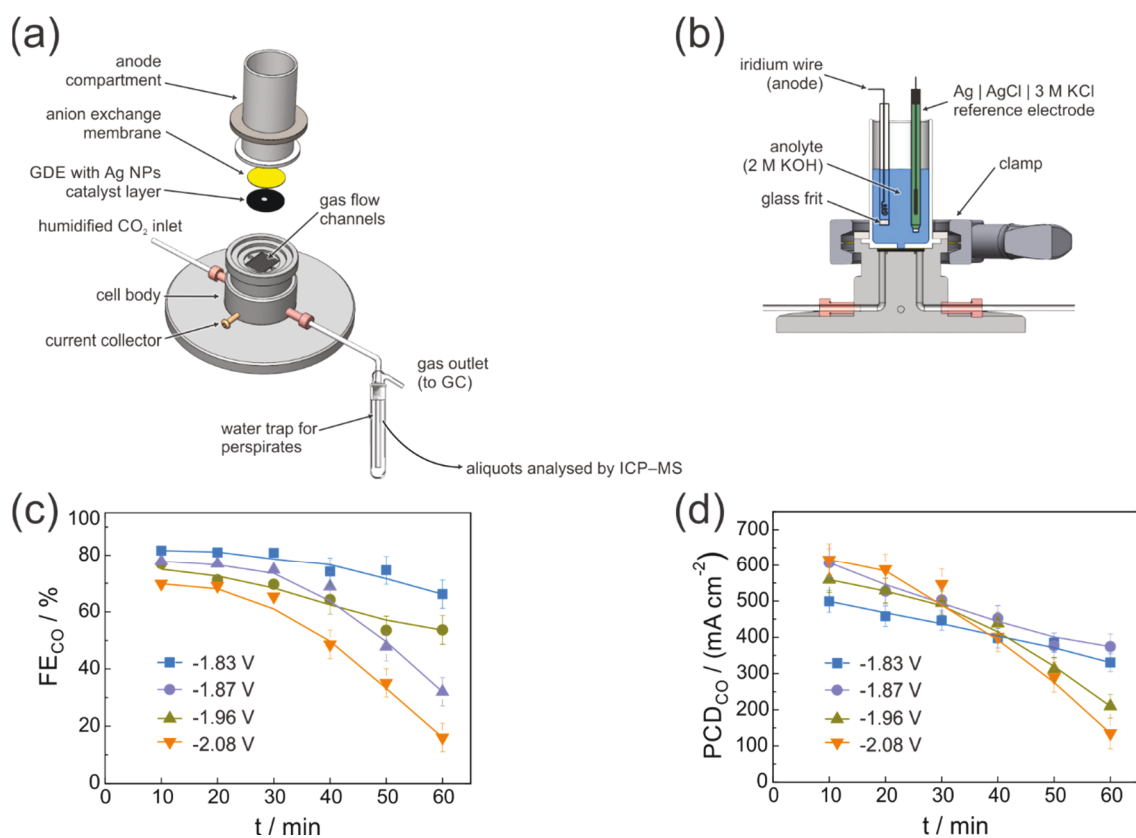
Fig 2.2 Schematic for (a) the exploded and (b) the cross-sectional view of the gas-fed zero-gap for the electrolysis of CO_2. (c) Faradic efficiencies of CO and (d) PCD of CO at different applied potentials with 2 M KOH in zero-gap flow cell for Ag NC catalysts. Adapted with permission from *ACS Catal.*, 2020, 10 (21), 13096-13108 [107]. Copyright 2020 American Chemical Society.

As discussed in section 1.5, CO_2 transport becomes a rate determining process at high current densities. To overcome this transport limitation, the gas-fed zero-gap electrolyzer was applied in the following studies. The schematic of a flow cell with a water trap for perspiration is represented

in Fig 2.2 (a-b). The faradic efficiencies of CO reach more than 70%, and the partial current densities (PCD) of CO achieve more than 500 mA/cm^2 for carbon-supported Ag NCs after 10 min electrolysis, as presented in Fig 2.2 (c-d). However, the performance of CO$_2$RR degrades as the electrolysis time increases (more details in Publication 5.5). Similar results are shown in Publication 5.4. The stability of the catalysts and the electrolyzer system were analyzed to address the key parameters for the degradation of electrochemical CO$_2$RR performance in this electrolyzer.

2.2 Stability and activity of colloidal Ag catalysts in zero-gap flow cells

The catalyst stability is as crucial as activity and selectivity for commercial application of CO$_2$RR. As discussed in section 2.1, relatively high selectivity and activity are achieved in the initial electrolysis on the colloidal Ag catalyst in the zero-gap gas-fed electrolyzer. The studies in this section prioritized the stability of nanocatalysts in the presence of capping agents. The colloidal Ag NPs with different capping agents were used for CO$_2$ electrolysis in the gas-fed zero-gap electrolyzer (Fig 2.2 (a-b)).

IL-SEM is a useful tool for structural alterations research during electrolysis; it links the morphological changes to the changes of the catalytic performance. However, IL-SEM shows its limitation in the case of the surfactant-capped catalysts. The activity of catalysts might be altered upon exposure to the electron beam of SEM during pre-electrolysis. The spot subjected to SEM shows no or little changes during the electrolysis, even the entire catalysts degrade. The details are shown in Publications 5.5 and 5.9. To avoid any misinterpretation caused by the IL-SEM technique, the following studies about Ag nanocatalysts degradation were collected using SEM images of several different spots at the electrodes.

Commercial PVP-capped Ag NPs with the sizes of 10, 40, and 100 nm were used. The Ag NPs were drop casted on the GDEs. The SEM images and size distribution of as-prepared Ag NPs deposited on the GDEs were shown in Fig 2.3 (d-f). The SEM images display the well disposition of Ag NPs on the MPL of GDEs, and the estimated sizes are in agreement with the values indicated by the company. According to SEM, the number of NPs (in terms of volume or mass) on the surface of GDE exhibited diversity that can be explained by the distribution of Ag NPs inside GDE. The Ag NPs with the sizes of 10 nm and 40 nm penetrate the MPL and the cracks of GDE to the

CFL. Whereas, the 100 nm Ag NPs were detected in GDE, except the areas of MPL far away from the big cracks. In other words, a large amount of Ag NPs is inside GDE, and the Ag NPs might not take part in the electrolysis reaction.
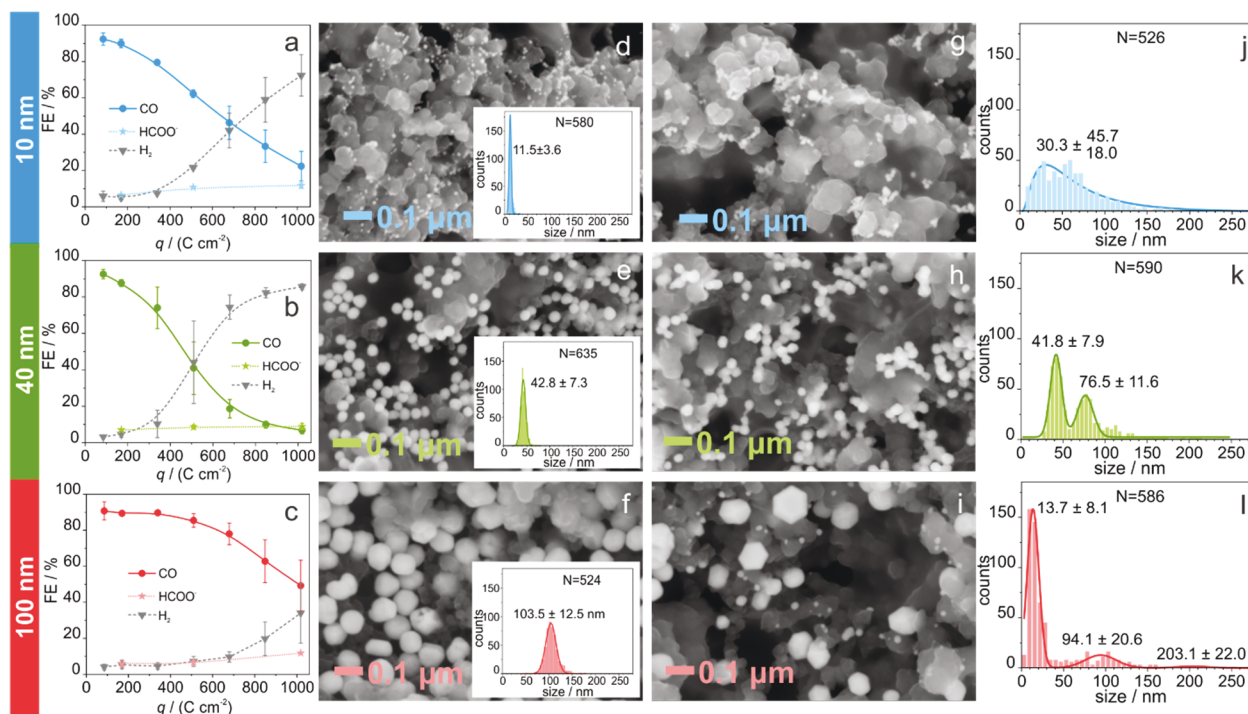
Fig 2.3 (a-c) FEs of CO, HCOO$^-$, and H$_2$ versus charge passed during galvanostatic CO$_2$ electrolysis at j = -283 mA/cm^2 employing Ag NPs catalysts. (d-f) SEM images of as-prepared Ag NPs catalysts on GDE. The inset shows a histogram representing the size distribution of the Ag NPs. (g-i) SEM images of Ag NPs and (j-l) histograms showing the particle size distribution of Ag NPs after galvanostatic CO$_2$ electrolysis at j = -283 mA/cm^2 with the charge of 1018.4 C/cm^2. The SEM images were measured after precipitation removal. The sizes of Ag NPs: (a, d, g, j) 10 nm, (b, e, h, k) 40 nm, (c, f, i, l) 100 nm. Adapted from ref. [108].

The formed products during galvanostatic CO$_2$ electrolysis at current density j = -283 mA/cm^2 and the structure changes of pre- and post-CO$_2$ electrolysis on Ag NPs catalysts are shown in Fig 2.3. The initial FE of CO reach ~90-93% during CO$_2$ electrolysis and is nearly identical for three sizes of NPs (Fig 2.3 (a-c)). The FE of CO drops drastically over time. After electrolysis, precipitation was found in GDEs. After water washing, the structural alterations were analyzed by

SEM (shown in Fig 2.3 (g-l)). In the case of 10 nm NPs, the particles tend to agglomerate, and some of them reach 100 nm. For 40 nm NPs, a large fraction of NPs remains on the initial size, and agglomerated NPs could be seen as well. The 100 nm NPs display the fragmentation and faceting of individual NPs, which is related to cathodic corrosion. The faceting of spherical NPs is opposite from the degradation behavior of Ag NCs fragmenting and changing the cubic shape to more spherical during CO_2 electrolysis, which could be found in Publication 5.5. More details are shown in Publication 5.2.
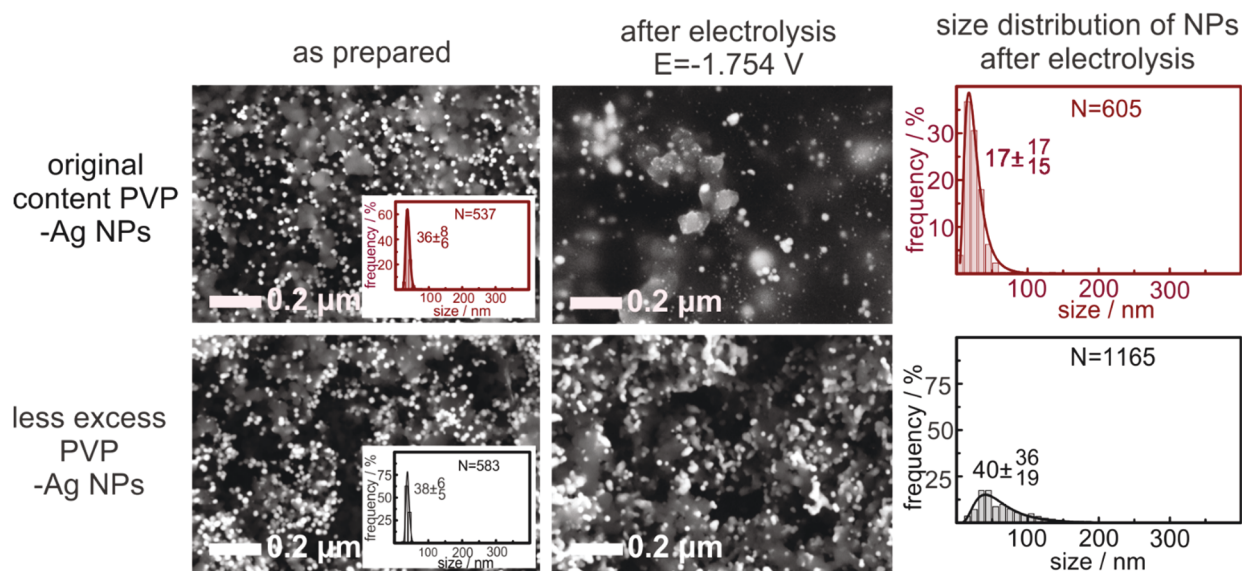
Fig 2.4 SEM and the particle size distribution of the Ag NPs with original content PVP and less excess PVP before and after electrolysis at potential of -1.754 V vs Ag/AgCl with the charge of 300 C/cm^2. Adapted from ref. [109].

In addition, the colloidal Ag NPs stabilized by four ligands (i.e., BPEI, PVP, PEG, and citrate) with the size of ~40 nm were used to investigate the effect of capping agent on structural alterations during CO_2 electrolysis in the zero-gap flow cell. The activities and structural alterations of Ag NPs capped with different ligands display distinctiveness that obviously depends on the chemical nature of capping agents. Moreover, the effect of the excess PVP on the degradation pathway was studied. The results were summarized in Fig 2.4. Most excess PVP was removed by centrifugation to obtain the Ag NPs with less excess PVP content. Compared with the original NPs from the manufacturer, the size distribution seems unaffected by the removal of the excess PVP.

Nevertheless, the structural alteration is markedly changed. The corrosion is observed for the original content PVP-Ag NPs while the Ag NPs with reduced PVP content show coalescence. It could be concluded that the degradation pathway is affected by the capping agent absorbed on the catalyst surface and also the excess capping agents in the catalyst ink. The details are in Publication 5.6.

Even though the Ag catalysts undergo structural degradation, the loss of the electrochemical CO_2RR performance could be regained at least in the initial electrolysis in the "recovery" experiments shown in Fig 2.5. The "recovery" experiments were performed as follows: place the GDEs after 1st electrolysis onto Milli-Q water for precipitate removal, then dry, and use the "cleaned" GDEs for electrolysis again (2nd electrolysis). The same phenomena are presented in Publications 5.2, 5.6, 5.8. In this case, it is safe to conclude that the loss of CO_2RR performance is not caused by the degradation of the Ag catalysts in this gas-fed zero-gap electrolyzer.
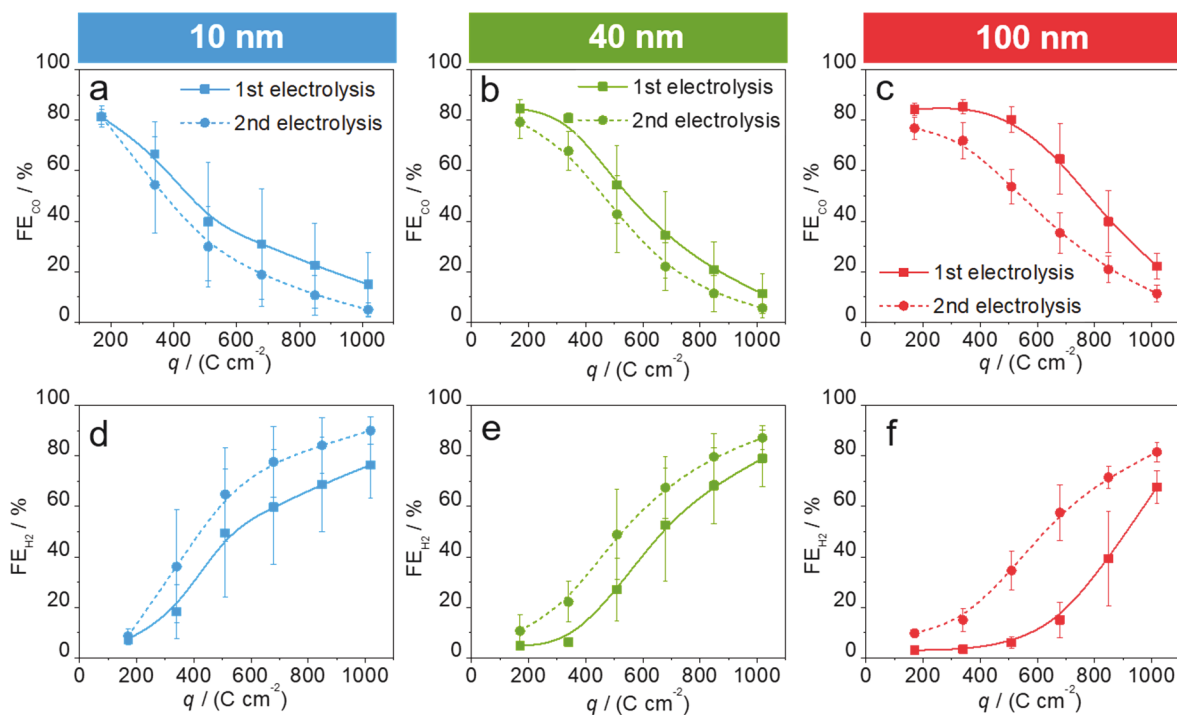
Fig 2.5 FEs of (a-c) CO and (d-f) H_2 versus charge passed during galvanostatic CO_2 electrolysis at j = -283 mA/cm^2 employing PVP-capped Ag NPs catalysts in gas-fed zero-gap electrolyzer for 1st and 2nd electrolysis. The size of NPs: (a, d) 10 nm, (b, e) 40 nm, (c, f) 100 nm. Reprinted from ref. [108].

2.3 Stability of gas-fed zero-gap electrolyzer

In section 2.2, it has been proved that the degradation of the Ag electrocatalysts is not responsible for the loss of the CO_2 electrolysis performance in the gas-fed zero-gap electrolyzer. As discussed in section 1.7.1, flooding and precipitation on GDE reduce CO_2RR performance in the flow cells. The flooding depends on diverse physical-chemical processes. One example is the architecture of GDEs: their hydrophobicity, thickness, and porosity [41,69,73]. A few other factors include the applied electrode potential, the pH of the electrolyte [65], the temperature and pressure, and the thickness of employed membranes [69]. For this PhD project, the influence of cracks of GDE and the excess surfactant were studied. The analytical approach, based on combination of EDX mapping and ICP-MS analysis, were employed to visualize and quantify the flooding-related phenomena in GDEs, as seen in Publication 5.7.

The four commercial GDEs with different ratios of cracks have been selected as Ag NWs supported electrodes in the gas-fed zero-gap electrolyzer. The GDEs with abundance of cracks show high and sustained catalytic activity, while the fast drop of CO_2RR performance was observed for non-cracked GDEs. Based on SEM and EDX elemental analysis combined with ICP-MS inspection, it is demonstrated that the cracks serve as preferential pathways for the electrolyte transport through the MPL and mitigate the flooding in GDEs. The details could be found in Publication 5.8.

The studies of excess surfactant influence were carried out on as-purchased PVP-capped Ag NPs from the company (referred as original PVP content-Ag NPs) and lower PVP content-Ag NPs obtained through the centrifugation to remove most of free PVP ligands in the catalyst ink. In one hour electrolysis experiments, the stability of CO_2RR decreases faster with increases in the loading of original PVP content-Ag NPs on the 10 nm Ag NPs catalysts. The potentials shift to more negative values that indicates the reaction transition from CO_2RR to HER. However, the FE of CO could be stabilized for an hour after removing the majority of excess PVP, even at high mass loading of Ag. Extending the electrolysis time to 2.5 hours on 10 nm NPs, the distinction is clearer (Fig 2.6 (a-b)). The FE of CO on original PVP content-NPs decrease to below 50% after 30 min electrolysis and the high FE of CO (~90%) extend to 60 min on lower content PVP-NPs. The EDX mapping of K element after one hour electrolysis is shown in Fig 2.6 (d). The precipitation has

covered the surface of MPL, and the entail of GDE for electrode that was deposited with original PVP content Ag NPs; for less PVP content Ag NPs, it appears in the cracks and leaves the catalyst layer active for CO_2RR. The perspiration is an important factor for the flooding. The perspiration was quantified by employing a liquid $K_2CO_3/KHCO_3$ trap in the gas outlet of the electrolyzer and analyzing via ICP-MS. The schematic of trapping perspiration was shown in Fig 2.2 (a). The amount of K in the trap constantly raises along with the function of the electrolysis time/charge. More perspiration appears from PVP-deficient GDE, as shown in Fig 2.6 (c). The correlation of the perspiration and the FE of CO demonstrates that the excess PVP blocks the microscale fluid channels of the GDE and decreases the perspiration, thus facilitating the flooding on the GDEs. The details could be found in Publication 5.3.
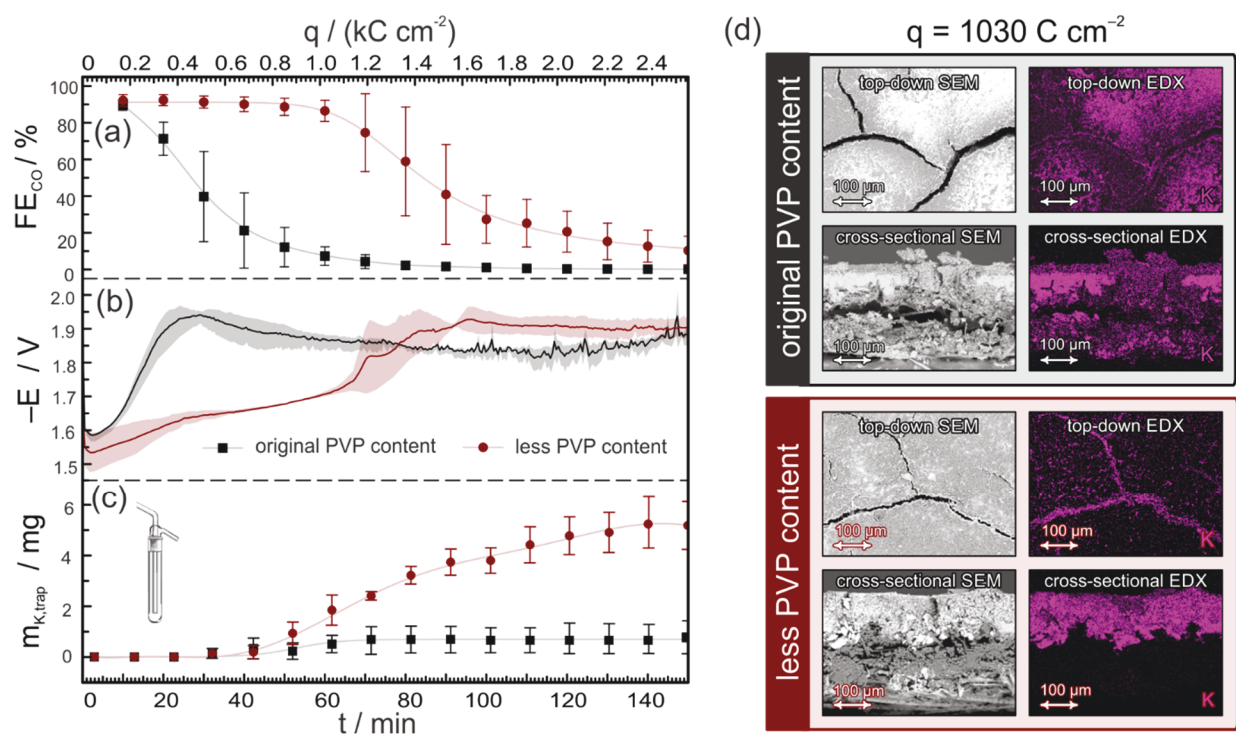
Fig 2.6 (a-c) Comparison of the performance of two GDEs deposited with original and less PVP content during galvanostatic CO_2 reduction in a gas-fed zero-gap electrolyzer at a constant current density of -283 mA/cm^2. Plane (a) shows the Faradaic efficiency of CO production, plane (b) shows the measured electrode potential vs Ag/Ag Cl (IR corrected) and plane (c) is the mass of K$^+$ ions collected in a liquid trap equipped in the gas outflow of the electrolyzer. (d) EDX mapping corresponding to the post-electrolysis of 1030 C/cm^2 at current densities of -283 mA/cm^2. Nominal size of the Ag NPs used as catalyst was ~10 nm and the applied mass loading was 300 μg/cm^2. Adapted from ref. [110].

Besides 10 nm Ag NPs, the sizes of 100 nm Ag NPs with original and less PVP content were employed under the same electrolysis conditions. The same phenomena were observed on 100 nm Ag NPs as that on 10 nm NPs that the stability could be maintained for longer time with the lower PVP content.

3. Conclusions and outlook

This PhD project aims to motivate electrochemical CO_2RR knowledge toward industrial applications. The colloidal Ag catalysts capped with different capping agents were applied for electrochemical CO_2 reduction. The influence of capping agents on the selectivity, activity, and stability of Ag nanocatalysts and the stability of the gas-fed zero-gap electrolyzer were investigated during CO_2 electrolysis.
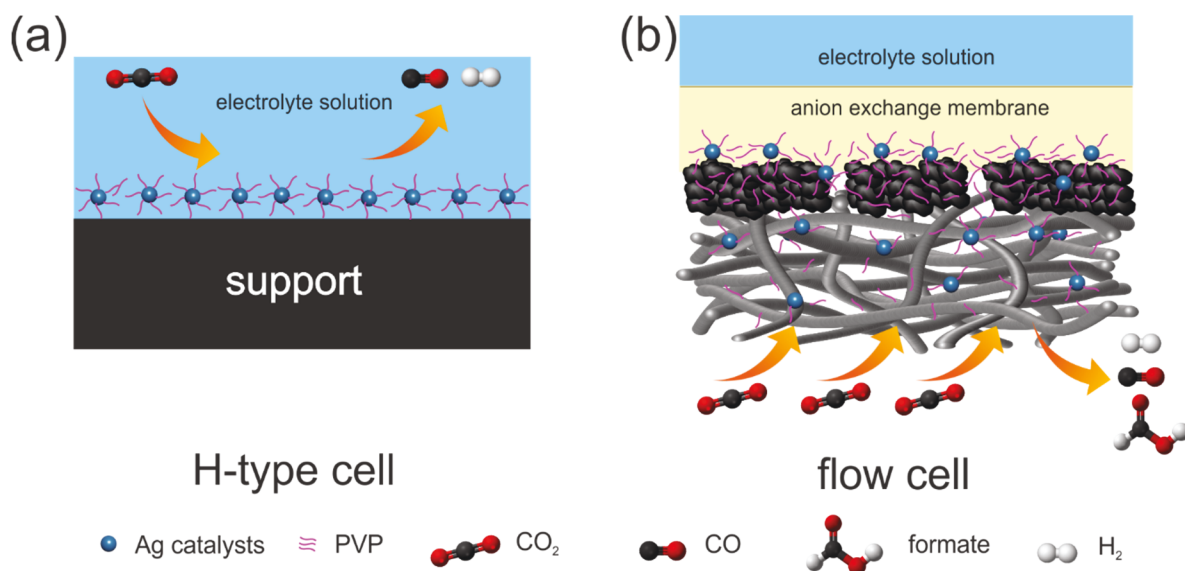
Fig 3.1 Overview of the PVP effect on Ag catalysts during CO_2RR. (a) PVP adsorbed on Ag catalysts surface influences the selectivity of CO_2RR in the H-type cell. (b) Excess PVP from the Ag catalyst ink affects the stability of CO_2RR in the gas-fed zero-gap electrolyzer.

The capping agents, including ligands adsorbed on the catalyst surface and free ligands in the catalyst ink, play significant roles during CO_2 electrolysis. The activity and selectivity of Ag NWs and NCs catalysts over CO_2RR are hindered in the presence of PVP. The electrochemical looping is a useful method to remove the PVP, which gives the high selectivity of Ag catalysts for CO_2RR. The degradation pathway of Ag catalysts during the CO_2 electroreduction depends on the chemical properties of capping agents as well as the sizes and shapes. The excess PVP in the ink not only influences the degradation pathway but also reduces the stability of the flow cell. Most importantly, this study demonstrates that the PVP capping agents adsorbed on Ag catalysts affect the selectivity and activity of CO_2RR at lower current density in the H-type electrolysis cell; however, it is the

35

excess of PVP capping agents from the Ag catalyst ink which determines the stability of CO_2RR at the high current density in the gas-fed zero-gap electrolyzer, as demonstrated in Fig 3.1.

Although the Ag catalysts with distinct sizes, morphologies and capping agents show dissimilar structural degradation for CO_2RR on gas-fed flow cell, the loss of CO_2RR performance could be regained after removing the precipitation on the GDEs. The durability is more dependent on the reactor and GDE design rather than the catalyst itself in this zero-gap flow cell. The cracks on the GDEs and the removal of excess PVP could mitigate the flooding and prolong the life-time of the electrolyzer system.

To advance towards commercial scale, efforts can be made to develop effective catalysts and optimize the reactors. For catalysts, the influence of capping agents should not be ignored, especially the excess capping agents. For electrochemical reactors, an appropriate flow cell should be designed and the operation conditions should be optimized to reach the high desired product partial current density with long-term stability.

4. References

[1] NOAA National centers for environmental information, state of the climate: monthly global climate report for annual 2021. https://www.ncei.noaa.gov/access/monitoring/monthly-report/global/202113 (accessed January 2022).

[2] Climate change: global sea level. https://www.climate.gov/news-features/understanding-climate/climate-change-global-sea-level (accessed April 19, 2022).

[3] Trends in atmospheric carbon dioxide https://gml.noaa.gov/ccgg/trends/ (accessed Augest 1, 2022).

[4] P. Friedlingstein, M. O'sullivan, M. W. Jones, R. M. Andrew, J. Hauck, A. Olsen, G. P. Peters, W. Peters, J. Pongratz, S. Sitch, C. Le Quéré, J. G. Canadell, P. Ciais, R. B. Jackson, S. Alin, L. E. O. C. Aragão, A. Arneth, V. Arora, N. R. Bates, M. Becker, A. Benoit-Cattin, H. C. Bittig, L. Bopp, S. Bultan, N. Chandra, F. Chevallier, L. P. Chini, W. Evans, L. Florentie, P. M. Forster, T. Gasser, M. Gehlen, D. Gilfillan, T. Gkritzalis, L. Gregor, N. Gruber, I. Harris, K. Hartung, V. Haverd, R. A. Houghton, T. Ilyina, A. K. Jain, E. Joetzjer, K. Kadono, E. Kato, V. Kitidis, J. I. Korsbakken, P. Landschützer, N. Lefèvre, A. Lenton, S. Lienert, Z. Liu, D. Lombardozzi, G. Marland, N. Metzl, D. R. Munro, J. E. M. S. Nabel, S. I. Nakaoka, Y. Niwa, K. O'brien, T. Ono, P. I. Palmer, D. Pierrot, B. Poulter, L. Resplandy, E. Robertson, C. Rödenbeck, J. Schwinger, R. Séférian, I. Skjelvan, A. J. P. Smith, A. J. Sutton, T. Tanhua, P. P. Tans, H. Tian, B. Tilbrook, G. Van Der Werf, N. Vuichard, A. P. Walker, R. Wanninkhof, A. J. Watson, D. Willis, A. J. Wiltshire, W. Yuan, X. Yue and S. Zaehle, Global carbon budget 2020. *Earth Syst. Sci. Data*, 2020, 12 (4), 3269-3340.

[5] U. Nations, Paris Agreement. 2015.

[6] R. M. Cuéllar-Franca and A. Azapagic, Carbon capture, storage and utilisation technologies: a critical analysis and comparison of their life cycle environmental impacts. *J. CO_2 Util.*, 2015, 9, 82-102.

[7] A. Meisen and X. Shuai, Research and development issues in CO_2 capture. *Energy Convers. Manag.*, 1997, 38, S37-S42.

[8] B. Singh, A. H. Strømman and E. G. Hertwich, Comparative life cycle environmental assessment of CCS technologies. *Int. J. Greenh. Gas Control.*, 2011, 5 (4), 911-921.

[9] B. Metz, O. Davidson, H. D. Coninck, M. Loos and L. Meyer, *IPCC special report on carbon dioxide capture and storage*. Cambridge University Press: Cambridge, United Kingdom and NewYork, NY, USA, 2005, 442.

[10] M. Pehnt and J. Henkel, Life cycle assessment of carbon dioxide capture and storage from lignite power plants. *Int. J. Greenh. Gas Control.*, 2009, 3 (1), 49-66.

[11] I. M. Abu-Reidah, Chapter 1-Carbonated beverages. In *Trends in Non-alcoholic Beverages*, C. M. Galanakis, Ed. Academic Press: 2020; p 1-36.

[12] P. Singh, A. A. Wani, A. A. Karim and H.-C. Langowski, The use of carbon dioxide in the processing and packaging of milk and dairy products: a review. *Int. J. Dairy Technol.*, 2012, 65 (2), 161-177.

[13] C. Vilela, M. Kurek, Z. Hayouka, B. Röcker, S. Yildirim, M. D. C. Antunes, J. Nilsen-Nygaard, M. K. Pettersen and C. S. R. Freire, A concise guide to active agents for active food packaging. *Trends Food Sci. Technol.*, 2018, 80, 212-222.

[14] I. Advanced Resources International and M. Consulting, *Optimization of CO_2 storage in CO_2 enhanced oil recovery projects*. 2010.

[15] Z. Dai, R. Middleton, H. Viswanathan, J. Fessenden-Rahn, J. Bauman, R. Pawar, S.-Y. Lee and B. Mcpherson, An integrated framework for optimizing CO_2 sequestration and enhanced oil recovery. *Environ. Sci. Technol. Lett.*, 2013, 1 (1), 49-54.

[16] L. Brennan and P. Owende, Biofuels from microalgae—a review of technologies for production, processing, and extractions of biofuels and co-products. *Renew. Sustain. Energy Rev.*, 2010, 14 (2), 557-577.

[17] M. Aresta, *Carbon dioxide as chemical feedstock*. John Wiley & Sons: 2010.

[18] Z. Jiang, T. Xiao, V. L. Kuznetsov and P. P. Edwards, Turning carbon dioxide into fuel. *Phil. Trans. R. Soc. A*, 2010, 368 (1923), 3343-3364.

[19] E. Alper and O. Yuksel Orhan, CO2 utilization: developments in conversion processes. *Petroleum*, 2017, 3 (1), 109-126.

[20] P. A. Alaba, A. Abbas and W. M. W. Daud, Insight into catalytic reduction of CO_2: catalysis and reactor design. *J. Clean. Prod.*, 2017, 140, 1298-1312.

[21] J. Qiao, Y. Liu and J. Zhang, *Electrochemical reduction of carbon dioxide: fundamentals and technologies*. CRC press: 2016.

[22] *Standard potentials in aqueous solution*. CRC Press: New York, USA, 1985.

[23] R. P. S. Chaplin and A. A. Wragg, Effects of process conditions and electrode material on reaction pathways for carbon dioxide electroreduction with particular reference to formate formation. *J. Appl. Electrochem.*, 2003, 33, 1107–1123.

[24] A. J. Bard, L. R. Faulkner and H. S. White, *Electrochemical methods: fundamentals and applications*. John Wiley & Sons: 2022.

[25] A. J. Martín, G. O. Larrazábal and J. Pérez-Ramírez, Towards sustainable fuels and chemicals through the electrochemical reduction of CO_2: lessons from water electrolysis. *Green Chem.*, 2015, 17 (12), 5114-5130.

[26] K. Zeng and D. Zhang, Recent progress in alkaline water electrolysis for hydrogen production and applications. *Prog. Energy Combust. Sci.*, 2010, 36 (3), 307-326.

[27] S. Garg, M. Li, A. Z. Weber, L. Ge, L. Li, V. Rudolph, G. Wang and T. E. Rufford, Advances and challenges in electrochemical CO_2 reduction processes: an engineering and design perspective looking beyond new catalyst materials. *J. Mater. Chem. A*, 2020, 8 (4), 1511-1544.

[28] Y. Hori, H. Konishi, T. Futamura, A. Murata, O. Koga, H. Sakurai and K. Oguma, "Deactivation of copper electrode" in electrochemical reduction of CO_2. *Electrochim. Acta*, 2005, 50 (27), 5354-5369.

[29] B. You and Y. Sun, Innovative strategies for electrocatalytic water splitting. *Acc. Chem. Res.*, 2018, 51 (7), 1571-1580.

[30] J.-F. Xie, Y.-X. Huang, W.-W. Li, X.-N. Song, L. Xiong and H.-Q. Yu, Efficient electrochemical CO_2 reduction on a unique chrysanthemum-like Cu nanoflower electrode and direct observation of carbon deposite. *Electrochim. Acta*, 2014, 139, 137-144.

[31] S. Popovic, M. Smiljanic, P. Jovanovic, J. Vavra, R. Buonsanti and N. Hodnik, Stability and degradation mechanisms of copper-based catalysts for electrochemical CO_2 reduction. *Angew. Chem. Int. Ed.*, 2020, 132 (35), 14736-14746.

[32] Y. Hori, H. Wakebe, T. Tsukamoto and O. Koga, Electrocatalytic process of CO selectivity in electrochemical reduction of CO_2 at metal electrodes in aqueous media. *Electrochim. Acta*, 1994, 39 (11), 1833-1839.

[33] D. L. T. Nguyen, H. H. Do, M. T. Nguyen, D.-V. N. Vo, V.-H. Nguyen, C. C. Nguyen, S. Y. Kim and Q. V. Le, Electrochemical conversion of carbon dioxide over silver-based catalysts: recent progress in cathode structure and interface engineering. *Chem. Eng. Sci.*, 2021, 234, 116403.

[34] Y. Cheng, S. Yang, S. P. Jiang and S. Wang, Supported single atoms as new class of catalysts for electrochemical reduction of carbon dioxide. *Small Methods*, 2019, 3 (9), 1800440.

[35] H. Xie, T. Wang, J. Liang, Q. Li and S. Sun, Cu-based nanocatalysts for electrochemical reduction of CO_2. *Nano Today*, 2018, 21, 41-54.

[36] X. Duan, J. Xu, Z. Wei, J. Ma, S. Guo, S. Wang, H. Liu and S. Dou, Metal-free carbon materials for CO_2 electrochemical reduction. *Adv. Mater.*, 2017, 29 (41).

[37] J. Qiao, Y. Liu, F. Hong and J. Zhang, A review of catalysts for the electroreduction of carbon dioxide to produce low-carbon fuels. *Chem. Soc. Rev.*, 2014, 43 (2), 631-675.

[38] D. M. Weekes, D. A. Salvatore, A. Reyes, A. Huang and C. P. Berlinguette, Electrolytic CO_2 reduction in a flow cell. *Acc. Chem. Res.*, 2018, 51 (4), 910-918.

[39] L. Zhang, Z. J. Zhao and J. Gong, Nanostructured materials for heterogeneous electrocatalytic CO_2 reduction and their related reaction mechanisms. *Angew. Chem. Int. Ed.*, 2017, 56 (38), 11326-11353.

[40] D. Faggion, Jr., W. D. G. Goncalves and J. Dupont, CO_2 electroreduction in ionic liquids. *Front. Chem.*, 2019, 7, 102.

[41] D. Higgins, C. Hahn, C. Xiang, T. F. Jaramillo and A. Z. Weber, Gas-diffusion electrodes for carbon dioxide reduction: a new paradigm. *ACS Energy Lett.*, 2018, 4 (1), 317-324.

[42] J. Durst, A. Rudnev, A. Dutta, Y. Fu, J. Herranz, V. Kaliginedi, A. Kuzume, A. A. Permyakova, Y. Paratcha, P. Broekmann and T. J. Schmidt, Electrochemical CO_2 reduction-a critical view on fundamentals, materials and applications. *Chimia*, 2015, 69 (12), 769-776.

[43] R. Snel, Olefins from syngas. *Catal. Rev.*, 1987, 29 (4), 361-445.

[44] A. Yahyazadeh, A. K. Dalai, W. Ma and L. Zhang, Fischer–Tropsch synthesis for light olefins from syngas: a review of catalyst development. *Reactions*, 2021, 2 (3), 227-257.

[45] T. Haas, R. Krause, R. Weber, M. Demler and G. Schmid, Technical photosynthesis involving CO_2 electrolysis and fermentation. *Nat. Catal.*, 2018, 1 (1), 32-39.

[46] M. González-Castaño, B. Dorneanu and H. Arellano-García, The reverse water gas shift reaction: a process systems engineering perspective. *React. Chem. Eng.*, 2021, 6 (6), 954-976.

[47] H. A. Hansen, J. B. Varley, A. A. Peterson and J. K. Norskov, Understanding trends in the electrocatalytic activity of metals and enzymes for CO_2 reduction to CO. *J. Phys. Chem. Lett.*, 2013, 4 (3), 388-392.

[48] H. Hu, M. Liu, Y. Kong, N. Mysuru, C. Sun, M. D. J. Gálvez-Vázquez, U. Müller, R. Erni, V. Grozovski, Y. Hou and P. Broekmann, Activation matters: hysteresis effects during electrochemical looping of colloidal Ag nanowire catalysts. *ACS Catal.*, 2020, 10 (15), 8503-8514.

[49] S. Liu, X.-Z. Wang, H. Tao, T. Li, Q. Liu, Z. Xu, X.-Z. Fu and J.-L. Luo, Ultrathin 5-fold twinned sub-25 nm silver nanowires enable highly selective electroreduction of CO_2 to CO. *Nano Energy*, 2018, 45, 456-462.

[50] K. Jiang, P. Kharel, Y. Peng, M. K. Gangishetty, H.-Y. G. Lin, E. Stavitski, K. Attenkofer and H. Wang, Silver nanoparticles with surface-bonded oxygen for highly selective CO_2 reduction. *ACS Sustain. Chem. Eng.*, 2017, 5 (10), 8529-8534.

[51] S. Verma, B. Kim, H. R. Jhong, S. Ma and P. J. Kenis, A gross-margin model for defining technoeconomic benchmarks in the electroreduction of CO_2. *ChemSusChem*, 2016, 9 (15), 1972-1979.

[52] P. Millet, R. Ngameni, S. A. Grigoriev, N. Mbemba, F. Brisset, A. Ranjbari and C. Etiévant, PEM water electrolyzers: from electrocatalysis to stack development. *Int. J. Hydrog. Energy*, 2010, 35 (10), 5043-5052.

[53] R. S. Jayashree, S. K. Yoon, F. R. Brushett, P. O. Lopez-Montesinos, D. Natarajan, L. J. Markoski and P. J. A. Kenis, On the performance of membraneless laminar flow-based fuel cells. *J. Power Sources*, 2010, 195 (11), 3569-3578.

[54] D. T. Whipple, E. C. Finke and P. J. A. Kenis, Microfluidic reactor for the electrochemical reduction of carbon dioxide: the effect of pH. *Electrochem. Solid-State Lett.*, 2010, 13 (9), B109.

[55] N. Gutiérrez-Guerra, L. Moreno-López, J. C. Serrano-Ruiz, J. L. Valverde and A. De Lucas-Consuegra, Gas phase electrocatalytic conversion of CO_2 to syn-fuels on Cu based catalysts-electrodes. *Appl. Catal. B: Environ.*, 2016, 188, 272-282.

[56] L. M. Aeshala, R. Uppaluri and A. Verma, Electrochemical conversion of CO_2 to fuels: tuning of the reaction zone using suitable functional groups in a solid polymer electrolyte. *Phys. Chem. Chem. Phys.*, 2014, 16 (33), 17588-17594.

[57] R. B. Kutz, Q. Chen, H. Yang, S. D. Sajjad, Z. Liu and I. R. Masel, Sustainion imidazolium-functionalized polymers for carbon dioxide electrolysis. *Energy Technology*, 2017, 5 (6), 929-936.

[58] D. A. Vermaas and W. A. Smith, Synergistic electrochemical CO_2 reduction and water oxidation with a bipolar membrane. *ACS Energy Lett.*, 2016, 1 (6), 1143-1148.

[59] F. P. García De Arquer, C.-T. Dinh, A. Ozden, J. Wicks, C. Mccallum, A. R. Kirmani, D.-H. Nam, C. Gabardo, A. Seifitokaldani, X. Wang, Y. C. Li, F. Li, J. Edwards, L. J. Richter, S. J. Thorpe, D. Sinton and E. H. Sargent, CO_2 electrolysis to multicarbon products at activities greater than 1 A cm−2. *Science*, 2020, 367 (6478), 661-666.

[60] W. Luo, J. Zhang, M. Li and A. Züttel, Boosting CO production in electrocatalytic CO_2 reduction on highly porous Zn catalysts. *ACS Catal.*, 2019, 9 (5), 3783-3791.

[61] S. Ren, D. Joulié, D. Salvatore, K. Torbensen, M. Wang, M. Robert and C. P. Berlinguette, Molecular electrocatalysts can mediate fast, selective CO_2 reduction in a flow cell. *Science*, 2019, 365 (6451), 367-369.

[62] C.-T. Dinh, F. P. García De Arquer, D. Sinton and E. H. Sargent, High rate, selective, and stable electroreduction of CO_2 to CO in basic and neutral media. *ACS Energy Lett.*, 2018, 3 (11), 2835-2840.

[63] T. Burdyny and W. A. Smith, CO_2 reduction on gas-diffusion electrodes and why catalytic performance must be assessed at commercially-relevant conditions. *Energy Environ. Sci.*, 2019, 12 (5), 1442-1453.

[64] S. Verma, Y. Hamasaki, C. Kim, W. Huang, S. Lu, H.-R. M. Jhong, A. A. Gewirth, T. Fujigaya, N. Nakashima and P. J. A. Kenis, Insights into the low overpotential electroreduction of CO_2 to CO on a supported gold catalyst in an alkaline flow electrolyzer. *ACS Energy Lett.*, 2017, 3 (1), 193-198.

[65] D. Wakerley, S. Lamaison, J. Wicks, A. Clemens, J. Feaster, D. Corral, S. A. Jaffer, A. Sarkar, M. Fontecave, E. B. Duoss, S. Baker, E. H. Sargent, T. F. Jaramillo and C. Hahn, Gas diffusion electrodes, reactor designs and key metrics of low-temperature CO_2 electrolysers. *Nat. Energy*, 2022, 7 (2), 130-143.

[66] J. J. Kaczur, H. Yang, Z. Liu, S. D. Sajjad and R. I. Masel, Carbon dioxide and water electrolysis using new alkaline stable anion membranes. *Front. Chem.*, 2018, 6, 263.

[67] M. E. Leonard, L. E. Clarke, A. Forner-Cuenca, S. M. Brown and F. R. Brushett, Investigating electrode flooding in a flowing electrolyte, gas-fed carbon dioxide electrolyzer. *ChemSusChem*, 2020, 13 (2), 400-411.

[68] Y. Hori, H. Ito, K. Okano, K. Nagasu and S. Sato, Silver-coated ion exchange membrane electrode applied to electrochemical reduction of carbon dioxide. *Electrochim. Acta*, 2003, 48 (18), 2651-2657.

[69] E. W. Lees, B. a. W. Mowbray, F. G. L. Parlane and C. P. Berlinguette, Gas diffusion electrodes and membranes for CO_2 reduction electrolysers. *Nat. Rev. Mater.*, 2022, 7 (1), 55-64.

[70] Y. Xu, J. P. Edwards, S. Liu, R. K. Miao, J. E. Huang, C. M. Gabardo, C. P. O'brien, J. Li, E. H. Sargent and D. Sinton, Self-cleaning CO_2 reduction systems: unsteady electrochemical forcing enables stability. *ACS Energy Lett.*, 2021, 6 (2), 809-815.

[71] B. De Mot, M. Ramdin, J. Hereijgers, T. J. H. Vlugt and T. Breugelmans, Direct water injection in catholyte-free zero-gap carbon dioxide electrolyzers. *ChemElectroChem*, 2020, 7 (18), 3839-3843.

[72] J. Y. T. Kim, P. Zhu, F.-Y. Chen, Z.-Y. Wu, D. A. Cullen and H. Wang, Recovering carbon losses in CO_2 electrolysis using a solid electrolyte reactor. *Nat. Catal.*, 2022, 5, 288-299.

[73] T. N. Nguyen and C. T. Dinh, Gas diffusion electrode design for electrochemical carbon dioxide reduction. *Chem. Soc. Rev.*, 2020, 49 (21), 7488-7504.

[74] B. Kim, F. Hillman, M. Ariyoshi, S. Fujikawa and P. J. A. Kenis, Effects of composition of the micro porous layer and the substrate on performance in the electrochemical reduction of CO_2 to CO. *J. Power Sources*, 2016, 312, 192-198.

[75] C.-T. Dinh, T. Burdyny, M. G. Kibria, A. Seifitokaldani, C. M. Gabardo, F. P. García De Arquer, A. Kiani, J. P. Edwards, P. D. Luna, O. S. Bushuyev, C. Zou, R. Quintero-Bermudez, Y. Pang, D. Sinton and E. H. Sargent, CO_2 electroreduction to ethylene via hydroxide-mediated copper catalysis at an abrupt interface. *Science*, 2018, 369 (6390), 783–787

[76] W. Ma, S. Xie, T. Liu, Q. Fan, J. Ye, F. Sun, Z. Jiang, Q. Zhang, J. Cheng and Y. Wang, Electrocatalytic reduction of CO_2 to ethylene and ethanol through hydrogen-assisted C–C coupling over fluorine-modified copper. *Nat. Catal.*, 2020, 3 (6), 478-487.

[77] P. Sonstrom and M. Baumer, Supported colloidal nanoparticles in heterogeneous gas phase catalysis: on the way to tailored catalysts. *Phys. Chem. Chem. Phys.*, 2011, 13 (43), 19270-19284.

[78] R. Jin, C. Zeng, M. Zhou and Y. Chen, Atomically precise colloidal metal nanoclusters and nanoparticles: fundamentals and opportunities. *Chem. Rev.*, 2016, 116 (18), 10346-10413.

[79] Y. Xia, Y. Xiong, B. Lim and S. E. Skrabalak, Shape-controlled synthesis of metal nanocrystals: simple chemistry meets complex physics? *Angew. Chem. Int. Ed.*, 2009, 48 (1), 60-103.

[80] M. Rycenga, C. M. Cobley, J. Zeng, W. Li, C. H. Moran, Q. Zhang, D. Qin and Y. Xia, Controlling the synthesis and assembly of silver nanostructures for plasmonic applications. *Chem. Rev.*, 2011, 111 (6), 3669-3712.

[81] E. A. Baranova, C. Bock, D. Ilin, D. Wang and B. Macdougall, Infrared spectroscopy on size-controlled synthesized Pt-based nano-catalysts. *Surf. Sci.*, 2006, 600 (17), 3502-3511.

[82] J. S. Spendelow and A. Wieckowski, Noble metal decoration of single crystal platinum surfaces to create well-defined bimetallic electrocatalysts. *Phys. Chem. Chem. Phys.*, 2004, 6 (22), 5094.

[83] N. Ortiz and S. E. Skrabalak, Manipulating local ligand environments for the controlled nucleation of metal nanoparticles and their assembly into nanodendrites. *Angew. Chem. Int. Ed.*, 2012, 124 (47), 11927-11931.

[84] Y. Sun and Y. Xia, Large-scale synthesis of uniform silver nanowires through a soft, self-seeding, polyol process. *Adv. Mater.*, 2002, 14 (11), 833-837.

[85] Y. Xiong, J. M. Mclellan, Y. Yin and Y. Xia, Synthesis of palladium icosahedra with twinned structure by blocking oxidative etching with citric acid or citrate ions. *Angew. Chem. Int. Ed.*, 2007, 46 (5), 790-794.

[86] Y. T. Guntern, V. Okatenko, J. Pankhurst, S. B. Varandili, P. Iyengar, C. Koolen, D. Stoian, J. Vavra and R. Buonsanti, Colloidal nanocrystals as electrocatalysts with tunable activity and selectivity. *ACS Catal.*, 2021, 11 (3), 1248-1295.

[87] J. Huang and R. Buonsanti, Colloidal nanocrystals as heterogeneous catalysts for electrochemical CO_2 conversion. *Chem. Mater.*, 2018, 31 (1), 13-25.

[88] Z. Y. Zhou, N. Tian, J. T. Li, I. Broadwell and S. G. Sun, Nanomaterials of high surface energy with exceptional properties in catalysis and energy storage. *Chem. Soc. Rev.*, 2011, 40 (7), 4167-4185.

[89] D. Gao, H. Zhou, J. Wang, S. Miao, F. Yang, G. Wang, J. Wang and X. Bao, Size-dependent electrocatalytic reduction of CO_2 over Pd nanoparticles. *J. Am. Chem. Soc.*, 2015, 137 (13), 4288-4291.

[90] G. L. De Gregorio, T. Burdyny, A. Loiudice, P. Iyengar, W. A. Smith and R. Buonsanti, Facet-dependent selectivity of Cu catalysts in electrochemical CO_2 reduction at commercially viable current densities. *ACS. Catal.*, 2020, 10 (9), 4854-4862.

[91] S. Liu, H. Tao, L. Zeng, Q. Liu, Z. Xu, Q. Liu and J. L. Luo, Shape-dependent electrocatalytic reduction of CO_2 to CO on triangular silver nanoplates. *J. Am. Chem. Soc.*, 2017, 139 (6), 2160-2163.

[92] J. Huang, M. Mensi, E. Oveisi, V. Mantella and R. Buonsanti, Structural sensitivities in bimetallic catalysts for electrochemical CO_2 reduction revealed by Ag-Cu nanodimers. *J. Am. Chem. Soc.*, 2019, 141 (6), 2490-2499.

[93] C. H. Bartholomew, Mechanisms of catalyst deactivation. *Appl. Catal. A: Gen.* , 2001, 212 (1), 17-60.

[94] P. Liu, R. Qin, G. Fu and N. Zheng, Surface coordination chemistry of metal nanomaterials. *J. Am. Chem. Soc.*, 2017, 139 (6), 2122-2131.

[95] C. A. Schoenbaum, D. K. Schwartz and J. W. Medlin, Controlling the surface environment of heterogeneous catalysts using self-assembled monolayers. *Acc. Chem. Res.*, 2014, 47 (4), 1438-1445.

[96] Q. Zhu, C. J. Murphy and L. R. Baker, Opportunities for electrocatalytic CO_2 reduction enabled by surface ligands. *J. Am. Chem. Soc.*, 2022, 144 (7), 2829-2840.

[97] C. Kim, T. Eom, M. S. Jee, H. Jung, H. Kim, B. K. Min and Y. J. Hwang, Insight into electrochemical CO_2 reduction on surface-molecule-mediated Ag nanoparticles. *ACS Catal.*, 2016, 7 (1), 779-785.

[98] E. Irtem, D. Arenas Esteban, M. Duarte, D. Choukroun, S. Lee, M. Ibáñez, S. Bals and T. Breugelmans, Ligand-mode directed selectivity in Cu–Ag core–shell based gas diffusion electrodes for CO_2 electroreduction. *ACS Catal.*, 2020, 10 (22), 13468-13478.

[99] Z. Niu and Y. Li, Removal and utilization of capping agents in nanocatalysis. *Chem. Mater.*, 2013, 26 (1), 72-83.

[100] N. Naresh, F. G. S. Wasim, B. P. Ladewig and M. Neergat, Removal of surfactant and capping agent from Pd nanocubes (Pd-NCs) using tert-butylamine: its effect on electrochemical characteristics. *J. Mater. Chem. A*, 2013, 1 (30), 8553-8559.

[101] M. Cargnello, C. Chen, B. T. Diroll, V. V. Doan-Nguyen, R. J. Gorte and C. B. Murray, Efficient removal of organic ligands from supported nanocrystals by fast thermal annealing enables catalytic studies on well-defined active phases. *J. Am. Chem. Soc.*, 2015, 137 (21), 6906-6911.

[102] S. Shaw, X. Tian, T. F. Silva, J. M. Bobbitt, F. Naab, C. L. Rodrigues, E. A. Smith and L. Cademartiri, Selective removal of ligands from colloidal nanocrystal assemblies with non-oxidizing He plasmas. *Chem. Mater.*, 2018, 30 (17), 5961-5967.

[103] C. Aliaga, J. Y. Park, Y. Yamada, H. S. Lee, C.-K. Tsung, P. Yang and G. A. Somorjai, Sum frequency generation and catalytic reaction studies of the removal of organic capping agents from Pt nanoparticles by UV−Ozone treatment. *J. Phys. Chem. C*, 2009, 113 (15), 6150-6155.

[104] Y. Hou, S. Bolat, A. Bornet, Y. E. Romanyuk, H. Guo, P. Moreno-García, I. Zelocualtecatl Montiel, Z. Lai, U. Müller, V. Grozovski and P. Broekmann, Photonic curing: activation and stabilization of metal membrane catalysts (MMCs) for the electrochemical reduction of CO_2. *ACS Catal.*, 2019, 9 (10), 9518-9529.

[105] H. Yang, Y. Tang and S. Zou, Electrochemical removal of surfactants from Pt nanocubes. *Electrochem. Commun.*, 2014, 38, 134-137.

[106] H. Gleiter, Nanostructured materials: basic concepts and microstructure. *Acta Mater.*, 2000, 48 (1), 1-29.

[107] M. De Jesus Gálvez-Vázquez, P. Moreno-García, H. Xu, Y. Hou, H. Hu, I. Z. Montiel, A. V. Rudnev, S. Alinejad, V. Grozovski, B. J. Wiley, M. Arenz and P. Broekmann, Environment matters: CO_2RR electrocatalyst performance testing in a gas-fed zero-gap electrolyzer. *ACS Catal.*, 2020, 10 (21), 13096-13108.

[108] H. Hu, M. Liu, Y. Kong, I. Z. Montiel, Y. Hou, A. V. Rudnev and P. Broekmann, Size-dependent structural alterations in Ag nanoparticles during CO_2 electrolysis in a gas-fed zero-gap electrolyzer. *ChemElectroChem*, 2022, 9 (17), e202200615.

[109] M. Liu, Y. Kong, H. Hu, N. Kovács, C. Sun, I. Zelocualtecatl Montiel, M. D. J. Gálvez Vázquez, Y. Hou, M. Mirolo, I. Martens, J. Drnec, S. Vesztergom and P. Broekmann, The capping agent is the key: structural alterations of Ag NPs during CO_2 electrolysis probed in a zero-gap gas-flow configuration. *J. Catal.*, 2021, 404, 371-382.

[110] H. Hu, Y. Kong, M. Liu, V. Kolivoška, A. V. Rudnev, Y. Hou, R. Erni, S. Vesztergom, and P. Broekmanna, Effective perspiration is essential to uphold the stability of zero-gap MEA-based cathodes used in CO_2 electrolysers. *J. Mater. Chem. A*, 2023, 11, 5083-5094.

5. Publications

The following section presents the main research works in which I participated during my PhD. The first three publications are the core of this project and the rest is the additional research works in that I was involved.

5.1 Activation matters: Hysteresis effects during electrochemical looping of colloidal Ag nanowire catalysts

Authors: **Huifang Hu**, Menglong Liu, Ying Kong, Nisarga Mysuru, Changzhe Sun, María de Jesús Gálvez-Vázquez, Ulrich Müller, Rolf Erni, Vitali Grozovski, Yuhui Hou,* and Peter Broekmann*

Highlights: Ag NWs synthesized via PVP-assisted polyol method are excellent catalyst for electrochemical CO_2RR after the activation by the electrochemical looping treatment. The electrochemical looping refers to a sequence of potentiostatic electrolysis experiments with well-defined starting, vertex, and end potentials. The CO formed during the CO_2RR is vital to remove the capping agents blocking the active sites. The potential window in the electrochemical looping, spanning from the starting potential of -0.6 V vs RHE to the vertex potential of -1.3 V vs RHE, achieves 100% faradaic efficiencies of CO at -1.0 V and -1.1 V vs RHE. The improvement of selectivity agrees with the decrease of PVP concentration on the electrodes. There is no significant structural alteration after the electrochemical looping treatment.

Contributions: I synthesized the Ag NW catalysts, prepared the electrodes and carried out most of the CO_2RR measurements. I also analyzed the results and participated in the manuscript writing process.

Activation Matters: Hysteresis Effects during Electrochemical Looping of Colloidal Ag Nanowire Catalysts

Huifang Hu, Menglong Liu, Ying Kong, Nisarga Mysuru, Changzhe Sun, María de Jesús Gálvez-Vázquez, Ulrich Müller, Rolf Erni, Vitali Grozovski, Yuhui Hou,* and Peter Broekmann*

ACCESS | 📊 Metrics & More | 📰 Article Recommendations | 🔲 Supporting Information
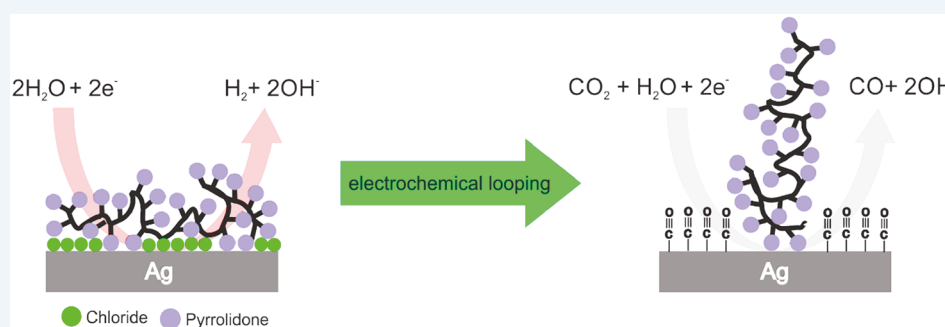
ABSTRACT: Colloidal electrocatalysts are commonly synthesized using organic capping agents (surfactants), which control the size distribution and shape of the resulting nano-objects and prevent them from agglomerating during and after synthesis. However, the presence of a surfactant shell on the catalyst is detrimental, as the resulting performance of the electrocatalyst depends crucially on the ability of reactants to access active surface sites. Techniques for postsynthesis deprotection are therefore mandatory for removing the capping agents from the otherwise blocked reactions sites without compromising the structural integrity of the nanocatalysts. Herein, we present silver nanowires (Ag-NWs)—produced via PVP-assisted polyol synthesis (PVP, polyvinylpyrrolidone)—as effective catalysts for the electrochemical CO_2 reduction reaction (ec-CO_2RR), which reach Faradaic efficiencies close to 100% for CO formation after deprotection by a so-called "electrochemical looping" (ec-l) pretreatment. Electrochemical looping refers to a sequence of potentiostatic CO_2 electrolysis experiments that exhibit well-defined starting (E_{start}), vertex (E_{vertex}), and end (E_{end}) potentials. The resulting product distribution undergoes a profound hysteresis in the forward and corresponding backward run of the electrochemical looping experiment, thus pointing to an effective deprotection of the catalyst as made evident by postelectrolysis XPS inspection. These results can be considered as a prime example demonstrating the importance of the catalyst's "history" for the resulting ec-CO_2RR performance. These transient (non-steady-state) effects are crucial in particular for the initial stage of the CO_2 electrolysis reaction and for catalyst screening approaches carried out on the time scale of hours.

KEYWORDS: CO_2 reduction reaction, silver nanowires, surfactant removal, catalyst deprotection, electrochemical looping

INTRODUCTION

The conversion of environmentally harmful carbon dioxide (CO_2) into value-added products is one of the major intersectoral challenges that we currently face.[1] In this context, electrochemical approaches of CO_2 valorization deserve particular attention as they can utilize the "green" electric power—generated by renewables such as solar or wind energy—as energy input for the highly endergonic process of CO_2 electrolysis, thereby rendering the overall process more sustainable.[2−4] One of the main target products of the electrochemical CO_2 reduction reaction (hereafter referred to as ec-CO_2RR) is carbon monoxide (CO), which is currently produced on an industrial scale via the "Boudouard" reaction and reaches a yearly production volume of approximately 210 000 Mt.[5] CO is considered to be a valuable intermediate (current market price: ≈0.65 \$ kg^{-1})[5] and has the potential to

be used as a reactant on a large scale (e.g., in the Fischer–Tropsch synthesis of aliphatic hydrocarbons [synthetic fuels] or alcohols).[6] Cost estimates suggest that the electrochemical coelectrolysis of water/CO_2 might indeed become competitive with more well-established routes of CO production.[5] The electrochemical production of CO via the coelectrolysis of water/CO_2 can be considered to be a versatile "synthesis module", which also can be coupled to other process units for

the production of valuable end products. A promising alternative to interlinking this process to the heterogeneous gas-phase Fischer−Tropsch reaction has recently been proposed by the Siemens/Evonik consortium[1,7] and couples the ec-CO₂RR (CO production; Siemens) to a biotechnological fermentation process (Evonik), thereby yielding fine chemicals such as butanol and hexanol as key intermediates for the production of specialty plastics.[7] The first test plant is expected to become operative in 2021[1] and thus demonstrates the enormous efforts that are currently underway to bring the ec-CO₂RR process from the lab to the market.[1]

Catalysts are essential for ec-CO₂RR, as they direct the electrolytic reaction toward the desired target product (e.g., CO). The pioneering work by Hori et al.[8−10] identified silver (Ag) as one of best (electro)catalysts, in addition to Au and Zn, which yielded CO with Faradaic efficiencies (FEs) that reached 81.5% ($E = -1.14$ V vs NHE).[8] In these early studies, catalyst screening was mainly based on the use of polycrystalline electrode materials as active catalysts (e.g., metal foils). However, substantial progress has been made during the last two decades in the development of tailored nanomaterials with an improved surface-to-volume ratio and well-defined shapes, the latter being important for the rational design of active surface sites.[11,12] In future, these nanomaterials have the potential to be used in gas diffusion electrodes (GDEs) as a key component of advanced gas-flow electrolyzer systems.[7,13−16] From a technical point of view, it is mandatory to use a gas-flow approach to reach the current densities that are targeted by industry (100 to 1000 mA cm⁻²) to cover the capital and operating costs of these systems.[13,17,18] Typically, these nanomaterials are produced via colloidal synthesis, which also allows the process to be easily scaled up and which is considered to be a key perquisite for any industrial application. A wide range of particle morphologies can be obtained using this colloidal approach, ranging from spheres,[19] cubic shapes,[20] and triangular platelets (confined 2-D systems)[21] to 1-D nano-objects such as rods[19] and wires.[22−26] To rationally design these nano-objects, a multiparameter space needs to be considered, which includes but is not limited to (i) the reaction temperature, (ii) the convective transport of reactants (e.g., stirring speed), (iii) the ratio of reactants (e.g., metal ion precursor, reducing agent, etc.), (iv) reaction times, and (v) the injection speed of chemicals.[27−29] However, the most important aspect to consider is the action of the so-called surfactants and capping agents.[19,25,30] Their presence in the reaction medium crucially affects the nucleation and growth kinetics of the nano-objects and could even cause crystal growth to be anisotropic, which is required for the synthesis of metallic nanowires (NWs).[31] The physical origin of this anisotropic growth behavior is the preferential surfactant adsorption on certain surface facets (e.g., [100] textured), which reduces their growth rate relative to surfaces with different surface orientations (e.g., [111]).[30,32−35] In this sense, the role of the surfactants is a result of the steric blocking of surface sites that are active for the (e-less) metal deposition by selectively limiting the access of precursor metal ions in the liquid reaction medium to the emerging surface of the nanocrystals (NCs).[36] Note that not only the monomeric[11,37] or polymeric (e.g., polyvinylpyrrolidone, PVP[38]) organic surfactants need to be considered, but also anionic species (e.g., halides) that are added to the reaction media along with the metal precursors. These counteranions usually play a crucial role in the initial nucleation process of the nano-objects (concept of self-seeded

growth[25,35]) and further tend to chemisorb on the emerging facets in an advanced stage of NC growth.[31]

While this facet-specific blocking by adsorbed surfactants is a mechanistic prerequisite for any anisotropic growth mode, it is highly detrimental to the desired (electro)catalytic performance of the nanocatalysts. As capping agents sterically block the access of reactants to the active catalyst sites during the electrocatalyzed reaction of interest,[37−40] various "soft" postsynthesis methods have been proposed to deprotect the "capped" nano-objects without compromising their structural integrity (e.g., loss of the shape, changes in size distribution, NP agglomeration, etc.). These deprotection techniques range from purely physical (e.g., thermal annealing[41,42] or exposure to light of particular wavelength and intensity[43,44]) to chemical treatments under nonreactive (e.g., "chemical" washing[38]) or reactive conditions (e.g., plasma treatment, the use of oxidizing or reducing agents, etc.).[37,38,44−51] Note that, under extremely drastic experimental conditions (e.g., thermal treatment at elevated temperatures), this type of catalyst pretreatment could lead to the loss of surface texture or to the agglomeration of nanoparticles.[52]

Also, electrochemical treatments (anodic or cathodic polarization) have successfully been applied to deprotect colloidal catalysts.[53−56] For example, Oezaslan et al.[54] reported on the efficient removal of a PVP capping shell from Pt nanocubes by applying an oxidative stressing protocol (electrochemical cycling up to +0.8 V vs reversible hydrogen electrode [RHE] in 0.1 M HClO₄), whereas the electrochemical deprotection failed under alkaline conditions. Also, the chemical nature of the capping agent (PVP versus oleylamine) has been shown to play a crucial role in the structural integrity of the nanocatalysts after electrochemical deprotection.[54]

So far, most studies on catalyst activation have considered only one single electrocatalytic reaction, (e.g., the oxygen reduction reaction [ORR],[53,54] the oxygen evolution reaction [OER], or the hydrogen evolution reaction [HER][37] etc.). For these single reactions, there are straightforward electrochemical descriptors and measuring approaches available to monitor the effectiveness of the applied deprotection technique (e.g., via the electrochemically active surface area [ECSA]), which is probed either by Faradaic or non-Faradaic processes. Their increase is directly proportional to the increase in the ECSA and is related to an overall improvement in the reaction rate.[37,40,49,53,54]

However, the situation is more complex when considering the ec-CO₂RR owing to the fact that the CO₂ electroreduction is necessarily superimposed on the parasitic HER when carried out in an aqueous reaction environment, which leads to a less-than-unity Faradaic efficiency of the ec-CO₂RR. Thus, the presence of the capping agents and the applied deprotection treatment affect not only the overall reaction rate (current density normalized to the geometric surface area) but also the resulting product distribution.

Herein, we present a comprehensive study on an approach to electrochemical catalyst activation (surfactant removal) that utilizes the ec-CO₂RR itself to achieve the desired catalyst deprotection. As the catalyst of choice, we applied silver nanowires (Ag-NWs) that were synthesized by a self-seeding polyol process using high-molecular-weight PVP as the capping agent.[24,27,32,57,58] The coelectrolysis of water/CO₂ that is performed over Ag catalysts yields only H₂ and CO as the reaction products.[8−10,59] In the present study, we sought to demonstrate that the formed CO acts as an excellent surfactant removal agent that is capable of deprotecting the Ag-NWs,

thereby further self-accelerating the *ec*-CO$_2$RR at the expense of the parasitic HER and leading to CO efficiencies of nearly 100%. This PVP removal by "cathodic" electrode polarization complements the "oxidative" approach that was proposed by Oezaslan et al.[54]

■ EXPERIMENTAL SECTION

Catalyst Synthesis. Ag nanowires (Ag-NWs) were synthesized in a three-necked flask according to a modified protocol introduced by Jiu et al. and others.[24,27,32,57,58] For this purpose, 0.2 g of PVP (M_w = 1 300 000 g mol^{-1}, Sigma-Aldrich; see Figure 1) was dissolved at room temperature under
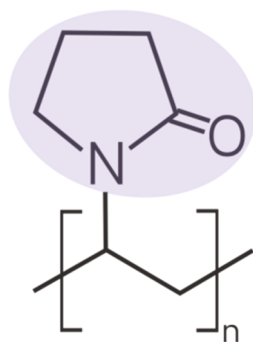

Figure 1. Polyvinylpyrrolidone (PVP) used as the capping agent for the Ag-NW synthesis. The pyrrolidone functionality attached to the linear aliphatic backbone is highlighted purple.

magnetic agitation in 25 mL of ethylene glycol (EG, Sigma-Aldrich, 99.8%). Subsequently, 0.25 g of silver nitrate (AgNO$_3$, Sigma-Aldrich, ACS reagent, ≥99.8%) was added to the PVP containing EG, followed by the addition of a solution of 1.95 mg of FeCl$_3$ (Sigma-Aldrich, 97%) predissolved in 2 mL of EG, which serves as a solvent and reducing agent.[24,32,57,58] This mixture was then stirred for an additional 2 min before the three-necked flask containing the transparent EG solution was transferred to a preheated oil bath. This solution was kept at 130 °C for a total of 5 h. During the first hour, the solution was continuously stirred, while no magnetic agitation was applied during the last 4 h of the thermal treatment. The resulting Ag-NW precipitate was separated from the EG solvent by centrifugation at 4000 rpm for 10 min, followed by three repetitive washing/centrifugation treatments using a mixture of Milli-Q water and acetone (V_{water}:V_{aceton} = 2:1), ultimately yielding 24 mg of the Ag-NW catalyst (denoted "as-synthesized"). The Ag-NW powder was finally redispersed in 8 mL of isopropanol (BASF SE, assay ≥99.0%).

Electrode Preparation. After 30 min of sonication, 50 μL of the Ag-NW suspension was drop-cast onto a glassy carbon support electrode (A = 0.8 cm^{-2}, Alfa Aesar, 2 mm thickness).

For the sake of comparison, Ag-NW catalysts were also dispersed onto a technical carbon support. For this purpose, 12 mg of the as-prepared Ag-NWs was suspended in 15 mL of isopropanol, followed by 1 h of sonication. Technical carbon powder (12 mg, Vulcan XC 72R, Cabot) was dispersed in 15 mL of isopropanol, and this was also followed by 1 h of sonication. Both suspensions were subsequently mixed and homogenized by sonicating for 30 min. The resulting suspension was dried under vacuum conditions and yielded a carbon-supported (C-supported) Ag-NW catalyst powder. This powder was redispersed in 4 mL of isopropanol containing 400 μL of Nafion solution (Aldrich, 5 wt % dissolved in a mixture of

lower aliphatic alcohols and water) and subjected to 30 min of sonication. Subsequently, 50 μL of the resulting ink was drop-cast onto the glassy carbon support electrode (see the aforementioned protocol).

Electrode Characterization. The morphologies of the Ag-NW films (nonsupported, C-supported) that were deposited on the glassy carbon support electrodes were characterized by means of scanning electron microscopy (Zeiss Gemini SEM450). Complementary white-light interferometry (ContourGT profilometer, Bruker) was applied to determine the thickness and roughness of the Ag-NW films. For the transmission electron microscopy (TEM) imaging and selective area electron diffraction, an FEI Titan Themis instrument was used with an accelerating voltage of 300 kV.

An X-ray photoelectron (XPS) inspection was performed on a Physical Electronics (PHI) Quantum 2000 scanning ESCA microprobe system using monochromated Al Kα radiation ($h\nu$ = 1486.7 eV). A hemispherical capacitor electron-energy analyzer, equipped with a channel plate and a position-sensitive detector, was operated under an electron takeoff angle of 45°. For the acquisition of the high-resolution Ag3d, Cl2p and N1s photoemission data, the analyzer was operated with a constant pass energy mode at 23.5 eV and an energy step width of 0.20 eV. The X-ray beam diameter was around 150 μm. The binding energy was calibrated using the Cu2$p_{3/2}$, Ag3$d_{5/2}$, and Au4$f_{7/2}$ emissions at 932.62, 368.21, and 83.96 eV, respectively, to within ±0.1 eV [see ISO 15472; 2010-05]. Built-in electron and argon ion neutralizers were applied in order to compensate for eventual surface charging effects. The base pressure of the XPS system was below 5 × 10^{-7} Pa. The XPS spectra were analyzed using the MultiPak 8.2B software package and were subjected to a Shirley background subtraction. The atomic concentrations were determined based on the corrected relative sensitivity factors that were provided by the manufacturer and normalized to 100 atom %. The uncertainty was estimated to be ca. 10%.

Electrochemical Experiments. For all electrochemical experiments, a potentiostat/galvanostat (Metrohm Autolab 302N) was used to control the potential, current density, and transferred charge. The electrolysis experiments were carried out using a custom-built, airtight glass-cell (H-type) as previously described (see Figure S1).[60−62] For the *iR* compensation, cell resistance was determined by means of impedance spectroscopy (FRA module, Autolab Nova). Hence, all potentials provided herein are *iR*-compensated to ~85% of the measured cell resistance.

The three-electrode arrangement used here consisted of a leakless Ag/AgCl$_{3M}$ electrode (Pine), a bright Pt-foil (15 mm × 5 mm), and the Ag-NW catalyst film (nonsupported, C-supported) serving as the reference, counter, and working electrodes, respectively.

For the sake of comparability, all potentials measured versus Ag/AgCl$_{3M}$ are referenced herein with respect to the reversible hydrogen electrode (RHE). The applied potentials (vs Ag/AgCl$_{3M}$) were converted to the RHE scale using the following equation:

$$E_{RHE} (V) = E_{Ag/AgCl(3M)} (V) + 0.210 \, V + (0.059 \, V \times pH)$$

Note that the anolyte and the catholyte were separated by a Nafion 117 membrane (Figure S1). This cell design also prevents the transfer of trace amounts of Pt ions from the anolyte to the catholyte when using Pt as the material for the counter electrode (see reference measurements presented in Figures S2−S5) as made evident by ICP-MS measurements
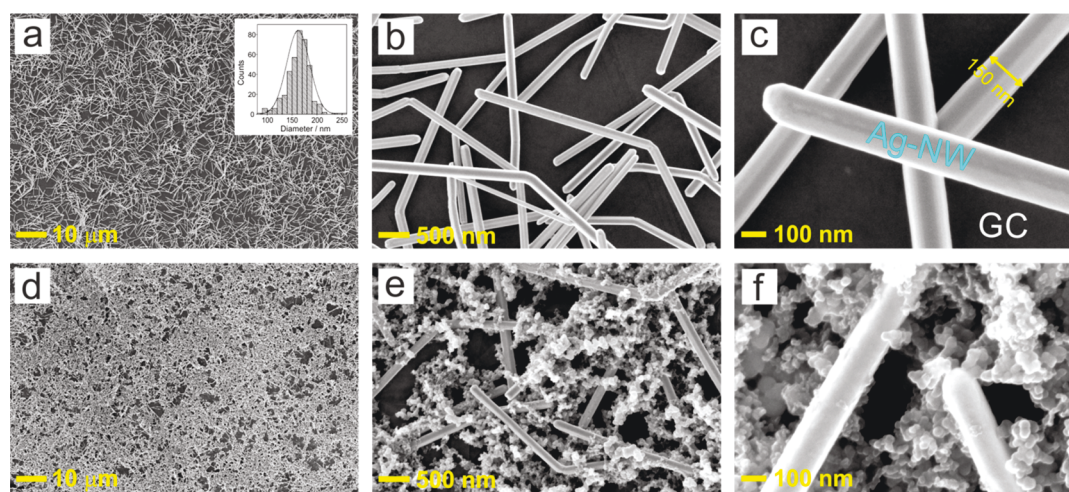
Figure 2. (a−c) Top-down SEM images of the Ag-NW film drop-cast on the glassy carbon (GC) support electrode; the inset in panel a shows a histogram representing the thickness distribution of the Ag-NWs. (d−f) Corresponding SEM images of the C-supported (Vulcan XC 72R) Ag-NWs drop-cast on the GC support electrode (for details, see the Experimental Section).

(NexION 2000 ICP-MS instrument, PerkinElmer). Also note that no change of the *ec*-CO_2RR product distribution is observed when exchanging the Pt counter electrode by Ir (see Figure S5).

Electrolysis experiments were carried out in 0.5 M $KHCO_3$ (ACS grade, Sigma-Aldrich) electrolyte solutions that were saturated with either Ar (blank) or CO_2 gas (99.999%, Carbagas). The pH of the CO_2- and Ar-saturated 0.5 M $KHCO_3$ was 7.5 and 8.9, respectively.

Technical details of the CO_2RR product analysis based on online gas-chromatography have been previously described.[60−62] A so-called single-catalyst approach was applied in order to demonstrate the pronounced hysteresis effects on the potential-dependent CO_2RR product distribution.[63] The same electrode was used for a defined sequence of potentiostatic electrolysis experiments, which differed in both the electrolysis time and the width of the potential window applied to the catalyst. In a further step a multicatalyst approach was applied,[63] in which a newly prepared (preconditioned) catalyst was used for each applied electrolysis potential to demonstrate the performance of the deprotected Ag-NW catalysts.

RESULTS AND DISCUSSION

Structural Characterization. Figure 2 displays top-down SEM images of the two types of Ag-NW catalysts used in this study. A three-dimensional network of randomly distributed and loosely packed Ag-NWs is formed after drop-casting the Ag-NW suspension on the glassy carbon support electrode (Figure 2a−c). Complementary white light interferometry reveals a homogeneous layer of Ag-NWs on the glassy carbon electrode with a root-mean-square (RMS) roughness and film thickness of 76 and 885 nm, respectively (Figure S6a−c). On the nm length scale the network of Ag-NWs shows a more inhomogeneous appearance. Note that the surface of the glassy carbon support remains visible in the top-down SEM inspection (Figure 2c). Therefore, the entirety of the Ag-NW film is, when exposed to the aqueous environment, likely to be wetted by the electrolyte down to the glassy carbon electrode. A statistical analysis of the SEM images reveals that the mean thickness of the Ag-NWs is approximately 162 nm (inset of Figure 2a), whereas they range in length from ca. 1 to several microns.

According to the literature,[22,64,65] the Ag-NWs exhibit a 5-fold twinned face-centered cubic (fcc) structure with a preferential orientation along the (110) crystallographic direction. The sidewalls of the Ag-NWs consist of five (100) textured facets, whereas the pentagonal apex of the Ag-NW is (111) terminated. These hexagonal facets represent the actual growth front in the Ag-NW synthesis in which the monovalent Ag^+ precursor ions are reduced and added to the developing nanowire. The origin of this highly anisotropic metal growth is the chemisorption of additives/surfactants (e.g., chloride and PVP), which is supposed to be weaker on the (111) facets, thereby rendering them more active for the e-less metal deposition than the (100) facets.[58] The latter experience a steric blocking by the more strongly chemisorbed surfactants.[22,66]

One drawback of the Ag-NW model catalyst drop-cast on the glassy carbon support is the potential loss of catalyst material during extended electrolysis, in particular when the electrolysis reaction involves massive gas evolution, e.g., by the parasitic HER that is inevitably superimposed on the CO_2RR in an aqueous environment.[43] This loss of catalyst material is a result of the weak adhesion of the NW layer to the glassy carbon support electrode and the loose packing of the Ag-NWs inside the catalyst film. One possible approach to circumventing this structural degradation is based on the mechanical stabilization of the NW film. This stabilization can be achieved by the use of a technical carbon support (e.g., Vulcan) in combination with a Nafion binder, thereby substantially improving both the adhesion of the catalyst film to the glassy carbon support and the cohesion inside the film.[67] Figure 2d−f depicts the corresponding top-down SEM images of the C-supported Ag-NW catalysts that were drop-cast on the glassy carbon electrode, demonstrating that individual Ag-NWs were embedded in the highly porous carbon support. However, one possible drawback of this approach could be an increase in the contribution of the porous carbon material to the resulting product distribution in the form of an increase in the parasitic HER (see the discussion of Figure 6 below). An alternative approach to catalyst stabilization, which is based on a so-called photonic curing, has recently been introduced by Hou et al.[43] This treatment induces a local melting and subsequent solidifying of the NWs at their points of contact. Photonically
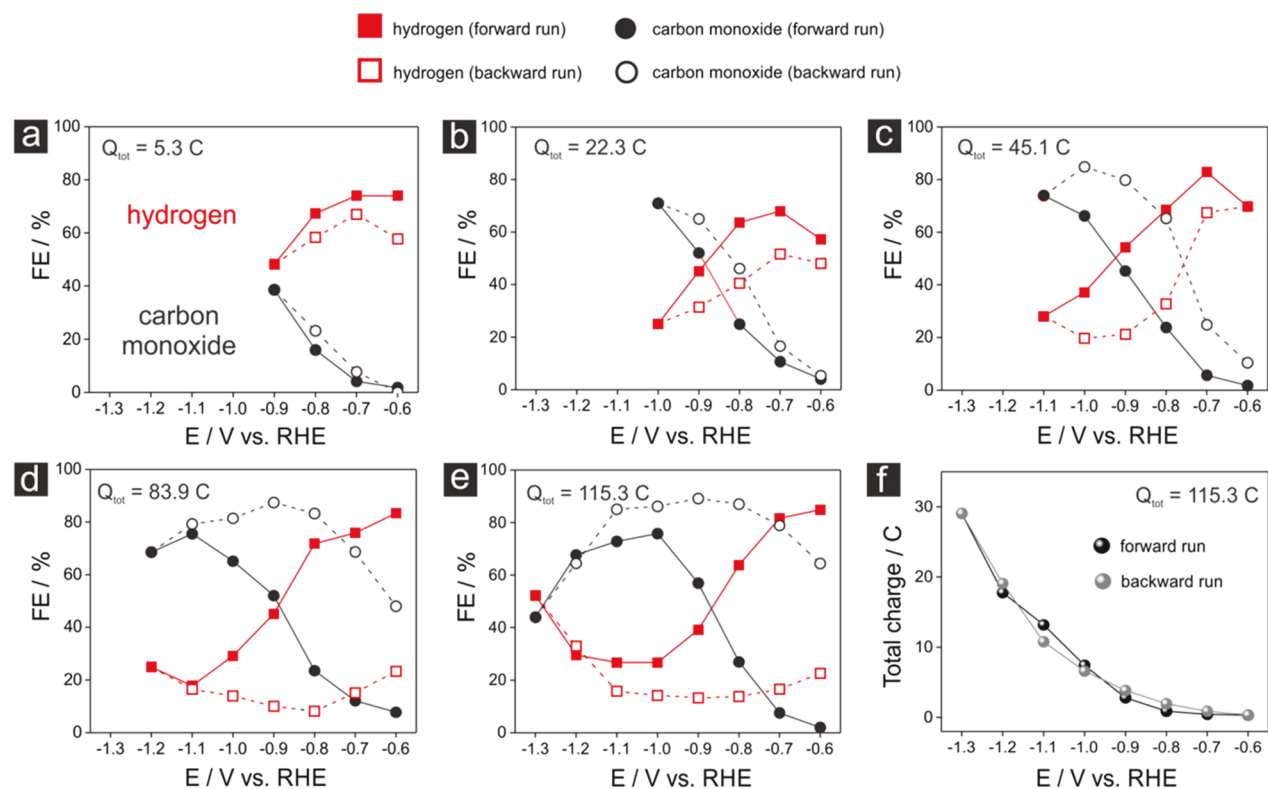
Figure 3. (a−e) Hysteresis effects appearing in the forward and backward runs of the electrochemical looping experiments (40 min duration at each potential) carried out over Ag-NW catalysts (see Figure 2a−c) in CO_2-saturated 0.5 M $KHCO_3$ (single catalyst approach); the total cathodic charges transferred during the "electrochemical looping" are indicated. (f) Graph showing the total integrated charge corresponding to the electrolysis experiments shown in panel e.

cured freestanding films of metallic nanowires were demonstrated to resist even massive gas-evolution reactions without any indication of structural degradation.[43]

Electrochemical Activation of Ag-NW Catalysts by Electrochemical Looping. The working hypothesis, which was to be verified in the following experiments, is that the surfactants (i.e., chloride and PVP) on the Ag surface of the deposited nanowires severely affect the product distribution of ec-CO_2RR and undergo substantial alterations over the course of the performed coelectrolysis reaction. An efficient catalyst activation that is induced by the electrolysis reaction itself can be deduced from the pronounced hysteresis characteristics observed in the potential-dependent product distribution, which is displayed in Figure 3 as Faradaic efficiency versus applied potential (FE versus E) plots (Table S1). These dedicated electrolysis experiments are referred to as "electrochemical looping" (ec-l), in which the applied electrolysis potentials of the individual 40 min long electrolyses were changed in a stepwise manner from a fixed starting point of E_{start} = −0.6 V vs RHE to a variable "lower" vertex potential (E_{vertex}) that ranged from −0.9 V vs RHE to −1.3 V vs RHE (Figure 3a−e). The electrolysis loop is closed through the corresponding backward run of electrolysis experiments and ends at the initial starting potential (E_{start} = E_{end}). The main products of the electrolysis in the CO_2-saturated 0.5 M $KHCO_3$ aqueous solution are CO (black circles, Figure 3) and H_2 (red squares, Figure 3). The filled and nonfilled circles/squares refer to FE values, which correspond to the forward and the corresponding backward runs of the electrochemical looping campaigns. As long as the lower vertex potential remains larger than or equal to −0.9 V vs RHE (Figure 3a), only a marginal deviation is

observed in the product distributions of the forward and the corresponding backward electrolysis runs (see also Figure S7). However, a minor trend toward increased CO efficiencies (decreased H_2 efficiencies) can be observed in the backward run. This positive trend of catalyst activation is continued by further shifting the lower vertex potential to more negative applied electrolysis potentials (Figure 3b−e). When extending the potential window of electrolysis to a vertex potential of E_{vertex} = −1.3 V vs RHE, CO efficiencies of >80% were achieved in the corresponding backward electrolysis run (Table S1e). In general, the shape of the product distribution in the FE versus E plot in Figure 3e displays an anticorrelated change in the FE values for CO and H_2, which exceed the maximum in CO efficiency (minimum in H_2 efficiency) at potentials between −1.0 and −1.1 V vs RHE (forward run). Interestingly, a more extended plateau of approximately 300 mV develops in the corresponding backward run in the potential range from −1.1 V to −0.8 V vs RHE, ultimately reaching CO efficiencies of >80%.

The FE_{CO} and FE_{H_2} values were the most substantially impacted by electrochemical looping at medium and low overpotentials (>−1.1 V vs RHE), whereas only minor differences were observed in the forward and backward runs for applied electrolysis potentials of < −1.2 V vs RHE (Figure 3e). In Figure 3e, the differences in potentials between the backward and the respective forward runs were ΔFE_{CO} = +10.3% at −1.0 V vs RHE, ΔFE_{CO} = +32.2% at −0.9 V vs RHE, ΔFE_{CO} = +60.0% at −0.8 V vs RHE, ΔFE_{CO} = +71.4% at −0.7 V vs RHE, and ΔFE_{CO} = +62.3% at −0.6 V vs RHE (see also Figure S7).

The absence of any substantial improvement in the FE_{CO} values at the lowest applied electrolysis potentials (<−1.2 V vs

RHE) can be rationalized by the onset of CO_2 mass transfer limitations, where the CO_2 concentration in the diffusion boundary layer is expected to drop down to zero as a result of increased CO_2RR rates (partial current densities). Therefore, the continuous activation of the catalyst material under CO_2 mass transport conditions does not lead to a further shift in the product distribution toward CO. The characteristics of pronounced hysteresis that can be seen at medium and low overpotentials (Figure 3a−e, Figure S7) are clearly indicative of the "activation" of the Ag-NW catalyst toward CO formation, which is mediated by the applied electrochemical looping. This is demonstrated in the first experiment, as the coelectrolysis of water/CO_2 resulted in the desired deprotection (chemical cleaning) of the catalyst surface. It can be hypothesized that changes in the composition of the surface are responsible for the observed changes in the potential-dependent product distribution (see discussion on the XPS analysis below). A first control experiment proving that the improved FE values (Figure 3) indeed originate from an effective removal of the surfactants from the catalyst surface during the ec-l treatment is shown in Figure S8. It compares the CO efficiencies of a Ag-NW catalyst before and after the ec-l treatment with the ones of a Ag-foil (GoodFellow, 99.95%, 0.25 mm thickness) which serves as a model system for a surfactant-free Ag catalyst. As expected, the CO efficiencies do not change by the ec-l treatment in the case of the Ag-foil catalyst. Further, we exclude severe structural or morphological changes of the Ag-NW catalyst in the course of the ec-l treatment as origin of the observed catalyst activation (see combined SEM and TEM analysis in Figure S9). It should be noted that, based on our experimental results, it cannot be concluded on which active sites of the Ag-NWs the HER and the ec-CO_2RR take place. Both experimental and theoretical studies on Ag single crystals strongly suggest, however, that defects, in particular steps and kink sites, are substantially more active toward CO formation than the planar (100) and (111) facets.[10,68]

One important aspect of this activation effect, discussed herein, is displayed in Figure 3f. In principle, the total (integrated) charge that is transferred at each electrolysis potential—derived from the respective j versus t (40 min) plots—exponentially increases with the applied overpotential (Table S2a). However, when comparing the forward and backward runs, it becomes obvious that the total transferred charge for a given electrolysis potential does not substantially change during electrochemical looping. This implies that only the product distribution (ratio of FE_{CO} and FE_{H_2} values) is altered by this treatment, whereas the total current density normalized to the geometric surface area (total transferred charge) remains unaffected. This is an important distinction between the current study and previous studies on catalyst activation processes in which only a single electrocatalytic reaction needs to be considered (e.g., ORR,[40,49,55] OER,[49] or HER[37]) and where increased reaction rates directly correlate with an increase of the electrochemically active surface area (ECSA).[53,54]

In order to elaborate on which experimental factors contribute to the observed change in the product distribution (e.g., nature of the formed CO_2RR reaction product, applied vertex potential [E_{vertex}], current density [j], electrolysis time, total transferred charge [Q], etc.), an extra electrochemical looping experiment was carried out in an Ar-saturated (CO_2-free) 0.5 M KHCO₃ electrolyte (pH = 8.9) while applying the

full range of electrolysis potentials (E_{vertex} = −1.3 V vs RHE). This approach excludes CO as a reaction product and exclusively produces H_2 during electrolysis. Note that bicarbonate can be neglected as a reactant when Ag is used as the catalyst.[63] Figure 4a compares the total transferred
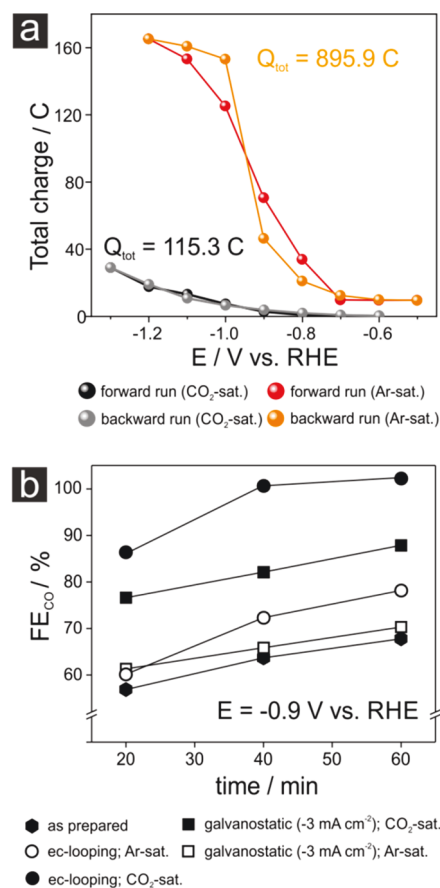
Figure 4. (a) Integrated cathodic charges of potentiostatic electrolysis reactions carried out in Ar- and CO_2-saturated 0.5 M KHCO₃ electrolytes (electrochemical looping). (b) Time-resolved FE_{CO} values derived from electrolysis reactions carried out at −0.9 V vs RHE after applying various activation protocols (for details, see the text).

charges of the chemical looping experiments carried out in the Ar- and the CO_2-saturated electrolyte (Table S2a). The most obvious difference is in the total amount of transferred charges, which is substantially higher for the CO_2-free case in which the HER is the only electrolytic reaction. These results suggest that the HER is not effectively hindered by the presence of the surfactants (chloride and PVP). Note that the expected exponential increase in the total transferred charge passes into a plateau regime at applied potentials that are more negative than −1.1 V vs RHE (Figure 4a). This particular feature originates from the partial blocking of the electrode surface by hydrogen bubbles, which appear at elevated current densities (surface area change under massive gas evolution; see Figure S10).

It becomes obvious from Figure 4a that the total transferred charges are substantially lower when CO is formed as one of the reaction products. This is likely owing to a high surface concentration of formed and temporarily adsorbed *CO (the asterisk represents an adsorption state), which therefore effectively sterically blocks those surface sites on the Ag-NW

that are active toward the competing HER. It is clear that the chemisorbed *CO acts as an efficient "suppressor" with regard to the HER.[63] The binding strength of *CO to the Ag catalyst is generally considered to be relatively low (i.e., in comparison to Cu),[69−71] thereby rationalizing the easy release of the formed *CO from the catalyst surface into the electrolyte phase (Figure 5). However, the *CO binding to the Ag-NW surface seems
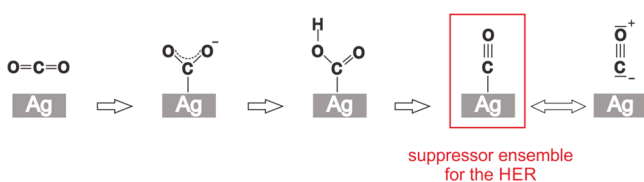
Figure 5. Reaction pathway of CO_2 conversion into CO on Ag catalysts; the strong suppressing action of the chemisorbed CO with regard to the HER is highlighted.

sufficiently high to remove surfactants from the surface during the water/CO_2 coelectrolysis reaction, which can be considered to be the origin of the profound hysteresis effects observed in the FE vs E plots (Figure 3). It can be hypothesized that the observed Ag-NW deprotection is based on the "chemisorptive displacement" of the surfactants by the *CO. The temporary presence of chemisorbed *CO on the Ag-catalyst surface has been previously demonstrated by operando vibrational (IR or Raman) spectroscopy.[72−74] The massive gas evolution (by H_2 and CO)—which is in agreement with the water/CO_2 coelectrolysis at high current densities (Figure S10)—can be considered to be an additional beneficial effect and facilitates the convectional transport of the released PVP from the catalyst surface into the bulk of the electrolyte phase. This process therefore prevents the readsorption of the PVP on the catalyst surface. Possible surfactant readsorption phenomena have been identified by Oezaslan et al.[54] as one possible drawback of the oxidative approach to PVP removal.

The chemical nature of the electrolysis product (H_2 or CO) that is formed during the electrochemical looping clearly plays a vital role in the deprotection of the desired catalyst. This effect can be denoted as surfactant removal by "chemical" cleaning. This has been demonstrated by additional experiments for CO_2 electrolysis, which were performed at a constant electrolysis potential of $E = -0.9$ V vs RHE using Ag-NW catalysts that had been subjected to a full chemical looping pretreatment ($E_{vertex} = -1.3$ V vs RHE) in either the CO_2-saturated or the CO_2-free (Ar-saturated) electrolyte. Figure 4b illustrates the time-dependent evolution of the FE_{CO} values of the electrolyses that were carried out in the CO_2-saturated electrolyte following the ec-l treatments.

For the purpose of comparison, the resulting FE_{CO} values of the as-prepared samples are also provided. It is clear that maximal CO efficiency (close to 100%) is most rapidly attained when preconditioning in the CO_2-saturated electrolyte, whereas the one subjected to the chemical looping in the Ar-saturated electrolyte demonstrates only marginally improved CO efficiencies. This finding is striking, as substantially higher charges were transferred, and higher current densities were applied during chemical looping in the Ar-saturated electrolyte ($Q_{tot} = 895.9$ C, $j_{max} = -85.6$ mA cm^{-2} at $E = -1.3$ V vs RHE, see Table S2a) in comparison to the CO_2-saturated electrolyte ($Q_{tot} = 115.3$ C, $j_{max} = -15.1$ mA cm^{-2} at $E = -1.3$ V vs RHE). The total charge is obviously not the key parameter for the

activation of the catalyst. Furthermore, the massive gas evolution alone does not seem to be sufficient for the deprotection of the Ag-NW catalyst (see also Figure S11).

As the total transferred charges were different in both electrochemical looping treatments (Ar- and CO_2-saturated electrolytes, Figure 4a) it is hard to compare them directly. We therefore applied two addition pretreatment techniques on the Ag-NW catalysts—based on galvanostatic electrolyses at $j = -3$ mA cm^{-2}—in both CO_2-saturated and CO_2-free electrolytes. In these cases, the total transferred charge was normalized to $Q_{tot} = 115.3$ C, which allowed for a direct comparison to the electrochemical looping experiment performed in the CO_2-containing electrolyte (Figure 4a). The corresponding FE_{CO} data for the subsequent CO_2 electrolysis reactions at -0.9 V vs RHE are included in the plot in Figure 4b. Again, pretreatment in the CO_2-free electrolyte yields poor FE_{CO} values in the actual CO_2 electrolysis experiment. Interestingly, the electrochemical looping in the CO_2-saturated electrolyte is superior to the galvanostatic pretreatment at $j = -3$ mA cm^{-2} that was carried out in the same electrolyte. Obviously, the applied electrolysis potential and the electrolysis time are important factors for the efficiency of surfactant removal (see also Figures S12 and S13, and discussion of the XPS data below). It can be assumed that, due to the increased CO partial current densities, the CO surface coverage is higher at lower vertex potentials thus also rationalizing the observed potential dependence of the hysteresis characteristics (Figure 3).

An extra electrolysis experiment was carried out using C-supported Ag-NWs as the catalyst in order to demonstrate that the electrochemical looping works when the NWs are embedded into a technical carbon matrix. The result of this ec-l experiment exhibits the desired trend of improved FE_{CO} values in the corresponding backward run of the electro-chemical looping (Figure 6), in which values of $FE_{CO} = 90.7\%$
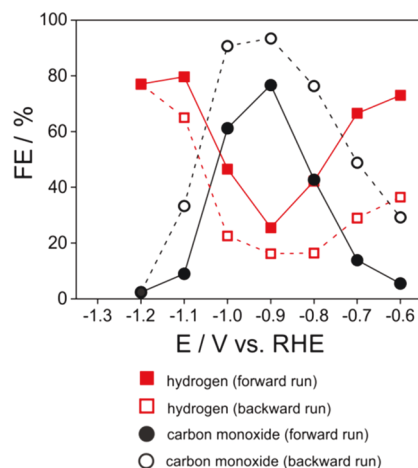
Figure 6. Activation of C-supported Ag-NW catalysts (see Figure 2d–f).

and $FE_{CO} = 93.4\%$ at $E = -1.0$ V and -0.9 V vs RHE were achieved. However, the HER is still dominating the product distribution at lower applied overpotentials in contrast to the nonsupported Ag-NWs (see Figure 3e). This observation can be rationalized by an effect that is mediated by the high surface area of the C-support, which is active toward the HER but not toward the CO_2RR. The increased FE_{H_2} values at the lowest overpotentials (Figure 6) are therefore the result of a surface

area effect of the component in the catalyst film, which is selective toward the HER (Vulcan and glassy carbon support electrode, see Figure S6d–f).

As the extended electrochemical looping ($E_{vertex} = -1.3$ V) was identified as the most effective pretreatment for the deprotection of the catalyst, a full set of additional electrolysis experiments were performed using a single catalyst approach[63] in which newly prepared and preconditioned catalyst (see Figures 2a–c and 3e) were used for 1 h long electrolysis experiments and applied potential. This approach guaranteed identical starting conditions for CO_2 electrolysis and minimized time-dependent changes on the selectivity of the CO_2RR products. Figure 7a represents the "true" potential-dependent
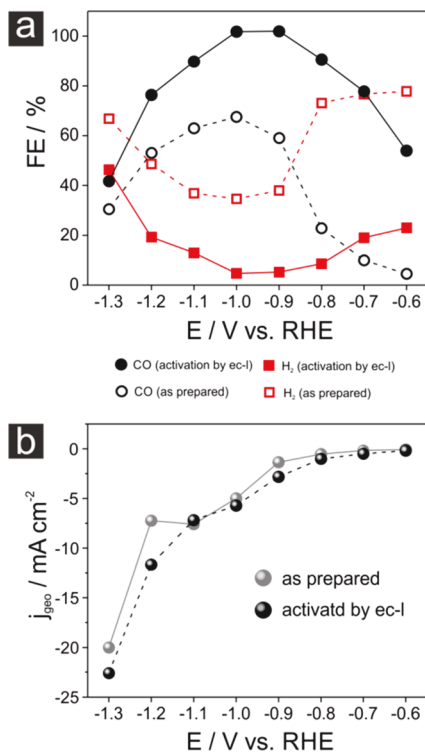
Figure 7. (a) *ec*-CO_2RR product distribution of 1 h lasting electrolysis experiments comparing the as prepared Ag-NW catalysts and those pretreated by an electrochemical looping ($E_{vertex} = -1.3$ V vs RHE, see Figure 3e). (b) Steady-state total current densities of the electrolysis experiments which correspond to the data in panel a.

product distribution of the Ag-NW catalyst after the successful deprotection of the Ag-NWs. For comparison purposes, the corresponding 1 h lasting *ec*-CO_2RR experiments of the as-prepared Ag-NW catalysts are also provided. CO efficiencies of ~100% are obtained after the ec-l preconditioning ($E_{vertex} = -1.3$ V vs RHE) in the potential range between −1.0 and −1.1 V. These efficiencies are competitive in comparison to previously published data.[20,21,63,75] Table S6 provides a comprehensive overview of the relevant benchmark studies that have used Ag as the *ec*-CO_2RR catalyst material, while Figure 7b demonstrates again that only the product selectivity is changed by the ec-l treatment, and not the overall reaction rate. The total (steady-state) current densities remain largely unaffected by electrochemical looping.

XPS Analysis. Our analysis of the *ec*-CO_2RR product distribution (Figures 3 and 7a) clearly demonstrates an activation of the Ag-NW catalyst by the chemical looping but

lacks deeper mechanistic insights into the chemical origin of the observed improved CO selectivity. Therefore, complementary XPS experiments were performed to provide information on the compositional changes of the catalyst surface. Figure 8a–c depicts spectra of the Ag3*d*, Cl2*p*, and N1*s* photoemissions that are representative of the as-prepared Ag-NW catalyst prior to its deprotection. These results demonstrate that both chloride and PVP are present on the surface of the as-prepared Ag-NWs, as indicated in the schematics of Figure 9. The performed electrolysis experiments clearly show that the HER does not effectively contribute to the deprotection of the desired catalyst (Figure 4b).

Figure 8d,e displays the integrated intensities of the N1*s* and Cl2*p* emissions normalized to the one of the respective Ag3*d* emissions. These data can be used to assess the effectiveness of the surfactant removal depending on the particular pretreatment protocol that is applied. Note that the (I_{Cl2p}:I_{Ag3d}) ratios are generally lower than the corresponding (I_{N1s}:I_{Ag3d}) values, irrespective of the applied pretreatment. One possible reason for this observation is that a layered structure of the surfactant shell was covering the Ag-NWs. Chloride is likely to be chemisorbed and would therefore be in direct contact with the Ag-NW surface.

These halide anions are considered to play a crucial role in the initial nucleation stage of Ag-NW formation (self-seeding via AgCl nuclei).[32] Furthermore, the (100) textured sidewalls of the Ag-NWs in particular exhibit a strong tendency toward specific chloride adsorption, which can result in a maximum (saturation) surface coverage of $\Theta = 0.5$ ML (normalized to the number of surface atoms on the [100] surface) when a Ag(100)-c(2 × 2)-Cl surface ad-layer is formed.[76−78] The high-molecular-mass PVP polymer ($M_w = 1\,300\,000$ g mol^{-1}) presumably constitutes the outermost shell of the as deposited Ag-NW. A "coiling" of the linear PVP around the Ag-NW is discussed in the literature, where the pyrrolidone acts as the anchor group of the polymer backbone to free metallic sites on the surface (Ag−O or Ag−N coordination).[32] Considering the high molecular mass of the PVP, it is likely that hydrophobic effects lead to an enhanced PVP agglomeration on the Ag-NWs beyond monolayer coverages. This layered configuration of surfactants, as depicted in Figure 9 (left panel), could also contribute to the reduced intensity observed in the Cl2*p* emission of the chloride that accumulated at the "buried" interface.

The electrochemical activation treatments applied to the Ag-NW catalysts exhibit strong variations in the PVP removal efficiency. The treatments in which H_2 was the exclusive electrolysis product (protocols 2 and 3 in Figure 8d) were less effective, while those using postsynthesis deprotection approaches involving the formation of CO (protocol 4 and 5 in Figure 8d) were more effective. The optimal PVP removal characteristics that were observed for the electrochemical looping approach ($E_{vertex} = -1.3$ V vs RHE) are in full agreement with our electrolysis data (Figures 4b and 7a). The XPS results also confirm that the PVP (and its removal) is the main origin for the observed hysteresis effects in the product distribution (Figure 3).

Interestingly, all pretreatments that were applied herein led to the near-complete removal of the chemisorbed chloride (Figure 8e). The origin of the chloride removal is the potential-dependent electrostatic repulsion of the chloride anions at the negatively polarized electrode surface.
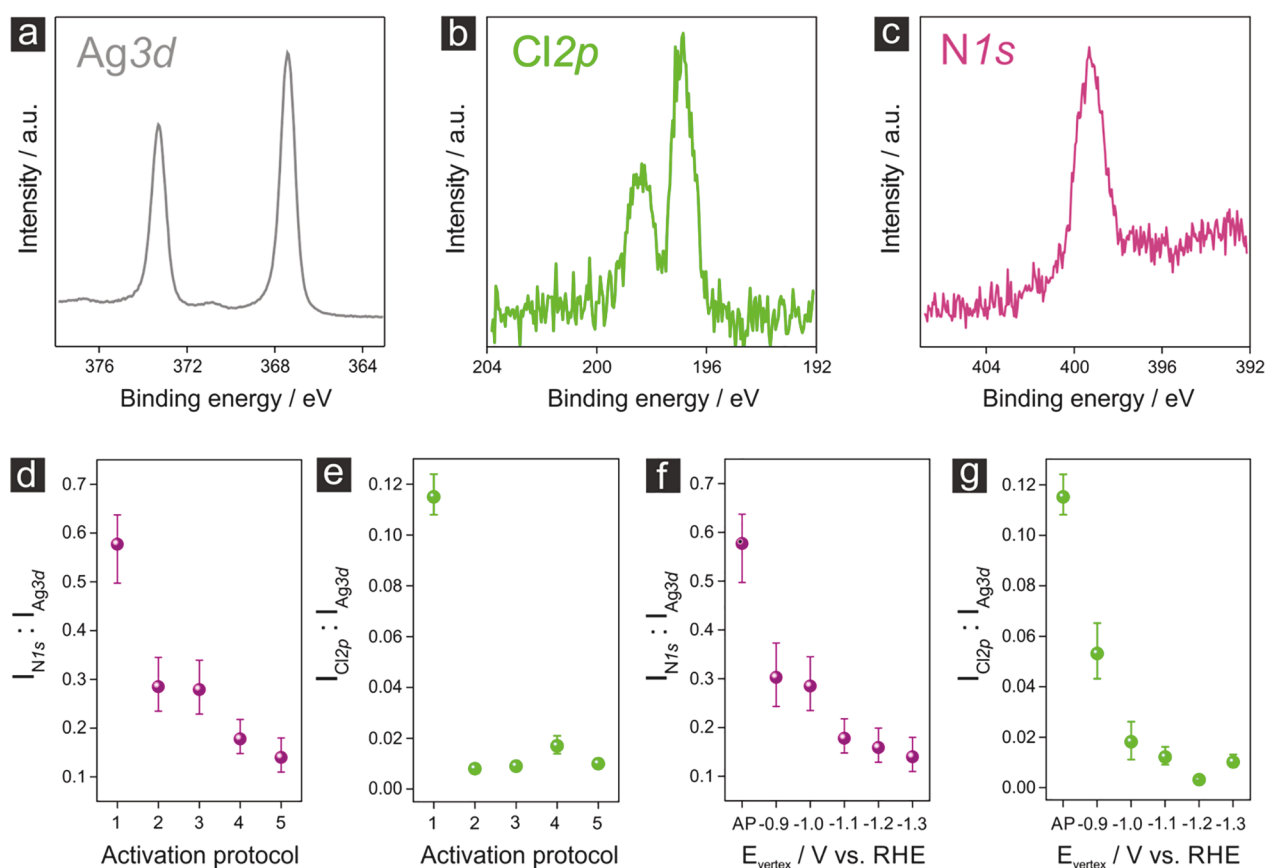
Figure 8. (a−c) Representative XPS spectra of the Ag3d, Cl2p, and N1s emissions derived from the Ag-NW catalyst on the GC support electrode (see Figure 2a−c). (d, e) Integrated intensities of the N1s and Cl2p emissions normalized to the corresponding integrated intensity of the Ag 3d emission; the digits on the x-axis indicate the respective catalyst activation protocols. **1**, as prepared; **2**, galvanostatic electrolysis in Ar-saturated (CO_2-free) 0.5 M KHCO$_3$ solution at $j = -3$ mA cm^{-2}, the total transferred charge was $Q = 115.3$ C; **3**, electrochemical looping (ec-l) in Ar-saturated 0.5 M KHCO$_3$ solution, the vertex potential was $E_{vertex} = -1.3$ V vs RHE, the total transferred charge was $Q = 895.9$ C; **4**, galvanostatic electrolysis in CO_2-saturated 0.5 M KHCO$_3$ solution at $j = -3$ mA cm^{-2}, the total transferred charge was $Q = 115.3$ C; **5**, electrochemical looping (ec-l) in CO_2-saturated 0.5 M KHCO$_3$ solution, the vertex potential was $E_{vertex} = -1.3$ V vs RHE, the total transferred charge was $Q = 115.3$ C (the activation conditions correspond to those in Figure 2b). (f, g) Integrated intensities of the N1s and Cl2p emissions normalized to the corresponding integrated intensity of the Ag3d emission measured after the electrochemical looping (ec-l) treatment; the respective vertex potentials are indicated on the x-axis (the activation conditions correspond to those in Figure 3).
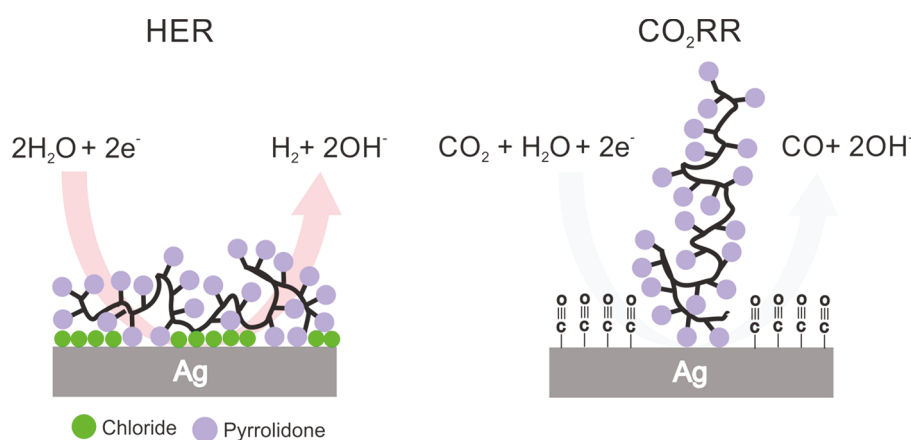
Figure 9. Schematics demonstrating the PVP and Cl terminated Ag surface which is still active for the HER (left panel) and the Ag surface which is activated upon CO production through PVP and Cl removal (right panel).

From these observations it can safely be concluded that it is the remaining PVP that disturbs the *ec*-CO_2RR rather than the chemisorbed chloride. Our analyses were further complemented by an extra XPS inspection of the catalyst films subjected to the systematic electrochemical looping experiments presented in Figure 3a−d. The results of this analysis are depicted in Figure 8f,g and clearly demonstrate that the vertex potential E_{vertex} and the width of the potential window that were applied to the catalysts in the electrochemical looping are necessary for the effectiveness of the surfactant removal. The

surface concentration of adsorbed chloride could be reduced to the minimum possible quantity when vertex potentials of E_{vertex} = −1.1 V vs RHE were applied, whereas the PVP surface coverage continued to decrease to an applied vertex potential of E_{vertex} = −1.3 V vs RHE. Our XPS results are also in full agreement with the working hypothesis made on the basis of the electrolysis data presented in Figure 3 and confirm that compositional changes at the catalyst surface are the origin of the hysteresis features observed in the electrochemical analysis (see also Figure S15). Complementary ^{1}H NMR measurements suggest that the PVP is removed structurally intact from the Ag surface. There are no PVP degradation products observed in the electrolyte after the electrolysis.

CONCLUSIONS AND OUTLOOK

Here, we demonstrate that the presence of surfactants (e.g., chloride and in particular PVP) on the surface of the colloidal silver catalyst negatively impacts the *ec*-CO$_2$RR selectivity and instead favors the HER in electrolysis reactions carried out in CO$_2$-saturated aqueous 0.5 M bicarbonate electrolytes.

The present work clearly demonstrates the importance of complete surfactant removal for the catalyst performance evaluation which might otherwise be superimposed by "transient artifacts", in particular in the initial stage of electrolysis (time scale of hours).

Electrochemical looping—a sequence of potentiostatic electrolysis experiments with defined starting, vertex, and ending potentials—has been demonstrated to be highly effective in the deprotection of catalysts, provided that CO is formed as the main electrolysis product. The chemical nature of the reaction product formed during electrolysis is found to be vital to the effectiveness of the activation of the catalysts via surfactant removal. An extended potential window in the electrochemical looping pretreatment, spanning from E_{start} = −0.6 V vs RHE to E_{vertex} = −1.3 V vs RHE, yields substantially improved CO efficiencies, which attained FE$_{CO}$ = 100% at −1.0 V (j_{CO} = −5.8 mA cm^{-2}) and −1.1 V vs RHE (j_{CO} = −6.5 mA cm^{-2}). This improvement in the product selectivity relative to the as-prepared Ag-NWs is in agreement with the observed decrease in the normalized PVP surface concentration. This catalyst deprotection protocol is also transferable to C-supported Ag-NW catalyst systems.

Our future research will address the application of these electrochemically activated Ag-NW catalysts in flow-cell electrolyzer systems in detail in order to demonstrate the importance of the environment (gaseous versus aqueous/liquid) for surfactant removal under *operando* experimental conditions.

ASSOCIATED CONTENT

Ⓢ Supporting Information

The Supporting Information is available free of charge at https://pubs.acs.org/doi/10.1021/acscatal.0c02026.

> Additional data and figures including a photograph, calibration curve, XPS spectrum, product distributions, white-light interferometric characterization, hysteresis characteristics, CO efficiencies, SEM images, TEM images, optical photographs, electrochemical looping, and ^{1}H NMR analysis (PDF)

AUTHOR INFORMATION

Corresponding Authors

Yuhui Hou − *Department of Chemistry and Biochemistry, University of Bern, Bern 3012, Switzerland;* ⓞ orcid.org/0000-0003-1616-562X; Email: yuhui.hou@dcb.unibe.ch

Peter Broekmann − *Department of Chemistry and Biochemistry, University of Bern, Bern 3012, Switzerland;* ⓞ orcid.org/0000-0002-6287-1042; Email: peter.broekmann@dcb.unibe.ch

Authors

Huifang Hu − *Department of Chemistry and Biochemistry, University of Bern, Bern 3012, Switzerland*

Menglong Liu − *Department of Chemistry and Biochemistry, University of Bern, Bern 3012, Switzerland*

Ying Kong − *Department of Chemistry and Biochemistry, University of Bern, Bern 3012, Switzerland*

Nisarga Mysuru − *Department of Chemistry and Biochemistry, University of Bern, Bern 3012, Switzerland*

Changzhe Sun − *Department of Chemistry and Biochemistry, University of Bern, Bern 3012, Switzerland*

María de Jesús Gálvez-Vázquez − *Department of Chemistry and Biochemistry, University of Bern, Bern 3012, Switzerland*

Ulrich Müller − *Surface Science and Coating Technology, Empa, Swiss Federal Laboratories for Materials Science and Technology, Dübendorf 8600, Switzerland*

Rolf Erni − *Electron Microscopy Center, Empa, Swiss Federal Laboratories for Materials Science and Technology, Dübendorf 8600, Switzerland;* ⓞ orcid.org/0000-0003-2391-5943

Vitali Grozovski − *Department of Chemistry and Biochemistry, University of Bern, Bern 3012, Switzerland*

Complete contact information is available at:
https://pubs.acs.org/10.1021/acscatal.0c02026

Notes

The authors declare no competing financial interest.

REFERENCES

(1) Change is in the air. *Nat. Catal.* **2018**, *1* (2), 93−93.

(2) Jhong, H.-R. M.; Ma, S.; Kenis, P. J. A. Electrochemical Conversion of CO$_2$ to Useful Chemicals: Current Status, Remaining Challenges, and Future Opportunities. *Curr. Opin. Chem. Eng.* **2013**, *2* (2), 191−199.

(3) Jones, J.-P.; Prakash, G. K. S.; Olah, G. A. Electrochemical CO$_2$ Reduction: Recent Advances and Current Trends. *Isr. J. Chem.* **2014**, *54* (10), 1451−1466.

(4) Whipple, D. T.; Kenis, P. J. A. Prospects of CO$_2$ Utilization via Direct Heterogeneous Electrochemical Reduction. *J. Phys. Chem. Lett.* **2010**, *1* (24), 3451−3458.

(5) Durst, J.; Rudnev, A.; Dutta, A.; Fu, Y.; Herranz, J.; Kaliginedi, V.; Kuzume, A.; Permyakova, A. A.; Paratcha, Y.; Broekmann, P.; Schmidt, T. J. Electrochemical CO$_2$ Reduction - A Critical View on Fundamentals, Materials and Applications. *Chimia* **2015**, *69* (12), 769−776.

(6) Samavati, M.; Santarelli, M.; Martin, A.; Nemanova, V. Production of Synthetic Fischer−Tropsch Diesel from Renewables: Thermoeconomic and Environmental Analysis. *Energy Fuels* **2018**, *32* (2), 1744−1753.

(7) Haas, T.; Krause, R.; Weber, R.; Demler, M.; Schmid, G. Technical photosynthesis involving CO_2 electrolysis and fermentation. *Nat. Catal.* **2018**, *1* (1), 32−39.

(8) Hori, Y.; Wakebe, H.; Tsukamoto, T.; Koga, O. Electrocatalytic Process of CO Selectivity in Electrochemical Reduction of CO_2 at Metal Electrodes in Aqueous Media. *Electrochim. Acta* **1994**, *39* (11−12), 1833−1839.

(9) Hori, Y.; Kikuchi, K.; Suzuki, S. Production of CO and CH_4 in Electrochemical Reduction of CO_2 at Metal-Electrodes in Aqueous Hydrogencarbonate Solution. *Chem. Lett.* **1985**, *14*, 1695−1698.

(10) Hoshi, N.; Kato, M.; Hori, Y. Electrochemical reduction of CO_2 on single crystal electrodes of silver Ag(111), Ag(100) and Ag(110). *J. Electroanal. Chem.* **1997**, *440* (1−2), 283−286.

(11) Boles, M. A.; Ling, D.; Hyeon, T.; Talapin, D. V. The surface science of nanocrystals. *Nat. Mater.* **2016**, *15* (2), 141−153.

(12) Back, S.; Yeom, M. S.; Jung, Y. Active Sites of Au and Ag Nanoparticle Catalysts for CO_2Electroreduction to CO. *ACS Catal.* **2015**, *5* (9), 5089−5096.

(13) Gabardo, C. M.; Seifitokaldani, A.; Edwards, J. P.; Dinh, C.-T.; Burdyny, T.; Kibria, M. G.; O'Brien, C. P.; Sargent, E. H.; Sinton, D. Combined high alkalinity and pressurization enable efficient CO_2 electroreduction to CO. *Energy Environ. Sci.* **2018**, *11* (9), 2531−2539.

(14) Salvatore, D. A.; Weekes, D. M.; He, J.; Dettelbach, K. E.; Li, Y. C.; Mallouk, T. E.; Berlinguette, C. P. Electrolysis of Gaseous CO_2 to CO in a Flow Cell with a Bipolar Membrane. *ACS Energy Lett.* **2018**, *3* (1), 149−154.

(15) Larrazábal, G. O.; Strøm-Hansen, P.; Heli, J. P.; Zeiter, K.; Therkildsen, K. T.; Chorkendorff, I.; Seger, B. Analysis of Mass Flows and Membrane Cross-over in CO_2 Reduction at High Current Densities in an MEA-Type Electrolyzer. *ACS Appl. Mater. Interfaces* **2019**, *11* (44), 41281−41288.

(16) Liu, Z.; Yang, H.; Kutz, R.; Masel, R. I. CO_2 Electrolysis to CO and O_2 at High Selectivity, Stability and Efficiency Using Sustainion Membranes. *J. Electrochem. Soc.* **2018**, *165* (15), J3371−J3377.

(17) Verma, S.; Kim, B.; Jhong, H.-R. M.; Ma, S.; Kenis, P. J. A. A Gross-Margin Model for Defining Technoeconomic Benchmarks in the Electroreduction of CO_2. *ChemSusChem* **2016**, *9* (15), 1972−1979.

(18) Martín, A. J.; Larrazábal, G. O.; Pérez-Ramírez, J. Towards sustainable fuels and chemicals through the electrochemical reduction of CO_2: lessons from water electrolysis. *Green Chem.* **2015**, *17* (12), 5114−5130.

(19) Kan, C. X.; Zhu, J. J.; Zhu, X. G. Silver nanostructures with well-controlled shapes: synthesis, characterization and growth mechanisms. *J. Phys. D: Appl. Phys.* **2008**, *41* (15), 155304.

(20) Liu, S.; Sun, C.; Xiao, J.; Luo, J.-L. Unraveling Structure Sensitivity in CO_2 Electroreduction to Near-Unity CO on Silver Nanocubes. *ACS Catal.* **2020**, *10*, 3158−3163.

(21) Liu, S.; Tao, H.; Zeng, L.; Liu, Q.; Xu, Z.; Liu, Q.; Luo, J.-L. Shape-Dependent Electrocatalytic Reduction of CO_2 to CO on Triangular Silver Nanoplates. *J. Am. Chem. Soc.* **2017**, *139* (6), 2160−2163.

(22) Zhang, S. H.; Jiang, Z. Y.; Xie, Z. X.; Xu, X.; Huang, R. B.; Zheng, L. S. Growth of silver nanowires from solutions: A cyclic penta-twinned-crystal growth mechanism. *J. Phys. Chem. B* **2005**, *109* (19), 9416−9421.

(23) Xi, W.; Ma, R.; Wang, H.; Gao, Z.; Zhang, W.; Zhao, Y. Ultrathin Ag Nanowires Electrode for Electrochemical Syngas Production from Carbon Dioxide. *ACS Sustainable Chem. Eng.* **2018**, *6* (6), 7687−7694.

(24) Sun, Y. G.; Yin, Y. D.; Mayers, B. T.; Herricks, T.; Xia, Y. N. Uniform silver nanowires synthesis by reducing $AgNO_3$ with ethylene glycol in the presence of seeds and poly(vinyl pyrrolidone). *Chem. Mater.* **2002**, *14* (11), 4736−4745.

(25) Li, X.; Wang, L.; Yan, G. Review: Recent research progress on preparation of silver nanowires by soft solution method and their applications. *Cryst. Res. Technol.* **2011**, *46* (5), 427−438.

(26) Li, B.; Ye, S.; Stewart, I. E.; Alvarez, S.; Wiley, B. J. Synthesis and Purification of Silver Nanowires To Make Conducting Films with a Transmittance of 99%. *Nano Lett.* **2015**, *15* (10), 6722−6726.

(27) Jiu, J.; Araki, T.; Wang, J.; Nogi, M.; Sugahara, T.; Nagao, S.; Koga, H.; Suganuma, K.; Nakazawa, E.; Hara, M.; Uchida, H.; Shinozaki, K. Facile synthesis of very-long silver nanowires for transparent electrodes. *J. Mater. Chem. A* **2014**, *2* (18), 6326−6330.

(28) Xia, Y.; Xiong, Y.; Lim, B.; Skrabalak, S. E. Shape-Controlled Synthesis of Metal Nanocrystals: Simple Chemistry Meets Complex Physics? *Angew. Chem., Int. Ed.* **2009**, *48* (1), 60−103.

(29) Coskun, S.; Aksoy, B.; Unalan, H. E. Polyol Synthesis of Silver Nanowires: An Extensive Parametric Study. *Cryst. Growth Des.* **2011**, *11* (11), 4963−4969.

(30) Gao, Y.; Jiang, P.; Song, L.; Liu, L. F.; Yan, X. Q.; Zhou, Z. Q.; Liu, D. F.; Wang, J. X.; Yuan, H. J.; Zhang, Z. X.; Zhao, X. W.; Dou, X. Y.; Zhou, W. Y.; Wang, G.; Xie, S. S. Growth mechanism of silver nanowires synthesized by polyvinylpyrrolidone-assisted polyol reduction. *J. Phys. D: Appl. Phys.* **2005**, *38* (7), 1061−1067.

(31) Kim, M. J.; Alvarez, S.; Chen, Z.; Fichthorn, K. A.; Wiley, B. J. Single-Crystal Electrochemistry Reveals Why Metal Nanowires Grow. *J. Am. Chem. Soc.* **2018**, *140* (44), 14740−14746.

(32) Sun, Y.; Xia, Y. Large-Scale Synthesis of Uniform Silver Nanowires Through a Soft, Self-Seeding, Polyol Process. *Adv. Mater.* **2002**, *14* (11), 833−837.

(33) Sun, D.; Xu, X.; Qin, Y.; Jiang, S. P.; Shao, Z. Rational Design of Ag-Based Catalysts for the Electrochemical CO_2 Reduction to CO: A Review. *ChemSusChem* **2020**, *13* (1), 39−58.

(34) Mourdikoudis, S.; Liz-Marzán, L. M. Oleylamine in Nano-particle Synthesis. *Chem. Mater.* **2013**, *25* (9), 1465−1476.

(35) Yang, H.-J.; He, S.-Y.; Tuan, H.-Y. Self-Seeded Growth of Five-Fold Twinned Copper Nanowires: Mechanistic Study, Character-ization, and SERS Applications. *Langmuir* **2014**, *30* (2), 602−610.

(36) Jin, M.; He, G.; Zhang, H.; Zeng, J.; Xie, Z.; Xia, Y. Shape-Controlled Synthesis of Copper Nanocrystals in an Aqueous Solution with Glucose as a Reducing Agent and Hexadecylamine as a Capping Agent. *Angew. Chem., Int. Ed.* **2011**, *50* (45), 10560−10564.

(37) Ung, D.; Cossairt, B. M. Effect of Surface Ligands on CoP for the Hydrogen Evolution Reaction. *ACS Appl. Energy Mater.* **2019**, *2* (3), 1642−1645.

(38) Luo, M.; Hong, Y.; Yao, W.; Huang, C.; Xu, Q.; Wu, Q. Facile removal of polyvinylpyrrolidone (PVP) adsorbates from Pt alloy nanoparticles. *J. Mater. Chem. A* **2015**, *3* (6), 2770−2775.

(39) Lopez-Sanchez, J. A.; Dimitratos, N.; Hammond, C.; Brett, G. L.; Kesavan, L.; White, S.; Miedziak, P.; Tiruvalam, R.; Jenkins, R. L.; Carley, A. F.; Knight, D.; Kiely, C. J.; Hutchings, G. J. Facile removal of stabilizer-ligands from supported gold nanoparticles. *Nat. Chem.* **2011**, *3* (7), 551−556.

(40) Naresh, N.; Wasim, F. G. S.; Ladewig, B. P.; Neergat, M. Removal of surfactant and capping agent from Pd nanocubes (Pd-NCs) using tert-butylamine: its effect on electrochemical character-istics. *J. Mater. Chem. A* **2013**, *1* (30), 8553−8559.

(41) Cargnello, M.; Chen, C.; Diroll, B. T.; Doan-Nguyen, V. V. T.; Gorte, R. J.; Murray, C. B. Efficient Removal of Organic Ligands from Supported Nanocrystals by Fast Thermal Annealing Enables Catalytic Studies on Well-Defined Active Phases. *J. Am. Chem. Soc.* **2015**, *137* (21), 6906−6911.

(42) Rioux, R. M.; Song, H.; Grass, M.; Habas, S.; Niesz, K.; Hoefelmeyer, J. D.; Yang, P.; Somorjai, G. A. Monodisperse platinum nanoparticles of well-defined shape: synthesise characterization, catalytic properties and future prospects. *Top. Catal.* **2006**, *39* (3−4), 167−174.

(43) Hou, Y.; Bolat, S.; Bornet, A.; Romanyuk, Y. E.; Guo, H.; Moreno-García, P.; Zelocualtecatl Montiel, I.; Lai, Z.; Müller, U.; Grozovski, V.; Broekmann, P. Photonic Curing: Activation and Stabilization of Metal Membrane Catalysts (MMCs) for the

Electrochemical Reduction of CO₂. *ACS Catal.* **2019**, *9* (10), 9518−9529.

(44) Bartholomew, C. H. Mechanisms of catalyst deactivation. *Appl. Catal., A* **2001**, *212* (1−2), 17−60.

(45) Shaw, S.; Tian, X. C.; Silva, T. F.; Bobbitt, J. M.; Naab, F.; Rodrigues, C. L.; Smith, E. A.; Cademartiri, L. Selective Removal of Ligands from Colloidal Nanocrystal Assemblies with Non-Oxidizing He Plasmas. *Chem. Mater.* **2018**, *30* (17), 5961−5967.

(46) Aliaga, C.; Park, J. Y.; Yamada, Y.; Lee, H. S.; Tsung, C.-K.; Yang, P.; Somorjai, G. A. Sum Frequency Generation and Catalytic Reaction Studies of the Removal of Organic Capping Agents from Pt Nanoparticles by UV−Ozone Treatment. *J. Phys. Chem. C* **2009**, *113* (15), 6150−6155.

(47) Rosen, E. L.; Buonsanti, R.; Llordes, A.; Sawvel, A. M.; Milliron, D. J.; Helms, B. A. Exceptionally Mild Reactive Stripping of Native Ligands from Nanocrystal Surfaces by Using Meerwein's Salt. *Angew. Chem., Int. Ed.* **2012**, *51* (3), 684−689.

(48) Doris, S. E.; Lynch, J. J.; Li, C. Y.; Wills, A. W.; Urban, J. J.; Helms, B. A. Mechanistic Insight into the Formation of Cationic Naked Nanocrystals Generated under Equilibrium Control. *J. Am. Chem. Soc.* **2014**, *136* (44), 15702−15710.

(49) Nelson, A.; Zong, Y.; Fritz, K. E.; Suntivich, J.; Robinson, R. D. Assessment of Soft Ligand Removal Strategies: Alkylation as a Promising Alternative to High-Temperature Treatments for Colloidal Nanoparticle Surfaces. *ACS Mater. Lett.* **2019**, *1* (1), 177−184.

(50) Menard, L. D.; Xu, F. T.; Nuzzo, R. G.; Yang, J. C. Preparation of TiO₂-supported Au nanoparticle catalysts from a Au-13 cluster precursor: Ligand removal using ozone exposure versus a rapid thermal treatment. *J. Catal.* **2006**, *243* (1), 64−73.

(51) Ansar, S. M.; Perera, G. S.; Ameer, F. S.; Zou, S. L.; Pittman, C. U.; Zhang, D. M. Desulfurization of Mercaptobenzimidazole and Thioguanine on Gold Nanoparticles Using Sodium Borohydride in Water at Room Temperature. *J. Phys. Chem. C* **2013**, *117* (26), 13722−13729.

(52) Hasché, F.; Oezaslan, M.; Strasser, P. In Situ Observation of the Thermally Induced Growth of Platinum-Nanoparticle Catalysts Using High-Temperature X-ray Diffraction. *ChemPhysChem* **2012**, *13* (3), 828−834.

(53) Li, D. G.; Wang, C.; Tripkovic, D.; Sun, S. H.; Markovic, N. M.; Stamenkovic, V. R. Surfactant Removal for Colloidal Nanoparticles from Solution Synthesis: The Effect on Catalytic Performance. *ACS Catal.* **2012**, *2* (7), 1358−1362.

(54) Safo, I. A.; Oezaslan, M. Electrochemical Cleaning of Polyvinylpyrrolidone-capped Pt Nanocubes for the Oxygen Reduction Reaction. *Electrochim. Acta* **2017**, *241*, 544−552.

(55) Safo, I. A.; Dosche, C.; Özaslan, M. Effects of Capping Agents on the Oxygen Reduction Reaction Activity and Shape Stability of Pt Nanocubes. *ChemPhysChem* **2019**, *20* (22), 3010−3023.

(56) Bong, S.; Jang, B.; Han, D.; Piao, Y. Effective Electrochemical Activation of Oleate-Residue-Fouled Pt Nanoparticle Catalysts for Methanol and Formic Acid Oxidation. *ACS Omega* **2019**, *4* (23), 20330−20334.

(57) Sun, Y. G.; Gates, B.; Mayers, B.; Xia, Y. N. Crystalline silver nanowires by soft solution processing. *Nano Lett.* **2002**, *2* (2), 165−168.

(58) Sun, Y. G.; Mayers, B.; Herricks, T.; Xia, Y. N. Polyol synthesis of uniform silver nanowires: A plausible growth mechanism and the supporting evidence. *Nano Lett.* **2003**, *3* (7), 955−960.

(59) Hori, Y. Electrochemical CO₂ Reduction on Metal Electrodes. In *Modern Aspects of Electrochemistry*; Springer: New York, 2008; pp 89−189.

(60) Dutta, A.; Rahaman, M.; Luedi, N. C.; Mohos, M.; Broekmann, P. Morphology Matters: Tuning the Product Distribution of CO₂ Electroreduction on Oxide-Derived Cu Foam Catalysts. *ACS Catal.* **2016**, *6* (6), 3804−3814.

(61) Dutta, A.; Rahaman, M.; Mohos, M.; Zanetti, A.; Broekmann, P. Electrochemical CO₂ Conversion Using Skeleton (Sponge) Type of Cu Catalysts. *ACS Catal.* **2017**, *7* (8), 5431−5437.

(62) Rahaman, M.; Dutta, A.; Broekmann, P. Size-Dependent Activity of Palladium Nanoparticles: Efficient Conversion of CO₂ into Formate at Low Overpotentials. *ChemSusChem* **2017**, *10* (8), 1733−1741.

(63) Dutta, A.; Morstein, C. E.; Rahaman, M.; Cedeño López, A.; Broekmann, P. Beyond Copper in CO₂ Electrolysis: Effective Hydrocarbon Production on Silver-Nanofoam Catalysts. *ACS Catal.* **2018**, *8*, 8357−8368.

(64) da Silva, R. R.; Yang, M.; Choi, S.-I.; Chi, M.; Luo, M.; Zhang, C.; Li, Z.-Y.; Camargo, P. H. C.; Ribeiro, S. J. L.; Xia, Y. Facile Synthesis of Sub-20 nm Silver Nanowires through a Bromide-Mediated Polyol Method. *ACS Nano* **2016**, *10* (8), 7892−7900.

(65) Niu, Z.; Cui, F.; Kuttner, E.; Xie, C.; Chen, H.; Sun, Y.; Dehestani, A.; Schierle-Arndt, K.; Yang, P. Synthesis of Silver Nanowires with Reduced Diameters Using Benzoin-Derived Radicals to Make Transparent Conductors with High Transparency and Low Haze. *Nano Lett.* **2018**, *18* (8), 5329−5334.

(66) Jiang, P.; Li, S.-Y.; Xie, S.-S.; Gao, Y.; Song, L. Machinable Long PVP-Stabilized Silver Nanowires. *Chem. - Eur. J.* **2004**, *10* (19), 4817−4821.

(67) Li, Y.; Cui, F.; Ross, M. B.; Kim, D.; Sun, Y.; Yang, P. Structure-Sensitive CO₂ Electroreduction to Hydrocarbons on Ultrathin 5-fold Twinned Copper Nanowires. *Nano Lett.* **2017**, *17* (2), 1312−1317.

(68) Clark, E. L.; Ringe, S.; Tang, M.; Walton, A.; Hahn, C.; Jaramillo, T. F.; Chan, K.; Bell, A. T. Influence of Atomic Surface Structure on the Activity of Ag for the Electrochemical Reduction of CO₂ to CO. *ACS Catal.* **2019**, *9* (5), 4006−4014.

(69) Kuhl, K. P.; Hatsukade, T.; Cave, E. R.; Abram, D. N.; Kibsgaard, J.; Jaramillo, T. F. Electrocatalytic Conversion of Carbon Dioxide to Methane and Methanol on Transition Metal Surfaces. *J. Am. Chem. Soc.* **2014**, *136* (40), 14107−14113.

(70) Liu, X. Y.; Xiao, J. P.; Peng, H. J.; Hong, X.; Chan, K.; Norskov, J. K. Understanding trends in electrochemical carbon dioxide reduction rates. *Nat. Commun.* **2017**, *8*, 15438.

(71) Hammer, B.; Morikawa, Y.; Nørskov, J. K. CO Chemisorption at Metal Surfaces and Overlayers. *Phys. Rev. Lett.* **1996**, *76* (12), 2141−2144.

(72) Zhu, S.; Li, T.; Cai, W.-B.; Shao, M. CO₂ Electrochemical Reduction As Probed through Infrared Spectroscopy. *ACS Energy Lett.* **2019**, *4* (3), 682−689.

(73) Schmitt, K. G.; Gewirth, A. A. In Situ Surface-Enhanced Raman Spectroscopy of the Electrochemical Reduction of Carbon Dioxide on Silver with 3,5-Diamino-1,2,4-Triazole. *J. Phys. Chem. C* **2014**, *118* (31), 17567−17576.

(74) Ichinohe, Y.; Wadayama, T.; Hatta, A. Electrochemical reduction of CO₂ on silver as probed by surface-enhanced Raman scattering. *J. Raman Spectrosc.* **1995**, *26* (5), 335−340.

(75) Liu, S.; Wang, X.-Z.; Tao, H.; Li, T.; Liu, Q.; Xu, Z.; Fu, X.-Z.; Luo, J.-L. Ultrathin 5-Fold Twinned Sub-25 nm Silver Nanowires Enable Highly Selective Electroreduction of CO₂ to CO. *Nano Energy* **2018**, *45*, 456.

(76) Fu, H.; Jia, L. L.; Wang, W. N.; Fan, K. N. The first-principle study on chlorine-modified silver surfaces. *Surf. Sci.* **2005**, *584* (2−3), 187−198.

(77) Bowker, M.; Waugh, K. C.; Wolfindale, B.; Lamble, G.; King, D. A. THE ADSORPTION OF CHLORINE AND CHLORIDATION OF AG(100). *Surf. Sci.* **1987**, *179* (2−3), 254−266.

(78) Lamble, G. M.; Brooks, R. S.; Campuzano, J. C.; King, D. A.; Norman, D. STRUCTURE OF THE C(2 × 2) COVERAGE OF CL ON AG(100) - A CONTROVERSY RESOLVED BY SURFACE EXTENDED X-RAY-ABSORPTION FINE-STRUCTURE SPECTROSCOPY. *Phys. Rev. B: Condens. Matter Mater. Phys.* **1987**, *36* (3), 1796−1798.

5.2 Size-dependent structural alterations in Ag nanoparticles during CO$_2$ electrolysis in a gas-fed zero-gap electrolyzer

Authors: **Huifang Hu**, Menglong Liu, Ying Kong, Iván Zelocualtecatl Montiel, Yuhui Hou, Alexander V. Rudnev*, and Peter Broekmann*

Highlights: The PVP capped-Ag NPs of different initial sizes (10, 40, and 100 nm) were applied to study the size effect on NPs degradation behavior during CO$_2$RR in the gas-fed zero-gap electrolyzer. After performing galvanostatic electrolysis, there is no considerable detachment of all Ag NPs catalyst from ICP-MS analysis of Ag loading. Although the flooding and harsh salt precipitation are found after CO$_2$ electrolysis, structural alterations are shown in SEM images after washing the GDEs. The Ag NPs with the size of 10 nm form agglomerates with the longest distance up to 200 nm. The 40 nm NPs agglomerate mainly, and small clusters can be found in the electrodes deposited with 40 nm NPs after the electrolysis. NPs of 100 nm tend to form agglomerates consisting of two to three NPs and undergo pronounced fragmentation into small NPs with the size of serval nanometers. The results indicated that on a long-term time scale, structural changes in catalysts play important roles in CO$_2$RR performance.

Contributions: I was the main responsible for the preparation of the electrodes and performing the electrochemical CO$_2$ reduction experiments. Moreover, I did most of the morphological characterization of the catalysts. I contributed to the results analysis, preparation of figures and manuscript.

ChemElectroChem

Research Article
doi.org/10.1002/celc.202200615

**Chemistry
Europe**
European Chemical
Societies Publishing

www.chemelectrochem.org

Size-Dependent Structural Alterations in Ag Nanoparticles during CO₂ Electrolysis in a Gas-Fed Zero-Gap Electrolyzer

Huifang Hu,[a] Menglong Liu,[a, b] Ying Kong,[a, b] Iván Zelocualtecatl Montiel,[a, b] Yuhui Hou,[a] Alexander V. Rudnev,*[a, c] and Peter Broekmann*[a, b]

Ag nanoparticles (NPs) are efficient electrocatalysts for electrochemical CO₂-to-CO conversion. However, NPs are thermodynamically unstable and can undergo structural alterations under electrolysis operating conditions. These structural changes may play a crucial role in the deterioration of CO₂ reduction reaction (CO₂RR) performance on the long-term electrolysis time scale. Here, we studied the effect of NP size on NP degradation during CO₂RR. Polyvinylpyrrolidone-capped 10, 40, and 100 nm Ag NPs deposited on a gas diffusion electrode were used as testbed catalysts in a gas-fed zero-gap electrolyzer. Inductively coupled plasma mass spectrometry indicated insignificant catalyst-material detachment after galvanostatic CO₂ electrolysis. Scanning electron microscopy analysis showed that smaller NPs tended to agglomerate during CO₂ electrolysis. 100 nm NPs formed agglomerates consisting of only two-three NPs and underwent pronounced fragmentation with the formation of particles several nanometers in size. The fragmentation was associated with cathodic corrosion of Ag NPs under conditions of intensive CO₂RR and hydrogen evolution.

Introduction

Electrochemical CO₂ conversion is a promising approach for the storage of renewable electricity in a sustainable manner and the production of synthetically or industrially valuable platform chemicals.[1] Currently, research on the electrochemical approach is driven primarily by the technological demand for catalyst and electrolyzer configurations that provide selective and stable progress of CO₂ reduction reaction (CO₂RR).

CO₂RR in H-type electrochemical cells (two-compartment cells with a membrane separating the cathode and anode compartments) suffers from mass transport limitations, owing to the low concentration of CO₂ in electrolyte solutions. The use of a zero-gap gas-flow electrolyzer unit with a gas diffusion electrode (GDE) overcomes these limitations, thus resulting in current densities of CO₂RR above 300 mA cm⁻².[2–5] Modern commercial GDEs consist of a carbon fiber support (CFS) and a microporous layer (MPL) with the catalyst layer deposited on the MPL.[6] In the zero-gap configuration, a humidified CO₂ gas diffuses through a porous gas diffusion layer (CFS and MPL) of the GDE to the active sites of the catalyst.

Metallic nanoparticles (NPs) deposited on a GDE can be used as efficient electrocatalysts for CO₂ reduction. High selectivity for CO₂-to-CO conversion has been achieved, for example with nanoparticulate or nanostructured Ag catalysts.[7–11] Relatively low loading of nanoparticulate catalyst material can be used to achieve a CO₂RR current density at an industrially relevant level. However, owing to their small size, NPs are thermodynamically unstable and can therefore undergo structural alterations under electrolysis operating conditions. Degradation mechanisms for fragmentation, reshaping, poisoning, agglomeration, dissolution (redeposition), detachment, and Oswald ripening have been reported for NPs under CO₂RR at negative potentials.[12,13] NP fragmentation can be considered as a phenomenon of cathodic corrosion.[14]

Although NP-catalyst degradation behavior during CO₂RR has been intensively studied in H-type and one-compartment cells (e.g., see Refs. [12,15–20]), the conclusions obtained in these studies might not be directly applicable to the zero-gap electrolyzer configuration.[2] In the latter case, the investigation of catalyst degradation has been hindered by the precipitation of (bi)carbonate salt at a three-phase GDE interface within several or few tens of minutes, thus severely suppressing CO₂RR.[2,3,21–23] Nevertheless, the study of NP-catalyst structural changes during CO₂RR in a zero-gap electrolyzer under harsh conditions (high current densities) is extremely important, because NP degradation is crucial for CO₂RR performance on the long-term electrolysis time scale.

Multiple factors affect NP degradation behavior. In our previous work, we have studied the effect of a capping agent on structural alterations of spherical Ag NPs after CO₂RR in a zero-gap electrolyzer.[3] Ag NPs 40 nm in size were stabilized by

[a] H. Hu, M. Liu, Y. Kong, I. Z. Montiel, Dr. Y. Hou, Dr. A. V. Rudnev,
     Prof. P. Broekmann
     Department of Chemistry, Biochemistry and Pharmaceutical Sciences
     University of Bern
     Freiestrasse 3, 3012 Bern, Switzerland
     E-mail: peter.broekmann@unibe.ch
            alexander.rudnev@unibe.ch
[b] M. Liu, Y. Kong, I. Z. Montiel, Prof. P. Broekmann
     National Centre of Competence in Research (NCCR) Catalysis
     University of Bern
     Freiestrasse 3, 3012 Bern, Switzerland
[c] Dr. A. V. Rudnev
     A. N. Frumkin Institute of Physical Chemistry and Electrochemistry
     Russian Academy of Sciences
     Leninskii pr. 31 bld. 4, 119071 Moscow, Russia

ChemElectroChem

Research Article
doi.org/10.1002/celc.202200615

Chemistry Europe
European Chemical
Societies Publishing

four capping agents: branched polyethylenimine (PEI), poly-vinylpyrrolidone (PVP), polyethylene glycol (PEG), and citrate. Although the NPs displayed identical size distributions, they differed in their activity toward CO_2RR in terms of faradaic efficiency for CO formation, FE_{CO}, and current densities in the course of potentiostatic electrolysis. Thus, the structural changes in NPs occurring during electrolysis were also affected by the chemical nature of the capping agent. Here, continuing our investigation of the degradation behavior of Ag NP catalysts, we focused on the effect of NP size on structural changes during CO_2RR in a zero-gap electrolyzer (the corresponding configuration has been described in detail in Refs. [3,23], Figure S1). Catalyst inks were prepared from commercially available PVP-capped 10, 40, and 100 nm Ag NPs. Through a set of post-electrolysis analyses of the NP-catalyst, we show that degradation pathways substantially depend on the initial NP size. Smaller NPs tend to agglomerate during CO_2 electrolysis. In particular, 10 nm NPs form agglomerates up to

200 nm in the longest dimension. In addition, 100 nm NPs form agglomerates consisting of only two or three NPs, and undergo pronounced fragmentation, thus forming large amounts of particles several nanometers in size, which are redeposited on the MPL. The fragmentation appears to be associated with cathodic corrosion of Ag NPs at negative potentials under conditions of intensive CO_2RR and hydrogen evolution reaction (HER).

Results and Discussion

Characterization of As-Prepared Ag NPs Deposited on GDE

The as-prepared Ag NP catalyst deposited on the GDE (Figure S2) was analyzed with scanning electron microscopy (SEM) (Figure 1a, e and i). The respective size distributions are shown in Figure 2. SEM images before electrolysis indicated that the
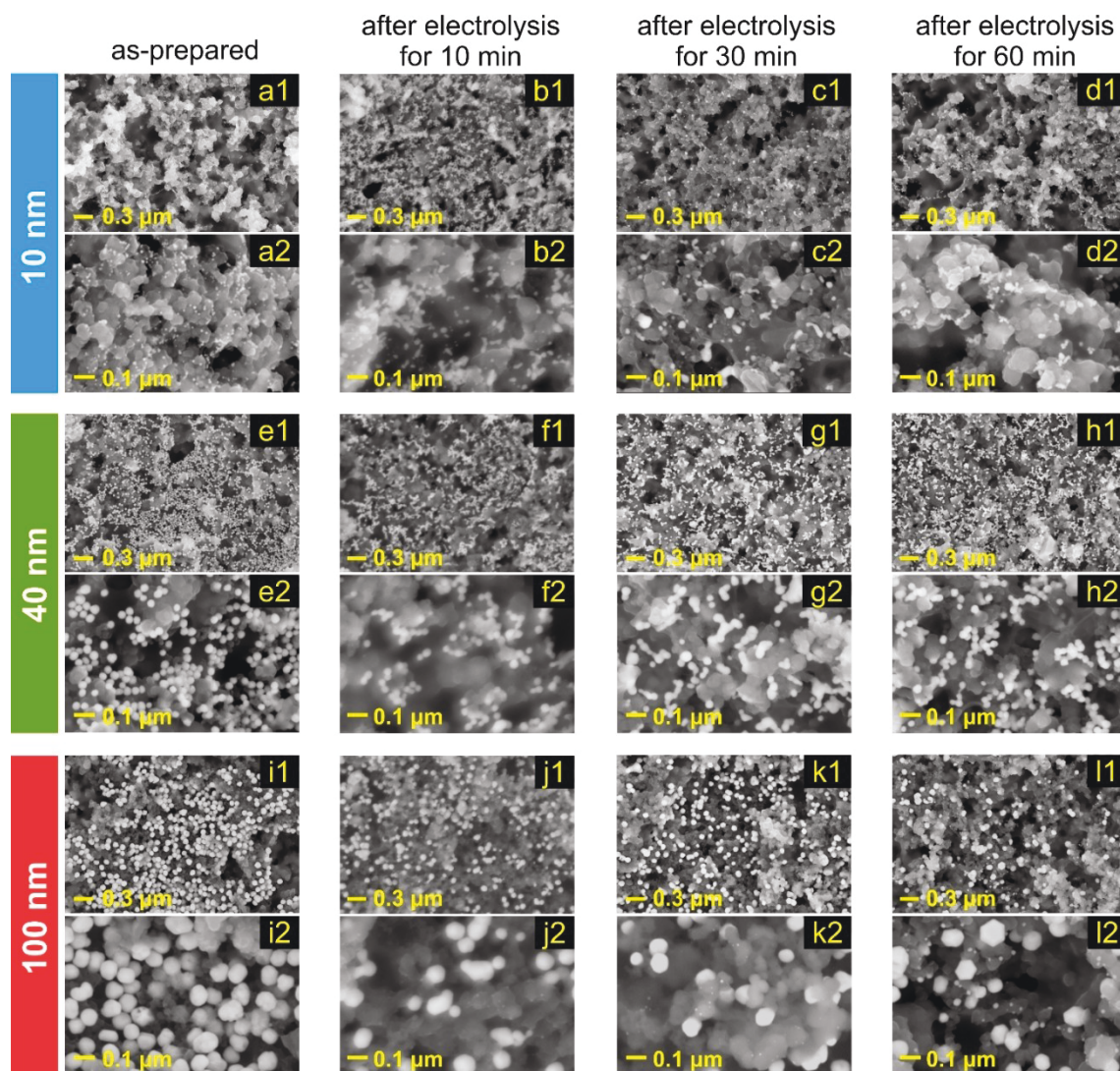
Figure 1. Representative SEM images of Ag NP-catalyst on GDEs. The size of NPs: (a–d) 10 nm, (e–h) 40 nm, (i–l) 100 nm. The SEM images were recorded (a, e, i) before ("as-prepared") and (b–d, f–h, j–l) after galvanostatic CO_2 electrolyses ($j=-283$ mA cm^{-2}) for different time (different passed charge): (b, f, j) 10 min (169.7 C cm^{-2}), (c, g, k) 30 min (509.2 C cm^{-2}), (d, h, l) 60 min (1018.4 C cm^{-2}). Two images of different magnification are shown for each sample.

ChemElectroChem

Research Article
doi.org/10.1002/celc.202200615

**Chemistry
Europe**
European Chemical
Societies Publishing
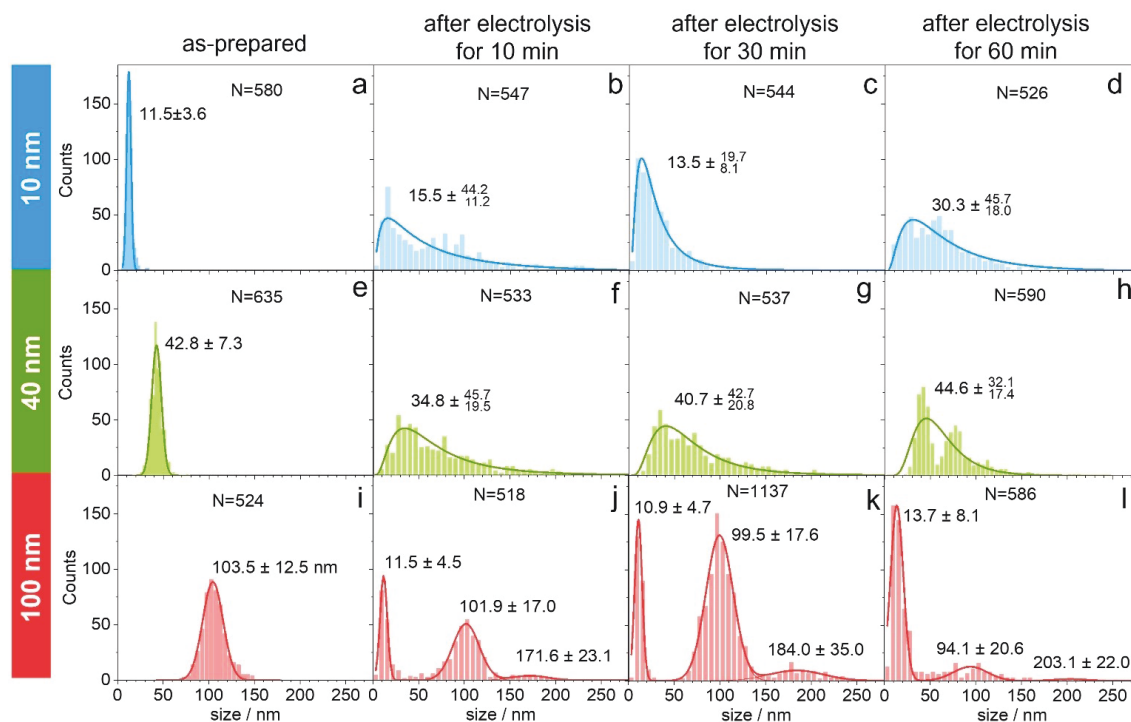
Figure 2. Histograms showing the particle size distribution of Ag NPs of different size: (a–d) 10 nm, (e–h) 40 nm, (i–l) 100 nm. The data were obtained for NP-catalysts (a, e, i) before and (b–d, f–h, j–l) after CO_2 electrolysis at $j = -283$ mA cm^{-2} for a certain time: (different passed charge): (b, f, j) 10 min (169.7 C cm^{-2}), (c, g, k) 30 min (509.2 C cm^{-2}), (d, h, l) 60 min (1018.4 C cm^{-2}). Expectation ranges of the particle size are shown for the fitted peak(s). Number of particles analyzed (N) is given in the graphs.

Ag NPs were fairly uniformly distributed over the MPL surface. Size analysis demonstrated a normal distribution of NP sizes on the GDE surface before electrolysis. The estimated mode values were close to the values indicated by the manufacturer (the values are given in the graphs, Figure 2). Inductively coupled plasma mass spectrometry (ICP-MS) data demonstrated that the actual mass loading for NPs of different sizes was nearly identical (Table 1). However, according to SEM data the number of NPs on the GDE surface (in terms of volume or mass) appeared dissimilar. The amount (volume and mass) of 10 nm NPs on the GDE surface seemed to be significantly less than those of 40 and 100 nm NPs. This finding is explained by the greater penetration of smaller NPs inside the GDE layers during drop-cast deposition. The cross-sectional SEM images in Figure 3 distinguished the boundary between MPL and CFS. The energy-dispersive X-ray spectroscopy (EDX) mapping of Ag demonstrated the presence of Ag NPs inside both MPL and CFS (Figure 3). Moreover, 10 nm NPs were distributed fairly uni-

formly in the microporous layer, with greater density around cracks and at the boundaries between microporous and microfiber layers. The amount of 10 nm NPs on the surface of the GDE was similar to that inside the microporous layer. This finding was supported by individual EDX spectra (cf. spectrum 1 with spectra 2 and 6 in Figure 3b). Spectrum 3 recorded at the area close to the microporous/microfiber layer boundary showed an enhanced Ag signal. The EDX mapping and spectra 4 and 5 unambiguously indicated that 10 nm NPs penetrated into the CFS.

A slightly less uniform distribution of 40 nm NPs was observed inside MPL (Figure 3c) with increased density on the top surface of MPL, at cracks, and around the MPL/CFS boundary. A smaller amount of Ag NPs was observed in CFS. This observation was supported by individual EDX spectra (Figure 3d). Spectra 1 to 3 showed Ag signals of slightly higher intensity than those in the spectra recorded at areas 4 and 5. A large fraction of 100 nm NPs after deposition were located on

Table 1. Loading of Ag in NP-catalyst as calculated from the drop-cast amount and as estimated by ICP-MS.

Ag NP-catalyst	Calculated loading [μg cm^{-2}]	Loading by ICP-MS [μg cm^{-2}]		
		As-prepared	After electrolysis[a]	After recovery experiments[b]
10 nm	300	290.52 ± 11.8	267.80 ± 20.7	266.65 ± 9.4
40 nm	300	297.31 ± 16.6	289.43 ± 17.0	277.04 ± 18.0
100 nm	300	303.02 ± 4.8	287.78 ± 18.2	270.68 ± 13.8

[a] After electrolysis at -283 mA cm^{-2} for 60 min. [b] After 2nd electrolysis at -283 mA cm^{-2} for 60 min.

ChemElectroChem

Research Article
doi.org/10.1002/celc.202200615

Chemistry Europe
European Chemical
Societies Publishing
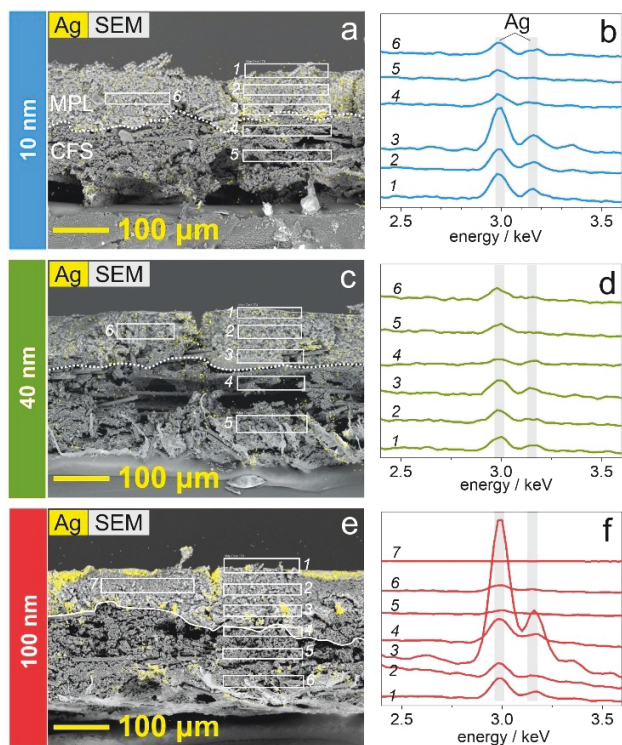
Figure 3. (a, c, e) Representative cross-sectional side-view SEM images and overlapped EDX Ag mapping of the microporous and microfiber GDE layers with deposited Ag NPs of different sizes: (a) 10 nm, (c) 40 nm, (e) 100 nm. Dotted lines indicate boundaries between MPL and CFS. (b, d, f) EDX spectra recorded for respective areas of GDE cross-sections (see numbering).

top of the MPL (Figure 3e). High density of NPs was also observed at cracks and at the MPL/CFS boundary, whereas NPs were scarcely detected inside MPL and CFS far from large cracks. This result was confirmed by EDX spectra (Figure 3f): spectra recorded at areas inside the layers (2 and 7 in MPL and 5 and 6 in CFS) showing weak or absent Ag signal, whereas the signal was stronger on the top of MPL (spectrum 1) or around the MPL/CFS boundary (spectra 3 and 4). These findings indicated that larger particles (such as 100 nm) scarcely penetrated through/into micropores of MPL, but a portion of these NPs passed through the MPL via cracks and accumulated at the MPL/CFS boundary.

Note that we used the same Ag mass loading for all NP-catalysts. Thus, the surface area of NP-catalysts would certainly depend on their initial size. In addition, the data in Figure 3 clearly show that a large fraction of particles penetrates the GDE and might not participate in the electrolysis reaction. Moreover, the amount of Ag NPs penetrated in CFS layer strongly depends on initial NP size. Estimation of the electro-active area of Ag NPs and the appropriate comparison of surface areas are hardly possible when solely based on the mass loading and size distribution data.

CO₂ Electrolysis: Loss of CO₂RR Performance

Figure 4 shows the FEs of three detected products (CO, H_2, and $HCOO^-$) formed during CO_2 galvanostatic electrolysis at $j = -283 \, \text{mA cm}^{-2}$ for 60 min (passed charge $q = 1018.4 \, \text{C cm}^{-2}$). The initial FE_{CO} was ~90–93% and was nearly identical for NPs of different sizes (Figure 4), in agreement with findings form studies on the size effect on CO_2RR. Au NPs and Cu NPs ~5 nm or larger have been reported to show similar CO_2RR performance in terms of faradaic efficiency.[24,25] Only smaller NPs showed a significant change in the product distribution. Typically, the use of Cu and Au NPs with sizes below 5 nm markedly increased faradaic efficiency of hydrogen formation, FE_{H2}, and decreased CO_2RR efficiency.[24,25]

However, over time or with a passed charge, the FE_{CO} drastically decreased, whereas the FE_{H2} correspondingly increased. No clear correlation was observed between the NP size and the CO_2RR performance deterioration. The fastest deterioration occurred for 40 nm NPs, whereas the slowest deterioration was observed for 100 nm NPs. The rate of FE_{CO} decrease over time was moderate for 10 nm NPs. Formate was also produced in a detectable amount in our experiments. Typically, FE_{HCOO^-} increased over time, reaching ~11% after 60 min of CO_2 electrolysis (1018.4 C cm⁻²).

The rapid loss in CO_2RR performance has been found to be associated primarily with potassium (bi)carbonate precipitation on the GDE.[2,3,21–23] The (bi)carbonate precipitation is caused by increased local alkalinity leading to an undesirable reaction of CO_2 with hydroxide ions. Several processes induce an increase in local pH. (i) CO_2RR and HER consume protons from water molecules, thus forming hydroxide ions. (ii) Driven by both
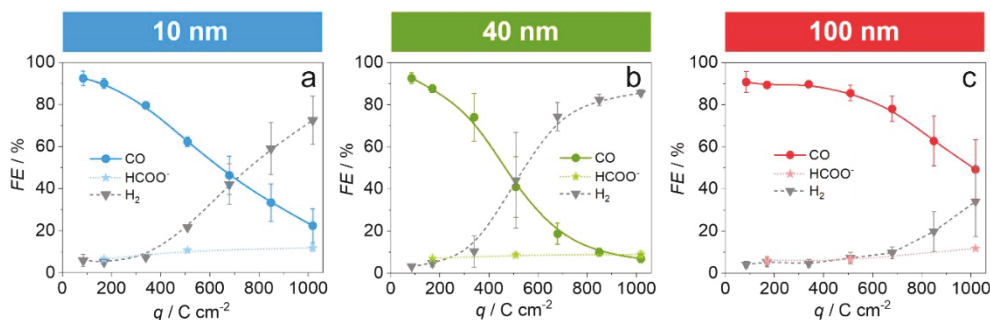
Figure 4. FEs of CO, $HCOO^-$, and H_2 versus charge passed during galvanostatic CO_2 electrolyses (at $j = -283 \, \text{mA cm}^{-2}$) employing Ag NP-catalysts. The size of NPs: (a) 10 nm, (b) 40 nm, (c) 100 nm. The total electrolysis time is 60 min.

ChemElectroChem

Research Article
doi.org/10.1002/celc.202200615

Chemistry Europe
European Chemical
Societies Publishing

chemical and electric potential gradients, K^+ ions penetrate even the anion exchange membrane.[26] (iii) Finally, the percolation of anolyte (KOH) from the anode compartment via membrane defects leads to flooding of the GDE. The electrolyte solution penetrating into GDE substantially slow down CO_2 diffusion to the active catalytic sites in MPL, thus, hindering CO_2RR consequently promoting HER.[23] On the other hand, the flooding of GDE induces the formation of (bi)carbonate at the three-boundary GDE interface. Because of the limited solubility of potassium (bi)carbonate (lower than the solubility of KOH), the salt precipitates and also leads to blocking of CO_2RR active sites.[21] The precipitation also results in a decreasing electrode potential during the galvanostatic CO_2 electrolysis (Figure S3). The potential at the beginning of the electrolysis at $j = -283\ mA\,cm^{-2}$ is around $-1.7\ V$ irrespective of the NP size and decreases with time, as the precipitate forms.

We also note that the precipitation issue may be affected by the amount of PVP-capping agent in the catalyst ink. Previously, we reported that PVP is present in ink not only as a capping agent adsorbed on Ag NPs but also in a dissolved/dispersed form (excess PVP).[3] The adsorption of PVP from ink on the GDE after catalyst drop-casting may change the interfacial properties of the electrode and influence the precipitation behavior. Alinejad et al. have recently demonstrated that a PVP-capped Au NP-catalyst displays worse CO_2RR performance (in terms of FE_{CO} and current density) than a PVP-free Au NP-catalyst in both an H-cell and a zero-gap electrolyzer.[27] Herein, we estimated the PVP content in supernatant solutions (Table 2). To quantify PVP surfactant, we determined the total nitrogen content in the supernatant solution (TN_{sup}), i.e., excess PVP, and in the solution of NPs redispersed in water after removal of excess PVP (TN_{NP}). We assumed that TN_{NP} corresponded to PVP directly attached to NPs. The data indicated that TN_{sup} (excess PVP) was approximately an order of magnitude higher than TN_{NP} (PVP on NPs) (Table 2). The results also indicated that the excess PVP decreased with NP size. That is, the concentration calculated for a PVP monomer, $c_{VP,sup}$, in the case of 100 nm NPs was half that for 10 nm NPs (135 vs. 250 ppm). Thus, the relatively slow deterioration of CO_2RR performance in the case of 100 nm NPs (Figure 4c) might also have been due to the smaller amount of PVP in the catalyst ink. The effect of PVP on the precipitation issue during CO_2 electrolysis in a zero-gap electrolyzer will be the focus of our follow-up work.

Despite the deterioration in CO_2RR performance associated with (bi)carbonate precipitation at the GDE, clear alterations in the NP-catalyst structure occurred after CO_2 electrolysis. These structural changes might lead to CO_2RR performance losses, which occur less rapidly than losses due to salt precipitation but can become considerable during long-term CO_2 electrolysis.

Of particular concern, NPs with certain preferential orientations (e.g., cubic NPs) display higher activity (lower overpotential) toward CO_2RR.

The structural disordering of such shaped NPs leads to catalyst deactivation.[20] In contrast, the degradation of even spherical NPs with no preferential surface orientation can lead to performance losses. For example, NP agglomeration decreases the electrochemically active surface area, whereas corrosion may promote the detachment of NPs, i.e., the loss of the contact between the catalyst and the support.

To confirm the fact that the large decrease in FE_{CO} within 60 min of CO_2 electrolysis (as shown in Figure 4) was associated primarily with (bi)carbonate precipitation, we performed so-called "recovery" experiment (Figures S4-S6). In this experiment, the GDE after the 1st electrolysis was washed accurately in water to remove the salt precipitate and used again in the 2nd electrolysis (details in Experimental Section). Of note, the washing procedure did not lead to any loss in Ag NP catalysts. ICP-MS data demonstrated nearly identical mass loading of Ag after the 1st and 2nd electrolyses (Table 1). Simultaneously, the washing allowed for removal of nearly all (bi)carbonate precipitate (as previously demonstrated by EDX analysis in Ref. [3]). Figure S4 shows the comparison of FEs for CO and H_2 production in the 1st and 2nd galvanostatic electrolyses at $j = -283\ mA\,cm^{-2}$. The CO_2RR performance almost completely recovered for the washed GDE: the initial FE_{CO} in the 2nd electrolysis was equal to or slightly less than that in the 1st electrolysis. The FE_{CO} decrease and the FE_{H2} increase over time (passed charge) were slightly faster in the case of the washed GDE in the 2nd electrolysis. However, beyond structural changes in NP catalysts, these effects may be associated with many other factors such as (partial) removal of the capping agent, PVP, slight changes in hydrophilicity of GDE, and/or remaining residual salt precipitate after the washing procedure.

CO_2 electrolysis was also performed at two other current densities in addition to $j = -283\ mA\,cm^{-2}$: -141 and $-566\ mA\,cm^{-2}$ (Figures S7–S12). In all cases, the charge passed during electrolysis was $509.2\ C\,cm^{-2}$, and therefore the electrolysis duration differed: 60 min at $-141\ mA\,cm^{-2}$, 30 min at $-283\ mA\,cm^{-2}$, and 15 min at $-566\ mA\,cm^{-2}$. When the FE_{CO} and FE_{H2} were plotted vs. electrolysis time (Figure S8), the deterioration rate of CO_2RR performance was higher at higher applied current density. However, when we compared data for the same charge passed, the decrease in FE_{CO} was highest for the lowest current density used (Figure S7). Overall, we concluded that the size of NPs had no considerable effect on CO_2RR performance deterioration, regardless of electrolysis duration or current density. This finding is in agreement with the conclusion that performance losses were due mainly to salt

Table 2. TN values for supernatant (TN_{sup}) and redispersed NPs (TN_{NP}) solutions after the removal of excess PVP and calculated respective concentrations of PVP monomers (vinylpyrrolidone, $c_{VP,sup}$ and $c_{VP,NP}$) assuming one nitrogen atom per monomer. The Ag content in the samples was $0.5\ mg\,mL^{-1}$.

Samples	TN_{sup} [ppm]	$c_{VP,sup}$ [ppm]	TN_{NP} [ppm]	$c_{VP,NP}$ [ppm]
10 nm	31.5	250	2.8	22
40 nm	21.7	172	2.3	18
100 nm	17.0	135	1.3	10

ChemElectroChem

Research Article
doi.org/10.1002/celc.202200615

**Chemistry
Europe**
European Chemical
Societies Publishing

precipitation. We also observed that increasing the current density of CO_2 electrolysis increased in FE_{HCOO^-} up to 17–19% (Figure S9). However, this change in the product distribution did not appear to depend on NP size: FE_{HCOO^-} increased with current density similarly for 10, 40, and 100 nm NPs. The dependencies of the electrode potential on the passed charge or time are also rather similar for NPs of different sizes (Figure S10). In general, the potential decreases during the galvanostatic electrolysis reaction. This decrease scales with the cathodic current applied.

Structural Changes in Ag NPs after CO_2 Electrolysis

The structural changes in NP catalysts were analyzed by SEM after CO_2 electrolyses. Because of massive salt precipitation, the GDE underwent the water washing procedure, as in the "recovery" experiments. A comparison of Ag mass loading estimated by ICP-MS before and after electrolysis indicated only a minor decrease (Table 1).

Representative SEM images of the Ag NP-catalyst layer after CO_2 electrolysis at $j = -283$ mA cm^{-2} are shown in Figure 1 for the three studied sizes of NPs. The size distributions of NPs are presented in Figure 2. Expected particle size ranges (mode ± deviation) were determined from the histograms shown in Figure 2, fitted by either symmetric Gaussians or asymmetric (skewed) log-normal functions.

The SEM images demonstrated that Ag NPs underwent agglomeration after CO_2 electrolysis even within 10 min (Figure 1). The agglomeration was characteristic for all three sizes of NPs under study. Furthermore, we observed the appearance of smaller particles after electrolysis with 100 nm NP catalyst (Figure 1j–l). From the fitting of NP size distribution, we made the following observations. In the case of 10 nm NPs, the size distribution was fitted by a log-normal function. The mode value increased with increasing electrolysis time (charge passed) from 11.5 up to 30.3 nm (Figure 2b–d), with some particles/agglomerates reaching 100 nm or greater (the longest dimension). Such agglomerated NPs were not observed before electrolysis, and as-prepared NPs had a fairly narrow expected range. In the case of 40 nm NPs (Figure 2f–h), the size distribution was also log-normal. Nevertheless, the mode value did not substantially shift after electrolysis; thus, a large fraction of NPs retained their initial size. Simultaneously, the expected range became broader, and skewness appeared with a larger contribution from agglomerated particles (as in the case of 10 nm NPs). The number of NPs smaller than 40 nm also increased after CO_2 electrolysis, thus indicating a degradation mechanism associated with partial NP fragmentation. The degradation behavior of 100 nm NPs was different. Three populations of NPs were distinguished and fitted with Gaussians (Figure 2j–l). The size distribution in the population with the mode value close to the initial value (100 nm) became broader after electrolysis: the deviation increased from 12.5 nm for the as-prepared catalyst up to 20.6 nm for the catalyst after 60-min electrolysis. Simultaneously, the mode value of this population slightly decreased from 103.5 to 94.1 nm after

electrolysis, thus, suggesting fragmentation of the NPs. A new population with a mode value of approximately 11–13 nm appeared after 10 min of CO_2 electrolysis. The number of these small NPs and the expected range of the population appeared to increase with electrolysis time (charge passed). SEM images in Figure 1j–l clearly displayed an increased number of small NPs. The formation of the small NPs was consistent with the decrease in the mode value of the initial NP distribution. Additionally, we resolved the third population with the mode value, which changed from 171.6 nm to 203.1 nm with increasing electrolysis time (Figure 2j–l). This population typically consisted of two or three agglomerated NPs. The agglomeration of 10 nm NPs was much more severe during CO_2 electrolysis: a large fraction of agglomerates exceeded the initial NP size by factors of 10 to 20 (Figure 2b–d). Thus, the agglomeration of 100 nm particles was a slower process than that for 10 nm NPs. On the basis of our results, we concluded that 100 nm NPs are more likely to undergo fragmentation than agglomeration.

Interestingly, we also observed the faceting of individual 100 nm NPs after electrolysis. For the as-prepared samples, virtually all NPs were spherical without any distinguishable facets. SEM images in Figure 5 (more images in Figure S13) showed that NPs underwent extensive restructuring and, after 60 min of electrolysis, acquired clear facets. Facet formation was characteristic of the cathodic corrosion process.[28,29] Although the mechanism of cathodic corrosion is not yet fully understood, it has been observed for many metals including Ag.[30] Elnagar et al. have demonstrated the formation of a (111) facet on a polycrystalline Au wire after cathodic polarization in concentrated KOH solution (5–20 M).[31] Au faceting was observed at −1.5 V vs. RHE (reversible hydrogen electrode) and became more pronounced at more negative potentials. After polarization at −3.5 V vs. RHE for just 60 s, the voltammetric response of Au wire was nearly identical to that for an Au(111) single crystal electrode. The authors in ref.[31] have concluded that HER and high near-surface concentration of K$^+$ ions are essential for the cathodic corrosion process and faceting. Such conditions can be fulfilled during CO_2 electrolysis in a gas-fed electrolyzer. Typically, the GDE cathode potential during galvanostatic polarization at $j = -283$ mA cm^{-2} is between −1.75 and −1.95 V, whereas high alkalinity and K$^+$ concentration are achieved because of HER and CO$_2$RR, K$^+$ ion penetration and KOH solution flooding via the membrane. In the case of 40 nm NPs the faceting was observed but in much
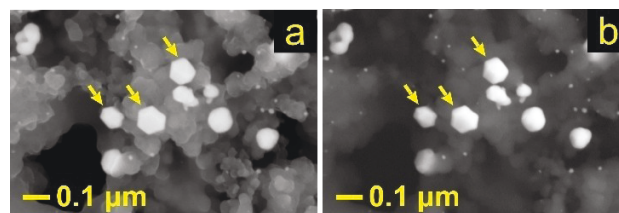

Figure 5. Representative SEM images of 100 nm Ag NP-catalysts on GDE after passing 1018.4 C cm^{-2} during CO_2 electrolysis (60 min) at $j = -283$ mA cm^{-2}. NPs indicated by arrows display clear faceting. Images were acquired using (a) InLens SE and (b) BSD detectors.

ChemElectroChem

Research Article
doi.org/10.1002/celc.202200615

Chemistry
Europe

European Chemical
Societies Publishing

less extent than for 100 nm NPs. Figure S14 demonstrates a few faceted NPs for a sample after the "recovery" experiment, i.e., two electrolyses at $j = -283\ \text{mA cm}^{-2}$ for 60 min each. For small NPs (10 nm), we did not observe pronounced faceting after CO_2 electrolysis, possibly because of insufficient SEM resolution as well as the tendency of the smaller particles to agglomerate.

The faceting of spherical NPs in this study (Figure 5) was opposite from the degradation behavior of cubic Ag NPs with the initial facet orientation of (100).[2] During electrolysis, the Ag nanocubes underwent fragmentation and changed their cubic shape, becoming more spherical during CO_2 electrolysis. Similarly, the fragmentation and destruction of (100) facets were found for cubic Cu NPs.[20]

In addition, we performed a reference experiment employing the 100 nm NP-catalyst, where we fed the GDE with $Ar + H_2O$ (no CO_2). Under these conditions only HER takes place at the cathode. Note, no precipitate was observed at the cathode after 60 min of electrolysis at $j = -283\ \text{mA cm}^{-2}$. This might be the reason why the electrode potential was much more stable during the water electrolysis than that in the course of CO_2 electrolysis (Figure S15a). Nevertheless, the MPL layer of the GDE was wet after the water electrolysis probably likely due to the KOH flooding. The SEM analysis after the electrolysis in the absence of CO_2 demonstrates much less pronounced formation of small clusters as compared to the samples after the CO_2 electrolysis at the same current density (Figure S15). This finding suggests that the fragmentation of 100 nm Ag NPs is more pronounced during CO_2RR (on CO_2-fed GDE). One possible explanation of this observation is that the (bi)carbonate precipitation on the CO_2-fed GDE blocks diffusion pathways for CO_2, H_2O, K^+, and OH^- ions and, thus, may lead to a greater local increase in alkalinity as compared to the situation where only Ar and H_2O are fed through the GDE.

Recently, we have reported that excess PVP influences the degradation behavior of 40 nm Ag NPs: the removal of excess PVP leads to more pronounced agglomeration of NPs after CO_2 electrolysis.[3] We assumed that excess PVP adsorbed on the carbon support rendered NPs immobile and thus hindered their agglomeration. The estimation of TN in NP-catalyst samples demonstrated a smaller amount of excess PVP in the case of larger NPs (cf. TN_{sup} values in Table 2). Thus, a greater tendency for agglomeration might be expected for NP catalysts containing smaller amounts of excess PVP. However, we observed an opposite trend: although the 100 nm NP-catalyst contained a smaller amount of excess PVP, the agglomeration was more characteristic for 10 and 40 nm NP catalysts (Figures 1 and 2). This result indicated that NP size plays a more decisive role in degradation behavior than excess PVP content observed in our experiments.

The SEM analysis of Ag NP catalysts after CO_2 electrolysis at different current densities (but with the same passed charge equal to $509.2\ \text{C cm}^{-2}$) is shown in Figures S11 and S12. For the 10 nm NPs, the increase in current density (-141, -283, and $-566\ \text{mA cm}^{-2}$) had a minor effect on the degradation behavior: the NPs tended to agglomerate at any current density (Figures S11a–d, S12a–d). The agglomeration of 40 nm NPs appeared to be more severe with increasing current density of

electrolysis (Figures S11e–f, S12e–f). At $j = -566\ \text{mA cm}^{-2}$, the NP size could scarcely be estimated because of massive agglomeration, whereas at $j = -141\ \text{mA cm}^{-2}$, many agglomerates consisted of two NPs, thus resulting in an additional peak in the size distribution histogram at 79.7 nm (Figure S12f). For 100 nm NPs, the agglomeration was insignificant at low current density $j = -141\ \text{mA cm}^{-2}$ (Figure S12j). At higher current densities (-283 and $-566\ \text{mA cm}^{-2}$), the difference in degradation behavior was minor (Figure S12k, l). At all current densities, the 100 nm NPs tended toward fragmentation with the formation of small particles with a mode size of 11–18 nm (Figure S12j–l).

We also performed SEM analysis of 40 nm catalyst after the "recovery" experiment, i.e., after the 2nd electrolysis at $j = -283\ \text{mA cm}^{-2}$ (product distribution data are shown in Figures S4, S5). The comparison of the morphology and size distribution of the NP catalysts after the 1st and 2nd electrolyses (Figure 6a–c) demonstrated further agglomeration and fragmentation of NPs in the 2nd electrolysis: the expected range became broader, and the deviations increased for both directions (toward smaller and larger sizes; Figure 6c). Thus, the continuation of CO_2 electrolysis after reactivation of GDE by removal of (bi)carbonate precipitate led to further degradation (agglomeration and fragmentation) of Ag NPs. SEM analysis of the 100 nm catalyst after the "recovery" experiment demonstrates even more pronounced changes in size distribution as compared to that after the 1st electrolysis (Figure 6d–f). The mode value of the population of small particles formed in the 1st electrolysis increased from 13.7 to 25.3 nm accompanied by a broadening of the expectation range. This finding suggests that at least part of small clusters agglomerated (in parallel to

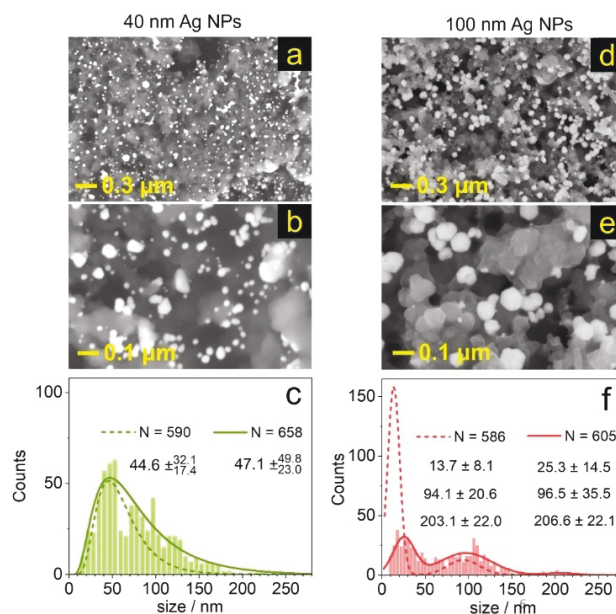**Figure 6.** (a, b, d, e) SEM images and (c, f) size histograms and fitting (solid line) of (a–c) 40 nm and (d–f) 100 nm NP-catalysts after "recovery" experiment, i.e., 2nd electrolysis at $j = -283\ \text{mA cm}^{-2}$. The fitting curves of size distribution for NP-catalysts after the 1st electrolysis are also shown by dashed lines. Number of particles analyzed (N), mode values, and deviations are given in the graphs.

ChemElectroChem

Research Article
doi.org/10.1002/celc.202200615

Chemistry
Europe
European Chemical
Societies Publishing

the formation of new small clusters due to fragmentation) in the course of the 2nd electrolysis. Moreover, some 100 nm NPs display signs of severe degradation of after the 2nd electrolysis as indicated in Figure S6.

Raw data and unprocessed measurement files serving as a basis of this article can be found elsewhere.[32]

Conclusion

Herein, we studied the effect of NP size on NP degradation behavior during CO_2 electrolysis in a gas-fed zero-gap electrolyzer. For this purpose, we performed galvanostatic electrolyses with PVP-capped spherical Ag NPs of different initial sizes (10, 40, and 100 nm). Post-electrolysis SEM and size-distribution analyses were used to explore structural changes. ICP-MS analysis of Ag loading before and after electrolysis showed no considerable detachment of the NP-catalyst, regardless of the NP size. However, SEM data demonstrated clear structural changes in NPs on the surface of GDE after electrolysis. The smallest 10 nm NPs underwent mainly agglomeration during galvanostatic CO_2 electrolysis, thus leading to the formation of larger agglomerates with the longest distance up to 200 nm. For 40 nm NPs, agglomeration was also prevalent, although the fragmentation of NPs with the formation of smaller clusters was also detected. The size distribution of both 10 and 40 nm NPs after CO_2 electrolysis was fitted well with a log-normal function, with a pronounced skewness toward larger sizes. In the case of 100 nm NPs, two new populations were distinguished with mode values of 11–13 nm and 170–200 nm after electrolysis. The mode values, particularly for the population of larger agglomerates, increased with electrolysis time (charge passed). The 100 nm NPs tended to form agglomerates consisting primarily of two or three initial particles. The population of smaller particles (mode of approximately 11–13 nm) was formed because of the fragmentation of initial NPs. The fragmentation appeared to be associated with cathodic corrosion of Ag NPs at negative potentials under conditions of intensive CO_2RR and HER. The GDE flooding with KOH solution, additional penetration of K^+ ions via a membrane, and accumulation of OH- ions due to cathodic reactions may facilitate the cathodic corrosion of Ag catalyst. Another sign of cathodic corrosion is the faceting of NPs, which was clearly distinguishable for the 100 nm NP-catalyst. We emphasise that the NP mass loading may also affect the degradation behavior. Simultaneously, the correlation between the structural changes and the CO_2RR performance losses in a zero-gap electrolyzer was not able to be established because of the flooding and the harsh salt precipitation at the GDE within a short time (minutes). However, the results clearly indicated that on a long-term time scale, structural changes in catalysts play important roles in CO_2RR performance. NP agglomeration would decrease the electrochemically active surface area, whereas fragmentation/corrosion would promote the detachment of NPs.

Experimental Section

Catalyst Preparation

PVP-capped Ag NPs of different sizes (~10 nm, ~40 nm, ~100 nm, and 1 mg mL^{-1} in water) were purchased from NanoComposix. Subsequently, 1 mL of as-received Ag NP suspension was diluted to 1.627 mL by the addition of isopropanol (VLSI Selectipur, BASF, Germany). Then 0.1765 mg of carbon powder (Vulcan XC 72R, Cabot, USA) was dispersed in 353 μL isopropanol by sonication for 1 hour. The two suspensions were subsequently mixed, and after the addition of 20 μL Nafion solution (5% Nafion, 15–20% water, Sigma–Aldrich), the new suspension with an Ag NP concentration of 0.5 mg mL^{-1} was sonicated for 5 min to yield a homogeneous catalyst ink. Next, 75 μL of the above suspension of carbon-supported Ag NPs was drop-cast on the hydrophobic surface of a GDE (circle with diameter d of 4 mm; Sigracet 36BB, Fuel Cell Store), as shown in Figure S2. The electrodes were dried under ambient conditions. The mass loading was 300±17 μg cm^{-2} (Table 1), as determined by inductively coupled plasma mass spectrometry (ICP-MS). A GDE (Sigracet 36BB) circle (d=4 mm) with an Ag-NP catalyst was inserted into the hole (d=4 mm) in the center of a larger-area GDE (d=20 mm, Freudenberg H23C8, Fuel Cell Store), as illustrated in Figure S2, and the assembled electrode was further inserted in an electrolyzer.

Assembly of Gas-Fed Zero-Gap Cell

The electrolyzer used in this work has been described elsewhere (Figure S1).[2,3] It consists of a stainless-steel cell body with gas flow channels used to feed the CO_2 from the backside of the GDE. The prepared electrode was placed on the top of the gas flow channels, with its catalyst modified surface facing upward. Subsequently, a hydroxide-functionalized Sustainion alkaline membrane (X3750 RT, Dioxide materials) and a PTFE (polytetrafluoroethylene) anolyte compartment were placed on top of the GDE. Then 10 mL of 2.0 M KOH was used as an electrolyte in the anolyte compartment. An Ag/AgCl (3M KCl, double junction design, Metrohm) electrode and Ir wire (99.9%, Goodfellow GmbH) were used as reference and counter electrodes. The counter electrode was placed inside a glass capillary tube with a glass frit. The PTFE anolyte compartment had a central orifice of 3 mm diameter at its bottom, thereby providing direct contact between the electrolyte and the underlying anion-exchange membrane, whereas the GDE cathode was prevented from direct contact with the supporting anolyte. Thus, we defined the geometric area of the GDE electrode as the area of this orifice, i.e., 0.0707 cm^2. During electrolysis, a humidified CO_2 stream (17 mL min^{-1}, 99.999%, Carbagas, Switzerland) was continuously fed through the gas flow channels of the cell body, adjacent to the GDE.

Electrochemical Measurements and Product Distribution Studies

CO_2 electrolysis was performed at room temperature (22±1 °C) in galvanostatic mode with an ECi-200 potentiostat (Nordic Electro-chemistry). The reported current and charge densities were normalized to the geometric surface area (0.0707 cm^2). The gaseous products of CO_2RR were quantitatively analyzed by on-line gas chromatography (SRI Instruments). A thermal conductivity detector for detecting H_2 and a flame ionization detector with a methanizer for detecting CO and hydrocarbons were applied in our studies. Among the possible dissolved products, only formate was detected in all experiments performed. Formate anions forming during CO_2 electrolysis diffused via the anion-exchange membrane to the

ChemElectroChem

Research Article
doi.org/10.1002/celc.202200615

**Chemistry
Europe**
European Chemical
Societies Publishing

anode compartment. Thus, formate was quantified by ion chromatography (Metrohm Ltd., Switzerland) analysis of anolyte samples collected after CO_2 electrolysis.

The faradaic efficiency (FE_i) of the gaseous product was calculated[33] as:

where x_i denotes the molar fraction of the products determined by gas chromatography with an independent calibration standard gas (Carbagas), n_i is the number of electrons involved in the reduction reaction to form a particular product ($n_i = 2$ for both CO and H_2 formation), $F = 96485.3 \, C\,mol^{-1}$ is Faraday's constant, v_m is the molar CO_2 gas flow rate measured by a universal flowmeter (7000 GC flowmeter, Ellutia), and I is the current set for the galvanostatic electrolysis.

The faradaic efficiency of formate FE_{HCOO^-} is calculated as:

$$FE_{HCOO^-} = \frac{C_{HCOO^-} V_{anolyte} F n_{HCOO^-}}{Q} \times 100\% \qquad (2)$$

where c_{HCOO^-} denotes the formate concentration in the anolyte determined by ion chromatography, $V_{anolyte}$ is the volume of anolyte in the electrolyzer, n_{HCOO^-} is the number of electrons involved in the formation of formate ($n_{HCOO^-} = 2$), and Q is the passed charge during galvanostatic CO_2 electrolysis. Every data point of FE (FE_{CO}, FE_{H2}, and FE_{HCOO^-}) was obtained from three independent experiments with new GDEs, and error bars represent standard deviations.

In the "recovery" experiments, the GDE after the 1st electrolysis was carefully placed onto the surface of Milli-Q water in a beaker with the catalyst layer facing downward. Water was exchanged at least five times every 15 min. Then the GDE was dried and again used for the electrolysis (2nd electrolysis). Details have been previously reported.[3]

SEM and EDX

For morphological analysis of catalysts, a Zeiss Gemini 450 scanning electron microscope equipped with the InLens secondary electron (InLens SE) and back-scattering detectors was used. SEM images obtained with the InLens SE detector are presented herein unless otherwise specified. An acceleration voltage of 5 kV and currents of 120 pA and 200 pA were applied at a working distance of 2.9–4.0 mm. The particle size was measured in Smile View software, and the particle size distribution was based on size estimations of 500–1100 individual particles and agglomerates for each catalyst in three randomly selected areas. The particle/agglomerate size was defined as the longest dimension in the case of anisotropic NPs (Figure S16). EDX spectra and 2D surface elemental maps of samples were obtained with AZtec 5.0 software (Oxford Instruments). An acceleration voltage of 10 kV and a current of 1000 pA were applied at a working distance of 8.5 mm for EDX measurements.

ICP-MS

The Ag mass loading of the electrodes was determined with a NExION 2000 ICP-MS instrument (Perkin Elmer). The Ag NPs on the GDE were dissolved in 1 mL HNO_3 (69.3%, BASF SE, Ludwigshafen, Germany). The obtained solutions were further diluted with 3% HNO_3 solution by a factor of 1000 and injected into the ICP-MS instrument to obtain the actual content of Ag on GDEs.

Total Nitrogen Content Determination

To quantify PVP surfactant in the dispersion of Ag NPs, we determined the total nitrogen content (TN). Sample solutions with Ag NPs (Ag content is $0.5 \, mg\,mL^{-1}$) were diluted by a factor of 4. Then 100 µL of diluted solution (Ag content is $0.125 \, mg\,cm^{-3}$) was further centrifuged to separate NPs from the supernatant. The centrifugation rate was 35000 rpm (for 40 min) for solutions with 40 and 100 nm NPs, whereas a solution with 10 nm NPs was centrifuged for 40 min at 35000 rpm, then 40 min more at 50000 rpm. The obtained supernatant was further fed into a DIMATOC 2100 instrument (Dimatec, Essen, Germany) to determine TN in supernatant solution (TN_{sup}). The organic compounds were oxidized at 850 °C on a Pt catalyst to CO_2/NO. A non-dispersive infrared gas sensor with a reflective diffuser and a chemiluminescence detector was used to detect NO. The separated NPs were further redispersed in Milli-Q water, and these prepared dispersions with the same Ag content ($0.5 \, mg\,mL^{-1}$) were again analyzed to determine the TN_{NP}.

Conflict of Interest

The authors declare no conflict of interest.

Data Availability Statement

The data that support the findings of this study are available from the corresponding author upon reasonable request.

[1] P. De Luna, C. Hahn, D. Higgins, S. A. Jaffer, T. F. Jaramillo, E. H. Sargent, *Science* **2019**, *364*, eaav3506.
[2] M. de Jesus Gálvez-Vázquez, P. Moreno-García, H. Xu, Y. Hou, H. Hu, I. Z. Montiel, A. V. Rudnev, S. Alinejad, V. Grozovski, B. J. Wiley, M. Arenz, P. Broekmann, *ACS Catal.* **2020**, *10*, 13096–13108.
[3] M. Liu, Y. Kong, H. Hu, N. Kovács, C. Sun, I. Zelocualtecatl Montiel, M. d J Gálvez Vázquez, Y. Hou, M. Mirolo, I. Martens, J. Drnec, S. Vesztergom, P. Broekmann, *J. Catal.* **2021**, *404*, 371–382.
[4] J. He, Y. Li, A. Huang, Q. Liu, C. Li, *Electrochem. Energy Rev.* **2021**, *4*, 680-717.
[5] Y. Gu, J. Wei, X. Wu, X. Liu, *Sci. Rep.* **2021**, *11*, 11136.
[6] Y. Wu, S. Garg, M. Li, M. N. Idros, Z. Li, R. Lin, J. Chen, G. Wang, T. E. Rufford, *J. Power Sources* **2022**, *522*, 230998.
[7] A. Salehi-Khojin, H.-R. M. Jhong, B. A. Rosen, W. Zhu, S. Ma, P. J. A. Kenis, R. I. Masel, *J. Phys. Chem. C* **2013**, *117*, 1627–1632.

ChemElectroChem

Research Article
doi.org/10.1002/celc.202200615

Chemistry Europe
European Chemical
Societies Publishing

[8] A. V. Rudnev, K. Kiran, A. Cedeño López, A. Dutta, I. Gjuroski, J. Furrer, P. Broekmann, *Electrochim. Acta* **2019**, *306*, 245–253.

[9] Q. Lu, J. Rosen, F. Jiao, *ChemCatChem* **2015**, *7*, 38–47.

[10] S. Liu, H. Tao, L. Zeng, Q. Liu, Z. Xu, Q. Liu, J.-L. Luo, *J. Am. Chem. Soc.* **2017**, *139*, 2160–2163.

[11] W. H. Lee, Y.-J. Ko, Y. Choi, S. Y. Lee, C. H. Choi, Y. J. Hwang, B. K. Min, P. Strasser, H.-S. Oh, *Nano Energy* **2020**, *76*, 105030.

[12] S. Popović, M. Smiljanić, P. Jovanovič, J. Vavra, R. Buonsanti, N. Hodnik, *Angew. Chem. Int. Ed.* **2020**, *59*, 14736–14746; *Angew. Chem.* **2020**, *132*, 14844–14854.

[13] C. Spöri, J. T. H. Kwan, A. Bonakdarpour, D. P. Wilkinson, P. Strasser, *Angew. Chem. Int. Ed.* **2017**, *56*, 5994–6021; *Angew. Chem.* **2017**, *129*, 6088–6117.

[14] B. Vanrenterghem, M. Bele, F. R. Zepeda, M. Šala, N. Hodnik, T. Breugelmans, *Appl. Catal. B* **2018**, *226*, 396–402.

[15] Y. Hou, N. Kovács, H. Xu, C. Sun, R. Erni, M. d J Gálvez-Vázquez, A. Rieder, H. Hu, Y. Kong, M. Liu, B. J. Wiley, S. Vesztergom, P. Broekmann, *J. Catal.* **2021**, *394*, 58–66.

[16] J. Huang, M. Mensi, E. Oveisi, V. Mantella, R. Buonsanti, *J. Am. Chem. Soc.* **2019**, *141*, 2490–2499.

[17] J. Huang, N. Hörmann, E. Oveisi, A. Loiudice, G. L. De Gregorio, O. Andreussi, N. Marzari, R. Buonsanti, *Nat. Commun.* **2018**, *9*, 3117.

[18] W. T. Osowiecki, J. J. Nussbaum, G. A. Kamat, G. Katsoukis, M. Ledendecker, H. Frei, A. T. Bell, A. P. Alivisatos, *ACS Appl. Energ. Mater.* **2019**, *2*, 7744–7749.

[19] H. Yun, J. Kim, W. Choi, M. H. Han, J. H. Park, H.-s. Oh, D. H. Won, K. Kwak, Y. J. Hwang, *Electrochim. Acta* **2021**, *371*, 137795.

[20] P. Grosse, D. Gao, F. Scholten, I. Sinev, H. Mistry, B. Roldan Cuenya, *Angew. Chem. Int. Ed.* **2018**, *57*, 6192–6197; *Angew. Chem.* **2018**, *130*, 6300–6305.

[21] M. E. Leonard, L. E. Clarke, A. Forner-Cuenca, S. M. Brown, F. R. Brushett, *ChemSusChem* **2020**, *13*, 400–411.

[22] L.-C. Weng, A. T. Bell, A. Z. Weber, *Energy Environ. Sci.* **2019**, *12*, 1950–1968.

[23] Y. Kong, H. Hu, M. Liu, Y. Hou, V. Kolivoška, S. Vesztergom, P. Broekmann, *J. Catal.* **2022**, *408*, 1–8.

[24] R. Reske, H. Mistry, F. Behafarid, B. Roldan Cuenya, P. Strasser, *J. Am. Chem. Soc.* **2014**, *136*, 6978–6986.

[25] H. Mistry, R. Reske, Z. Zeng, Z.-J. Zhao, J. Greeley, P. Strasser, B. R. Cuenya, *J. Am. Chem. Soc.* **2014**, *136*, 16473–16476.

[26] J. J. Kaczur, H. Yang, Z. Liu, S. D. Sajjad, R. I. Masel, *Front. Chem.* **2018**, *6*, 263.

[27] S. Alinejad, J. Quinson, G. K. H. Wiberg, N. Schlegel, D. Zhang, Y. Li, S. Reichenberger, S. Barcikowski, M. Arenz, *ChemRxiv.* **2021**. DOI: https://doi.org/10.26434/chemrxiv-2021-1t50s-v3.

[28] M. M. Elnagar, J. M. Hermann, T. Jacob, L. A. Kibler, *Curr. Opin. Electrochem.* **2021**, *27*, 100696.

[29] T. J. P. Hersbach, I. T. McCrum, D. Anastasiadou, R. Wever, F. Calle-Vallejo, M. T. M. Koper, *ACS Appl. Mater. Interfaces* **2018**, *10*, 39363–39379.

[30] J. Feng, D. Chen, A. S. Sediq, S. Romeijn, F. D. Tichelaar, W. Jiskoot, J. Yang, M. T. M. Koper, *ACS Appl. Mater. Interfaces* **2018**, *10*, 9532–9540.

[31] M. M. Elnagar, J. M. Hermann, T. Jacob, L. A. Kibler, *Electrochim. Acta* **2021**, *372*, 137867.

[32] H. Hu, M. Liu, Y. Kong, Y. Hou, I. Zelocualtecatl Montiel, A. V. Rudnev, P. Broekmann, *Zenodo* **2022**. DOI: https://doi.org/10.5281/zenodo.6840454.

[33] A. V. Rudnev, in *Encyclopedia of Interfacial Chemistry* (Ed.: K. Wandelt), Elsevier, Oxford, **2018**, pp. 321–325.

5.3 Effective perspiration is essential to uphold the stability of zero-gap MEA-based cathodes used in CO₂ electrolysers

Authors: **Huifang Hu**, Ying Kong, Menglong Liu, Viliam Kolivoška, Alexander V. Rudnev, Yuhui Hou, Rolf Erni, Soma Vesztergom*, and Peter Broekmann*

Highlights: The effect of excess capping agents (e.g. PVP) on the stability of gas-fed zero-gap electrolyzer was investigated. PVP was used to stabilize the Ag NPs, and the catalysts with the PVP were deposited on the GDE when preparing the electrodes. The PVP blocks the perspiration channels of MPL and thus accelerates the flooding. The excess PVP were removed through an ultracentrifugation to obtain the catalyst with less PVP. The GDE modified with reduced PVP content shows a longer life-time of CO₂ electrolysis. It is highlighted that the effective perspiration is essential to maintain the stability of gas-fed zero-gap electrolyzer.

Contributions: I executed most of the electrochemical measurements, SEM and EDX characterization of the electrodes, and did the ICP-MS analysis. Moreover, I analyzed the results and wrote the first draft of the manuscript.

Check for updates

Effective perspiration is essential to uphold the stability of zero-gap MEA-based cathodes used in CO2 electrolysers†

Huifang Hu, [ID] [a] Ying Kong, [a] Menglong Liu, [a] Viliam Kolivoška, [ID] [b]
Alexander V. Rudnev, [ID] [ac] Yuhui Hou, [a] Rolf Erni, [ID] [d] Soma Vesztergom [ID] *[ae]
and Peter Broekmann [ID] *[a]

The application of gas diffusion electrodes (GDEs) for the electrochemical reduction of CO_2 to value-added products creates the possibility of achieving current densities of a few hundred mA cm^{-2}. To achieve stable operation at such high reaction rates remains, however, a challenging task, due to the flooding of the GDE. In order to mitigate flooding in a zero-gap membrane-electrode assembly (MEA) configuration, paths for effective electrolyte perspiration inside the GDE structure have to be kept open during the electrolysis process. Here we demonstrate that apart from the operational parameters of the electrolysis and the structural properties of the supporting gas diffusion layers, also the chemical composition of the applied catalyst inks can play a decisive role in the electrolyte management of GDEs used for CO_2 electroreduction. In particular, the presence of excess amounts of polymeric capping agents (used to stabilize the catalyst nanoparticles) can lead to a blockage of micropores, which hinders perspiration and initiates the flooding of the microporous layer. Here we use a novel ICP-MS analysis-based approach to quantitatively monitor the amount of perspired electrolyte that exits a GDE-based CO_2 electrolyser, and we show a direct correlation between the break-down of effective perspiration and the appearance of flooding—the latter ultimately leading to a loss of electrolyser stability. We recommend the use of an ultracentrifugation-based approach by which catalyst inks containing no excess amount of polymeric capping agents can be formulated. Using these inks, the stability of electrolyses can be ensured for much longer times.

1 Introduction

Global warming, caused by the burning of fossil fuels and the resulting rapid increase of atmospheric CO_2 levels, is regarded as one of the most serious problems faced by human society. From this respect, electrochemical CO_2 reduction deserves special attention. Propelled by excess renewable energy sources, this process may not only provide viable means to reduce CO_2

[a]NCCR Catalysis, University of Bern, Department of Chemistry, Biochemistry and Pharmaceutical Sciences, Freiestrasse 3, 3012 Bern, Switzerland. E-mail: peter. broekmann@unibe.ch; vesztergom@chem.elte.hu

[b]J. Heyrovský Institute of Physical Chemistry of the Czech Academy of Sciences, Dolejškova 3, 182 23 Prague, Czechia

[c]A. N. Frumkin Institute of Physical Chemistry and Electrochemistry, Russian Academy of Sciences, Leninsky Prospekt 31, 119071 Moscow, Russia

[d]Swiss Federal Laboratories for Materials Science and Technology (EMPA), Electron Microscopy Center, Überlandstrasse 129, 8600 Dübendorf, Switzerland

[e]Eötvös Loránd University, MTA-ELTE Momentum Interfacial Electrochemistry Research Group, Pázmány Péter Sétány 1/A, 1117 Budapest, Hungary

† Electronic supplementary information (ESI) available. See DOI: https://doi.org/10.1039/d2ta06965b

emissions, but it can also create the possibility of converting excess energy into the form of storable fuels.[1]

The successful design of industrial level CO_2 electrolysers that can be operated for extended periods of time, converting CO_2 to a set of desired products at high rate and at low energy costs, requires a well-coordinated interplay of all electrolyser constituents.[2–5] From the chemistry, yet not from the overall efficiency point of view, the most essential part of a CO_2 electrolyser unit is the cathode catalyst: this is the scene where the actual transition of CO_2—its reduction to value-added products—takes place. In the past three decades, huge research efforts have thus been invested in the development of electrocatalysts that can achieve considerable reaction yields, preferably at low overvoltages.[6,7]

Today, researchers agree that apart from their chemical composition it is also the nanoscale structure of electrocatalysts that mostly affect their performance in CO_2 electroreduction.[8–10] Metallic catalysts of nanoparticulate (NP) form, for example, usually exhibit a much higher mass-normalised activity than planar metallic surfaces.[11] This is mostly due to the large surface area of NPs that offers more active sites with low coordination numbers, enabling improved performances.[12] Metallic

This journal is © The Royal Society of Chemistry 2023

J. Mater. Chem. A, 2023, **11**, 5083–5094 | 5083

NPs thus seem to become the most favoured catalysts used in today's CO_2 electrolysers, and the reason for this is not only their low raw material cost, but also that they can easily be applied in gas diffusion electrodes (GDEs).

The main advantage of using GDEs as cathodes for CO_2 electroreduction is that they circumvent the problem of limited solubility and slow transport in aqueous media, by allowing CO_2 to access the catalyst layer mostly in a gas phase.[13] In GDEs, the catalyst is supported by a gas diffusion layer (GDL) that is composed of a carbon fibrous layer (CFL) and a microporous layer (MPL), as shown in Fig. 1a. Besides enabling fast reactant delivery, the GDL also facilitates the release of gaseous reaction products, serves as a mechanical support and electrical contact for the catalyst, and plays important role in controlling the amount of electrolyte in the catalyst layer.[14]

In so-called zero-gap membrane-electrode assemblies (MEAs, see Fig. 1a for a model-scale version), the GDE is directly interfaced to an anion exchange membrane, the primary role of which is to control the amount of water (an important reactant of cathodic CO_2 reduction) reaching the catalyst layer, while anionic species (carbonate or hydroxide ions) can be transported away from it,[15] in the direction of the anode. The membrane should further assure that no volatile cathode-generated products can cross over to the anode, thereby reducing the efficiency of electrolysis.[16] When zero-gap MEA cathodes are employed in electrolyser set-ups similar to that shown in Fig. 1, current densities ranging a few hundred mA cm^{-2} can be achieved.[17]

Provided that at a given catalyst CO_2 reduction yields only gas-phase carbon-containing products, the configuration shown in Fig. 1 indeed provides an excellent platform for the performance and stability testing of catalyst materials. We have recently shown, for example, that when Ag nanocubes are used to catalyse CO_2 electroreduction (on Ag, the reaction almost exclusively yields CO), catalyst corrosion at stringent cathodic conditions occurs, and leads to truncated cube morphologies

and the appearance of smaller Ag NPs.[17] When using, on the other hand, Ag nanospheres protected by different ligands as a catalyst, degradation was shown to follow different pathways including corrosion, aggregation and even Ostwald ripening[18]— all depending on the chemical nature of the stabilizing ligand. In ref. 17 and 18 we have also found, however, that the degradation of Ag NPs, while it does occur at harshly cathodic operating conditions, is not in itself responsible for the observed, often severe, stability issues of the CO_2 electrolysis process performed in zero-gap MEA cathode configurations.

In zero-gap MEA cathode-based electrolysers, stability losses rather occur due to the flooding of the MPL during prolonged electrolyses. Flooding is the excess hydration of the GDE that can severely limit or even block the access of CO_2 to the catalyst layer, leading to the decrease of the observable faradaic efficiency (FE) of CO_2 reduction products and the appearance of parasitic hydrogen evolution.[14,19,20] The rapid flooding of GDEs, and the related stability issues are currently recognised as the biggest obstacle in front of the scale-up prospects[21] of CO_2 electroreduction. As a result, the focus of studies in the field of CO_2 electrolysis has recently shifted from the identification of new catalyst materials to other, more engineering-related tasks that include the optimisation of electrolyser geometries, the design of GDEs and membranes, and the fine-tuning of the applied process parameters.[2]

Amongst these tasks, the adaptation of design strategies that can help prevent, or at least slow down flooding-related stability losses are of prime importance. It was recently shown, for example, that the presence of sub-millimeter wide cracks in the MPL can effectively mitigate the flooding of GDEs during CO_2 electrolysis utilizing Ag nanowire catalysts.[20] Rapid flooding, in this case, was avoided by a pathway that the surface cracks of the MPL enabled for electrolyte perspiration[22,23] in addition to those provided by micropores.[20]

At this point it is important to emphasize the conceptual difference between electrolyte perspiration and flooding.

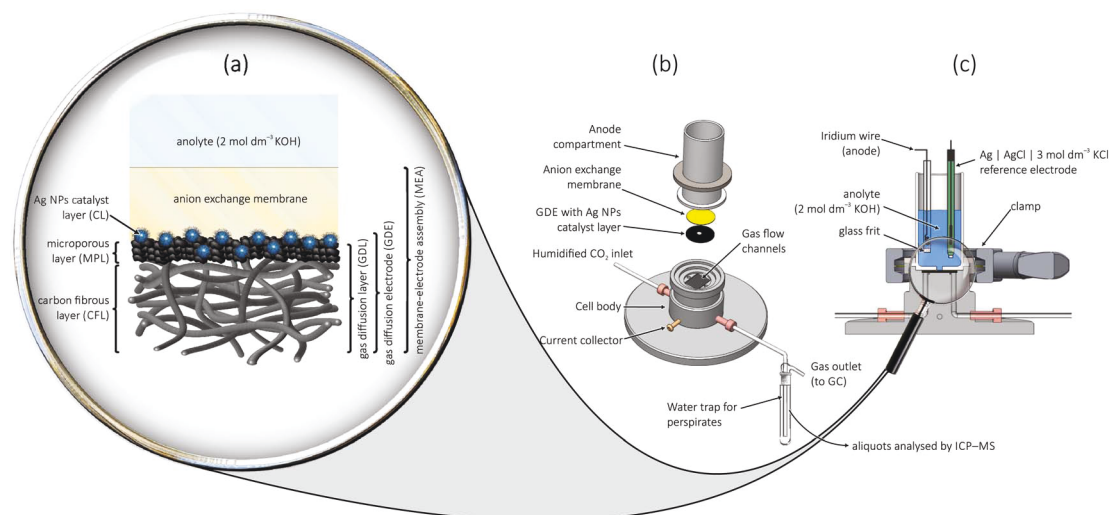**Fig. 1** A zero-gap membrane-electrode assembly (MEA) cathode employing a gas diffusion electrode, used in a flow-cell for the electrolysis of CO_2. Part (a) shows a close-up view of the MEA, parts (b) and (c) show the exploded and the cross-sectional view of the model-scale electrolyser.

5084 | *J. Mater. Chem. A*, 2023, **11**, 5083–5094

This journal is © The Royal Society of Chemistry 2023

Perspiration (a term we owe to Jeanty *et al.*[22]) refers to the crossover of electrolyte through the GDE structure, which ultimately results in the appearance of electrolyte droplets on the back side of the GDE, and even in the gas outflow of the cathode gas compartment. The somewhat interrelated effect of flooding occurs when the electrolyte that entered the GDE structure has no means to escape it, so it remains adhered to the MPL. This trapped electrolyte, due to its large KOH concentration, reacts with CO_2 and forms a large amount of carbonate (or bicarbonate) plaques that will limit and eventually block the access of CO_2 to the catalyst particles.

As was recently pointed out,[20,22,23] the flooding of the catalyst layer and the entrapment of electrolyte inside the GDE structure can be avoided by taking measures to uphold optimal perspiration rates, *e.g.*, by the selection of appropriate cathode-side CO_2 flow rates[22,23] or the application of GDLs with cracked surfaces.[20] Apart from optimizing the structure of MPLs or the operational parameters of electrolyses there is, however, more room for development, especially if we consider that essentially all parts of the MEA can influence flooding and perspiration phenomena. In this vein, the aim of the present paper will be to identify a critical point of zero-gap MEA cathode fabrication for CO_2 reduction: that is, the excess use of polymeric capping agents (CAs) in the catalyst ink formulations of Ag NP-based catalysts, and its flooding promoting—perspiration blocking— effect.

CAs are commonly used in the synthesis of metallic NPs to achieve uniform and stable size distribution of the particles. By adsorbing to the surface of the NPs, CAs prevent their aggregation either by providing sterical or electro-repulsive protection.[24] For the synthesis of Ag NPs, poly-(vinylpyrrolidone) (PVP) and branched polyethylenimine (BPEI) are very often used polymeric CAs that provide sterical protection to the NPs,[17,25–28] while on the other hand citrate ions are often used as a nonpolymeric (coulombic repulsion based) stabilizer.[29]

Practically regardless of the nature of the stabilizing CA, in aqueous Ag NP dispersions—either self-synthesised or purchased off-the-shelf—CAs are usually present at a rather high concentration, with not all of the ligand molecules adsorbed on the surfaces of NPs, but a majority of them being dissolved in the liquid phase.

In this study we show that the excess polymeric CA content, if not removed from the catalyst ink, blocks perspiration channels and acts as a promoter of flooding, thereby causing serious stability issues observed in zero-gap MEA cathode-based electrolysers used for CO_2 electroreduction.[30] In the paper we utilize a novel ICP-MS analysis-based approach to quantitatively monitor the amount of perspired electrolyte that exits the zero-gap MEA cathode and ends up in the water trap equipped to the gas outflow channel of the electrolyser (see Fig. 1b). We show a direct correlation between the breakdown of effective perspiration and the appearance of flooding in the MPL—the latter ultimately leading to a loss of electrolyser stability. We also present a simple ultracentrifugation technique, by which the polymeric CA content of formulated catalyst inks can be reduced, and we show that this strategy in itself helps to provide longer time stability to CO_2 electrolysers

operated at high current densities. In the paper we work with PVP- and BPEI-capped Ag NPs as representatives of polymeric CA-stabilised catalysts, and we also extend our tests to Ag NPs stabilised by citrate ligands (see Fig. 2 for the applied ligand structures). We come to the conclusion that the small, monomeric ligand (citrate) has less adverse effects on the electrolysis durability.

The use of the model scale electrolyser shown in Fig. 1 for the electrochemical stress-test of GDE cathodes in a zero-gap cathode MEA configuration is particularly advantageous, since due to its small effective cross-section (that limits the geometric surface area of the cathode to 0.0707 cm^2, see the Experimental section for details) the cell enables high current densities to be reached at the cost of relatively small applied currents (see Fig. S1 in ESI†). Furthermore, due to more pronounced edge effects introduced by the small cathode area,[31] cell failures already manifest during relatively short (few hours long) electrolyses, making our test system a promising tool for the accelerated durability testing[32] of CO_2-to-CO converting GDEs.

2 Experimental

Ag NP suspensions: CA removal

PVP-capped spherical Ag NP suspensions (of ~10 nm and ~100 nm diameter), BPEI-capped spherical Ag NP suspensions (of ~50 nm diameter) and citrate-capped Ag NP suspensions (also of ~50 nm diameter) were purchased from Nano-Composix (all water-based, with a concentration of 1 mg cm^{-3}). The suspensions were either used as-purchased for the preparation of catalyst inks, or—in order to remove at least some of their CA content—were made subject to centrifugation. In this latter case, the suspensions were first diluted 8-fold, and then centrifuged in an Optima XPN-80 Ultracentrifuge (Beckman Coulter) for 40 min at 35 000 rpm.
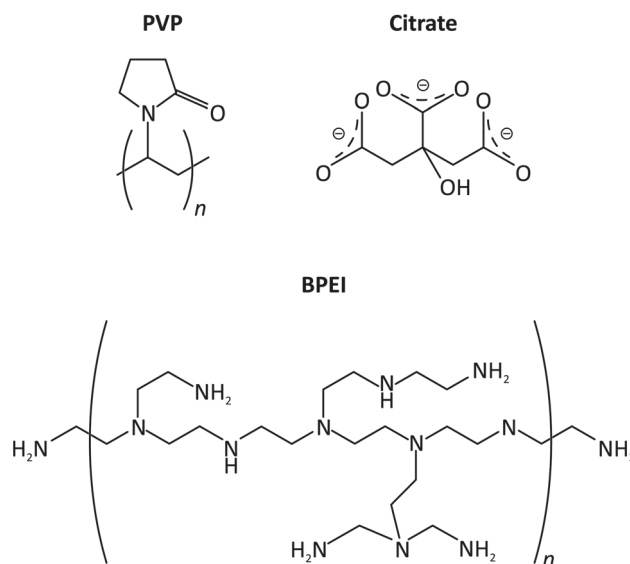

Fig. 2 The structure of CAs studied in this paper, used for the stabilisation of Ag NP suspensions.

This journal is © The Royal Society of Chemistry 2023

J. Mater. Chem. A, 2023, **11**, 5083–5094 | **5085**

(Suspensions with a nanoparticle diameter of ~10 nm were centrifuged for an additional 40 min at 50 000 rpm.) Following decantation of the supernatant, NPs in the pellet were re-dispersed in ultrapure water (Milli-Q by Merck Millipore, 18.2 MΩ cm specific resistance) to restore the original concentration of 1 mg cm^{-3}. The 8-fold dilution/centrifugation/re-dispersion steps were then repeated once for an as thorough as possible removal of the CA content (steps are illustrated by Fig. 3). To quantify the effectiveness of CA removal, total organic carbon content (TOC) and total nitrogen content (TNC) measurements were made for the supernatant of the first centrifugation step and for the finally obtained (for better comparability, 8-fold diluted) CA-deficient suspension (see Table 1 for results). For TOC and TNC determination, 0.1 cm^3 sample volumes were fed into a DIMATOC 2100 instrument (Dimatec Analysentechnik GmbH, Essen, Germany). The organic compounds were oxidized at 850 °C with Pt catalyst to CO_2 and NO, the amounts of which were quantified by a non-dispersive infrared gas sensor with a reflective diffuser and a chemiluminescence detector, respectively.

Catalyst ink preparation

Ag NP suspensions with 1 mg cm^{-3} Ag content (either as-purchased or centrifuged) were used for the catalyst ink preparation. A 1 cm^3 volume of the Ag NP suspension was mixed with 627 µl of isopropanol (VLSI Selectipur, BASF, Germany). A second suspension was then made by dispersing carbon black (Vulcan XC 72R, Cabot) in isopropanol in a 0.5 mg cm^{-3} concentration by 1 hour sonication. The Ag NP suspension and 353 µl of the carbon black suspension were then intermixed, 20 µl of Nafion solution (5% in a mixture of lower aliphatic alcohols and water, Sigma-Aldrich) was added, and the resulting ink was homogenised by 5 min sonication.

Table 1 Total organic carbon content (TOC) and total nitrogen content (TNC) determined in the Ag NP suspensions. Before: values measured in the supernatant of the first centrifugation step. After: values measured in the finally obtained 1 mg cm^{-3} suspension, following 8-fold dilution. *Cf.* to Fig. 3

Capping agent	Nominal size of Ag NPs	TOC/ppm		TNC/ppm	
		Before	After	Before	After
PVP	~10 nm	43.15	6.12	7.88	0.69
PVP	~100 nm	28.51	4.45	4.24	0.33
BPEI	~50 nm	7.53	3.81	3.09	—
Citrate	~50 nm	15.21	2.88	—	—

Preparation of the GDEs

75 µl of the prepared catalyst ink was drop-cast on the microporous surface of a circular Sigracet 36BB (FuelCellStore) GDL with 4 mm of diameter to form a GDE. Electrodes were dried at ambient conditions. Drop-casting 75 µl of the catalyst ink resulted in a nominal mass loading of ~300 µg cm^{-2} for silver. GDEs with lower loading were prepared by drop-casting proportionally less amount of the catalyst ink.

Assembly of the electrolyser

The electrolyser shown in Fig. 1 was used to carry out electrochemical CO_2 reduction. The bottom part of the electrolyser is made of stainless steel and is equipped with gas flow channels. The small circular GDEs containing the Ag NP catalyst were placed in a centrally located 4 mm diameter hole of a Freudenberg H23C8 (FuelCellStore) carbon paper with an external diameter of 2 cm, with the catalyst layer facing upwards and the bottom CFL facing the gas flow channels. The GDE was covered by a hydroxide-functionalised Sustainion anion exchange membrane (X3750 RT, Dioxide Materials, diameter of 2 cm) from above, before fixing the Teflon-made anode compartment on top. The anode compartment has a central orifice on its bottom, allowing access of the anolyte to the membrane. The orifice is of 3 mm diameter and it determines the geometric surface area (0.0707 cm^2) of the GDE. The anode compartment is filled with 10 cm^3 of 2 mol per dm^3 KOH solution (reagent grade, 90%, Sigma-Aldrich), and contains an Ag|AgCl|3 mol per dm^3 KCl reference electrode (double junction, Metrohm) and an Ir wire anode (99.9%, Goodfellow GmbH). The anode is placed inside a small chamber and is separated from the rest of the anolyte by glass frit, as shown in Fig. 1.

Electrochemical measurements and product analysis

All electrochemical measurements were carried out using an ECi-200 potentiostat (Nordic Electrochemistry) at constant current. The applied currents of −20, −10 and −5 mA correspond to geometric surface area normalised current densities of −283.0, −141.5 and −70.7 mA cm^{-2}. Cathode potentials reported in the paper are all referred to the applied Ag|AgCl|3 mol per dm^3 KCl reference electrode, and are corrected for IR drop (the cell resistance was followed by high frequency impedance measurements). On the Ag NP catalysts used in our studies, CO was the only detectable gaseous
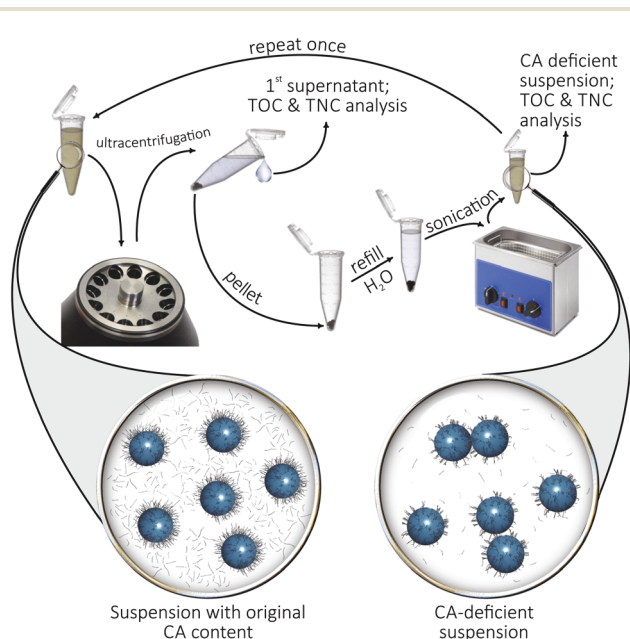

Fig. 3 Scheme of the ultracentrifugation-based method used for the removal of the excess CA content of Ag NP suspensions.

5086 | *J. Mater. Chem. A*, 2023, **11**, 5083–5094

This journal is © The Royal Society of Chemistry 2023

product of CO_2 reduction with H_2 formed as the product of parasitic hydrogen evolution. Gaseous reaction products were analysed by connecting the gas outlet of the electrolyser to a gas chromatograph (SRI Instruments Multigas Analyzer). The continuous flow of the carrier CO_2 gas through the electrolysis cell carried reaction products from the gas outlet of the electrolyser into the sampling loops of the gas chromatograph. The partial current I_i, corresponding to the formation of a gaseous product i, can be calculated[33] as

$$I_i = x_i n_i F v_m, \qquad (1)$$

where x_i denotes the mole fraction of the products, determined by GC using an independent calibration standard gas (Carbagas); n_i is the number of electrons involved in the reduction reaction to form a particular product ($n = 2$ for both CO and H_2 formation); $F = 96\,485.3$ C mol^{-1} is Faraday's constant; and v_m is the molar CO_2 gas flow rate measured by a universal flowmeter (7000 GC flowmeter, Ellutia) at the gas outlet of the electrolyser. The faradaic efficiency (FE) of a given reaction product was determined by dividing the respective partial current, calculated from eqn (1), by the total current. A thermal conductivity detector (TCD, for the detection of H_2) and a flame ionization detector (FID, for the detection of CO) were equipped to the gas chromatograph. In our experiments, the formed CO and H_2 amounts accounted for an about 90% FE. Following long time electrolyses, some amounts of formate ($HCOO^-$) were detected in the anolyte compartment, which could account for the less than 100% total FE, although an exact quantification of this product is not possible (due to the fact that formate is partially consumed by oxidation at the anode).

Scanning electron microscopy (SEM), energy-dispersive X-ray spectroscopy (EDX), and transmission electron microscopy (TEM)

A Zeiss Gemini 450 scanning electron microscope equipped with an InLens secondary electron detector and a back-scattering detector was used for the morphological analysis of GDEs, prior to and following electrolyses. An accelerating voltage of 5 kV and currents of 70 to 100 pA were applied at a working distance of 4.0 to 5.1 mm. The Smile View software was used to measure the size of particles. Particle size distribution histograms were created by determining the size of at least 500 individual particles based on micrographs taken from at least three randomly selected areas.[18] EDX spectra were acquired and elemental composition maps were composed by using the AZtec 5.0 software (Oxford Instruments). The applied acceleration voltage and current were 10 kV and 1 nA, respectively, and a working distance of 8.5 mm was set for all EDX measurements. For the transmission electron microscopy (TEM) imaging, an FEI Titan Themis instrument was used with an accelerating voltage of 300 kV.

Inductively coupled plasma mass spectrometry (ICP-MS)

ICP-MS (NExION 2000, PerkinElmer) was applied to determine the mass of potassium that perspired through the membrane

and the GDE, and exited the electrolyser through the gas outlet. A trap containing 15 cm^3 of ultrapure water was used to collect perspired potassium salts. Aliquots of the collected perspired material were diluted by an appropriate amount of 2% HNO_3 solution (BASF SE, Ludwigshafen, Germany) and the resulting solution samples were injected into the ICP-MS to obtain the content of potassium in perspiration.

Raw data, as well as unprocessed measurement files serving as a basis of this publication can be downloaded from Zenodo.[34]

3 Results and discussion

In this paper we use Ag NPs stabilised by different capping agents (PVP, BPEI and citrate, Fig. 2) for the creation of cathode GDEs that we integrate in the zero-gap MEA configuration (Fig. 1) to carry out durability tests at high current density. In order to study the effect of CAs exerted on the electrolysis stress-tests, in some cases we removed the majority of the CA content from the Ag NP suspensions before preparing the catalyst ink by using the ultracentrifugation-based method described in the Experimental section.

The possibility that (especially, polymeric) CAs can have an adverse effect on the stability of electrolyses first occurred to us when we used as-purchased, PVP-stabilised Ag NPs of ~10 nm nominal diameter in order to formulate catalyst inks with a carbon black support, and we attempted to define the optimal loading of the catalyst by one hour-long galvanostatic electrolyses.

These tests gave the rather counter-intuitive result (Fig. 4) that by increasing the nominal mass loading of Ag, the obtained GDEs became less stable, tending to lose their (initially high) CO production efficiency more quickly, and beginning to form H_2 after shorter and shorter times. Concomitantly with the loss of CO faradaic efficiency, the cathode potential also shifted to more negative values as instead of CO_2 reduction, hydrogen evolution became the dominant electrode reaction.

We found that the above equivocal result (higher loading—less stability) can be explained by another experiment, in which we reduced, by ultracentrifugation, the PVP content of the applied Ag NP dispersion before it was used for the preparation of the catalyst ink. By 2 times centrifugation, the majority of the PVP-content of the ~10 nm Ag NP suspension was removed (see Table 1 in the Experimental section for details), and this helped to maintain the stability of electrolysis even when the catalyst was applied at high loading. Indeed, comparing the plots of the bottom row of Fig. 4 immediately makes it apparent that it was the excess amount of PVP present in the catalyst ink—and not the increase of the silver loading in itself—that exerted a detrimental effect on the stability of electrolysis.

In order to unravel the exact reasons of this effect, we made two GDEs (one prepared from an Ag NP suspension of the original PVP content, other with less PVP) subject to further investigation.

The top-down SEM images (Fig. 5) obtained from the two catalyst layers (one prepared with the original, another with reduced PVP content) reveal only slight differences. Silver NPs well-dispersed in a matrix of carbon flakes over the MPL are well
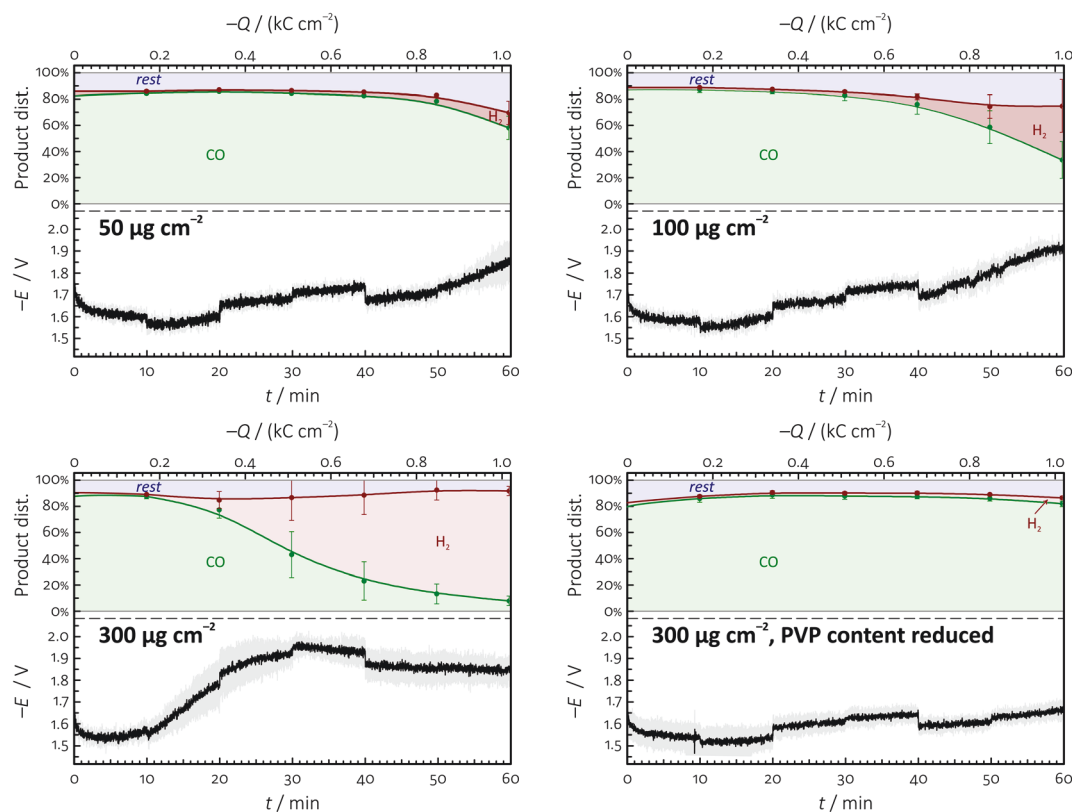
This journal is © The Royal Society of Chemistry 2023

J. Mater. Chem. A, 2023, **11**, 5083–5094 | **5087**

Fig. 4 Temporal variation of the product distribution of CO_2 reduction (top panels) and the measured cathode potential (bottom panels) during one hour long galvanostatic electrolyses (geometric surface area-normalised current density: -283 mA cm^{-2}) conducted on GDEs prepared with different Ag NP loadings shown in the figure. Error bars represent 95% confidence intervals. Nominal size of the Ag NPs used as catalyst: $\sim$10 nm. The area labelled "rest" in the product distribution plots can mostly be attributed to the production of small amounts of formate during electrolyses, see the Experimental section for details.

distinguishable in both cases. If the catalyst ink is prepared using the as-purchased NP suspension (nominal diameter: $\sim$10 nm) of high PVP content, the size distribution of the NPs is fairly symmetric and is centred at about 11.5 nm. If on the other hand the majority of the PVP content is removed by centrifugation, and the catalyst ink is prepared using a suspension gained by re-dispersing the particles in pure water, slight aggregation of the particles can be observed, resulting in a broadened and tailed size distribution histogram with a slightly increased maximum located at 16.2 nm. This indicates that removing the majority of PVP from the suspension of the Ag NPs results in a detectable but minor agglomeration of the particles on the GDE surface.

In order to determine to which extent the catalyst particles penetrate the microporous layer, we carried out cross-sectional SEM/EDX investigations, the results of which are shown in the bottom row of Fig. 5. EDX signals collected from different depth of the MPL all show strong peaks related to Ag, indicating that the NPs well penetrate the micropores of the MPL, practically regardless to whether they originate from as-purchased or centrifuged (PVP-deficient) suspensions.

Fig. 5 thus reveals no significant differences between GDEs prepared from Ag NP suspensions of the originally high PVP content and those prepared from PVP-deficient suspensions.

Yet, when the two GDEs are made subject to prolonged electrolysis lasting 2.5 hours, differences between their stability immediately become apparent, as shown in Fig. 6.

It is clearly visible in the product distribution plots of Fig. 6 that both normal and PVP-deficient GDEs exhibit a high ($>$90%) faradaic efficiency for CO production at the start of the electrolysis. However, in GDEs of high excess PVP content the initially high selectivity towards CO formation is quickly lost, and in less than 30 minutes the FE of CO formation drops down to below 50%. On the other hand, FE_{CO} values measured on PVP-deficient GDEs remain rather high, with significant decrease appearing only after 1 hour, and the efficiency dropping below 50% only after about 90 minutes of electrolysis. That the shortage of CO production is due to the appearance of hydrogen evolution is also indicated by the E vs. t plots of Fig. 6, showing cathode potentials shifting to more negative values concomitantly with the observed FE_{CO} loss.

That the observed stability losses—both on GDEs with originally high and of reduced PVP content—occur due to flooding can be demonstrated by the post-electrolysis top-down and cross-sectional SEM and EDX mapping of the GDEs. The SEM micrographs and K elemental maps shown in Fig. 6, recorded after 60 and 150 minutes of electrolyses, clearly indicate the presence of a significant amount of K$^+$ (in the form of K$_2$CO$_3$/

5088 | J. Mater. Chem. A, 2023, **11**, 5083–5094

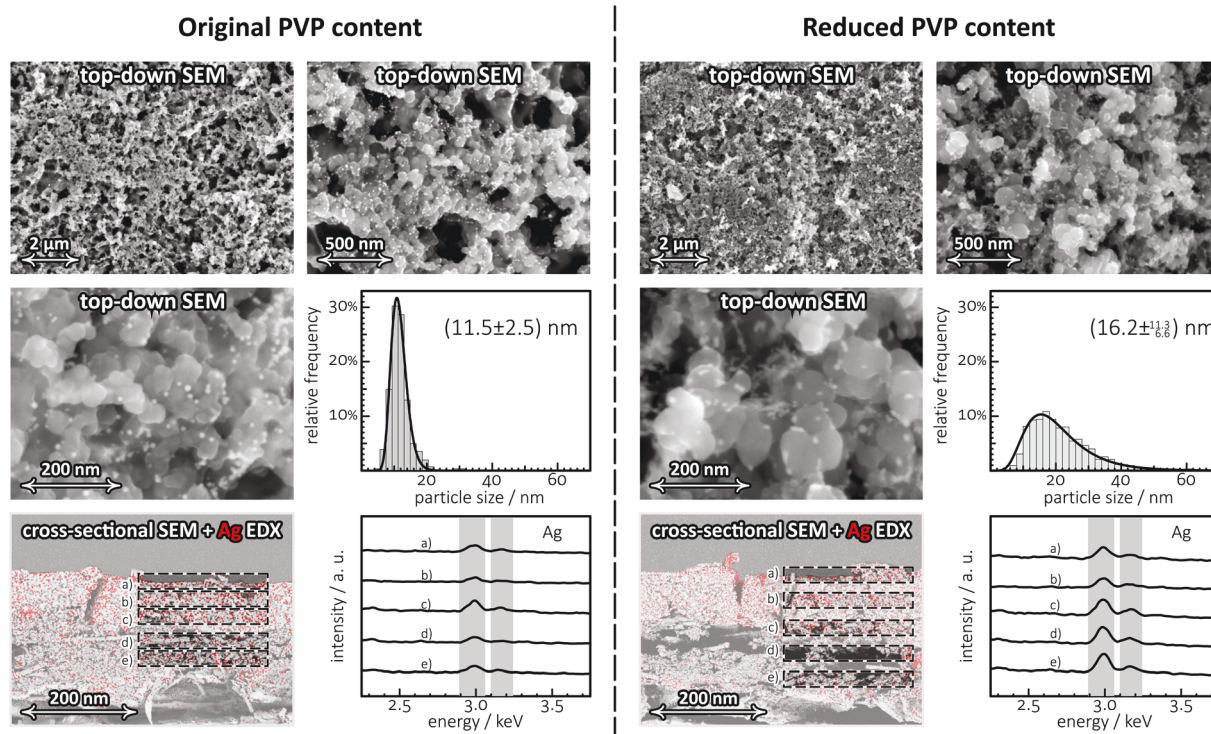This journal is © The Royal Society of Chemistry 2023

Fig. 5 Top-down SEM images of different magnification, showing catalyst layers containing the original (to the left) and reduced amount of PVP (to the right). Reducing, by ultracentrifugation, the amount of the stabilizing agent PVP leads to a broadening of the size distribution of the NPs as shown by the histograms. The cross-sectional view of the MPLs prove that the partial removal of the PVP content from the Ag NP suspensions exerts no considerable effect on the vertical distribution of the NPs. The EDX-based Ag elemental map (with red pixels corresponding to high Ag concentration) is superimposed on the cross-sectional SEM micrographs. EDX signals averaged over some selected areas, labelled from (a)–(e) clearly exhibit peaks assigned to Ag with no particular vertical intensity variation. Nominal size of the Ag NPs used as catalyst: ~10 nm, applied mass loading: 300 μg per cm^2 Ag. For more details on the structure of PVP-capped Ag NPs (TEM images), see Fig. S2 of the ESI.†

KHCO$_3$ precipitates) both on-top and inside the GDE structure. The appearance of K$^+$ in the cathode GDE serves as a direct proof of anolyte cross-over through the membrane, and as such, the formation pattern of K$^+$ precipitates inside the GDE acts as a tracer of electrolyte intrusion to the GDE.[19,20]

While the as-prepared GDEs are essentially potassium-free, the post-electrolysis determination of the K-content of GDEs by digestion in concentrated HNO$_3$ and follow-up ICP-MS measurements indicate that already at the first 60 minutes of electrolysis, K$^+$ ions accumulate within the GDE structure in an amount of approximately 4 mg cm^{-2}, normalised to the geometric surface area of the GDE (see Fig. 6 for exact values).

While the total amount of precipitated K$^+$ (determined by ICP-MS) seems not to vary much (at least, after 60 minutes) with the time of electrolysis, nor it seems to depend significantly on whether the original CA-content of the Ag NPs was reduced, a marked difference with regard to the spatial distribution of the precipitates can clearly be observed in Fig. 6, especially if we compare the top-down EDX elemental maps recorded on the two electrodes (PVP-deficient and original) after 60 min electrolysis.

These elemental maps show that for the GDE containing PVP in the original (high) concentration, precipitates first appear on top of flat parts of the catalyst layer, while in case of the GDE with reduced PVP content, precipitates tend to appear

preferentially inside the cracks of the MPL, leaving the catalyst layer—at least, for some time—mostly uncovered. (In a later stage, following 2.5 hours of electrolysis, precipitates already seem to cover the entire MPL.) This observation can be explained by assuming that the excess PVP content of the catalyst ink facilitates the flooding of the GDE, and leads to a blockage of CO$_2$ access to the catalyst NPs. On GDEs of a reduced PVP content, this effect occurs only in a later stage of electrolysis, with precipitates first appearing not on-top of the active catalyst layer but rather inside cracks of the MPL, also penetrating deeper parts of the GDE structure.

Note here that the cross-over of K$^+$ ions through the membrane is a naturally occurring (and in fact unavoidable) phenomenon, and does not (or should not) in itself lead to a blockage of the catalyst. *E.g.*, in case of the PVP-deficient catalyst, the electrolyte penetrating the GDE structure does not get trapped in the MPL but—through cracks and micropores—drains to deeper layers of the GDE and finally exits the cell in the form of small liquid drops through the gas flow channels of the cathode. This latter phenomenon was termed perspiration by Jeanty et al.,[22] and we quantitatively monitor it here for the first time, by applying a liquid trap to collect K$_2$CO$_3$/KHCO$_3$ perspirates at the gas out-flow of the electrolyser (see Fig. 1b).
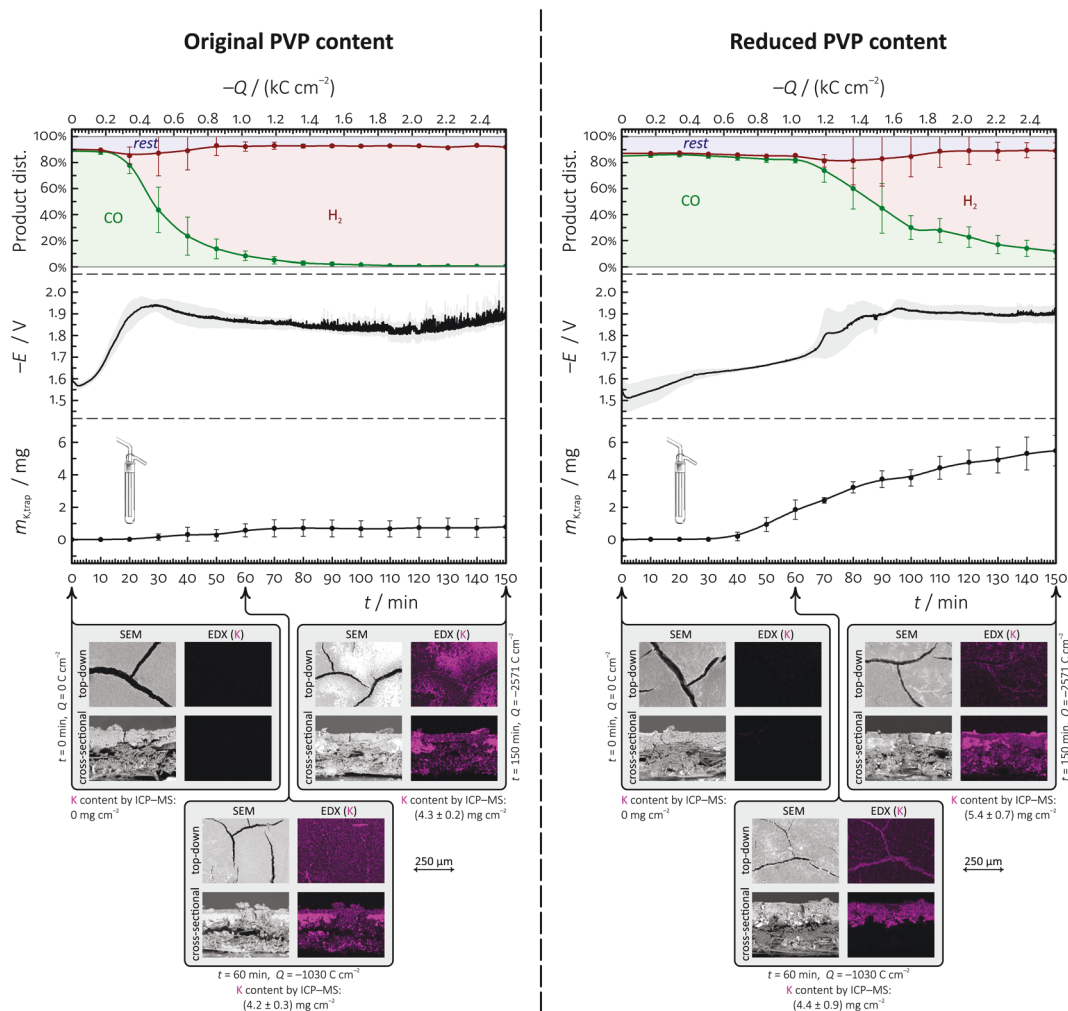
Fig. 6 Comparison of the results of electrolysis stress-tests on two different GDEs prepared with PVP-capped Ag NPs of 10 nm nominal diameter. The PVP content of the Ag NP suspensions was either unchanged (left side) or was reduced by ultracentrifugation (right side) during the course of catalyst ink preparation; in both cases, the catalyst was applied at a mass loading of 300 μg per cm^2 Ag. The plots show the variation of the product distribution of CO_2 reduction, the measured electrode potential E (referenced vs. an Ag|AgCl|3 mol per dm^3 KCl electrode), and the mass of K$^+$ ions collected in the liquid trap equipped to the gas outflow of the electrolyser, as a function of both time and passed charge, for galvanostatic electrolyses carried out at −283 mA cm^{-2}. Structural changes of the applied GDEs were monitored by recording top-down and cross-sectional SEM/EDX images of the GDEs obtained before, as well as 60 and 150 min after the electrolysis.

If we plot the amount of K$^+$ present in this outlet trap as a function of time (see the $m_{K,trap}$ vs. t plots of Fig. 6), we see that perspiration does occur (and the amount of K$^+$ in the trap constantly rises) up to the point at which the actual flooding of the catalyst layer takes place, the access of CO_2 to the catalyst layer becomes blocked, and the overall performance drops down.

Our results clearly indicate that the (at least partial) removal of PVP from the catalyst layer delays the flooding of the GDE and aids the electrolyte management of the cathode MEA by facilitating perspiration. The correlation of the $m_{K,trap}$ vs. t curves and the product distribution plots of Fig. 6 demonstrate that the faradaic efficiency of CO production can only be efficiently upheld until the electrolyte (and, with it, K$^+$) can effectively perspire through the system. The distribution of precipitates on-top and within the GDE structure, visualised by the EDX

maps of Fig. 6, point out that excess amounts of the capping agent PVP can easily clog the micropores of the GDL, and emphasize the role of the PVP content of Ag NP catalyst inks in creating erratic electrolysis performances.

From what was written above, the question immediately follows: is it only PVP, or other polymeric CAs as well, the presence of which in catalyst inks can have such detrimental effect on the operation of CO_2-to-CO electrolysing GDEs? While we cannot give a generally valid answer to this question, we did perform additional tests on BPEI-capped Ag NPs and, similarly to the case of PVP-stabilised ones, we found that the ultracentrifugation-based removal of the excess BPEI content of the Ag NP suspensions increases the durability of GDEs in the course of high current density electrolyses (Fig. 7).

By comparing Fig. 6 and 7 one can immediately see that BPEI, present in catalyst inks at high amount, decreases the FE

5090 | J. Mater. Chem. A, 2023, **11**, 5083–5094

This journal is © The Royal Society of Chemistry 2023

of CO formation already at the start of the electrolysis, which is in agreement with previous observations.[18] As the electrolysis proceeds, CO selectivity is dropping quickly and within 25 minutes H_2 already becomes the dominant product. As HER takes over the place of CO_2 reduction, massive precipitate formations can be observed, especially on-top of the catalyst layer, with precipitates showing typical burst patterns around the edges of cracks.

When the catalyst ink is prepared from BPEI-deficient (Table 1) suspensions (Fig. 7, to the right), the formation of the burst-like precipitate patterns can only be observed at later stages of the electrolysis. In this case the (also initially higher) FE of CO production breaks down to below 50% only after ~75 minutes of electrolysis. With a certain delay (that is due to the time needed for the formed precipitates to get transported out of the

electrolyser) the measured $m_{K,trap}$ vs. t curves of Fig. 7 show the same tendency: following the drop-down of FE_{CO} the amount of K^+ in the down-flow trap will also grow less rapidly. This points to that the cell seems to remain active for CO_2 reduction as long as the pores of the MPL remain unclogged.

From Fig. 6 and 7 it is obvious that removing some of the (originally high) polymeric CA content of Ag NP suspensions before turning these into catalyst inks does seem to be an advisable strategy, as this will increase the durability of the prepared GDEs. We note here, however, that the effect seems observable only in the case when polymeric CAs are used for the Ag NP preparation. The operation of GDEs prepared from Ag NPs stabilised by (monomeric) citrate ligands, for example, seems less to depend on whether the citrate content of the NP suspension was reduced or not (Table 1). As shown in Fig. 8,

Fig. 7 Comparison of the results of electrolysis stress-tests on two different GDEs prepared with BPEI-capped Ag NPs of 50 nm nominal diameter. The BPEI content of the Ag NP suspensions was either unchanged (left side) or was reduced by ultracentrifugation (right side) during the course of catalyst ink preparation; in both cases, the catalyst was applied at a mass loading of 300 μg per cm^2 Ag. The plots show the variation of the product distribution of CO_2 reduction, the measured electrode potential E (referenced vs. an Ag|AgCl|3 mol per dm^3 KCl electrode), and the mass of K^+ ions collected in the liquid trap equipped to the gas outflow of the electrolyser, as a function of both time and passed charge, for galvanostatic electrolyses carried out at −283 mA cm^{-2}. Structural changes of the applied GDEs were monitored by recording top-down and cross-sectional SEM/EDX images of the GDEs obtained before, as well as 60 and 150 min after the electrolysis. For more details on the structure of BPEI-capped Ag NPs (TEM images), see Fig. S3 of the ESI.†

citrate removal seems to exert no considerable effect either on the measurable product distribution, electrode potential and trapped K^+ plots, or on the formed precipitate patterns.

In order to further demonstrate, for the case of polymeric CA-stabilised Ag NPs, the detrimental effect of the excess CA content of catalyst inks on the stability of CO_2 electrolysers, we also created GDEs using PVP-capped Ag NPs of ~100 nm (as opposed to the previously used ~10 nm) diameter. The suspensions of larger size Ag NPs inherently contains less PVP,[28] although the PVP content could again be further reduced by ultracentrifugation (see Table 1). When used for the fabrication of GDEs, the 100 nm diameter NPs seemed to penetrate the MPL lot less efficiently than the ~10 nm particles did, and remained more concentrated in the catalyst layer on-top of the MPL, with some NPs penetrating through cracks of the MPL into the CFL, as shown by the cross-sectional EDX maps of Fig. S4 of the ESI.†

Decreasing the amount of PVP in the catalyst ink helped, also in case of the ~100 nm diameter PVP-capped Ag NPs to increase the stability time of electrolysis (see Fig. S5 of the ESI†), proving that the durability impairments reported in this paper are indeed caused by the excess amounts of polymeric CAs clogging the pores (perspiration pathways) of the MPL (scheme shown in Fig. 9) and are not due to particle size effects.

The importance of maintaining the ability of GDEs to uphold effective perspiration pathways is further emphasized by the results of sessile water drop contact angle measurements made on the as-prepared GDEs, shown in Fig. 10. These measurements all show that the ultracentrifugation-based partial removal of the excess amount of capping agents from the NP suspensions in the course of catalyst ink preparation does increase, however only a bit, the hydrophobicity of the catalyst layer. This increase of hydrophobicity can, however, not explain
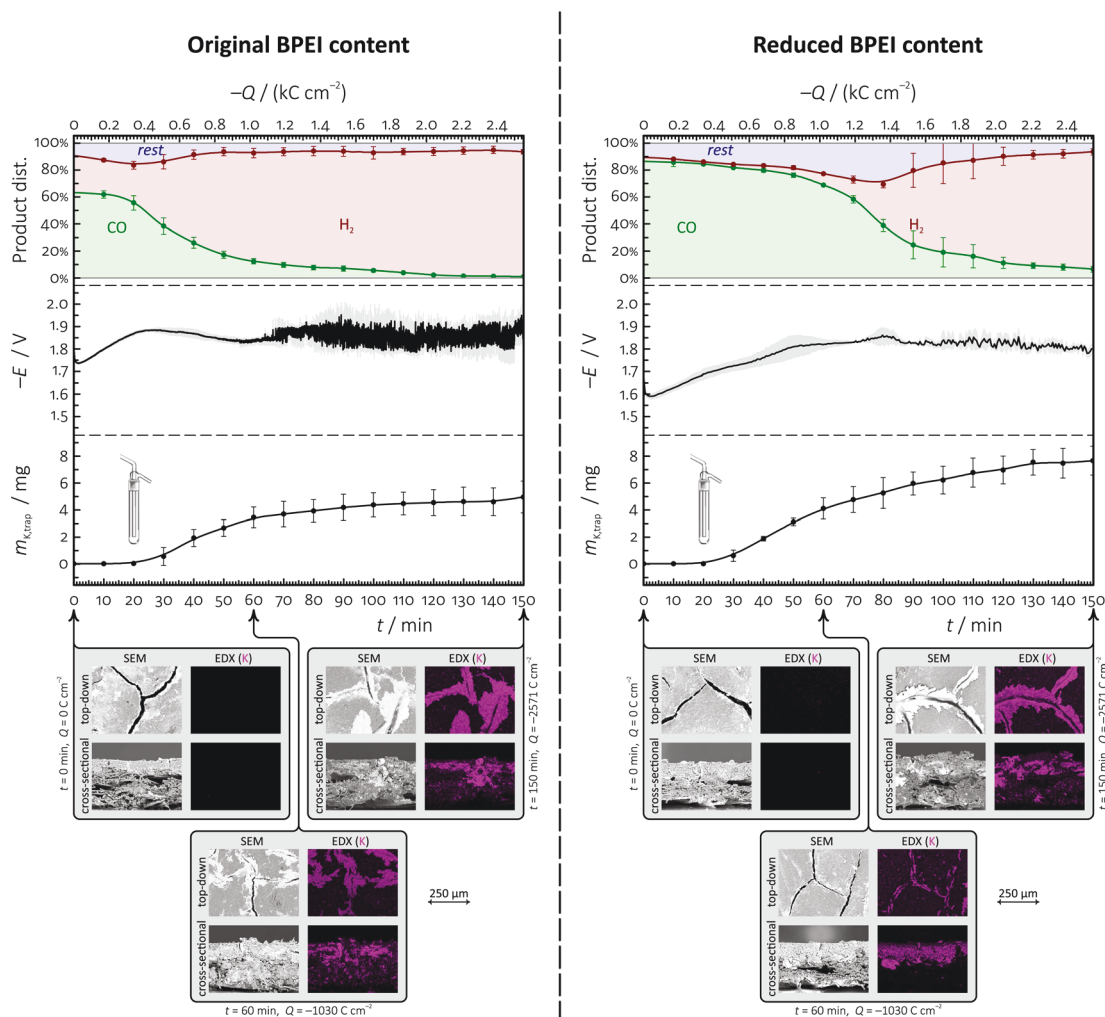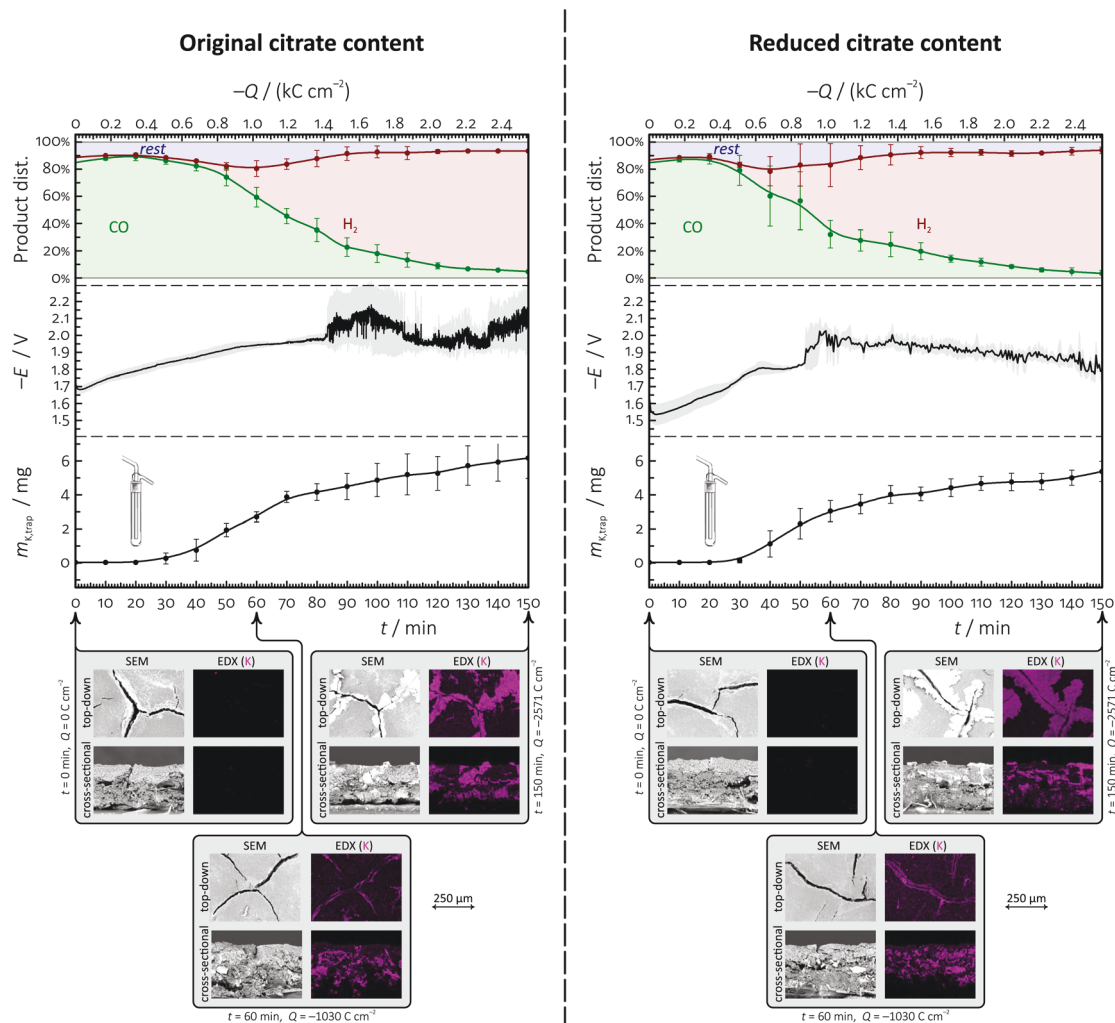

Fig. 8 Comparison of the results of electrolysis stress-tests on two different GDEs prepared with citrate-capped Ag NPs of 50 nm nominal diameter. The citrate content of the Ag NP suspensions was either unchanged (left side) or was reduced by ultracentrifugation (right side) during the course of catalyst ink preparation; in both cases, the catalyst was applied at a mass loading of 300 μg per cm^2 Ag. The plots show the variation of the product distribution of CO_2 reduction, the measured electrode potential E (referenced vs. an Ag|AgCl|3 mol per dm^3 KCl electrode), and the mass of K^+ ions collected in the liquid trap equipped to the gas outflow of the electrolyser, as a function of both time and passed charge, for galvanostatic electrolyses carried out at -283 mA cm^{-2}. Structural changes of the applied GDEs were monitored by recording top-down and cross-sectional SEM/EDX images of the GDEs obtained before, as well as 60 and 150 min after the electrolysis.

5092 | J. Mater. Chem. A, 2023, **11**, 5083–5094

This journal is © The Royal Society of Chemistry 2023

Fig. 9 Schematic illustration of the clogging effect of polymeric CAs, disallowing effective perspiration through the micropores of GDEs. (Figure not to scale, micropores are depicted magnified for better visibility.)

Fig. 10 Contact angles (of sessile water drops) measured on different GDEs (as-prepared, prior to electrolyses) used in this study.

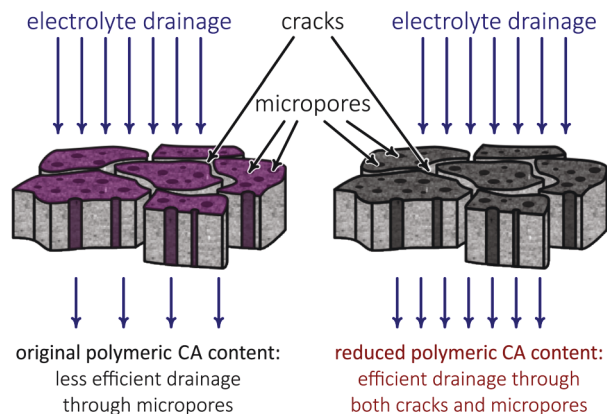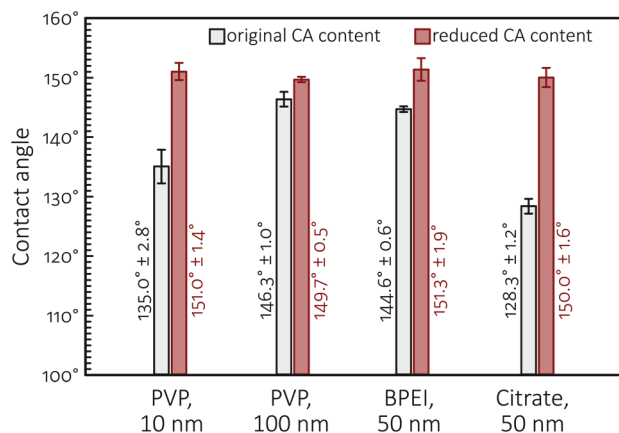the durability improvements caused by the removal of polymeric capping agents from the catalyst ink, pointing to that—in contrast to prevailing views[5,35,36]—the perspiration properties of GDEs are probably even more important than their non-wettability in efficient, long time CO_2 electrolysis.

4 Conclusion

Zero-gap MEA cathodes employing catalysts distributed over the surface of a gas diffusion layer allow CO_2 reduction to be carried out at extreme high rate and good selectivity. E.g., by using Ag NPs with well-chosen structure and size distribution, current densities in the range of few hundreds of mA cm^{-2} and an almost 100% faradaic efficiency of CO production can be achieved. This efficiency increase comes, however, at the cost of severe stability issues that are mostly all related to the flooding of the GDE by the employed electrolyte. Flooding is currently recognised as the biggest obstacle in front of the scale-up prospects of CO_2 electroreduction, thus the identification and possible elimination of phenomena that can lead to flooding in

CO_2 electrolysers is a primary goal of today's electrocatalysis studies.

In the above vein, we identified in this paper one important contributor to flooding; that is, the excessive presence of polymeric capping agents in the catalyst layer of gas diffusion electrodes. CAs have an important role in stabilising Ag NPs in suspension, however when these suspensions are turned into catalyst inks and deposited on the surface of a gas diffusion layer, polymeric CAs can clog the perspiration channels of the MPL and can thus act as an initiator to flooding. The detrimental effect of polymeric CAs (PVP and BPEI were studied in this paper) present in catalyst inks can in fact be so strong that it overshadows other tendencies. E.g., it was shown in the paper that by increasing the mass loading of PVP-capped Ag NP catalysts, a counter-intuitive stability loss can often be observed. This stability loss, as we showed, is however not a result of the increased loading in itself, but of the increase of the PVP concentration in the catalyst layer.

In the paper we used a combination of electrochemical performance tests, during which we monitored the faradaic efficiency of CO production, the cathode potential, and also, using a novel ICP-MS detection-based approach, the outflow of electrolyte perspirates. We combined these measurements with ex situ SEM and EDX-based investigations of the GDEs, carried out at various stages of the electrolysis. Our investigations proved that the presence of excess amount of polymeric capping agents (PVP and BPEI) in the catalyst ink can cause a rapid flooding of the GDE cathode and can thus exert disastrous effects on the stability of zero-gap MEA cathode-based electrolysers. No such effects were observed when a monomeric CA (citrate) was used as a stabilizing ligand of Ag NPs. In order to attenuate the concentration of polymeric capping agents in the used catalyst inks, an ultracentrifugation-based method has been described in the paper, the application of which in the catalyst ink formulation immediately resulted in an improved electrolyser stability.

Author contributions

Huifang Hu: investigation, experiments, data curation, writing – first draft. Ying Kong and Menglong Liu: investigation, experiments. Viliam Kolivoška, Alexander V. Rudnev and Yuhui Hou: conceptualization, methodology. Rolf Erni: TEM measurements. Soma Vesztergom: conceptualization, methodology, visualization, data analysis, writing, funding acquisition. Peter Broekmann: conceptualization, methodology, writing – review & editing, supervision, funding acquisition.

Conflicts of interest

There are no conflicts to declare.

Acknowledgements

This journal is © The Royal Society of Chemistry 2023

J. Mater. Chem. A, 2023, **11**, 5083–5094 | **5093**

Notes and references

1 D. R. Feldman, W. D. Collins, P. J. Gero, M. S. Torn, E. J. Mlawer and T. R. Shippert, *Nature*, 2015, **519**, 339–343.

2 A. Gawel, T. Jaster, D. Siegmund, J. Holzmann, H. Lohmann, E. Klemm and U.-P. Apfel, *iScience*, 2022, **25**, 104011.

3 J.-B. Vennekoetter, R. Sengpiel and M. Wessling, *Chem. Eng. J.*, 2019, **364**, 89–101.

4 C. M. Gabardo, A. Seifitokaldani, J. P. Edwards, C.-T. Dinh, T. Burdyny, M. G. Kibria, C. P. O'Brien, E. H. Sargent and D. Sinton, *Energy Environ. Sci.*, 2018, **11**, 2531–2539.

5 U. O. Nwabara, A. D. Hernandez, D. A. Henckel, X. Chen, E. R. Cofell, M. P. de Heer, S. Verma, A. A. Gewirth and P. J. A. Kenis, *ACS Appl. Energy Mater.*, 2021, **4**, 5175–5186.

6 J. Li, S. U. Abbas, H. Wang, Z. Zhang and W. Hu, *Nano-Micro Lett.*, 2021, **13**, 216.

7 H.-R. M. Jhong, S. Ma and P. J. A. Kenis, *Curr. Opin. Chem. Eng.*, 2013, **2**, 191–199.

8 F. Yu, P. Wei, Y. Yang, Y. Chen, L. Guo and Z. Peng, *Nano Mater. Sci.*, 2019, **1**, 60–69.

9 D. Sun, X. Xu, Y. Qin, S. P. Jiang and Z. Shao, *ChemSusChem*, 2019, **13**, 39–58.

10 D. Xue, H. Xia, W. Yan, J. Zhang and S. Mu, *Nano-Micro Lett.*, 2020, **13**, 5.

11 J. Y. Choi, W. Choi, J. W. Park, C. K. Lim and H. Song, *Chem.–Asian J.*, 2019, **15**, 253–265.

12 Y. Pei, H. Zhong and F. Jin, *Energy Sci. Eng.*, 2021, **9**, 1012–1032.

13 D. M. Weekes, D. A. Salvatore, A. Reyes, A. Huang and C. P. Berlinguette, *Acc. Chem. Res.*, 2018, **51**, 910–918.

14 N. T. Nesbitt, T. Burdyny, H. Simonson, D. Salvatore, D. Bohra, R. Kas and W. A. Smith, *ACS Catal.*, 2020, **10**, 14093–14106.

15 A. Marcos-Madrazo, C. Casado-Coterillo, J. Iniesta and A. Irabien, *Membranes*, 2022, **12**, 783.

16 G. Díaz-Sainz, M. Alvarez-Guerra, J. Solla-Gullón, L. García-Cruz, V. Montiel and A. Irabien, *J. CO2 Util.*, 2019, **34**, 12–19.

17 M. de J. Gálvez-Vázquez, P. Moreno-García, H. Xu, Y. Hou, H. Hu, I. Z. Montiel, A. V. Rudnev, S. Alinejad, V. Grozovski, B. J. Wiley, M. Arenz and P. Broekmann, *ACS Catal.*, 2020, **10**, 13096–13108.

18 M. Liu, Y. Kong, H. Hu, N. Kovács, C. Sun, I. Z. Montiel, M. de J. G. Vázquez, Y. Hou, M. Mirolo, I. Martens, J. Drnec, S. Vesztergom and P. Broekmann, *J. Catal.*, 2021, **404**, 371–382.

19 Y. Kong, H. Hu, M. Liu, Y. Hou, V. Kolivoška, S. Vesztergom and P. Broekmann, *J. Catal.*, 2022, **408**, 1–8.

20 Y. Kong, M. Liu, H. Hu, Y. Hou, S. Vesztergom, M. de J. G. Vázquez, I. Z. Montiel, V. Kolivoška and P. Broekmann, *Small Methods*, 2022, **6**, 2200369.

21 K. Yang, R. Kas, W. A. Smith and T. Burdyny, *ACS Energy Lett.*, 2020, **6**, 33–40.

22 P. Jeanty, C. Scherer, E. Magori, K. Wiesner-Fleischer, O. Hinrichsen and M. Fleischer, *J. CO2 Util.*, 2018, **24**, 454–462.

23 B. De Mot, J. Hereijgers, M. Duarte and T. Breugelmans, *Chem. Eng. J.*, 2019, **378**, 122224.

24 C. V. Restrepo and C. C. Villa, *Environ. Nanotechnol., Monit. Manage.*, 2021, **15**, 100428.

25 S. H. Im, Y. T. Lee, B. Wiley and Y. Xia, *Angew. Chem.*, 2005, **117**, 2192–2195.

26 J. Zhang, Q. Wang, X. Zhang, J. Wang, M. Guo, B. J. Wiley, C. Li and C. Hu, *Inorg. Chem. Front.*, 2016, **3**, 547–555.

27 M. de J. Gálvez-Vázquez, S. Alinejad, H. Hu, Y. Hou, P. Moreno-García, A. Zana, G. K. H. Wiberg, P. Broekmann and M. Arenz, *Chimia*, 2019, **73**, 922.

28 K. M. Koczkur, S. Mourdikoudis, L. Polavarapu and S. E. Skrabalak, *Dalton Trans.*, 2015, **44**, 17883–17905.

29 Q. Zhang, N. Li, J. Goebl, Z. Lu and Y. Yin, *J. Am. Chem. Soc.*, 2011, **133**, 18931–18939.

30 S. Alinejad, J. Quinson, G. K. H. Wiberg, N. Schlegel, D. Zhang, Y. Li, S. Reichenberger, S. Barcikowski and M. Arenz, *ChemElectroChem*, 2022, **9**, e20220034.

31 K. Ehelebe, D. Seeberger, M. T. Y. Paul, S. Thiele, K. J. J. Mayrhofer and S. Cherevko, *J. Electrochem. Soc.*, 2019, **166**, F1259–F1268.

32 U. O. Nwabara, M. P. de Heer, E. R. Cofell, S. Verma, E. Negro and P. J. A. Kenis, *J. Mater. Chem. A*, 2020, **8**, 22557–22571.

33 A. V. Rudnev, *Encyclopedia of Interfacial Chemistry*, Elsevier, Amsterdam, 2018, pp. 321–325.

34 H. Hu, Y. Kong, M. Liu, V. Kolivoška, A. V. Rudnev, Y. Hou, R. Erni, S. Vesztergom and P. Broekmann, Raw data for the article "Effective perspiration is essential to uphold the stability of zero-gap MEA-based cathodes used in CO$_2$ electrolysers, *Zenodo*, 2022, **https://doi.org/10.5281/zenodo.7002917**.

35 M. Li, M. N. Idros, Y. Wu, T. Burdyny, S. Garg, X. S. Zhao, G. Wang and T. E. Rufford, *J. Mater. Chem. A*, 2021, **9**, 19369–19409.

36 M. E. Leonard, M. J. Orella, N. Aiello, Y. Román-Leshkov, A. Forner-Cuenca and F. R. Brushett, *J. Electrochem. Soc.*, 2020, **167**, 124521.

5094 | *J. Mater. Chem. A*, 2023, **11**, 5083–5094

This journal is © The Royal Society of Chemistry 2023

5.4 Testing a silver nanowire catalyst for the selective CO$_2$ reduction in a gas diffusion electrode half-cell setup enabling high mass transport conditions

Authors: María de Jesús Gálvez-Vázquez, Shima Alinejad, **Huifang Hu**, Yuhui Hou, Pavel Moreno-García, Alessandro Zana, Gustav K. H. Wiberg, Peter Broekmann*, and Matthias Arenz*

Highlights: The CO$_2$RR on the Ag NW catalyst has been tested in a gas-fed zero-gap electrolyzer as well as a traditional H-type cell. The partial current densities of CO are limited below 20 mA/cm^2 in the H-type cell whereas it reaches over 100 mA/cm^2 in the gas-fed zero-gap electrolyzer that overcomes the CO$_2$ transport limitation. The results demonstrate that the development of flow cell is critical for electrochemical CO$_2$RR.

Contributions: I synthesized all the Ag NW catalysts and prepared the catalyst inks. Moreover, I was involved in the manuscript writing process.

Testing a Silver Nanowire Catalyst for the Selective CO$_2$ Reduction in a Gas Diffusion Electrode Half-cell Setup Enabling High Mass Transport Conditions

María de Jesús Gálvez-Vázquez[a§], Shima Alinejad[a§], Huifang Hu[a§], Yuhui Hou[a], Pavel Moreno-García[a], Alessandro Zana[a], Gustav K. H. Wiberg[b], Peter Broekmann*[a], and Matthias Arenz*[a]

Abstract: In this work, we discuss the application of a gas diffusion electrode (GDE) setup for benchmarking electrocatalysts for the reductive conversion of CO$_2$ (CO$_2$RR: CO$_2$ reduction reaction). Applying a silver nanowire (Ag-NW) based catalyst, it is demonstrated that in the GDE setup conditions can be reached, which are relevant for the industrial conversion of CO$_2$ to CO. This reaction is part of the so-called 'Rheticus' process that uses the CO for the subsequent production of butanol and hexanol based on a fermentation approach. In contrast to conventional half-cell measurements using a liquid electrolyte, in the GDE setup CO$_2$RR current densities comparable to technical cells (>100 mA cm^{-2}) are reached without suffering from mass transport limitations of the CO$_2$ reactant gas. The results are of particular importance for designing CO$_2$RR catalysts exhibiting high faradaic efficiencies towards CO at technological reaction rates.

Keywords: CO$_2$ reduction · Gas diffusion electrode · Silver nanowire catalyst

María de Jesús Gálvez-Vázquez studied chemistry and received her MSc Specialization in Materials Science at the Benemérita Universidad Autónoma de Puebla (Mexico). In 2017 she started her PhD project in the group of Prof. Peter Broekmann at the University of Bern (Switzerland). Her main focus is the study of different catalyst materials applied to the electrochemical reduction of carbon dioxide under controlled mass transport conditions.

Shima Alinejad obtained her MSc in materials engineering from the University of Tehran (Iran). In 2018, she joined NanoElectroCatalysis group of Matthias Arenz at the University of Bern (Switzerland) as a researcher assistant, and in 2019 she started her PhD in the same group. Her PhD project focuses on developing new measuring platform for the electrocatalysts.
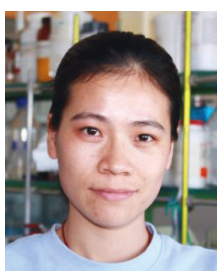
Huifang Hu obtained her MSc in Materials Science and Engineering from Fuzhou University (China). After a short experience in technical college, she joined the Interfacial Electrochemistry Group of Prof. Peter Broekmann as a PhD student in 2019. Her PhD project focuses on the electrochemical conversion of CO$_2$ into value-added products.

Dr. Yuhui Hou received her PhD degree in physical chemistry from Xiamen University, China in 2015. Before joining Prof. Peter Broekmann's group at University of Bern, Switzerland, she worked as a postdoctoral fellow in Hokkaido University in Japan, where she mainly focused on methane conversion. Her current research interest is to develop electrocatalysts *via* colloidal synthesis approach for electrochemical CO$_2$ reduction. She is also interested in investigation of material degradation under electrochemical CO$_2$ reduction conditions by identical-location electronic microscopy.

Dr. Pavel Moreno-García carried out his PhD degree in science of chemistry and molecular science at the University of Bern under the supervision of Prof. Thomas Wandlowski from 2009 to 2013. During this period, his work was devoted to the study of electronic transport characteristics through nano objects at electrified solid-liquid interfaces by *in situ* STM techniques. In 2013 he joined the group of Prof. Peter Broekmann where he has been involved in electrocatalytic topics related to the direct electrochemical conversion of carbon dioxide into more valuable products and instrumental development and studies using laser ablation/ionization mass spectrometry.

Dr. Alessandro Zana has worked in the group of Professor Arenz, first at the University of Copenhagen (2011–2016) then at the University of Bern, after receiving his PhD. He is currently working in the field of electrochemistry/electrocatalysis, interfaces and collective properties of nanoparticles. He is interested in studying electronic properties of nano systems and developing new solutions for renewable energy sources.

Dr. Gustav K. H. Wiberg received his PhD in electrochemistry from the Technical University of Munich, Germany (2010) and an MSc in engineering physics from Chalmers University of Technology, Sweden (2006). He has worked as a post-doctoral fellow at Argonne National Laboratory (ANL), USA (2010–2013), at the University of Copenhagen, Denmark (2013–2014), and at the University of Bern, Switzerland (2016). Currently, he is a lecturer of chemistry and physics at Harold Washington College – one of the City Colleges of Chicago, USA (2017–present). His current research focuses on electrocatalysis for energy conversion, as well as instrumentation and experimentation method development.

Prof. Peter Broekmann obtained his MSc in chemistry (1998) and a PhD (2000) from the University of Bonn. After a post-doctoral stay in 2001 at the University of Twente, he became project leader at the Institute of Physical Chemistry in Bonn. Since 2008 Prof. Broekmann holds a lecturer position for electrochemistry at the University of Bern (Switzerland). His research focuses on metal deposition processes for semiconductor and electrocatalysis applications.

Prof. Matthias Arenz studied physics with chemistry minor in Bonn (Germany) and received his diploma (Physical Chemistry) in 1999 and in 2002 his PhD on model electrodes for electrocatalysis with Prof. K. Wandelt. Already during his PhD studies he spent seven months in the group of Dr. P. N. Ross and Dr. N. M. Markovic at the Lawrence Berkeley National Laboratory

(USA) and returned to the group in 2002 with a Feodor Lynen Fellowship (A.v. Humboldt Foundation) for two years of post-doctoral work. Back in Germany, in 2004, he joined the group of Prof. U. Heiz in Ulm and Munich, before establishing in Munich (2006) an independent Emmy Noether Group of the German Science Foundation (DFG). In 2010 he became tenured Associate Professor at the University of Copenhagen (Denmark) and in 2016 Full Professor at the University of Bern (Switzerland). His group focusses on electrocatalytic reactions related to energy conversion and storage.

1. Introduction

The mitigation of the increase of the greenhouse gas CO_2 in our atmosphere is one of the major societal challenges we are currently facing. The large-scale conversion of CO_2 captured from the atmosphere, into high-value products is considered a technologically feasible approach to address this goal. If combined with renewables (hydro, wind, and solar) that provide 'clean' electric power, the electrochemical CO_2 reduction (CO_2RR: CO_2 reduction reaction) is particularly interesting and significant R&D efforts are addressed to develop selective electrocatalysts.[1] A prime example of such a CO_2RR process is the so-called 'Rheticus' process which combines an electrochemical conversion of CO_2 into CO, an essential reactant for the subsequent production of butanol and hexanol based on a fermentation approach.[2] Thus the CO_2RR might become not only sustainable but also economically feasible.

In the search for cheap, abundant and selective electrocatalysts for the CO_2RR many academic studies apply so-called H-type electrochemical cells with liquid electrolyte. The cells are designed as electrochemical half-cells containing the working electrode (WE) and the reference electrode (RE) in one compartment, and the counter electrode (CE) in another one. These two compartments are separated by a membrane to avoid product crossover,[3] (Fig. 1). The reactant (CO_2 gas) is physically dissolved into the liquid electrolyte where it reaches the active catalyst *via* convection and diffusion. The advantage of such a setup is its straightforward use in screening different electrode materials under defined conditions. However, the product formation can easily be affected by mass transport limitations due to the low gas solubility in the electrolyte, which is limited to about 35 mM, as well as relative slow gas diffusion in liquids. Therefore, in liquid electrolytes the limited availability of CO_2 reactant influences the overall reaction rate as well as the product selectivity. While the CO_2 concentration at the catalyst surface is limited, water, (or protons depending on the electrolyte pH) the reactant to form H_2 gas, is readily available. As a consequence, in more applied studies often electrochemical reactors with a two (or three) electrode setup are used.[4] Such setups are technologically relevant as they allow realistic reaction rates. However, the different factors that determine such rates are often complex and

Fig. 1. Schematic drawings of a) typical measurement configuration using an H-type cell in a three-electrode configuration; the CO_2 reactant is dissolved in the liquid electrolyte b) measurement configuration using the GDE setup; the CO_2 reactant is led to the catalyst layer through the GDL and does not need to pass through liquid electrolyte; at the same time a three-electrode configuration is maintained.
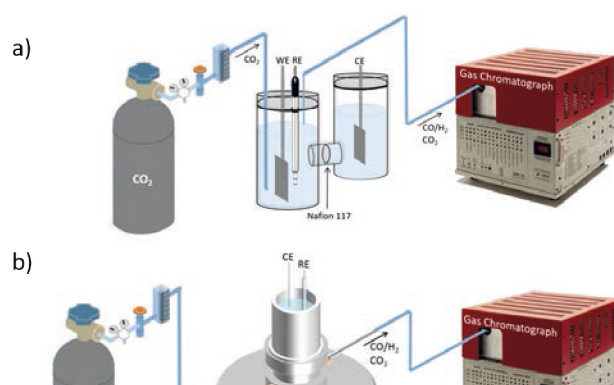
difficult to distinguish. Furthermore, cathode (CO₂RR) and anode processes (oxygen evolution reaction; OER) might influence each other and often no information of the individual electrode potentials is obtained.[5]

In the present work, we demonstrate an 'intermediate' setup that bridges measurements in H-type cells and electrochemical reactors, *i.e.* a gas diffusion electrode (GDE) setup with a three-electrode configuration. The GDE setup has originally been developed to benchmark oxygen reduction reaction (ORR) electrocatalysts under realistic mass transport conditions.[6] Similar to a real fuel cell, in the GDE setup the gaseous reactant is guided to the catalyst layer through a gas diffusion layer (GDL) avoiding mass transport limitations typically experienced when working with liquid electrolyte. The catalyst layer is not in contact with any liquid electrolyte, but instead a membrane electrolyte separates the working electrode (catalyst layer) compartment from an electrochemical cell housing the liquid electrolyte, the CE and the RE. Thus a realistic condition for the WE environment is combined with the advantages offered by a three electrode setup.[6] To investigate CO₂RR catalysts the setup has been slightly adapted, as described below. Applying a silver nanowire (Ag-NW) based catalyst that has been previously tested in an H-type cell,[7] it is demonstrated that high currents (reaction rates) can be reached without mass transport limitation of the CO₂ reactant.

2. Experimental

2.1 *Synthesis of Silver Nanowires (Ag-NWs)*

Ag-NWs were synthesized according to a modified protocol introduced by Liu *et. al.*[7] 125 mg of polyvinylpyrrolidone (M = 1,300,000 g/mol, Acros Organic) were dissolved in 20 mL of ethylene glycol (Sigma-Aldrich, 99.8%) and heated to 160 °C for 1 h in an oil bath. The solution was thoroughly agitated (320 rpm). Subsequently, 250 µL of 50 mM sodium bromide (Alfa Aesar, 99.0%) was added to the previous solution. After 15 min, 7.5 mL of 100 mM silver nitrate (Alfa Aesar, 99%) was dropwise injected within 65 min. After the complete addition of the AgNO₃ solution, the reaction bath was kept at 160 °C for 35 min, followed by immersion in an ice-water bath. The formed Ag-NWs were washed 3 times with acetone (Honeywell) followed by centrifugation. Finally, the Ag-NWs were thoroughly washed (3 times) with H₂O.

2.2 *Preparation of the Ag-NWs Ink*

For the preparation of the carbon-supported Ag-NW ink, 5 mg of the Ag NWs and 0.9 mg of carbon black (Vulcan XC 72R, Cabot) were separately dispersed in 10 mL of isopropanol (VLSI Selectipur, BASF) by 1 h sonication. Both suspensions were intermixed, sonicated for 1 h and dried using a Rotavapor. Thus, the obtained carbon-supported Ag-NWs were re-dispersed in 1 mL of isopropanol containing 50 µL of Nafion (5 wt.%, 15–20% water, Sigma-Aldrich). This suspension was subjected to sonication for 1 h yielding a homogeneous catalyst ink (85% Ag-NW and 15% C black).

2.3 *Electrochemical Reduction of CO₂ (CO₂RR) Using Ag-NWs as Electrocatalyst*

Gas diffusion electrodes were prepared using Sigracet 39 BC carbon paper as the GDL substrate. The Sigracet 39 BC carbon paper is covered by a microporous layer (MPL) treated with 5% of PTFE (Fuel Cell Store). The carbon paper was cut into circular pieces (2 cm in diameter) and subsequently placed onto a nylon membrane filter (pore size 0.22 µm, Fischerbrand) on top of the funnel of a vacuum filtrating system. This assembly was then covered with a paper mask bearing a central hole of 3 mm in di-

tained GDEs were dried at ambient conditions for at least 30 min. The employed flow-cell was assembled by placing the prepared GDE on the lower cell body, and a Sustainion X37-50 RT alkaline membrane (Dioxide materials) on top of it. 10 mL of 2 M KOH (solution pH: 14.3, ≥85%, Merck) were used as supporting electrolyte placed above the membrane. The Ag-NW catalyst had no direct contact with the supporting electrolyte. A Ag/AgCl electrode (3 M KCl, Metrohm, double junction design) and Pt wire served as reference and counter electrode, respectively. Both ECi-200 (Nordic electrochemistry) and Autolab PGSTAT128 N (Metrohm) potentiostats were used to perform the CO₂RR electrolysis experiments.

During electrolysis, a humidified CO₂ stream (16 ml min⁻¹, 99.999% Carbagas, Switzerland) was continuously fed through the channels of the stainless-steel cell body adjacent to the prepared GDEs. Potentiostatic CO₂ electrolysis experiments were carried out for 1 h at selected applied electrode potentials. To avoid a possible influence of catalyst layer degradation on the product distribution, a newly prepared GDE was used for each CO₂ electrolysis experiment. Analysis of the gaseous products was carried out every 10 min by online gas chromatography (GC) triggered by the potentiostat.

The continuous flow of humidified CO₂ was used to transport the gaseous products from the GDE flow-cell to the sample loop of the gas chromatograph (Model 8610C, SRI Instruments) equipped with a thermal conductivity detector (TCD) and a flame ionization detector (FID) coupled to a methanizer to detect hydrogen and carbon monoxide, respectively. To avoid damage the column of the GC, the outlet gas of the CO₂RR was passed by a drying tube to remove the excess of water (Cole-Parmer Drierite, Fisher Scientific) before reaching the sample loop of the GC. Eqn (1) was used to determine the faradaic efficiency (FE) for a given gaseous product *i*:

$$FE_i = \frac{I_i}{I_{total}} = \frac{c_i \cdot v \cdot F \cdot z}{10^6 \cdot V_m \cdot I_{total}} \qquad (1)$$

where I_i represents the partial current for the conversion of CO₂ into product *i*, c_i its concentration in ppm measured by online GC using an independent calibration standard gas (Carbagas, Switzerland), ν the gas flow rate (measured by a universal flowmeter 7,000 GC by Ellutia), *F* represents Faraday's constant, *z* the number of electrons involved in the formation of the particular product, V_m the molar volume and I_{total} the total current at the time of the measurement.

Electrochemical impedance spectroscopy measurement was conducted to determine the solution resistance between RE and WE (iR drop).

The electrolyte was analyzed after the electrolysis (*post reaction*) to quantify the formate content by means of ion exchange chromatography (Metrohm Ltd., Switzerland). This chromatograph was coupled to a L-7100 pump, a separation and an ion exclusion column (Metrosep A Supp 7-250, columns) and a conductivity detector.

For comparison, the performance of the catalyst was also tested in a conventional half-cell configuration using a custom-built gas-tight H-type glass cell with a proton exchange membrane (Nafion 117, Sigma Aldrich) separating the catholyte and the anolyte. The working electrode consisted of a rectangular piece (0.8 cm × 3 cm) of a carbon paper prepared in a similar way as the electrodes for the GDE measurements. The back side and the edges of the electrode were masked with Teflon tape thus leading to a geometric surface area of 0.2 cm⁻². A single junction Ag/AgCl

were both filled with 30 mL of 0.5 M $KHCO_3$ (ACS grade, Sigma-Aldrich) electrolyte solution and saturated with CO_2 for 30 min, achieving a final pH value of 7.2. The CO_2 flow was kept constant throughout the potentiostatic CO_2 electrolysis and enabled the transport of gaseous products from the headspace of the catholyte to the sample loop of the GC. The CO_2 electrolysis experiments in the half-cell configuration were performed in an analogous way as the ones carried out in the GDE set up. The analysis of gaseous products was carried out in intervals of 20 min. The total electrolysis time per applied potential was 1 hour

The catalyst layers were characterized before and after CO_2 electroreduction by means of scanning electron microscopy (Zeiss Gemini 450 SEM equipped with an Inlens SE detector). An accelerating voltage of 1.5 kV was applied at a working distance of 2–3 mm.

3. Results and Discussion

Potentiostatic CO_2 electroreduction experiments on carbon-supported Ag-NWs (85 wt.% Ag-NWs and 15 wt.% of C black) were carried out in the GDE setup to investigate their activity and selectivity as a function of the applied electrolysis potential. Fig. 2 displays the resulting potential-dependent product distribution in terms of faradaic efficiencies (FEs, panel a) and partial current densities (PCDs, panel b). CO and H_2 were the only gaseous products detected by GC analysis. As a third product formate could be detected and quantified *post reaction* in the (liquid) electrolyte compartment of the cell (see Fig. 1) by means of ionic exchange chromatography. Note that in our experiments, the FE of formate is substantially higher than the typically reported values on polycrystalline Ag electrocatalysts (commonly ~ 8% at -1.4 V vs RHE).[8]

The FE vs E plot (Fig. 2a) can be subdivided into three characteristic sections. Hydrogen is the predominant electrolysis product in the first potential regime (> −1.55 V vs Ag/AgCl) with FE_{H2} values never dropping below to 40%, while FE_{CO} does not exceed 35%. In the second characteristic potential section ranging from −1.55 to −1.9 V vs Ag/AgCl FE_{H2} starts to decrease and the CO efficiency passes a maximum of about 70% at −1.75 V vs Ag/AgCl. From Fig. 2a it becomes evident that the FE values for CO and H_2 are strongly anti-correlated to each other, similar to what is known from polycrystalline Ag catalysts tested in a liquid electrolysis environment.[8c] Formate appears as a by-product of the CO_2 electrolysis at applied potentials of < −1.6 V vs Ag/AgCl and reaches a maximum of about 25% at −1.9 V vs Ag/AgCl. In the third characteristic section of the FE vs E plot, at E < −1.9 V

vs Ag/AgCl, the parasitic HER becomes the dominant electrolysis process on the expense of the CO_2RR.

The corresponding potential-dependent PCDs for CO, H_2 and formate production are displayed in Fig. 2b. It is seen that by using gas diffusion electrodes, CO_2RR current densities can be achieved which are ~1 order of magnitude higher than the ones typically observed in classical half-cell electrolysis measurements carried out in unstirred aqueous electrolytes.[9] In the present case, a PCD_{CO} of ~130 mA cm^{-2} (normalized to the geometric surface area) at FE_{CO} = 70% was determined at a potential of ~ −1.78 V vs Ag/AgCl. Pre-screening experiments on the same catalyst, carried out in classical H-type half-cell arrangements, resulted in a higher selectivity of the Ag-NWs reaching CO faradaic efficiencies of >95% (Fig. 3), those results are comparable to the previously reported results by Liu *et. al.* However, the PCD for CO production was substantially higher in this present study. Liu *et. al.* reported a maximum PCD for CO of −3 mAcm^{-2} at ~ −1.2 V vs RHE[7] whereas in our pre-screening experiments a maximum PCD of ~16 mA cm^{-2} was achieved at a potential of −1.73 V vs Ag/AgCl.

As discussed above, the significantly lower CO_2RR current densities in the conventional H-type cells using aqueous electrolyte environment as compared to the GDE setup can be explained by transport limitations. In the liquid electrolyte the CO_2 solubility is limited and diffusion significantly inhibited as compared to the gas phase. A direct comparison of the overpotentials in both setups is less straightforward. The thermodynamic CO_2 reduction potentials are pH and product dependent. At pH 7 the reduction potential of CO_2 to CO with respect to NHE (recall that at pH 7 and 1 atm of H_2, the H_2/H^+ couple is −0.420 V) is:[10]

$$CO_2 \text{ (g)} + 2 H^+ + 2 e^- \rightarrow CO \text{ (g)} + H_2O, \quad E^\circ_{redox} = -0.520 \text{ V}$$
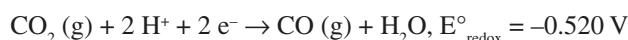
Thus in both setups significant overpotentials are observed. To refer to the pH-independent RHE scale one needs to establish the pH of the reaction environment. In the conventional H-type cell this is straightforward and all measured electrode potentials can be easily plotted on an RHE scale. In the GDE setup the pH at the RE might be different from the one the catalyst experiences. Thus a referral to RHE with regard of the pH in the liquid electrolyte enclosing the RE might lead to misleading shifts in the reduction potentials.

It should be further noted that it is expected that both the partial CO_2RR current densities and the corresponding faradaic efficiencies observed for the Ag-NW catalyst in the GDE setup can be further improved. In the GDE setup the overall GDE performance
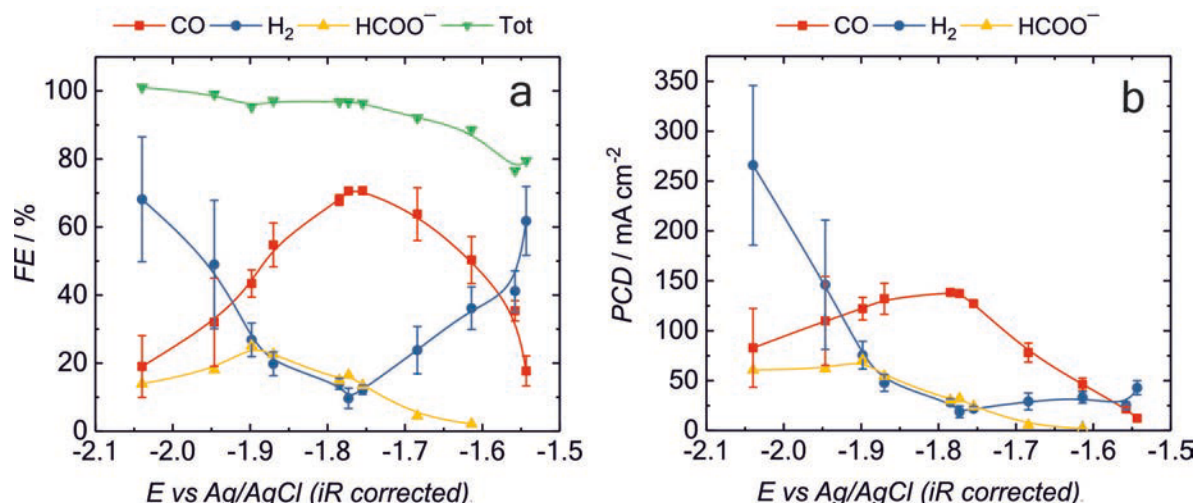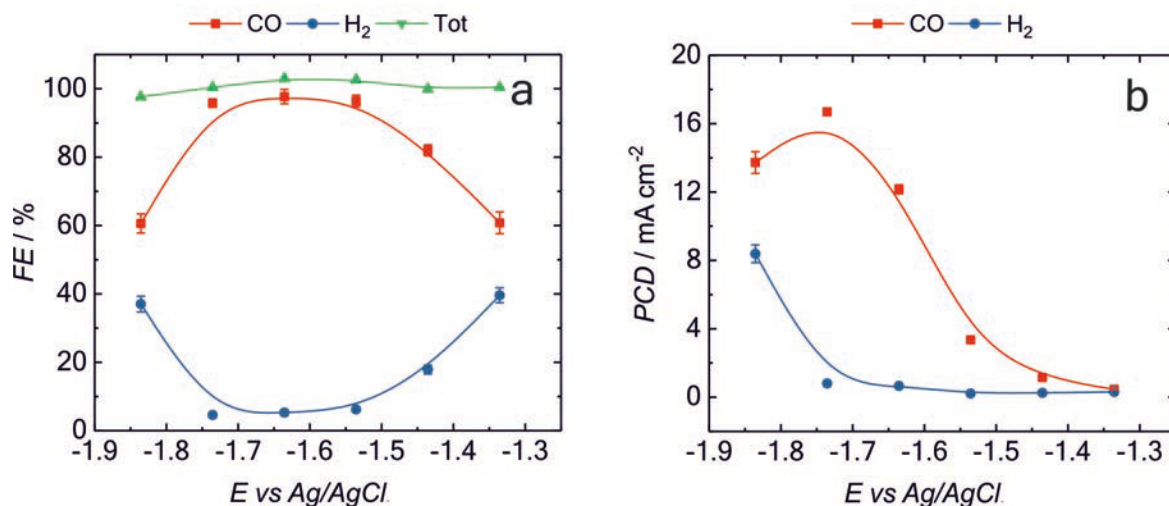
Fig. 3. a) Product distribution of the CO_2RR carried out in an H-type cell over Ag-NW based electrocatalysts (85% wt.% Ag NW and 15% wt.% C) at different applied potentials (0.5 M $KHCO_3$ electrolyte); b) corresponding partial current densities (PCDs).
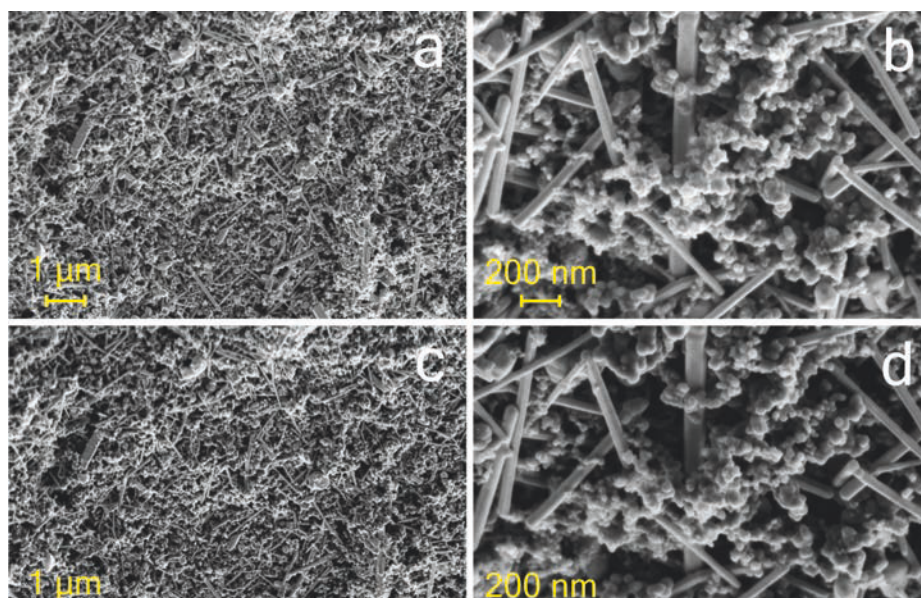
depends not only on the intrinsic electrocatalytic properties of the Ag-NWs but also on their particular mass loading, their spatial distribution inside the GDE, the local pH as well as the pore distribution. For example, in initial tests of the GDE setup with the same Ag-NW catalyst, a Nafion membrane and/or acidic electrolyte in the upper compartment were used. This led to a significant increase in hydrogen production (FE_{H2}) and almost no CO could be detected (not shown). We addressed this behavior to the acidic pH of Nafion and a simple exchange of the membrane and electrolyte in the CE and RE compartment led to a drastic improvement in CO formation.

Not only are the activity and selectivity of importance for the evaluation of the overall catalyst performance but also its stability. Particularly the higher current densities at higher applied overpotentials might lead to an undesired detachment of the active NWs from the carbon support or might cause other structural degradation processes. Therefore, in an effort to shed light into this issue, identical location (IL) scanning electron microscopy was applied to the Ag-NWs catalyst before (Fig. 4a,b) and after (Fig. 4c,d) the CO_2 electrolysis. The carbon-supported Ag-NW/C catalyst was stressed for 133 min at –0.83 V vs RHE (total charge density

2,453C cm^{-2}). Clearly, there are no severe morphological changes visible in the IL-SEM inspection by comparing the catalyst morphology at the same location before and after CO_2 electrolysis, suggesting that the Ag-NW/C catalyst exhibits superior structural stability, at least under the given experimental conditions.

4. Conclusions

Herein we present a study of a Ag-NW catalyst for the selective CO_2RR to CO. The catalyst performance has been tested in a GDE setup allowing high CO_2 reactant mass transport as well as in a classic H-type cell using liquid electrolyte. In the GDE setup current densities sufficient for technological applications (>100 mA cm^{-2}) are reached with FE_{CO} up to 70%, depending on the applied electrode potential. Comparison to the same catalyst in liquid electrolyte environment suggests that the FE towards CO can be further improved by optimizing the catalyst layer with respect to mass loading, spatial distribution, pore distribution, local pH, *etc*. Our results highlight that for technical applications, catalyst testing in H-type cells and aqueous electrolyte environment is not sufficient, and GDE setups such as the one presented in this work can bridge basic and applied catalyst development.

Notes

Acknowledgements

Received: September 25, 2019

[1]   a) S. Nitopi, E. Bertheussen, S. B. Scott, X. Y. Liu, A. K. Engstfeld, S. Horch, B. Seger, I. E. L. Stephens, K. Chan, C. Hahn, J. K. Norskov, T. F. Jaramillo, I. Chorkendorff, *Chem. Rev.* **2019**, *119*, 7610, DOI: 10.1021/acs.chemrev.8b00705; b) M. Rahaman, A. Dutta, A. Zanetti, P. Broekmann, *Acs Catal.* **2017**, *7*, 7946, DOI: 10.1021/acscatal.7b02234; c) J. Durst, A. Rudnev, A. Dutta, Y. C. Fu, J. Herranz, V. Kaliginedi, A. Kuzume, A. A. Permyakova, Y. Paratcha, P. Broekmann, T. J. Schmidt, *Chimia* **2015**, *69*, 769, DOI: 10.2533/chimia.2015.769.

[2]   T. Haas, R. Krause, R. Weber, M. Demler, G. Schmid, *Nat. Catal.* **2018**, *1*, 32, DOI: 10.1038/s41929-017-0005-1.

[3]   A. V. Rudnev, in 'Encyclopedia of Interfacial Chemistry', Ed. K. Wandelt, Elsevier, Oxford, **2018**, p. 321, DOI: https://doi.org/10.1016/B978-0-12-409547-2.13564-4.

[4]   J. B. Vennekoetter, R. Sengpiel, M. Wessling, *Chem. Eng. J.* **2019**, *364*, 89, DOI: 10.1016/j.cej.2019.01.045.

[5]   O. G. Sánchez, Y. Y. Birdja, M. Bulut, J. Vaes, T. Breugelmans, D. Pant, *Curr. Opin. Green Sust. Chem.* **2019**, *16*, 47, DOI: https://doi.org/10.1016/j.cogsc.2019.01.005.

[6]   a) M. Inaba, A. W. Jensen, G. W. Sievers, M. Escudero-Escribano, A. Zana, M. Arenz, *Energ. Environ. Sci.* **2018**, *11*, 988, DOI: 10.1039/c8ee00019k; b) G. K. H. Wiberg, M. Fleige, M. Arenz, *Rev. Sci. Instrum.* **2015**, *86*, DOI: Artn 02410210.1063/1.4908169; c) G. W. Sievers, A. W. Jensen, V. Brüser, M. Arenz, M. Escudero-Escribano, *Surfaces* **2019**, *2*, 336.

[7]   S. Liu, X.-Z. Wang, H. Tao, T. Li, Q. Liu, Z. Xu, X.-Z. Fu, J.-L. Luo, N*ano Energy* **2018**, *45*, 456, DOI: https://doi.org/10.1016/j.nanoen.2018.01.016.

[8]   a) Y. Hori, H. Wakebe, T. Tsukamoto, O. Koga, *Electrochim. Acta* **1994**, *39*, 1833, DOI: https://doi.org/10.1016/0013-4686(94)85172-7; b) N. Hoshi, M. Kato, Y. Hori, *J. Electroanal. Chem.* **1997**, *440*, 283, DOI: https://doi.org/10.1016/S0022-0728(97)00447-6; c) T. Hatsukade, K. P. Kuhl, E. R. Cave, D. N. Abram, T. F. Jaramillo, *Phys. Chem. Chem. Phys.* **2014**, *16*, 13814, DOI: 10.1039/c4cp00692e; d) Y.-C. Hsieh, S. D. Senanayake, Y. Zhang, W. Xu, D. E. Polyansky, *Acs Catal.* **2015**, *5*, 5349, DOI: 10.1021/acscatal.5b01235; e) S. Kaneco, K. Iiba, K. Ohta, T. Mizuno, A. Saji, *Electrochim. Acta* **1998**, *44*, 573, DOI: https://doi.org/10.1016/S0013-4686(98)00178-9; f) F. Quan, M. Xiong, F. Jia, L. Zhang, *Appl. Surf. Sci.* **2017**, *399*, 48, DOI: https://doi.org/10.1016/j.apsusc.2016.12.069.

[9]   a) H.-R. M. Jhong, S. Ma, P. J. A. Kenis, *Curr. Opin. Chem. Engin.* **2013**, *2*, 191, DOI: https://doi.org/10.1016/j.coche.2013.03.005; b) D. M. Weekes, D. A. Salvatore, A. Reyes, A. Huang, C. P. Berlinguette, *Acc. Chem. Res.* **2018**, *51*, 910, DOI: 10.1021/acs.accounts.8b00010; c) B. Endrödi, G. Bencsik, F. Darvas, R. Jones, K. Rajeshwar, C. Janáky, *Progr. Ener. Comb. Sci.* **2017**, *62*, 133, DOI: https://doi.org/10.1016/j.pecs.2017.05.005.

[10] A. M. Appel, J. E. Bercaw, A. B. Bocarsly, H. Dobbek, D. L. DuBois, M. Dupuis, J. G. Ferry, E. Fujita, R. Hille, P. J. A. Kenis, C. A. Kerfeld, R. H. Morris, C. H. F. Peden, A. R. Portis, S. W. Ragsdale, T. B. Rauchfuss, J. N. H. Reek, L. C. Seefeldt, R. K. Thauer, G. L. Waldrop, *Chem. Rev.* **2013**, *113*, 6621, DOI: 10.1021/cr300463y.

5.5 Environment matters: CO₂RR electrocatalyst performance testing in a gas-fed zero-gap electrolyzer

Authors: María de Jesus Gálvez-Vázquez, Pavel Moreno-García*, Heng Xu, Yuhui Hou, **Huifang Hu**, Iván Zelocualtecatl Montiel, Alexander V. Rudnev, Shima Alinejad, Vitali Grozovski, Benjamin J. Wiley, Matthias Arenz, and Peter Broekmann*

Highlights: The Ag NC catalyst was chosen as a model catalyst to study CO_2RR performance on GDE in a gas-fed zero-gap configuration. The FE_CO reaches ~85%, and the PCD_CO achieves ~625 mA/cm^2 with 2 M KOH electrolyte in the electrolyzer. However, the FE_CO and PCD_CO decrease as electrolysis time increases at the negative potentials (< -1.8 V vs Ag/AgCl), and the small particles are found at these harsher cathodic conditions. The complementary experiments carried out in flow cell and H-type cell in 2 M $KHCO_3$ suggest that the loss of CO_2 performance is attributed more to the flooding and precipitation of GDE than the morphological degradation of the catalysts. Moreover, the reaction environment influence the products distribution. It is proposed that CO_2RR studies should be conducted using technical approaches because the knowledge obtained from the H-type cell might not be applied to the flow cell studies directly.

Contributions: I was involved in the scientific discussion of the results especially about synthesis of Ag NCs.

Environment Matters: CO₂RR Electrocatalyst Performance Testing in a Gas-Fed Zero-Gap Electrolyzer

María de Jesus Gálvez-Vázquez,[⊥] Pavel Moreno-García,*[⊥] Heng Xu, Yuhui Hou, Huifang Hu, Iván Zelocualtecatl Montiel, Alexander V. Rudnev, Shima Alinejad, Vitali Grozovski, Benjamin J. Wiley, Matthias Arenz, and Peter Broekmann*

ABSTRACT: Among the electrolyzers under development for CO₂ electro-reduction at practical reaction rates, gas-fed approaches that use gas diffusion electrodes (GDEs) as cathodes are the most promising. However, the insufficient long-term stability of these technologies precludes their commercial deployment. The structural deterioration of the catalyst material is one possible source of device durability issues. Unfortunately, this issue has been insufficiently studied in systems using actual technical electrodes. Herein, we make use of a morphologically tailored Ag-based model nanocatalyst [Ag nanocubes (NCs)] assembled on a zero-gap GDE electrolyzer to establish correlations between catalyst structures, experimental environments, electrocatalytic performances, and morphological degradation mechanisms in highly alkaline media. The morphological evolution of the Ag−NCs on the GDEs induced by the CO₂ electrochemical reduction reaction (CO₂RR), as well as the direct mechanical contact between the catalyst layer and anion-exchange membrane, is analyzed by identical location and post-electrolysis scanning electron microscopy investigations. We find that at low and mild potentials positive of −1.8 V versus Ag/AgCl, the Ag−NCs undergo no apparent morphological alteration induced by the CO₂RR, and the device performance remains stable. At more stringent cathodic conditions, device failure commences within minutes, and catalyst corrosion leads to slightly truncated cube morphologies and the appearance of smaller Ag nanoparticles. However, comparison with complementary CO₂RR experiments performed in H-cell configurations in a neutral environment clearly proves that the system failure typically encountered in the gas-fed approaches does not stem solely from the catalyst morphological degradation. Instead, the observed CO₂RR performance deterioration is mainly due to the local high alkalinity that inevitably develops at high current densities in the zero-gap approach and leads to the massive precipitation of carbonates which is not observed in the aqueous environment (H-cell configuration).

KEYWORDS: CO₂ electroreduction, gas diffusion electrodes, zero-gap electrolyzer, carbon monoxide, exchange membrane electrode assembly
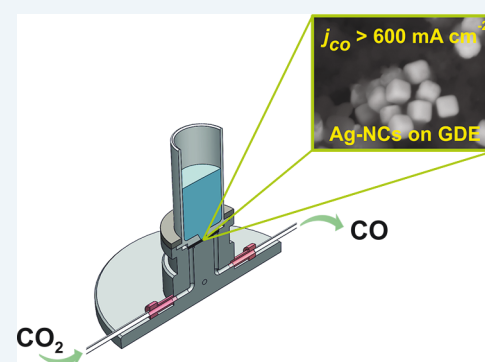
INTRODUCTION

Powering the electrochemical reduction reaction of carbon dioxide (CO₂RR) with renewable energy sources has emerged as a compelling alternative to other approaches to CO₂ valorization,[1,2] toward meeting the increasing demand for commodity/platform chemicals and thereby contributing to efforts to close the anthropogenic carbon cycle.[3,4] In recent decades, significant progress has been made to understand the reaction mechanisms of this process through the development of cutting-edge catalyst materials that increase the activity [partial current density (PCD) of generated products] and selectivity (faradaic efficiency, FE) of the process. Strong cases of commercial viability have been made for formate (HCOO⁻) and CO production, which require the transfer of only two electrons from the electrocatalyst to the CO₂ reactant molecule.[5,6] Formate is efficiently formed on Sn-, Bi-, In-, and Pb-based catalysts, whereas CO forms preferably on Ag-,

Au-, and Zn-based catalysts.[7] CO is a particularly appealing product because it can be used as a stockpile for subsequent transformation either in the Fischer−Tropsch process[8] or in sequential electrochemical[9] and fermentation methods.[10]

Using catalyst screening methods based on H-cell experiments in which reactant CO₂ gas is usually dissolved in an aqueous bicarbonate-based electrolyte, a significant number of works have reported that Ag-,[11−13] Au-,[14,15] and Zn-based[16−18] cathode materials provide excellent CO selectivity and
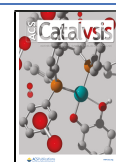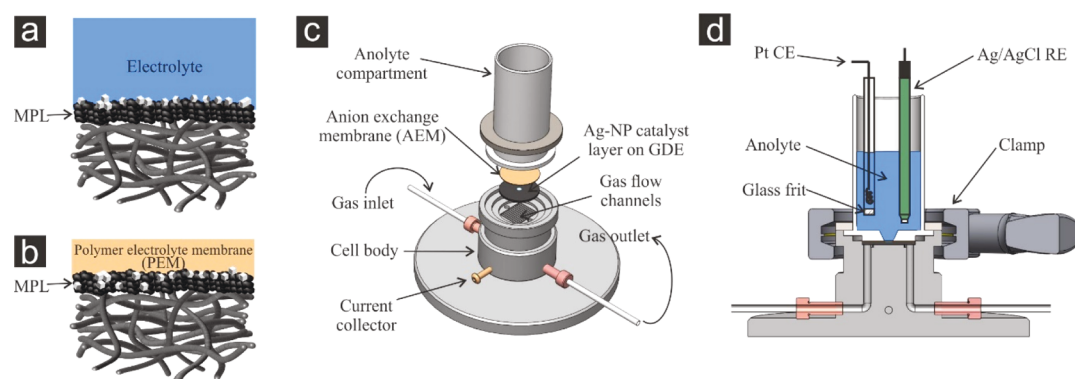
Figure 1. Schematics of the reaction interfaces in (a) liquid flow-cell electrolyzer and (b) exchange membrane electrode assembly (MEA) or zero-gap assembly. (c) Depiction and assembly of the zero-gap flow cell used in this work for the CO_2RR. (d) Cross-sectional view of the assembled cell with reference and counter electrodes (CE and RE, respectively) immersed in the anolyte compartment. MPL in panels (a,b) stands for the MPL on which the catalyst material (Ag−NCs) is embedded.

operational stability. Many works have also reported insightful correlations between the use of a tailored catalyst nanostructure and electrocatalytic performance.[19,20] In addition, diverging from the bicarbonate-based electrolyte that was once used almost ubiquitously, it has been found that highly concentrated (potassium) hydroxide-based catholyte solutions suppress the parasitic hydrogen evolution reaction (HER) and improve the CO_2RR performance because OH^- ions exhibit excellent ionic conductivity and reduce the activation energy barriers for CO_2 electroreduction.[9,21−24] Through these and other improvements, the field has reached a significant level of maturity so that currently, the associated research is driven by more ambitious endeavors, namely, scaling up the CO_2RR process to practical realization.[10,25] Toward this end, experimental platforms have been developed to circumvent or attenuate the mass transport limitations that are intrinsic to traditional H-type cell measurements[26−28] and arise from the low solubility of the dissolved CO_2 reactant in aqueous electrolytes. This pursuit opens a new avenue to the CO_2RR and related fields because the insights extracted from H-cell measurements with either stationary or rotating disk electrodes do not necessarily hold for their gas-fed homologues and both approaches bear fundamental kinetic differences that must be addressed to approach process commercialization.[29−31]

Among the various types of CO_2 electrolyzers under development, gas-fed approaches that use gas diffusion electrodes (GDEs) as cathodes and that are inspired by polymer electrolyte fuel cell technologies are considered to be the most promising.[1,21,30,32−36] Consequently, studies on Ag−GDEs in contact with flowing alkaline electrolytes (Figure 1a) have grown in popularity to achieve higher PCD_{CO} and FE_{CO} values as well as lower CO_2RR onset potentials and to explore possible enhancements to performance longevity.[37−41] However, electrolyzer designs that rely on this cell configuration are not without shortcomings that affect device performance and stability, thereby overshadowing their intrinsic electrocatalytic activity. These issues stem from (i) high ohmic losses owing to the electrolyte layer separating the electrodes,[30] (ii) electrolyte percolation through the microporous layer (MPL) of GDEs and concomitant carbonate salt precipitation,[42,43] and (iii) CO_2 crossover from the cathodic to the anodic compartment upon CO_2 neutralization by OH^- ions to HCO_3^-/CO_3^{2-}.[32,44,45]

Motivated by this, a few recent works on alternative cell designs with only an aqueous anolyte between the membrane

and anode and no liquid electrolyte layer between the catalyst layer and (an)ion-exchange membrane [indistinctively called exchange membrane electrode assemblies (MEAs) or catholyte-free or zero-gap membrane assemblies, see Figure 1b][1,32,46] have been reported, enabling comparably reduced ohmic overpotentials, enhanced stability, and excellent CO selectivity.[25,47,48] This zero-gap configuration not only affords reduced ohmic losses but also attenuates complications that arise from poor membrane hydration and electrode flooding at high current densities, which are otherwise problematic to fully gas-fed electrolyzers[46,49] (note that exchange MEA electrolyzers may still suffer from the parasitic uptake of CO_2 at the interface of the cathode and anion-exchange membrane, thus facilitating the undesirable CO_2 discharge on the anode surface).[43,44,50] Nonetheless, one persistent hurdle that precludes the commercial deployment of these technologies is insufficient long-term device stability, which continues to fall short of the minimum target value of 8×10^4 h.[5] Efforts to identify the factors that lead to process failure have been undertaken, and strategies to alleviate such failures have been proposed (e.g., appropriate selection of the reactor design, electrode production method and hydrodynamics,[1] management of electrolyte percolation through the GDE,[39,51] and carbonation tolerance of the electrodes[43,44]).

In this context, another aspect that may also be a source of device durability issues and that has been minimally investigated using actual technical electrodes on which very large current densities (>300 mA cm^{-2}) are enforced is the structural deterioration of the catalyst material.[31,40] In particular, studies of the catalyst morphological evolution of Ag-based exchange MEAs induced by the CO_2RR reaction itself are lacking, as well as studies of the effect of direct mechanical contact between the catalyst layer and anion-exchange membrane (Figure 1b). To shed light on this unexplored aspect of CO_2RR on Ag−GDEs, we make use of morphologically tailored Ag-based model nanocatalysts [Ag nanocubes (Ag−NCs)] assembled on zero-gap GDEs to establish correlations between structure, environment, electrocatalytic performance, and degradation mechanisms under the abovementioned most favorable CO_2RR conditions (i.e., a highly alkaline membrane adjacent to the catalyst layer). Submonolayer surface coverages are purposely employed to unambiguously address possible structure degradation at the level of a single Ag−NC. Besides investigation of the catalyst activity and selectivity, we devote particular attention to the

time evolution of both the electrochemical performance of the process and the material's nanostructure induced upon CO_2 electrolysis at large current densities, as enforced on the model exchange Ag−MEAs. We find that our testbed enables among the highest CO partial current densities and competitive FE_{CO} values (−625 mA cm^{-2} and 85%, respectively) even at the applied sub-monolayer catalyst coverages. Two distinct electrode potential regimes were observed, each exhibiting significantly different behaviors. At low and mild applied potentials ($E \geq -1.8$ V vs Ag/AgCl), stability prevails across the PCD_{CO} and FE_{CO}, electrolyzer performance, and catalyst structure. Conversely, at greater cathodic potentials, the process selectivity and activity severely degrade, leading to performance failure even though the catalyst morphology undergoes significantly less deterioration. Thus, this work enables the deconvolution of catalyst structural stability from system performance stability. Finally, a comparison with standard H-type reference measurements reveals that CO_2RR product selectivity is influenced by electrolyzer design and, therefore, that the knowledge developed using such batch-type approaches should not be regarded as directly transferable to gas-fed platforms. Overall, the results underscore that more effort must be devoted to the understanding and optimization of system design parameters (e.g., water management, prevention of salt precipitation, CO_2 flow rate, and electrolyte flow rate) that have a more significant impact on the product spectrum and longevity of the exchange MEA electrolyzers than that of the structural degradation of the catalyst, which is shown to be mild.

■ EXPERIMENTAL SECTION

Synthesis of Ag−NCs. Silver NCs were synthesized using a previously reported method with minor modification.[52] 5 mL of ethylene glycol (EG, J. T. Baker) was added to a 250 mL two-neck flask preheated to 160 °C. A light N_2 flow was introduced just above the EG for the first 10 min, followed by heating the solvent for another 50 min. Next, 3 mL EG solution of AgNO$_3$ (94 mM) and 3 mL EG solution containing polyvinylpyrrolidone (PVP, M_w = 55,000, 144 mM) and NaCl (0.22 mM) were simultaneously injected into the flask at a rate of 45 mL/h, with the solution observed to turn yellow during this process. Under continuous stirring at 160 °C, the solution exhibited a color transition series from yellow to clear yellow, brown, greenish, and finally ochre and opaque. The whole process required 16 h to 24 h for completion. After the solution had turned opaque, the reaction was quenched by adding 22 mL of acetone to the hot solution, followed by cooling in an ice-water bath. To purify the NCs, the solution was first centrifuged at 2000g for 30 min, and then, the precipitate was dispersed and centrifuged 3× in 10 mL of deionized water at 9000g for 10 min per run.[53] The product was finally dispersed in 5 mL of deionized water for future use.

Preparation of Ag−NC Catalyst Ink. To prepare the carbon-supported Ag−NC ink, 1.5 mg of the prepared Ag−NCs and 0.26 mg of carbon black (Vulcan XC 72R, Cabot) were separately dispersed in 10 mL of isopropanol (VLSI Selectipur, BASF SE, Ludwigshafen, Germany) by 1 h of sonication. Both suspensions were intermixed, sonicated for 1 h, and dried using a Rotary evaporator (Buchi R210, 45 °C, 85 mbar). The obtained carbon-supported Ag−NCs (85 wt % Ag−NC and 15 wt % C black) were then redispersed in 1 mL of isopropanol containing 50 μL of Nafion (5 wt %, 15−20% water, Sigma-Aldrich). The resulting suspension was subjected

to sonication for 1 h yielding a homogeneous catalyst ink. For the sake of reproducibility and comparison, catalyst inks were also prepared with commercial Ag−NCs (NanoXact, nano-Composix) and used for complementary CO_2RR experiments.

Preparation of the Ag−NC−GDEs. The model catalyst material in this work consists of cubic Ag nanoparticles (Ag−NCs) with an average edge length of (113.1 ± 10.6) nm. The Ag−NC−GDEs for all electrochemical and characterization experiments were prepared as follows: a defined circular area of 7.07×10^{-2} cm^2 on the GDEs' hydrophobic surface (diameter of 2 cm, Sigracet 39 BC, Fuel Cell Store) was modified by dropcasting 50 μL of carbon-supported Ag−NC ink onto its top surface. This catalyst solution was percolated through the porous body of the GDEs by a vacuum filtration system placed on the backside of the electrode, and subsequent drying at ambient conditions was allowed for at least 30 min. Analysis by inductively coupled plasma−mass spectrometry (ICP−MS) of freshly prepared samples was used to determine the catalyst mass loading, which amounted to ~7.1×10^{-2} mg$_{Ag}$ cm^{-2}.

Assembly of the Gas Flow Cell. The assembly and main components of the zero-gap gas-flow cell employed in this work to investigate correlations between the catalyst structure and process performance of CO_2RR to CO on Ag−NC−GDEs are schematically depicted in Figure 1c,d. This assembly consists of a stainless-steel cell body with the gas flow channels used to feed the CO_2 from the backside of the prepared Ag−NC−GDEs mounted on the outermost location of the central portion. Other components incorporated into the cell include a current collector and a gas inlet and outlet to control the supply of the CO_2 reactant (99.999%, Carbagas, Switzerland) and analysis of the gaseous products, respectively. All CO_2RR experiments were set up by placing a freshly prepared Ag−NC−GDE on top of the gas flow channels, with its catalyst-modified surface facing upward. Subsequently, a clean hydroxide-functionalized Sustainion alkaline membrane (X37-50 RT, Dioxide materials) and a poly(tetrafluoroethylene) (PTFE) anolyte compartment were carefully placed on top of the Ag−NC−GDE. A clamp was then used to ensure cell tightness and mechanical stability. KOH electrolyte-supporting solution (10 mL, 2 M; pH: 14.3, Sigma-Aldrich) was added to the anolyte compartment, and a Ag/AgCl (3 M KCl, double junction design, Metrohm) electrode and a Pt mesh (99.99%, MaTeck) separated by a glass frit served as the reference and counter electrodes, respectively. Note that the PTFE anolyte compartment has a central orifice (7.07×10^{-2} cm^2) in its bottom part that provides direct contact between the electrolyte and the underlying anion-exchange membrane, while the Ag−NC−GDE is prevented from establishing physical contact with the supporting anolyte. During electrolysis, a humidified CO_2 stream (16 mL min^{-1}) was continuously fed through the gas flow channels of the stainless-steel cell body adjacent to the prepared Ag−NC−GDEs.

Electrochemical Reduction of CO_2 (CO_2RR) Using Ag−NC−GDEs. All electrolytes were prepared using chemicals of at least ACS reagent grade and deionized water (Millipore, 18.2 MΩ cm, 3 ppb toc). Both ECi-200 (Nordic electro-chemistry) and Autolab PGSTAT128 N (Metrohm) potentio-stats were used to perform all electrochemical experiments. Electrochemical impedance spectroscopy measurements were conducted before and after every CO_2 electrolysis experiment, and the results were considered to build the potential-dependent product distributions and partial current densities displayed and mentioned throughout the text. Potentiostatic
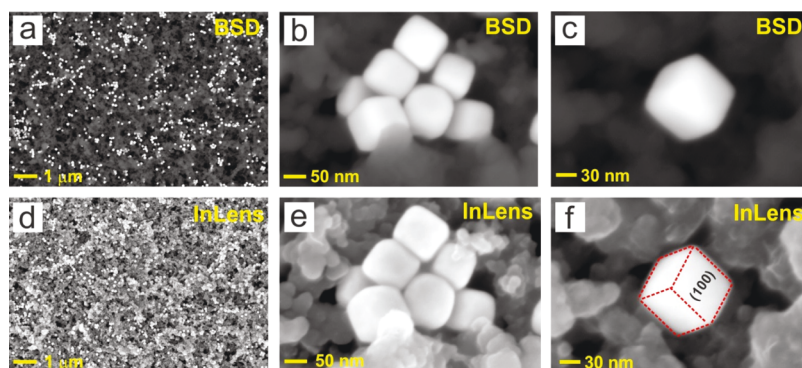
Figure 2. Representative SEM images at different magnifications showing the surface of an as-prepared Ag−NC−GDE cathode for CO$_2$RR. (a,d) Ag−NC catalyst sub-monolayer coverage on the MPL of the GDE. (b,c) and (e,f) reveal the well-defined cubic morphology of the Ag−NCs. Images (a−c) were acquired using the BSD detector of the scanning electron microscope. (d−f) Correspond to the same sample surface areas shown in the upper panels but were recorded with the InLens SE detector.

CO$_2$ electrolysis experiments were carried out at selected applied electrode potentials for 1 h, during which time the electrogenerated gaseous products were analyzed by online gas chromatography (SRI Instruments) in sequential intervals of 10 min. The electrolyte was analyzed after the applied electrolysis condition (post reaction) to quantify the produced formate by means of ion-exchange chromatography (Metrohm Ltd., Switzerland). For comparison, the performance of the Ag−NC−GDEs was also tested by dedicated reference measurements using 2 M KHCO$_3$ as the electrolyte in both the gas-flow cell and the conventional H-cell configurations. For the H-cell measurements, a proton-exchange membrane (Nafion 117, Sigma-Aldrich) separated the catholyte from the anolyte, and the working electrode consisted of a rectangular piece of carbon paper (0.8 × 3 cm) prepared in the same way as the Ag−NC−GDEs for zero-gap measurements. The back side and the edges of these electrodes were masked with the PTFE tape, thus leaving an uncovered geometric surface area of 0.2 cm^2. A single junction Ag/AgCl electrode (saturated KCl, Pine Research) and a Pt foil (2.5 × 0.8 cm, 99.99%, MaTeck) were used as the reference and counter electrodes, respectively. All electrode potential values in this work are in reference to the standard Ag/AgCl$_{3M}$ reference electrode. The data corresponding to the product selectivity and partial current densities of all experiments are displayed in Tables S2− S6. A thorough description of complementary experimental details is presented in a previous publication.[36]

Scanning Electron Microscopy and Energy-Dispersive X-ray Spectroscopy Characterization. Morphological characterization of the prepared Ag−NC−GDEs and assessment of the spatial distribution of the Ag−NCs over the samples was carried out with scanning electron microscopy (SEM) imaging experiments. Imaging was performed before (for the as-prepared electrodes) and after having sustained defined CO$_2$RR time intervals at selected applied electrode potentials. The analysis was conducted sequentially with a Zeiss Gemini 450 scanning electron microscope with both InLens secondary electron and backscattered electron detectors (Inlens SE and BSD detectors, respectively). An accelerating voltage of 5 kV and a current of 200 pA were applied at a working distance of 6.6−6.8 mm. The BSD detector enables clear identification of the Ag−NCs along the surface of the GDE's MPL because this technique is highly sensitive to the atomic number of the elements being imaged. However, the images acquired with the InLens SE detector

provide better morphological resolution of the Ag−NCs. The use of both imaging operational modes coupled to energy-dispersive X-ray analysis (EDX) analysis made it possible to track morphological catalyst changes induced by CO$_2$ electrolysis and/or physical contact between the catalyst material and anion-exchange membrane on the Ag−NC− GDEs used. Complementary identical location (IL−SEM) experiments were conducted on Ag−NC−GDEs for which selected sample positions were imaged by the SEM instrument before and after CO$_2$RR experiments.

AZtec 4.2 software (Oxford Instruments) was used to acquire EDX spectra and surface mappings of selected Ag− NC−GDEs. An acceleration voltage of 10 kV and a current of 1.2 nA were applied at a working distance of 8.5 mm.

Catalyst Loading and Post-electrolysis Electrolyte and Ag−NC−GDE Analysis by ICP−MS. Freshly prepared Ag−NC−GDEs were immersed in 3 mL HNO$_3$ (BASF SE, Ludwigshafen, Germany) for 24 h to dissolve the Ag−NCs embedded on their surfaces. The resulting solutions were diluted with 3% HNO$_3$ solution by a factor of 500 and were then fed into a NExION 2000 ICP−MS instrument (PerkinElmer) to obtain the Ag mass loading of the electrodes. To identify possible Pt dissolution from the employed Pt counter electrode during CO$_2$ electrolysis, the following ICP− MS and EDX control experiments were conducted. First, 10 μL of post-reaction anolyte (after CO$_2$RR at −2.0 V for 60 min in 2 M KOH) was diluted with 10 mL of 3% HNO$_3$ solution for ICP−MS analysis. No Pt dissolution was detected in two independent measurements. Additionally, two post-electrolysis Ag−NC−GDEs were immersed in 3 mL aqua regia for 24 h and the solutions were diluted by factor 100 with 3% HNO$_3$. The corresponding ICP−MS spectra showed no signal other than the background further confirming the absence of Pt on the catalyst surface and supporting GDE. Finally, EDX analysis of a Ag−NC−GDE sample after being subjected to similar CO$_2$RR conditions also excluded the presence of any Pt deposited on the employed cathodes (see Figure S8).

X-ray Diffraction Catalyst Characterization. The crystallinity of the Ag−NCs was determined by means of X-ray diffraction (XRD) techniques (Bruker D8) using Cu Kα radiation (λ = 0.1540 nm, 40 mA) generated at 40 keV. Scans were recorded at 1° min^{-1} for 2θ values between 20 and 100°. The samples were prepared by dropcasting Ag−NCs dispersed in isopropanol on a graphite foil (0.13 mm, 99.8%, Alfa Aesar) and then allowing the solution to dry under ambient
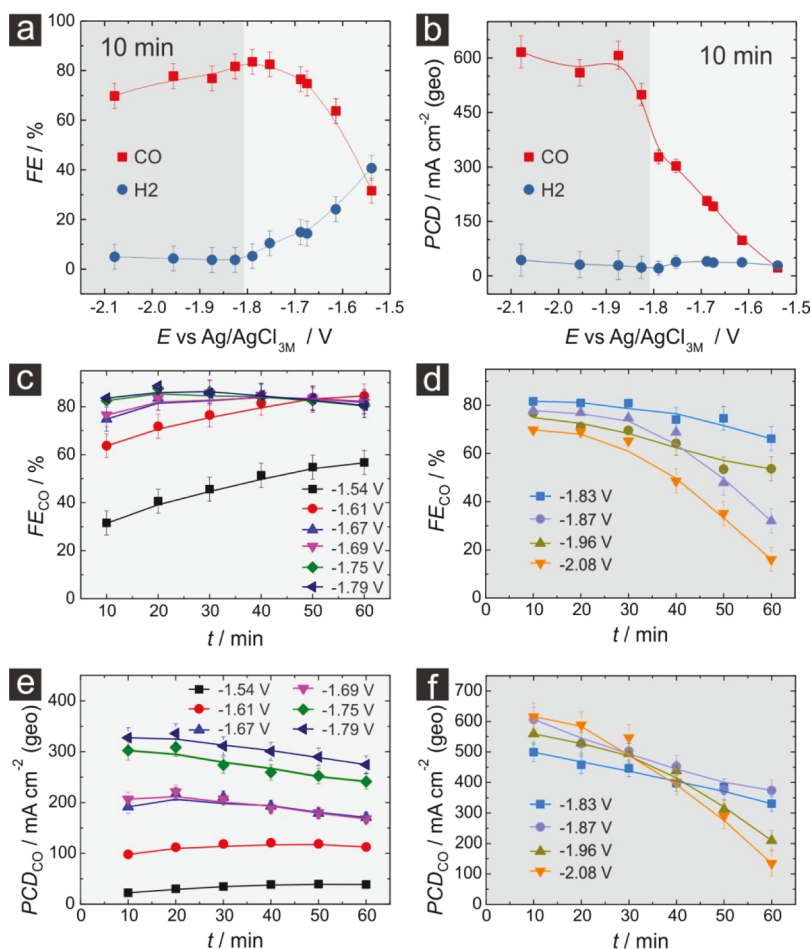
Figure 3. Potential-dependent FEs (a) and PCDs (b) of the gaseous products obtained from CO_2RR on the gas-fed Ag−NC−GDEs 10 min after beginning CO_2 electrolysis. Time evolution of the FE_{CO} at (c) mild (-1.5 V > E > -1.8 V) and (d) high applied potentials (-1.83 V > E > -2.1 V). Corresponding time evolution of the PCD_{CO} at mild (e) and high (f) applied potentials. All experiments were carried out using 2 M KOH in the anolyte compartment. The solid lines in all panels are guides to the eye to better observe the trends. The experimental error was accounted for using $\pm5\%$ error bars.

conditions. The obtained XRD patterns were analyzed and compared with JCPD (Joint Committee on Powder Diffraction) for peak assignment.

■ RESULTS AND DISCUSSION

Characterization of Ag−NC−GDEs by SEM. Figure 2 shows representative SEM images of an as-prepared Ag−NC−GDE. We present data acquired sequentially at the same position with both the BSD and InLens SE detectors of the scanning electron microscope. Clear distinction between the Ag−NCs (bright) and the supporting GDE (dark) is provided by the BSD detector, which is sensitive to the atomic number of the analyzed material (Figure 2a−c). We observe a highly dispersed sub-monolayer of Ag−NC surface coverage built up by both single Ag−NCs and sparse groups of the particles (Figure 2b,c). This observation implies that the electrochemical performance of the Ag−NC−GDEs will be partially determined by parasitic side reactions (e.g., HER) taking place also on catalyst-free regions. This is supported by the combined SEM−EDX analysis of an as-prepared Ag−NC−GDE sample displayed in Figure S1a−d. The images acquired using the InLens SE detector (Figure 2d−f) offer improved morphological resolution of single Ag−NCs and their cubic shape, which is more easily observed at large magnifications

(Figure 2e−f). Statistical analysis of more than 400 Ag−NCs provided an average edge length of 113.1 ± 10.6 nm, while XRD characterization confirmed the high crystallinity of the assembled Ag−NCs (Figure S1e,f). Recent theoretical and experimental studies in H-cell configurations have reported the superior and stable catalytic performance of cubic Ag nanoparticles compared to their octahedral and spherical counterparts.[19,20]

Electrocatalytic Performance of Ag−NC−GDEs for CO_2RR in Zero-Gap Electrolyzer. Potentiostatic CO_2RR experiments at selected applied potentials ranging between -1.55 and -2.1 V versus Ag/AgCl were conducted for 1 h using a dedicated Ag−NC−GDE as the cathode in a zero-gap gas flow-cell configuration (Figure 1b−d) for every potential. A favorable alkaline reacting environment was provided by the 2 M KOH electrolyte used in the anolyte compartment.[42] Figure 3a displays the potential-dependent product distribution of the gaseous products obtained after 10 min of CO_2 electrolysis. Besides the modest FE_{CO} observed at $E \sim -1.55$ V, all obtained FE_{CO} values at potentials more negative than -1.6 V surpassed 65%, reaching a maximum value of approximately 85% at -1.8 V. Diverging from previous reports in which an abrupt decay of FE_{CO} was observed with progressively higher potentials/current densities, only a slight decrease of CO
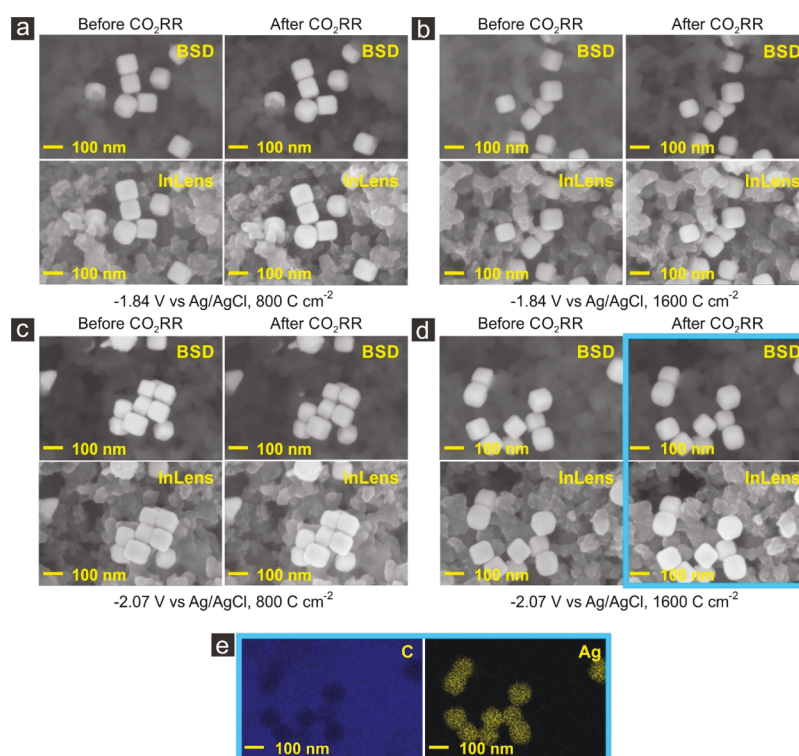
Figure 4. Representative IL−SEM images of Ag−NC−GDE cathode surfaces before and after having conducted dedicated gas-fed CO_2RR experiments at −1.84 V for (a) 30 min (800 C cm^{-2}) and (b) 60 min (1600 C cm^{-2}) and at −2.07 V for (c) 13 min (800 C cm^{-2}) and (d) 32 min (1600 C cm^{-2}) captured using both BSD and InLens SE detectors. (e) Elemental EDX mappings showing the spatial distribution of C (dark blue) and Ag (yellow) corresponding to the sample location highlighted by the blue rectangle in (d). All CO_2RR experiments were carried out using 2 M KOH in the anolyte compartment.

selectivity was detected at the harshest applied cathodic conditions due to an emerging formate contribution. However, it should be noted that in those previous reports either a bipolar membrane or a 0.5 M $KHCO_3$ buffer layer was used between the cathode and proton-exchange membrane.[32,54,55] The efficiency of parasitic H_2 stayed at FE_{H_2} levels ≤10% for potentials more negative than −1.75 V. The corresponding dependence of the partial current densities PCD_{CO} and PCD_{H_2} on the enforced potentials is shown in Figure 3b. The PCD_{CO} increases steeply as the cathodic potential increases from −1.54 to −1.87 V reaching highly competitive levels at approximately −600 mA cm^{-2} (see Table S1). Further cathodic polarization to approximately −2.1 V leads to a slightly increased PCD_{CO} reaching approximately −625 mA cm^{-2}. The PCD_{H_2} did not exceed −50 mA cm^{-2} at all applied potentials. These CO selectivities and partial current densities stand out considering that for the as-prepared Ag−NC−GDEs, a significant portion of the three-phase boundary layer where the fed CO_2, polymer electrolyte, and catalyst material meet is constituted by the unmodified MPL of the support GDEs (Figure 2a). Clearly, an increase of the catalyst loading would lead to even better CO efficiencies and activities.[31] However, it is important to remember that a low catalyst surface coverage on the GDEs was deliberately applied to successfully monitor the morphological evolution of the Ag−NC catalyst at the single nanoparticle level (see below).

Distinct temporal evolution of both FE_{CO}s and PCD_{CO}s was found to depend on the magnitude of the applied potentials. Based on the temporal stability that these values promoted, two apparent potential regimes were identified for FE_{CO} and PCD_{CO}. These regimes are highlighted by different color codes

in Figure 3. The panels corresponding to applied potentials that sustained the above-described performance throughout the duration of the experiments are highlighted by light gray rectangles (−1.5 V > E > −1.8 V). The panels highlighted in darker gray stand for results derived from applied potentials that led to the decay of FE_{CO} and PCD_{CO} values from their initial levels. Figure 3 panels c and e show that both CO selectivity and activity either improve or stay fairly stable across the lifespan of the experiments, provided that the applied potential was always less negative than −1.8 V. Conversely, when the potential surpassed this value, both CO production figures decreased over time. This decline was initially mild but intensified abruptly after 30 min with an increase of the applied potential (Figure 3 panels d and f).

Morphology Evolution of Ag−NC-Based Catalyst Induced by CO_2RR in Zero-Gap Flow Cell and H-Type Cell. To determine whether the observed decay in device performance during CO_2RR at the specific time intervals and applied potentials observed in Figure 3 panels d and f arises from morphological transformations of the cathodes (through morphological changes of the Ag−NCs or through their local rearrangement along the GDE surface), we analyzed Ag−NC− GDEs that were used for CO_2RR under those same conditions using *ex situ* SEM imaging experiments. Note that in the present study, our Ag−NC catalyst was subjected to significantly harsher cathodic conditions as compared to those reported in ref 61 reaching over two orders higher current densities and ~400 mV more cathodic potentials.

In the first attempt, we employed the so-called IL−SEM-based technique.[56,57] This analysis is meant to provide the structural evolution of electrocatalyst materials by comparing
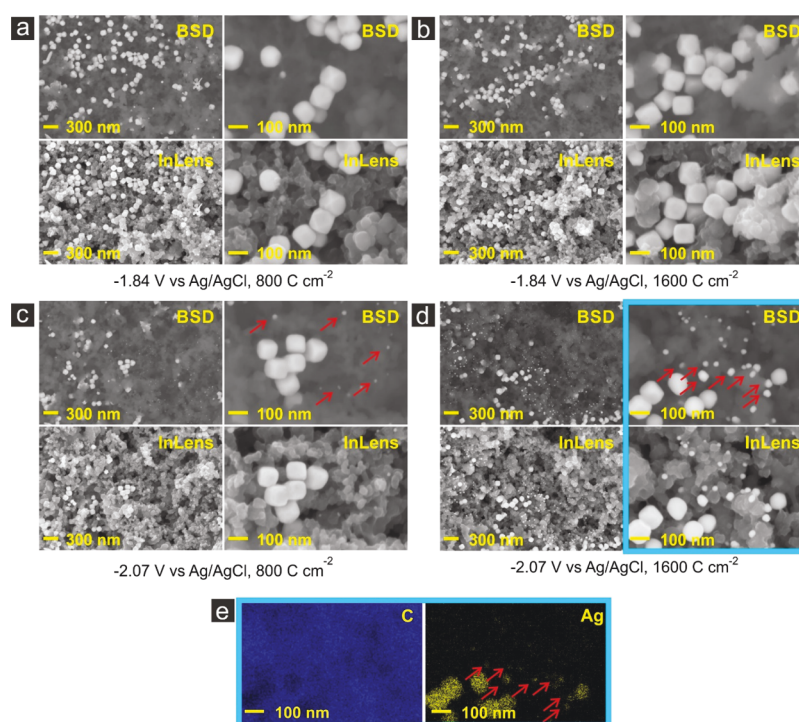
Figure 5. Representative SEM images of Ag−NC−GDE cathode surfaces after having conducted dedicated gas-fed CO_2RR experiments at −1.84 V for (a) 30 min (800 C cm^{-2}) and (b) 60 min (1600 C cm^{-2}) and at −2.07 V for (c) 13 min (800 C cm^{-2}) and (d) 32 min (1600 C cm^{-2}) captured using both BSD and InLens SE detectors. (e) Elemental EDX mappings showing the spatial distribution of C (dark blue) and Ag (yellow) of the sample location highlighted by the blue rectangle in (d). Red arrows identify Ag nanoparticles formed upon cathodic corrosion of the Ag−NC catalyst. All CO_2RR experiments were carried out using 2 M KOH in the anolyte compartment.

their morphology at the same sample location before and after being subjected to electrolysis.[56,57] We have previously employed this strategy to successfully assess structure−activity correlations caused by CO_2RR on bare porous metal electrocatalysts.[17,58] Herein, we monitored the structural evolution of Ag−NC−GDEs by IL−SEM for samples that were subjected to high cathodic potential values at which CO partial current densities reached −500 mA cm^{-2} and −620 mA cm^{-2} (−1.84 and −2.07 V, respectively). For each applied potential, the electrolysis was carried out until charge densities of 800 and 1600 C cm^{-2} were passed on dedicated Ag−NC−GDEs. These selected conditions are key for enabling insightful correlation between the SEM-based post-electrolysis studies and the data presented in Figure 3c−f.

Figure 4a−d presents representative IL−SEM images corresponding to Ag−NC−GDEs that were subjected to such CO_2RR conditions. Surprisingly, comparison of SEM images acquired before and after CO_2 electrolysis show that neither detachment nor degradation of the Ag−NCs seem to arise regardless of the specific applied potential, passed charge, or electrolysis duration. Post-electrolysis EDX mappings on sample regions that were scrutinized by IL−SEM also hint at the absence of cathodic corrosion and redeposition phenomena (compare Figures 4e and S1b,d). Furthermore, complementary IL−SEM experiments in which five sequential CO_2RR cycles were applied to a Ag−NC−GDE sample at the most stringent cathodic conditions are displayed in Figure S2. Although this sample was electrochemically stressed more severely (total cumulated Q = 13306 C cm^{-2} and t ∼ 4.5 h), the combined IL−SEM−EDX analysis showed again no apparent sample degradation. These results alone would imply, at first sight, that the developed Ag−NC−GDEs tested

in the proposed zero-gap flow cell do not undergo morphological degradation upon CO_2RR at all and that the undermined catalytic performance observed in Figure 3 at harsh cathodic conditions should originate from another failure source. However, an important aspect that did not need consideration in our previously reported IL−SEM structural CO_2RR studies and that can be the source of SEM imaging misinterpretation when studying colloidal nanocatalysts is the influence of surfactants that are left behind on their surfaces following their synthesis. Indeed, it has been shown that electron beam irradiation on nanomaterials synthesized by additive-assisted colloidal methods can lead to their improved structural stability through transformation of the adsorbed surfactants into dense carbonaceous shells.[59] Moreover, local surface passivation induced by SEM imaging has been identified on PVP-capped Ag NCs that hinders diffusion of Ag surface atoms.[60] This suggests that IL−SEM experiments might not accurately reveal the morphological evolution of colloidal catalyst materials as the initial electron irradiation conducted before the electrolysis step stabilizes and deactivates the scrutinized locations. Therefore, a second series of SEM imaging experiments were performed on the surface of Ag−NC−GDEs that were subjected to the same CO_2RR conditions as shown in Figure 4 but whose surfaces were not exposed to the electron beam of the SEM prior to the electrolysis.

Figure 5a−b displays representative images of Ag−NC−GDEs after having been subjected to −1.84 V. The Ag−NCs in panels a and b have undergone insignificant morphological changes after either 30 or 60 min of electrolysis (800 C cm^{-2} and 1600 C cm^{-2}, respectively). Furthermore, the images acquired with the BSD detector revealed the absence of
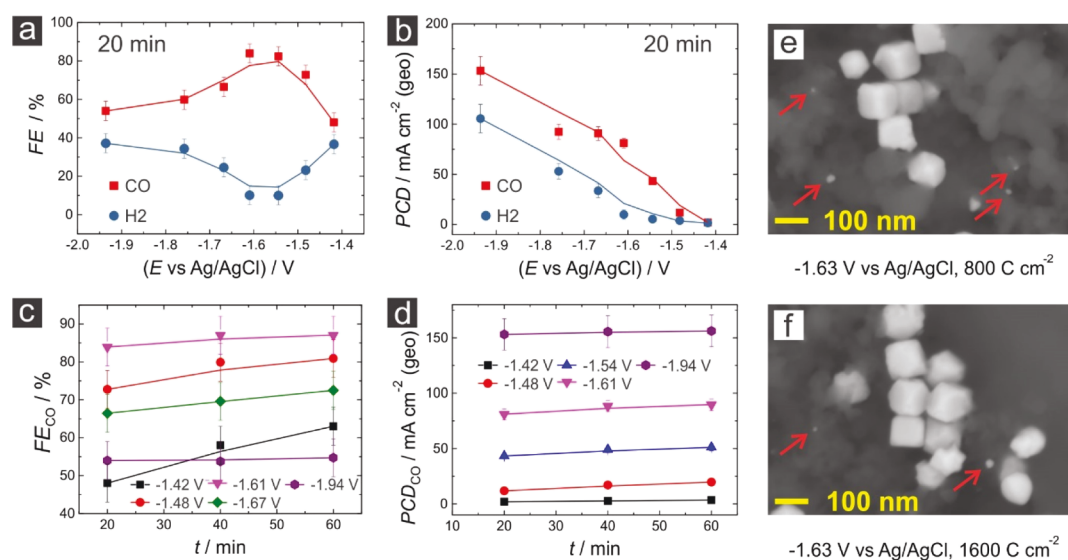
Figure 6. Potential-dependent FEs (a) and PCDs (b) obtained on the Ag−NC−GDE in the H-cell configuration. Both variables were recorded 20 min after the CO_2 electrolysis experiment was initialized. Time evolution of the FE_{CO} (c) and PCD_{CO} (d) at ($-1.42\,V \geq E \geq -1.94\,V$). Representative SEM images of cathode surfaces after having conducted dedicated CO_2RR experiments at $-1.63\,V$ for (e) 196 min (800 C cm^{-2}) and (f) 304 min (1600 C cm^{-2}). Complementary SEM images of cathode surfaces subjected to $-1.92\,V$ are shown in Figure S6. These CO_2RR experiments were carried out with an H-type cell using 2 M $KHCO_3$ as the electrolyte. The solid lines in panels (a−d) are guides to the eye to better observe the trends. The experimental error was accounted for using ±5% error bars.

material removal from the Ag−NCs that would be redeposited in the form of smaller nanoparticles along the electrode surface under the applied cathodic conditions.[61] Importantly, excellent electrochemical performance figures ($PCD_{CO} \geq 300$ mA cm^{-2} and $FE_{CO} \sim 80\%$) are attained and sustained if the potential remains just positive of this applied value (-1.8 V vs Ag/AgCl, see Figure 3 panels c and e). Because of the morphological integrity of the actual catalyst observed under these conditions, it is reasonable to think that the purely electrochemical performance of the Ag−NCs−GDEs should be sustained over long electrolysis periods if the other system parameters do not lead to failure (e.g., salt precipitation, electrolyte penetration into the adjacent GDE, etc). However, diverging from what was observed in IL−SEM analysis, the electrodes exposed to more demanding cathodic conditions revealed alteration of the Ag−NC structure that may be linked to the deterioration of PCD_{CO}s and FE_{CO}s observed in Figure 3 panels d and f. Figure 5c shows representative images of a Ag−NC−GDE cathode that underwent CO_2RR at -2.07 V for 13 min (800 C cm^{-2}). Although the Ag−NCs maintained their overall cubic appearance, the BSD−SEM images reveal smaller, randomly distributed Ag nanoparticles (<5 nm) that arise from these more stringent CO_2 electrolysis conditions. The red arrows in the upper right image of Figure 5c indicate the appearance of particles adsorbed on regions of the GDE that were not covered by the Ag−NC catalyst material prior to CO_2RR. This phenomenon was more evident on cathodes subjected to 32 min (1600 C cm^{-2}) of electrolysis. Figure 5d demonstrates that the particles formed near the Ag−NCs when treated with these longer reaction times increased not only in size (~10 nm) but also in population along the formerly catalyst-free substrate regions. This is also supported by the EDX mapping shown in Figure 5e acquired on the sample location highlighted by the blue rectangle in Figure 5d. Additionally, analysis of single Ag−NCs indicated that the material source for these electrochemically formed particles stems mainly from the cube's vertices, eventually leading to the appearance of

small (111) planes of truncated cube-like particles (Figure S3). Thus, it is clear that monitoring of the electrochemically induced morphological evolution of the colloidal catalyst is accurately described provided that the nanoparticles are not passivated by electron beam irradiation prior to electrolysis (as is the case in IL−SEM investigations). We suggest, however, that the observed mild morphological alteration of the Ag−NC catalyst on the GDE surfaces alone cannot be the physical origin for the significantly affected PCD_{CO}s and FE_{CO}s, as shown in Figure 3 panels d and f, at potentials more negative than -1.8 V.

To elucidate whether this decay in performance originates instead from the high bulk pH value (~14) of the electrolyte used, reference CO_2RR electrochemical and SEM experiments similar to those shown in Figures 3 and 5 were carried out on Ag−NC−GDEs, employing a significantly less basic 2 M $KHCO_3$ electrolyte (pH ~8). These results are displayed in Figures S4 and S5 following the same color code and image representation as of Figures 3 and 5. Figure S4a,b shows the corresponding FEs and PCDs of the electrogenerated gaseous products. Besides a slightly lower PCD_{CO} at most cathodic applied potentials (-1.86 V $\geq E \geq -2.14$ V), all other displayed quantities (PCD_{H2}, FE_{CO}, and FE_{H2}) exhibited the same qualitative potential- and time-dependent behaviors after 10 min CO_2 electrolysis, as discussed above, when the 2 M KOH electrolyte was used (compare Figure 3c−f with Figure S4c−f). The reduction in PCD_{CO} at high applied potentials might be related to the lower ionic conductivity of the HCO_3^- ion in comparison to that of OH^- and its relative deficiency to lower the CO_2 activation energy barrier.[42] Interestingly, suppression of the parasitic HER was equally effective when using both supporting electrolytes. The fact that the temporal dependence of FE_{CO} and PCD_{CO} as the electrolysis proceeded revealed again a stability bifurcation that depended on the potential window examined (Figure S4c−f) but not on the specific bulk pH is not surprising. Indeed, it has been predicted that the local pH adjacent to the three-phase boundary layer of

a gas-fed GDE at CO_2RR reaction rates above 50 mA cm^{-2} becomes rather similar for both neutral and highly alkaline electrolytes due to the driven cathode half reactions (both CO_2 and water reduction generate OH$^-$ as a byproduct).[30] The difference in the local pH at the cathode between both electrolyte solutions under CO_2RR reacting conditions at targeted $j_s \geq$ 200 mA cm^{-2} might actually be negligible.[30] Similar to the experiments conducted in the 2 M KOH electrolyte, as shown in Figure 5, SEM analysis of a Ag−NC−GDE after 60 min CO_2RR at mild applied potential ($E = $ −1.84 V, 1600 C cm^{-2}) in 2 M KHCO$_3$ showed minor structural degradation of the Ag−NCs (Figure S5). This finding suggests that the performance decay in our gas-fed zero-gap flow cell at large CO_2RR rates might be more significantly influenced by the increased local alkalinity rather than the relatively minor structural degradation of the Ag−NCs and the original bulk pH. Furthermore, an increasingly high alkalinity at the three-boundary layer in GDEs has been found to lead to issues related to electrolyte carbonation, electrolyte penetration through the GDE body (electrode flooding), and salt precipitation.[39,43,44,49,51] Electrolyte intrusion beyond the MPL of the Ag−NC−GDEs at high cathodic potentials also contributes to the decay in FE$_{CO}$ and PCD$_{CO}$, as observed in Figure 3d,f and S4d,f, due to an increase of the CO_2 diffusion length. This is in agreement with recently reported work by Leonard et al.[43] who observed a clear increase of flooding propensity and loss of the nominal MPL hydrophobicity under stringent CO_2RR reductive conditions.

To further support this argument, we resorted to investigations performed in conventional H-cell configurations in which none of these detrimental aspects would influence the supply of dissolved CO_2 to the cathode through the liquid electrolyte. Figure 6a,b summarizes these experimental results. In comparison to the gas-fed experiments, significantly lower PCD$_{CO}$s are observed in all of the inspected potential window due to the dominant effect of the mass transport limitations of CO_2 dissolved in the used 2 M KHCO$_3$ electrolyte. In addition, the use of this non-optimal,[9,21−24] almost neutral electrolyte leads to larger PCD$_{H2}$s (as great as PCD$_{H2} \sim$ 100mA cm^{-2}) at high cathodic potentials relative to the values observed in the zero-gap experiments. The potential-dependent product selectivity shows an increase of FE$_{CO}$ as the potential varied from low to mild applied values (−1.4 V $\geq E \geq$ −1.6 V), although in contrast to the observed trends for the more technical approach, the CO efficiency significantly decreases as the competing HER benefits at more negative values. Moreover, in contrast to the results from the zero-gap experiments, neither FE$_{CO}$ nor PCD$_{CO}$ decays from its initial value as the electrolysis reaction proceeds, regardless of the applied potential (Figure 6c,d). Considering that the Ag−NCs used in these H-cell experiments seem to have undergone a similar degree of degradation and associated mechanism at mild and high applied potentials relative to that of the zero-gap counterparts (Figures 6e−f and S6), it seems evident that the system stability issues acting at high potentials and longer electrolysis times in the gas-fed configuration stem mainly from a sub-optimal reactor design and the high local alkalinity at high current densities. Indeed, we found a clear correlation between the decaying FE$_{CO}$ and PCD$_{CO}$ and occurrence of GDE flooding and salt precipitation, which cause device performance failure at high cathodic potentials in the gas-fed approach. Figure S7a,b shows typical contact angle images for

water droplets on Ag−NC−GDEs before and after being submitted to CO_2RR at −2.07 V for 32 min. The decrease of contact angle indicates that the barrier properties of the MPL are to some extent undermined upon electrolysis. The corresponding EDX spectra additionally show a clear decay of the F signal due to degradation of the hydrophobic PTFE coating of the MPL (Figure S7c). Moreover, Figure S8a presents optical images showing the typical appearance of the employed GDEs at different experimental stages (as-received GDE, as-prepared Ag−NC−GDE and Ag−NC−GDE after having sustained CO_2RR at −2.07 V for 32 min and 1600 C cm^{-2}). The EDX spectra and mapping displayed in Figure S8b,c further support that, under these drastic cathodic conditions, carbonate/bicarbonate precipitation on the catalyst-modified GDE surface and its periphery takes place. Additionally, Figures S9 and S10 show that these undesired events (flooding and precipitation) can even be observed on the backside of such electrodes, irrespectively of the employed electrolyte. We would like to emphasize that this kind of massive salt precipitation is only observed in the GDE approach, irrespective of the used electrolyte, but not in the H-type cell configuration where the partial current densities of CO formation are mass transport limited and remain stable during electrolysis.

Comparison of CO_2RR Product Distribution in Zero-Gap Flow Cell and H-Type Cell. Finally, another important aspect that requires attention is the spectrum of products yielded from CO_2RR processes, which might also be affected by the specificities of the experimental approach employed (cell design and environment).[62] Along these lines, fundamental differences regarding the product selectivity were observed between the gas-fed- and H-cell-based approaches. As illustrated in Figure S11, formate was detected as a CO_2 electrolysis product over a large potential window using alkaline as well as almost basic electrolytes when the zero-gap testbed was used. This finding is in agreement with reports by Sargent, Sinton et al. on increased formate production on Ag−GDEs in highly alkaline aqueous environments (Figure 1a).[40] These authors proposed that the enhanced formate production when using highly alkaline environments adjacent to the Ag−GDE might be due to the limited ability of a temporary H$_3$O$^+$ molecule that is believed to assist the first protonation step of the adsorbed *COOH intermediate on the CO reaction pathway.[63] Accordingly, Figure S11 shows that both FE$_{HCOO^-}$ and PCD$_{HCOO^-}$ were more prominent when the hydroxide-based solution was employed and peaked at $E \sim$ −1.87 V, amounting to non-negligible values of FE$_{HCOO^-} \sim$20.1% and PCD$_{HCOO^-} \sim$148 mA cm^{-2}, respectively. This result agrees with a recent report by Seger et al. who identified formate as a significant CO_2RR side reaction using a zero-gap electrolyzer combined with a basic anolyte at high current densities ≥200 mA cm^{-2}.[46] Conversely, our experiments in the H-cell yielded only a minor formate contribution at the highest applied potential (FE$_{HCOO^-} \sim$2.6% and PCD$_{HCOO^-} \sim$7.5 mA cm^{-2}). This result underlines the fact that the vast knowledge developed through batch-type CO_2RR experiments does not necessarily translate to more practical approaches aimed at industrial CO_2 reduction. Therefore, more effort must be devoted to understanding the particularities inherent to gas-fed CO_2RR platforms by going beyond a purely catalyst development-oriented approach and focusing more on rational electrolyzer design, engineering solutions, and process optimization to provide more robust and stable gas−liquid

interfaces. Precipitation and flooding phenomena might, for instance, be prevented through incorporation of application-tailored microstructures and wettability into novel GDE designs.[43] Encouraging efforts in this direction are being made, for instance, by Schmid et al.[64] who have recently addressed the importance of optimized operating modes, electrolyzer design, and materials selection that enable nearly practical scale electrochemical CO_2-to-CO conversion. One key finding of these investigations that enables stable and long-term CO_2RR operation at -200 mA cm^{-2} is the attenuation of salt precipitation, GDE flooding, and CO_2 crossover to the anode compartment by utilizing a carbonate-free, sulfate-based neutral electrolyte in a liquid flow-cell electrolyzer.

◼ CONCLUSIONS

We studied the performance of a model Ag–NC catalyst for CO_2RR to carbon monoxide on technical GDE in a zero-gap configuration and highly alkaline environments. The system exhibited remarkable CO_2 to CO conversion figures in terms of FE and PCD (FE$_{CO}$ ~ 625 mA cm^{-2} and PCD$_{CO}$ ~ 85%) even at sub-monolayer Ag–NC catalyst coverages on the GDEs. Based on the temporal system stability that they promoted, two apparent potential regimes were identified for FE$_{CO}$ and PCD$_{CO}$. At mild applied potentials (-1.5 V > E vs Ag/AgCl > -1.8 V), the CO_2RR process improved or remained stable over time reaching PCD$_{CO}$s > 300 mA cm^{-2} and FE ~ 85%. However, at greater cathodic potentials, both CO production figures were initially more prominent but then weakened over time. This decline was initially mild but intensified abruptly after ~30 min with increasing applied potential. The morphological evolution of the Ag–NCs on the GDEs induced by the CO_2RR as well as the direct mechanical contact between the catalyst layer and anion-exchange membrane was analyzed by IL–SEM and post-electrolysis SEM investigations. The former approach turned out to be unsuitable for structural characterization of electrolysis-induced changes on colloidal catalysts that bear a surfactant shell on their surface left behind from the synthesis method. On the other hand, post-electrolysis SEM studies enabled the true morphological evolution of the catalyst that strongly depended on the applied electrolysis conditions. Regardless of the applied experimental conditions, no detachment of Ag–NC particles from the GDEs was detected. It was found that at low and mild potentials, the Ag–NCs undergo insignificant morphological alteration. However, at harsher cathodic conditions, smaller Ag nanoparticles begin to appear, adsorbed on formerly catalyst-free substrate regions. The material source of these electrochemically generated nanoparticles seems to come from the corners of the Ag–NCs. The observed mild cathodic corrosion of the catalyst leads to slightly truncated cube morphologies. However, complementary CO_2RR experiments in a neutral environment on Ag–NC–GDEs conducted in both zero-gap and conventional H-type cell configurations suggest that system failure is rooted in more factors than the observed morphological degradation of the catalyst. That is, the high alkalinity level at the three-phase boundary layer where the fed CO_2, catalyst material, and polymer electrolyte meet leads, to a significant degree, to the observed CO_2RR performance decline. The high alkalinity level inevitably develops at the reaction interface in the zero-gap electrolyzers at high cathodic reaction rates >300 mA cm^{-2} even when the starting bulk electrolyte is neutral, thereby causing electrolyte percolation through the GDEs, electrode flooding, and salt

precipitation. Thus, this work enables the deconvolution of catalyst structural stability from system performance stability. Although the application of higher catalyst loadings on the GDEs would probably alleviate these issues, a more robust, long-lasting solution to the intrinsic challenges posed by gas-fed approaches must be proposed to near industrial CO_2RR deployment. Finally, as stated by some other recent works, we suggest that CO_2RR studies should increasingly be performed using technical approaches because the conclusions extracted from H-type cell experiments might not be directly translatable to electrolyzer-based studies.

◼ ASSOCIATED CONTENT

Ⓢ Supporting Information

The Supporting Information is available free of charge at https://pubs.acs.org/doi/10.1021/acscatal.0c03609.

> SEM, EDX, XRD, and edge size distribution of Ag–NCs; literature survey on CO_2RR to CO on Ag–GDEs; IL–SEM of Ag–NC–GDEs subjected to zero-gap CO_2RR in 2 M KOH; SEM image of single Ag–NCs after zero-gap CO_2RR in 2 M KOH at high cathodic potentials; potential-dependent FEs and PCDs from zero-gap CO_2RR in 2 M KHCO$_3$; SEM imaging of Ag–NCs–GDEs after zero-gap CO_2RR in 2 M KHCO$_3$; SEM imaging of Ag–NCs–GDEs after CO_2RR in H-type cell; optical micrographs of employed GDEs at different experimental stages and EDX characterization of a Ag–NC–GDE after CO_2RR in 2 M KOH at stringent cathodic conditions; potential-dependent FE$_{HCOO^-}$ and PCD$_{HCOO^-}$ from zero-gap CO_2RR in 2 M KOH and 2 M KHCO$_3$; and complete database of all experiments (PDF)

◼ AUTHOR INFORMATION

Corresponding Authors

Pavel Moreno-García — *Department of Chemistry and Biochemistry, University of Bern, Bern 3012, Switzerland;* ⓞ orcid.org/0000-0002-6827-787X; Email: pavel.moreno@dcb.unibe.ch

Peter Broekmann — *Department of Chemistry and Biochemistry, University of Bern, Bern 3012, Switzerland;* ⓞ orcid.org/0000-0002-6287-1042; Email: peter.broekmann@dcb.unibe.ch

Authors

María de Jesús Gálvez-Vázquez — *Department of Chemistry and Biochemistry, University of Bern, Bern 3012, Switzerland*

Heng Xu — *Department of Chemistry, Duke University, Durham, North Carolina 27708-0354, United States*

Yuhui Hou — *Department of Chemistry and Biochemistry, University of Bern, Bern 3012, Switzerland;* ⓞ orcid.org/0000-0003-1616-562X

Huifang Hu — *Department of Chemistry and Biochemistry, University of Bern, Bern 3012, Switzerland*

Iván Zelocualtecatl Montiel — *Department of Chemistry and Biochemistry, University of Bern, Bern 3012, Switzerland*

Alexander V. Rudnev — *Department of Chemistry and Biochemistry, University of Bern, Bern 3012, Switzerland; A.N. Frumkin Institute of Physical Chemistry and Electrochemistry Russian Academy of Sciences, Moscow 119071, Russia*

Shima Alinejad — *Department of Chemistry and Biochemistry, University of Bern, Bern 3012, Switzerland;* orcid.org/0000-0002-1151-3333

Vitali Grozovski — *Department of Chemistry and Biochemistry, University of Bern, Bern 3012, Switzerland*

Benjamin J. Wiley — *Department of Chemistry, Duke University, Durham, North Carolina 27708-0354, United States;* orcid.org/0000-0002-1314-6223

Matthias Arenz — *Department of Chemistry and Biochemistry, University of Bern, Bern 3012, Switzerland;* orcid.org/0000-0001-9765-4315

Complete contact information is available at:
https://pubs.acs.org/10.1021/acscatal.0c03609

Author Contributions

[⊥]M.J.G.-V. and P.M.G. contributed equally. The manuscript was written through contributions of all authors. All authors have given approval to the final version of the manuscript.

Notes

The authors declare no competing financial interest.

REFERENCES

(1) Vennekoetter, J.-B.; Sengpiel, R.; Wessling, M. Beyond the catalyst: How electrode and reactor design determine the product spectrum during electrochemical CO_2 reduction. *Chem. Eng. J.* **2019**, *364*, 89−101.

(2) Wang, Y.; Xia, Q.; Bai, X.; Ge, Z.; Yang, Q.; Yin, C.; Kang, S.; Dong, M.; Li, X. Carbothermal activation synthesis of 3D porous g-C_3N_4/carbon nanosheets composite with superior performance for CO_2 photoreduction. *Appl. Catal., B* **2018**, *239*, 196−203.

(3) Jhong, H.-R. M.; Ma, S.; Kenis, P. J. Electrochemical conversion of CO_2 to useful chemicals: current status, remaining challenges, and future opportunities. *Curr. Opin. Chem. Eng.* **2013**, *2*, 191−199.

(4) Seh, Z. W.; Kibsgaard, J.; Dickens, C. F.; Chorkendorff, I.; Nørskov, J. K.; Jaramillo, T. F. Combining theory and experiment in electrocatalysis: Insights into materials design. *Science* **2017**, *355*, No. eaad4998.

(5) Kibria, M. G.; Edwards, J. P.; Gabardo, C. M.; Dinh, C. T.; Seifitokaldani, A.; Sinton, D.; Sargent, E. H. Electrochemical CO_2 Reduction into Chemical Feedstocks: From Mechanistic Electrocatalysis Models to System Design. *Adv. Mater.* **2019**, *31*, 1807166.

(6) Fan, M.; Prabhudev, S.; Garbarino, S.; Qiao, J.; Botton, G. A.; Harrington, D. A.; Tavares, A. C.; Guay, D. Uncovering the Nature of Electroactive Sites in Nano Architectured Dendritic Bi for Highly Efficient CO_2 Electroreduction to Formate. *Appl. Catal., B* **2020**, *274*, 119031.

(7) Hori, Y. *Electrochemical CO2 Reduction on Metal Electrodes in Modern Aspects of Electrochemistry*; Springer: NY, 2008; p 89−189.

(8) Bushuyev, O. S.; De Luna, P.; Dinh, C. T.; Tao, L.; Saur, G.; van de Lagemaat, J.; Kelley, S. O.; Sargent, E. H. What Should We Make with CO_2 and How Can We Make It? *Joule* **2018**, *2*, 825−832.

(9) Jouny, M.; Luc, W.; Jiao, F. High-rate electroreduction of carbon monoxide to multi-carbon products. *Nat. Catal.* **2018**, *1*, 748−755.

(10) Haas, T.; Krause, R.; Weber, R.; Demler, M.; Schmid, G. Technical photosynthesis involving CO_2 electrolysis and fermentation. *Nat. Catal.* **2018**, *1*, 32−39.

(11) Ma, S.; Liu, J.; Sasaki, K.; Lyth, S. M.; Kenis, P. J. A. Carbon Foam Decorated with Silver Nanoparticles for Electrochemical CO_2 Conversion. *Energy Technol.* **2017**, *5*, 861−863.

(12) Dutta, A.; Morstein, C. E.; Rahaman, M.; Cedeño López, A.; Broekmann, P. Beyond Copper in CO_2 Electrolysis: Effective Hydrocarbon Production on Silver-Nanofoam Catalysts. *ACS Catal.* **2018**, *8*, 8357−8368.

(13) Hatsukade, T.; Kuhl, K. P.; Cave, E. R.; Abram, D. N.; Jaramillo, T. F. Insights into the electrocatalytic reduction of CO_2 on metallic silver surfaces. *Phys. Chem. Chem. Phys.* **2014**, *16*, 13814−13819.

(14) Chen, Y.; Li, C. W.; Kanan, M. W. Aqueous CO_2 Reduction at Very Low Overpotential on Oxide-Derived Au Nanoparticles. *J. Am. Chem. Soc.* **2012**, *134*, 19969−19972.

(15) Nursanto, E. B.; Jeon, H. S.; Kim, C.; Jee, M. S.; Koh, J. H.; Hwang, Y. J.; Min, B. K. Gold catalyst reactivity for CO_2 electroreduction: From nano particle to layer. *Catal. Today* **2016**, *260*, 107−111.

(16) Won, D. H.; Shin, H.; Koh, J.; Chung, J.; Lee, H. S.; Kim, H.; Woo, S. I. Highly Efficient, Selective, and Stable CO_2 Electroreduction on a Hexagonal Zn Catalyst. *Angew. Chem., Int. Ed.* **2016**, *55*, 9297−9300.

(17) Moreno-García, P.; Schlegel, N.; Zanetti, A.; Cedeño López, A.; Gálvez-Vázquez, M. d. J.; Dutta, A.; Rahaman, M.; Broekmann, P. Selective Electrochemical Reduction of CO_2 to CO on Zn-Based Foams Produced by Cu^{2+} and Template-Assisted Electrodeposition. *ACS Appl. Mater. Interfaces* **2018**, *10*, 31355−31365.

(18) Luo, W.; Zhang, Q.; Zhang, J.; Moioli, E.; Zhao, K.; Züttel, A. Electrochemical reconstruction of ZnO for selective reduction of CO_2 to CO. *Appl. Catal., B* **2020**, *273*, 119060.

(19) Yang, M.; Zhang, J.; Cao, Y.; Wu, M.; Qian, K.; Zhang, Z.; Liu, H.; Wang, J.; Chen, W.; Huang, W. Facet Sensitivity of Capping Ligand-Free Ag Crystals in CO_2 Electrochemical Reduction to CO. *ChemCatChem* **2018**, *10*, 5128−5134.

(20) Liu, S.; Tao, H.; Zeng, L.; Liu, Q.; Xu, Z.; Liu, Q.; Luo, J.-L. Shape-Dependent Electrocatalytic Reduction of CO_2 to CO on Triangular Silver Nanoplates. *J. Am. Chem. Soc.* **2017**, *139*, 2160−2163.

(21) Dinh, C.-T.; Burdyny, T.; Kibria, M. G.; Seifitokaldani, A.; Gabardo, C. M.; García de Arquer, F. P.; Kiani, A.; Edwards, J. P.; De Luna, P.; Bushuyev, O. S.; Zou, C.; Quintero-Bermudez, R.; Pang, Y.; Sinton, D.; Sargent, E. H. CO_2 electroreduction to ethylene via hydroxide-mediated copper catalysis at an abrupt interface. *Science* **2018**, *360*, 783−787.

(22) Hoang, T. T. H.; Verma, S.; Ma, S.; Fister, T. T.; Timoshenko, J.; Frenkel, A. I.; Kenis, P. J. A.; Gewirth, A. A. Nanoporous Copper−Silver Alloys by Additive-Controlled Electrodeposition for the Selective Electroreduction of CO_2 to Ethylene and Ethanol. *J. Am. Chem. Soc.* **2018**, *140*, 5791−5797.

(23) Kim, B.; Hillman, F.; Ariyoshi, M.; Fujikawa, S.; Kenis, P. J. A. Effects of composition of the micro porous layer and the substrate on performance in the electrochemical reduction of CO_2 to CO. *J. Power Sources* **2016**, *312*, 192−198.

(24) Liu, M.; Pang, Y.; Zhang, B.; De Luna, P.; Voznyy, O.; Xu, J.; Zheng, X.; Dinh, C. T.; Fan, F.; Cao, C.; de Arquer, F. P. G.; Safaei, T. S.; Mepham, A.; Klinkova, A.; Kumacheva, E.; Filleter, T.; Sinton, D.; Kelley, S. O.; Sargent, E. H. Enhanced electrocatalytic CO_2 reduction via field-induced reagent concentration. *Nature* **2016**, *537*, 382−386.

(25) Liu, Z.; Yang, H.; Kutz, R.; Masel, R. I. CO_2 Electrolysis to CO and O_2 at High Selectivity, Stability and Efficiency Using Sustainion Membranes. *J. Electrochem. Soc.* **2018**, *165*, J3371−J3377.

(26) Kas, R.; Hummadi, K. K.; Kortlever, R.; de Wit, P.; Milbrat, A.; Luiten-Olieman, M. W. J.; Benes, N. E.; Koper, M. T. M.; Mul, G. Three-dimensional porous hollow fibre copper electrodes for efficient

and high-rate electrochemical carbon dioxide reduction. *Nat. Commun.* **2016**, *7*, 10748.

(27) Ma, S.; Sadakiyo, M.; Luo, R.; Heima, M.; Yamauchi, M.; Kenis, P. J. A. One-step electrosynthesis of ethylene and ethanol from CO₂ in an alkaline electrolyzer. *J. Power Sources* **2016**, *301*, 219−228.

(28) Moreno-García, P.; Kovács, N.; Grozovski, V.; Gálvez-Vázquez, M. d. J.; Vesztergom, S.; Broekmann, P. Toward CO₂ Electroreduction under Controlled Mass Flow Conditions: A Combined Inverted RDE and Gas Chromatography Approach. *Anal. Chem.* **2020**, *92*, 4301−4308.

(29) Kim, C.; Dionigi, F.; Beermann, V.; Wang, X.; Möller, T.; Strasser, P. Alloy Nanocatalysts for the Electrochemical Oxygen Reduction (ORR) and the Direct Electrochemical Carbon Dioxide Reduction Reaction (CO₂RR). *Adv. Mater.* **2019**, *31*, 1805617.

(30) Burdyny, T.; Smith, W. A. CO₂ reduction on gas-diffusion electrodes and why catalytic performance must be assessed at commercially-relevant conditions. *Energy Environ. Sci.* **2019**, *12*, 1442−1453.

(31) De Gregorio, G. L.; Burdyny, T.; Loiudice, A.; Iyengar, P.; Smith, W. A.; Buonsanti, R. Facet-dependent selectivity of Cu catalysts in electrochemical CO₂ reduction at commercially viable current densities. *ACS Catal.* **2020**, *10*, 4854−4862.

(32) Delacourt, C.; Ridgway, P. L.; Kerr, J. B.; Newman, J. Design of an Electrochemical Cell Making Syngas (CO+H₂) from CO₂ and H₂O Reduction at Room Temperature. *J. Electrochem. Soc.* **2008**, *155*, B42.

(33) Dufek, E. J.; Lister, T. E.; McIlwain, M. E. Bench-scale electrochemical system for generation of CO and syn-gas. *J. Appl. Electrochem.* **2011**, *41*, 623−631.

(34) Higgins, D.; Hahn, C.; Xiang, C.; Jaramillo, T. F.; Weber, A. Z. Gas-Diffusion Electrodes for Carbon Dioxide Reduction: A New Paradigm. *ACS Energy Lett.* **2019**, *4*, 317−324.

(35) Weekes, D. M.; Salvatore, D. A.; Reyes, A.; Huang, A.; Berlinguette, C. P. Electrolytic CO₂ Reduction in a Flow Cell. *Acc. Chem. Res.* **2018**, *51*, 910−918.

(36) Gálvez-Vázquez, M. d. J.; Alinejad, S.; Hu, H.; Hou, Y.; Moreno-García, P.; Zana, A.; Wiberg, G. K. H.; Broekmann, P.; Arenz, M. Testing a Silver Nanowire Catalyst for the Selective CO₂ Reduction in a Gas Diffusion Electrode Half-cell Setup Enabling High Mass Transport Conditions. *Chimia* **2019**, *73*, 922−927.

(37) Verma, S.; Lu, X.; Ma, S.; Masel, R. I.; Kenis, P. J. A. The effect of electrolyte composition on the electroreduction of CO₂ to CO on Ag based gas diffusion electrodes. *Phys. Chem. Chem. Phys.* **2016**, *18*, 7075−7084.

(38) Verma, S.; Hamasaki, Y.; Kim, C.; Huang, W.; Lu, S.; Jhong, H.-R. M.; Gewirth, A. A.; Fujigaya, T.; Nakashima, N.; Kenis, P. J. A. Insights into the Low Overpotential Electroreduction of CO₂ to CO on a Supported Gold Catalyst in an Alkaline Flow Electrolyzer. *ACS Energy Lett.* **2018**, *3*, 193−198.

(39) Dinh, C.-T.; García de Arquer, F. P.; Sinton, D.; Sargent, E. H. High Rate, Selective, and Stable Electroreduction of CO₂ to CO in Basic and Neutral Media. *ACS Energy Lett.* **2018**, *3*, 2835−2840.

(40) Gabardo, C. M.; Seifitokaldani, A.; Edwards, J. P.; Dinh, C.-T.; Burdyny, T.; Kibria, M. G.; O'Brien, C. P.; Sargent, E. H.; Sinton, D. Combined high alkalinity and pressurization enable efficient CO₂ electroreduction to CO. *Energy Environ. Sci.* **2018**, *11*, 2531−2539.

(41) Dufek, E. J.; Lister, T. E.; McIlwain, M. E. Influence of Electrolytes and Membranes on Cell Operation for Syn-Gas Production. *Electrochem. Solid-State Lett.* **2012**, *15*, B48.

(42) Bhargava, S. S.; Proietto, F.; Azmoodeh, D.; Cofell, E. R.; Henckel, D. A.; Verma, S.; Brooks, C. J.; Gewirth, A. A.; Kenis, P. J. A. System Design Rules for Intensifying the Electrochemical Reduction of CO₂ to CO on Ag Nanoparticles. *ChemElectroChem* **2020**, *7*, 2001−2011.

(43) Leonard, M. E.; Clarke, L. E.; Forner-Cuenca, A.; Brown, S. M.; Brushett, F. R. Investigating Electrode Flooding in a Flowing Electrolyte, Gas-Fed Carbon Dioxide Electrolyzer. *ChemSusChem* **2020**, *13*, 400−411.

(44) Pătru, A.; Binninger, T.; Pribyl, B.; Schmidt, T. J. Design Principles of Bipolar Electrochemical Co-Electrolysis Cells for Efficient Reduction of Carbon Dioxide from Gas Phase at Low Temperature. *J. Electrochem. Soc.* **2019**, *166*, F34−F43.

(45) Ma, M.; Clark, E. L.; Therkildsen, K. T.; Dalsgaard, S.; Chorkendorff, I.; Seger, B. Insights into the carbon balance for CO₂ electroreduction on Cu using gas diffusion electrode reactor designs. *Energy Environ. Sci.* **2020**, *13*, 977−985.

(46) Larrazábal, G. O.; Strøm-Hansen, P.; Heli, J. P.; Zeiter, K.; Therkildsen, K. T.; Chorkendorff, I.; Seger, B. Analysis of Mass Flows and Membrane Cross-over in CO₂ Reduction at High Current Densities in an MEA-Type Electrolyzer. *ACS Appl. Mater. Interfaces* **2019**, *11*, 41281−41288.

(47) Liu, Z.; Masel, R. I.; Chen, Q.; Kutz, R.; Yang, H.; Lewinski, K.; Kaplun, M.; Luopa, S.; Lutz, D. R. Electrochemical generation of syngas from water and carbon dioxide at industrially important rates. *J. CO2 Util.* **2016**, *15*, 50−56.

(48) Kutz, R. B.; Chen, Q.; Yang, H.; Sajjad, S. D.; Liu, Z.; Masel, I. R. Sustainion Imidazolium-Functionalized Polymers for Carbon Dioxide Electrolysis. *Energy Technol.* **2017**, *5*, 929−936.

(49) Weng, L.-C.; Bell, A. T.; Weber, A. Z. Towards membrane-electrode assembly systems f or CO₂ reduction: a modeling study. *Energy Environ. Sci.* **2019**, *12*, 1950−1968.

(50) Yin, Z.; Peng, H.; Wei, X.; Zhou, H.; Gong, J.; Huai, M.; Xiao, L.; Wang, G.; Lu, J.; Zhuang, L. An alkaline polymer electrolyte CO₂ electrolyzer operated with pure water. *Energy Environ. Sci.* **2019**, *12*, 2455−2462.

(51) Jeanty, P.; Scherer, C.; Magori, E.; Wiesner-Fleischer, K.; Hinrichsen, O.; Fleischer, M. Upscaling and continuous operation of electrochemical CO₂ to CO conversion in aqueous solutions on silver gas diffusion electrodes. *J. CO2 Util.* **2018**, *24*, 454−462.

(52) Wiley, B.; Sun, Y.; Xia, Y. Polyol Synthesis of Silver Nanostructures: Control of Product Morphology with Fe(II) or Fe(III) Species. *Langmuir* **2005**, *21*, 8077−8080.

(53) Skrabalak, S. E.; Au, L.; Li, X.; Xia, Y. Facile synthesis of Ag nanocubes and Au nanocages. *Nat. Protoc.* **2007**, *2*, 2182−2190.

(54) Li, Y. C.; Zhou, D.; Yan, Z.; Gonçalves, R. H.; Salvatore, D. A.; Berlinguette, C. P.; Mallouk, T. E. Electrolysis of CO2 to Syngas in Bipolar Membrane-Based Electrochemical Cells. *ACS Energy Lett.* **2016**, *1*, 1149−1153.

(55) Salvatore, D. A.; Weekes, D. M.; He, J.; Dettelbach, K. E.; Li, Y. C.; Mallouk, T. E.; Berlinguette, C. P. Electrolysis of Gaseous CO₂ to CO in a Flow Cell with a Bipolar Membrane. *ACS Energy Lett.* **2018**, *3*, 149−154.

(56) Mayrhofer, K. J. J.; Meier, J. C.; Ashton, S. J.; Wiberg, G. K. H.; Kraus, F.; Hanzlik, M.; Arenz, M. Fuel cell catalyst degradation on the nanoscale. *Electrochem. Commun.* **2008**, *10*, 1144−1147.

(57) Hodnik, N.; Zorko, M.; Bele, M.; Hočevar, S.; Gaberšček, M. Identical Location Scanning Electron Microscopy: A Case Study of Electrochemical Degradation of PtNi Nanoparticles Using a New Nondestructive Method. *J. Phys. Chem. C* **2012**, *116*, 21326−21333.

(58) Rahaman, M.; Dutta, A.; Zanetti, A.; Broekmann, P. Electrochemical Reduction of CO₂ into Multicarbon Alcohols on Activated Cu Mesh Catalysts: An Identical Location (IL) Study. *ACS Catal.* **2017**, *7*, 7946−7956.

(59) Luo, B.; Fang, Y.; Li, J.; Huang, Z.; Hu, B.; Zhou, J. Improved Stability of Metal Nanowires via Electron Beam Irradiation Induced Surface Passivation. *ACS Appl. Mater. Interfaces* **2019**, *11*, 12195−12201.

(60) Tan, S. F.; Bosman, M.; Nijhuis, C. A. Molecular Coatings for Stabilizing Silver and Gold Nanocubes under Electron Beam Irradiation. *Langmuir* **2017**, *33*, 1189−1196.

(61) Huang, J.; Hörmann, N.; Oveisi, E.; Loiudice, A.; De Gregorio, G. L.; Andreussi, O.; Marzari, N.; Buonsanti, R. Potential-induced nanoclustering of metallic catalysts during electrochemical CO₂ reduction. *Nat. Commun.* **2018**, *9*, 3117.

(62) Wang, G.; Pan, J.; Jiang, S. P.; Yang, H. Gas phase electrochemical conversion of humidified CO₂ to CO and H₂ on proton-exchange and alkaline anion-exchange membrane fuel cell reactors. *J. CO2 Util.* **2018**, *23*, 152−158.

(63) Seifitokaldani, A.; Gabardo, C. M.; Burdyny, T.; Dinh, C.-T.; Edwards, J. P.; Kibria, M. G.; Bushuyev, O. S.; Kelley, S. O.; Sinton, D.; Sargent, E. H. Hydronium-Induced Switching between CO_2 Electroreduction Pathways. *J. Am. Chem. Soc.* **2018**, *140*, 3833−3837.

(64) Reinisch, D.; Schmid, B.; Martić, N.; Krause, R.; Landes, H.; Hanebuth, M.; Mayrhofer, K. J. J.; Schmid, G. Various CO_2-to-CO Electrolyzer Cell and Operation Mode Designs to avoid CO_2-Crossover from Cathode to Anode. *Z. Phys. Chem.* **2020**, *234*, 1115−1131.

■ NOTE ADDED AFTER ASAP PUBLICATION

This paper was published on October 27, 2020, before all final corrections were made. The corrected version was reposted on November 6, 2020.

5.6 The capping agent is the key: Structural alterations of Ag NPs during CO$_2$ electrolysis probed in a zero-gap gas-flow configuration

Authors: Menglong Liu, Ying Kong, **Huifang Hu**, Noémi Kovács, Changzhe Sun, Iván Zelocualtecatl Montiel, María de Jesús Gálvez Vázquez, Yuhui Hou*, Marta Mirolo, Isaac Martens, Jakub Drnec, Soma Vesztergom*, and Peter Broekmann*

Highlights: Ag NPs stabilized by different ligands (i.e., BPEI, PVP, PEG, and citrate) were deposited on GDE to utilize for CO$_2$RR in a gas-fed zero-gap configuration. The structural alterations of Ag NPs depend on the chemical nature of capping agent during CO$_2$RR. There are no significant changes in size for BPEI-capped Ag NPs because of strong binding interactions between the amino groups of BPEI and Ag NPs. Most PVP stabilized NPs tend to undergo corrosion due to the reduce mobility of NPs by PVP. In the case of PEG, NPs undergo coalescence. The application of citrate leads more to aggregate; some agglomerates form through Ostwald ripening owing to only the electrostatic force between the citrate and Ag. Moreover, the studies on capping agent removal and exchange show that the excess capping agents play a decisive role in catalyst degradation pathways.

Contributions: I prepared the catalyst ink and involved in analyzing product quantification. I also contributed to the morphological studies after the CO$_2$ electrolysis, and took part in the discussion of the results.

The capping agent is the key: Structural alterations of Ag NPs during CO_2 electrolysis probed in a zero-gap gas-flow configuration

Menglong Liu [a,b], Ying Kong [a,b], Huifang Hu [a], Noémi Kovács [a], Changzhe Sun [a,b], Iván Zelocualtecatl Montiel [a], María de Jesús Gálvez Vázquez [a], Yuhui Hou [a,*], Marta Mirolo [c], Isaac Martens [c], Jakub Drnec [c], Soma Vesztergom [a,d,*], Peter Broekmann [a,b,*]

[a] University of Bern, Department of Chemistry, Biochemistry and Pharmaceutical Sciences Freiestrasse 3, 3012 Bern, Switzerland
[b] National Centre of Competence in Research (NCCR) Catalysis, University of Bern Freiestrasse 3, 3012 Bern, Switzerland
[c] European Synchrotron Radiation Facility, Experimental Division, Avenue des Martyrs 71, 38000 Grenoble, France
[d] Eötvös Loránd University, Department of Physical Chemistry Pázmány Péter sétány 1/A, 1117 Budapest, Hungary

ARTICLE INFO

ABSTRACT

We apply silver nanoparticles (Ag NPs) as catalysts of CO_2 reduction in a zero-gap gas-flow electrolyser. Ag NPs stabilized by different ligands —branched polyethylenimine (BPEI), polyvinylpyrrolidone (PVP), polyethylene glycol (PEG), and citrate— are used in the experiments. The as-prepared NPs have almost identical initial size distributions, yet their catalytic performance, in terms of achievable current and CO selectivity, is different. During electrolysis all Ag NPs exhibit unambiguous morphology changes; the degradation pathway they follow, however, markedly depends on the chemical nature of the capping agent stabilizing them. Scanning electron micrographs obtained before and after constant-charge electrolyses carried out at different potentials reveal that amongst the studied ligands, BPEI seems to be the most effective stabilizer of Ag NPs; in turn, however, BPEI also limits CO formation the most. In case of PVP, mostly corrosion (particle shrinkage) is observed at practically relevant electrolysing potentials, while the application of PEG leads more to particle coalescence. Ostwald ripening seems to appear only at high applied (H_2 forming) potentials in case of the three afore-mentioned ligands while in case of citrate it becomes significant already at mild (CO forming) voltages. By studying the effects of capping agent removal and exchange we demonstrate that apart from ligands directly attached to the Ag NPs, also the excess of capping agents (adsorbed on the electrode surface) plays a decisive role in determining the extent and mode of catalyst degradation. The results of SEM-based particle sizing are also confirmed by synchrotron based wide-angle X-ray scattering measurements that provide further insight into the evolution of crystallite size and lattice strain in the applied Ag NPs during electrolysis.

1. Introduction

The electrochemical reduction of CO_2 into value-added products is a quickly developing field of electrocatalysis, mostly because it opens new perspectives in front of climate change mitigation [1]. Due to the considerable thermodynamic stability of carbon dioxide, the electrochemical CO_2 reduction reaction (CO_2RR) requires high negative potentials, and the application of catalyst materials that favour CO_2RR over the competing hydrogen evolution reaction (HER). The design of new catalyst materials that not only meet this requirement, but can also selectively direct CO_2RR towards the formation of a desired product at suitable rate and at low energy cost has thus become the forefront of electrochemical research in the past 20 years [2].

Although examples to the contrary already exist [3], metals or metal oxides (either in bulk [4], foam [5], or nanoparticulate [6] form) are still considered as catalysts of first choice for CO_2RR. While on bulk metal electrodes with large planar surfaces it is primarily the chemical nature of the metal [4] that determines the

* Corresponding authors at: University of Bern, Department of Chemistry, Biochemistry and Pharmaceutical Sciences, Freiestrasse 3, 3012 Bern, Switzerland (Y. Hou and P. Broekmann); Eötvös Loránd University, Department of Physical Chemistry, Pázmány Péter sétány 1/A, 1117 Budapest, Hungary (S. Vesztergom).
E-mail addresses: menglong.liu@unibe.ch (M. Liu), ying.kong@unibe.ch (Y. Kong), huifang.hu@unibe.ch (H. Hu), noemi.kovacs@unibe.ch (N. Kovács), changzhe.sun@unibe.ch (C. Sun), ivan.zelocualtecatl@unibe.ch (I. Zelocualtecatl Montiel), maria.galvez@dcb.ch (M.J. Gálvez Vázquez), yuhui.hou@unibe.ch (Y. Hou), marta.mirolo@esrf.fr (M. Mirolo), isaac.martens@esrf.fr (I. Martens), jakub.drnec@esrf.fr (J. Drnec), vesztergom@chem.elte.hu (S. Vesztergom), peter.broekmann@dcb.unibe.ch (P. Broekmann).

majority product (CO, formate, hydrocarbons, alcohols), in case of catalysts with nanosized features (nanoparticles or hierarchic foams) also the nanoscale structure has a pivotal role in determining selectivity [6,7]. In case of Cu nanoparticles (NPs), for example, a direct correlation between particle size and product distribution has already been established [8], and also for other metallic NPs (like Sn [9] or Ag [10]) intense research has been carried out to correlate the activity and selectivity of nanoparticulate catalysts to their morphology and physical structure. To use metals (or their oxides) in a nanoparticulate form for the catalysis of the CO_2RR is a very straightforward approach especially because of the many facile synthesis routes available that allow the design of NPs with fine-tuned catalytic properties.

Using metals in a nanoparticulate form for the catalysis of CO_2-RR has the obvious advantage that comes with the low raw material cost — small sized NPs can be applied in a relatively low loading to achieve an already considerable current of CO_2 reduction [5]. A significant drawback of nanoparticulate catalysts stems, however, also from the small size of NPs, which makes them thermodynamically unstable. Maintaining the stability of NPs under the operating conditions of electrolysis, that is, at high applied potentials, strong flow of current and intense gas formation, thus becomes a key question of research. In other fields of electrocatalysis (*e.g.,* in fuel cell research [11]) the degradation of catalyst NPs is well studied. In relation to CO_2RR on the other hand, only a few researchers seem to place emphasis on elucidating possible degradation mechanisms [9,10,12–16].

Ag is considered an appealing catalyst material for CO_2 reduction because it produces a single yet very sought-after product over a broad potential window and under different operating conditions: CO. CO is a remarkably versatile precursor of the production of synthetic fuels [17], and industrial applications already exist, for example, for the coupling of CO_2-to-CO/water-to-H_2 electrolysers to a fermentation module where CO and H_2 are converted to butanol and hexanol with high carbon selectivity [18]. In addition, the two-electron transfer required by the CO_2-to-CO conversion provides a large profit margin compared to other multiple-electron transfer products requiring larger energy inputs [17].

While in existing industrial electrolysers Ag is usually applied in a bulk form for the production of CO [18], it was recently shown in lab scale experiments that when Ag is used in a nanoparticulate form, stable CO formation can be achieved over a much broader potential window, and thus better conversion metrics can be achieved compared to the case when electrolysis is carried out on planar Ag cathodes [10].

In a recent study we made the first step in the direction of up-scaling towards practical application by using Ag NPs as catalysts of CO_2RR in a zero-gap gas-flow electrolyser unit [15]. Zero-gap gas-flow electrolysers allow the realisation of large current densities ($\gg$300 mA cm^{-2}, normalized to geometric cathode surface area) and create an ideal playground for catalyst stability testing under harsh operating conditions.

The use of capping agents is essential in Ag nanoparticle synthesis as they control the shape and size of the grown nanoparticles, and prevent their aggregation over time [19]. Capping agents usually achieve long-term stabilization of the particle size [20] either by steric hindrance (such ligands usually have bulky protecting groups) or by an electrostatic repulsion between ligands bearing the same charge (such capping agents are usually ionic species). While essentially both types of ligands can work well in stabilizing NPs in dispersion, they both have significant drawbacks when it comes to fixing the NPs on an electrode surface and using them as electrocatalysts. In such cases NPs stabilized by charged ligands are often found to quickly agglomerate either due to screening effects arising from high ionic strengths or as a result of the electric field of the working electrode. NPs stabilized by steric hindrance

are usually more stable, however in this case the strong adsorption of ligands often blocks the access of reactants to the NPs, leading to an overall decrease of the catalytic activity.

The structural changes metallic NP-based catalyst layers undergo in the course of the catalysed process can take many forms, including the *detachment* of particles from the support (which ultimately results in catalyst loss), the *corrosion* of the NPs (leading to an overall decrease of the average nanoparticle size), the *aggregation* of NPs on the catalyst support (leading to the formation of larger particles) and the phenomenon known as Ostwald ripening (as a result of which some particles grow larger on the expense of smaller ones disappearing). These structural changes (an illustration is shown in Fig. 1) all result in distortions of the particle size distribution of the NPs, and as such, they are commonly referred to as means of *degradation* — practically regardless to whether they have any measurable effect, either negative or positive, on the observed catalytic performance.

In practical electrolysers degradation rarely takes a single route, and in most cases it is a combination of several of the above-described degradation phenomena that determines the fate of catalyst NPs. The means and extent of degradation heavily depends on the operating conditions of the electrolyser (voltage and current, the intensity of gas formation, etc.), as well as on the chemical nature of the stabilizing (capping) agents applied either during the synthesis of the NPs or later for the formulation of the catalyst ink.

As capping agents not only adsorb on the surface of the NPs but also on the (usually carbon) cathode support, they may also play a decisive role in determining the surface adherence and the mobility of the NPs. While strongly bonding capping agents may preserve the initial particle size distribution of the NPs more efficiently than others, such ligands may also decrease catalytic performance by blocking the access of reactants to active catalyst sites. In such cases, the onset of "degradation" can even have an unexpected positive effect on the performance of electrolysis, as it can enable the participation of new, previously unaccessible sites in the catalysed process [21]. Apart from such exceptions, however, the degradation of NPs usually manifests in a long-term loss of the catalytic performance. This is primarily due to a loss of the active catalyst surface area that accompanies all degradation modes (including corrosion that often leads to the detachment of the smaller particles). A secondary degradation effect that may also account for performance losses is related not to the changing size distribution of the particles, but rather to a consequence of this: an internal structural change of the NPs, during which the (from a catalytic point of view, highly active) open crystalline sites re-organize to less ordered and more compact amorphous structures.

In this study we use Ag NPs capped by different ligands — branched polyethylenimine (BPEI), polyvinylpyrrolidone (PVP), polyethylene glycol (PEG), and citrate— with an initially narrow size distribution centred at $\sim$ 40 nm for the preparation of catalyst inks that we disperse on a gas diffusion layer. The thus prepared Ag NP GDE (Fig. 2) is in direct contact with the anion exchange membrane of the zero-gap gas-flow electrolyser (see also Figure S1 of the Supporting Information) that contains an electrolyte solution only on the anode side. The reactant gas (CO_2) is directly fed by a constant flow to the GDE, and the configuration does not only assure reduced ohmic losses but it also attenuates complications that arise from poor membrane hydration and electrode flooding at high current densities [15].

We show that in case of all four applied capping agents, the efficiency of CO_2RR considerably drops over time in a manner that is similar for all capping agents. While this performance loss, occurring due to the formation of carbonate plaques at high current densities over the electrode surface, is not a direct result of the structural changes that catalyst NPs suffer during electrolysis, the zero-gap gas flow cell still provides means to study the morpholog-
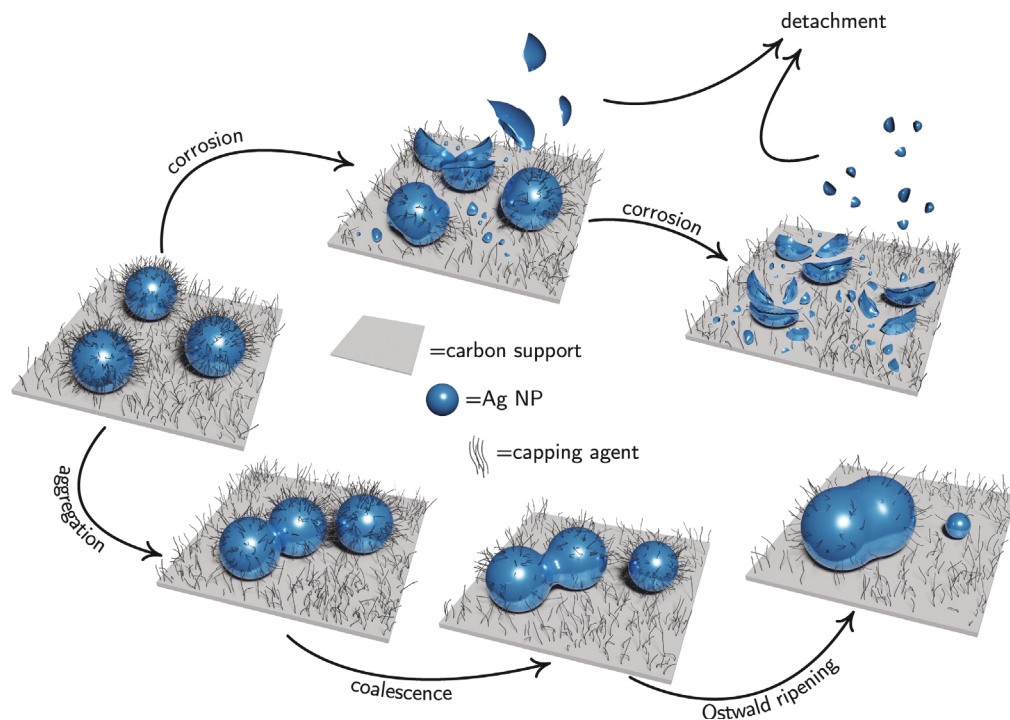
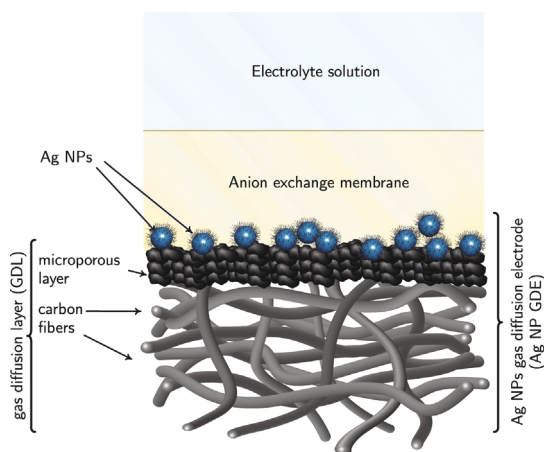**Fig. 1.** Degradation pathways of Ag NPs used for CO$_2$RR.

Fig. 2. The gas diffusion electrodes (Ag NP GDEs) used in this study are formed by drop-casting an Ag NPs containing catalyst ink on a gas diffusion layer (GDL). The latter is a bilayer structure consisting of a macroporous backing material (carbon fiber paper support) and a carbon-based microporous layer. The Ag NP GDE is separated by an anion exchange membrane from the electrolyte solution that contains the anode and a reference electrode.

ical changes of Ag NPs during intense CO$_2$RR/HER stressing. Following a removal of the formed carbonate plaques by careful dip-washing, structural changes can be investigated by a set of state-of-the-art nanoparticle characterization techniques including scanning electron microscopy (SEM) and wide-angle X-ray scattering (WAXS) measurements. These methods can clearly demonstrate that depending on the nature of their stabilizing ligands, Ag NPs undergo different degradation pathways on the course of electrolysis. By a set of ligand removal and exchange experiments we also demonstrate that apart from ligand molecules directly attached to the NPs, ligands adsorbed on the supporting carbon matrix also play a role in determining the dominant degradation mode.

2. Experimental Section

Preparation of the Ag NPs-containing catalyst ink. To prepare the carbon-supported Ag NP catalyst ink, 0.25 cm^3 of the as-received parent catalyst suspension (NanoComposix, Ag mass concentration of 1 mg cm^{-3}) was diluted to 0.55 cm^3 by the addition of Milli-Q water. A second suspension (volume: 0.44 cm^3) was made by dispersing carbon black (Vulcan XC 72r, Cabot) in isopropanol (VLSI Selectipur, BASF SE, Ludwigshafen, Germany) in a 0.1 mg cm^{-3} concentration. Both suspensions were sonicated separately for 10 and 30 min, respectively, following which the suspensions were intermixed and, after the addition of 10 $\mu\ell$ Nafion solution (5% Nafion, 15–20% water, Sigma–Aldrich), the new suspension was sonicated for further 10 min. The same ink preparation protocol was applied to all four nanoparticulate catalysts used herein. BPEI, PVP, PEG and citrate-capped Ag NPs with an average particle size of $\sim$ 40 nm were purchased from a supplier (NanoComposix) and were used directly for the ink preparation. In order to carry out experiments by removing some of the excess PVP capping agent, the parent Ag NP suspension was first subjected to centrifugation (at 35 000 rpm, 40 min, Beckmann Coulter ultracentrifuge, SW60 rotor). This treatment allowed for a separation of the surfactant-capped Ag NPs and the free surfactants that remained, at least to a large extent, in the liquid (aqueous) phase. The separated Ag NPs were then suspended in Milli-Q water to keep the Ag concentration the same as that of the parent suspension, and the ink preparation protocol described above was followed. The separated Ag NPs and the aqueous matrix phase were both subjected to a total organic carbon concentration (TOC) analysis with the aim to estimate the amount of surfactants that is either attached to the Ag NPs or is present in solution (see Table S5 in Supporting Information).

Preparation of the Ag NP GDEs. GDEs were formed by drop-casting 40 $\mu\ell$ of either one of the above-described catalyst inks onto the masked hydrophobic surface of a GDL (H23C8, FuelCellStore, see Figure S2 of the Supporting Information for SEM charac-

terization). The GDE was in contact with the membrane through a circular opening with a diameter of 3 mm, and the corresponding geometric area (7.07 mm^2) is used for the surface normalization of current to current density. The catalyst ink was percolated through the porous body of the GDE by a vacuum filtration system placed on the backside of the electrode, followed by drying at ambient conditions. The resulting mass loading was in the range of (43±5) μg cm^{-2}, as confirmed by inductively coupled plasma mass spectrometry (ICP–MS, see Table S1 in Supporting Information for detailed loading data).

Assembly of the gas flow-cell. The assembly and main components of the zero-gap gas-flow cell employed in this work have been described elsewhere [15]. The cell (see also Figure S1 in Supporting Information) consists of a stainless steel body with the gas flow channels used to feed the CO_2 from the backside of the prepared Ag NPs GDE mounted on the outermost location of the central portion. Other components incorporated into the cell include a current collector and a gas inlet and outlet to control the supply of the CO_2 reactant (99.999%, Carbagas, Switzerland) and analysis of gaseous products, respectively. All the CO_2 reduction experiments were set up by placing a freshly prepared Ag NPs GDE on top of the gas flow channels, with its catalyst modified surface facing upward. Subsequently, a new hydroxide-functionalised Sustainion alkaline membrane (X3750 RT, Dioxide materials) and a poly-(tetrafluoroethylene) anolyte compartment were placed on top of the GDE. A clamp was then used to guarentee cell tightness and mechanical stability. 10 cm^3 of 2.0 mol dm^{-3} KOH was used as electrolyte for the anolyte compartment. An Ag|AgCl|3 mol dm^{-3} KCl electrode (double junction design, Metrohm) was used as a reference, and an Ir wire (99.9%, MaTeck Material-Technologie & Kristalle GmbH, Germany) separated by a glass frit was used as a counter electrode. Note that the PTFE anolyte compartment has a central orifice (of 3 mm diameter, corresponding to a geometric surface area of 7.07mm^2) in its bottom part that provides direct contact between the electrolyte and the underlying anion-exchange membrane, while the Ag NPs GDE is prevented from direct contact with the supporting anolyte. During electrolysis, a humidified CO_2 stream (16 cm^3 min^{-1}) was continuously fed through the gas flow channels of the stainless steel cell body, adjacent to the GDE.

Electrochemical measurements and product distribution studies. An ECi-200 potentiostat (Nordic Electrochemistry) was used to perform all electrolysis experiments. The electro-generated gaseous products (CO and H$_2$) were determined by means of on-line gas chromatography (SRI Instruments) in fixed (10 or 4 min) time intervals. The electrolyte solution was also analysed after full electrolyses, to check for any soluble products formed, by means of ion exchange chromatography (Metrohm Ltd., Switzerland). As formate (in different amounts, see Table S3 in Supporting Information) was found as the sole dissolved product in the electrolyte solution, it was assumed that whenever the GC-based detection of volatile products could not account for a 100% of Faradaic efficiency, the rest of the passed current was turned into formate production.

Electron microscopy measurements. For the morphological characterization of the Ag NPs on GDEs, a Zeiss Gemini 450 scanning electron microscope equipped with an InLens secondary electron detector and a back-scattering detector was used. An accelerating voltage of 5 kV and a current of 120 pA were applied at a working distance of 3.8–4.2 mm. Using the Smile View software for particle sizing, ca. 500–900 particles were analysed per experimental setting for the creation of the particles size distribution shown in Figs. 7, 9 and 10. The particle size was defined as the longest measurable dimension in case of anisotropic NPs, see Figure S13 in the Supporting Information. To acquire EDX point spectra and 2D

surface mappings of selected samples, the AZtec 4.2 software (Oxford Instruments) was used. An acceleration voltage of 10 kV and a current of 500 pA were applied at a working distance of 8.5 mm for EDX measurements. For high-angle annular dark-field scanning transmission electron microscopy (HAADF–STEM) combined with energy-dispersive X-ray spectroscopy (EDX), a Talos F200X (Thermo Fisher Scientific) instrument equipped with a SuperEDX detector was used with an acceleration voltage of 200 kV.

Contact angle measurements. Contact angle measurements were carried out using a Krüss Advance Drop Shape Analyzer DSA25 (Krüss GmbH, Hamburg, Germany). Electrodes were mounted on a flat stage and water drops (milli-Q water, 1.4 μL) were deposited at room temperature.

Synchrotron Wide-Angle X-ray Scattering (WAXS) measurements. Crystallite size and microstrain were measured via WAXS measurements at the ID31 beamline of the European Synchrotron Radiation facility (ESRF) in Grenoble, France. The high energy X-ray beam (75 keV) was focused on the Ag NP GDEs, and the scattered signal was collected using a Dectris Pilatus CdTe 2 M detector positioned 520 mm behind the sample. The energy, detector distance and tilts were calibrated using a standard CeO$_2$ powder and the 2D diffraction patterns were reduced to the presented 1D curves using the pyFAI software package [22]. Rietveld refinement of the WAXS patterns was performed to extract the phase structure, crystallite size, lattice parameter and microstrain using the cubic Fm–$3m$ structure of Ag metal and the GSASII software [23], see Figure S14 in Supporting Information for a representative fit. The instrumental parameters were determined by the refinement of a CeO$_2$ standard sample. Air scattering was removed from each pattern. The measurement consists in a height scan acquiring WAXS pattern at different positions in the sample. The pattern of the GDE is considered as background and removed for each sample. The fitting is performed using crystallites of uniaxial orientation along the (111) direction.

White light interferometry (WLI) analysis. The mesoscopic surface morphology of the Ag NP GDEs was analyzed by means of white light interferometry (Contour GT, Bruker, see Figure S5). Vision64 software (Bruker) was used for operating the instrument and for data analysis.

Inductively coupled plasma mass spectrometry (ICP-MS). GDE samples were immersed for 24 h in 1 cm^3 HNO$_3$ (69.3%, BASF SE, Ludwigshafen, Germany) to dissolve all Ag NPs. The resulting solutions were diluted with 3% HNO$_3$ solution by a factor of 500 and were then fed into a NExION 2000 ICP-MS instrument (Perkin Elmer) to obtain the Ag mass loading of the electrodes (see Tables S1 and S4 in Supporting Information).

Total organic content (TOC) determination. To quantify surfactants in each solution, 100 $\mu\ell$ of free surfactant solutions obtained by centrifugation of Ag NP suspensions (0.25 mg cm^{-3}) and surfactant-capped Ag NP suspensions (0.25 mg cm^{-3}) which do not contain free surfactants were fed into a DIMATOC 2100 instrument (Dimatec, Essen, Germany). The organic compounds were oxidized at 850 °C with Pt as catalyst to CO_2/NO. Non-dispersive infrared (NDIR) gas sensor with a reflective diffuser and a chemiluminescence detector were used to detect CO_2 and NO, respectively.

3. Results and Discussion

Characterization of the as-prepared Ag NP GDEs. Essentially regardless to the nature of the stabilizing ligand (BPEI, PVP, PEG or citrate), all our studied Ag NP GDEs exhibited very similar physical characteristics (Fig. 3). Representative SEM images of (PVP-capped) Ag NP GDEs are shown in Fig. 3a and c, revealing isotropic and uniformly dispersed NPs with an almost uniform particle size
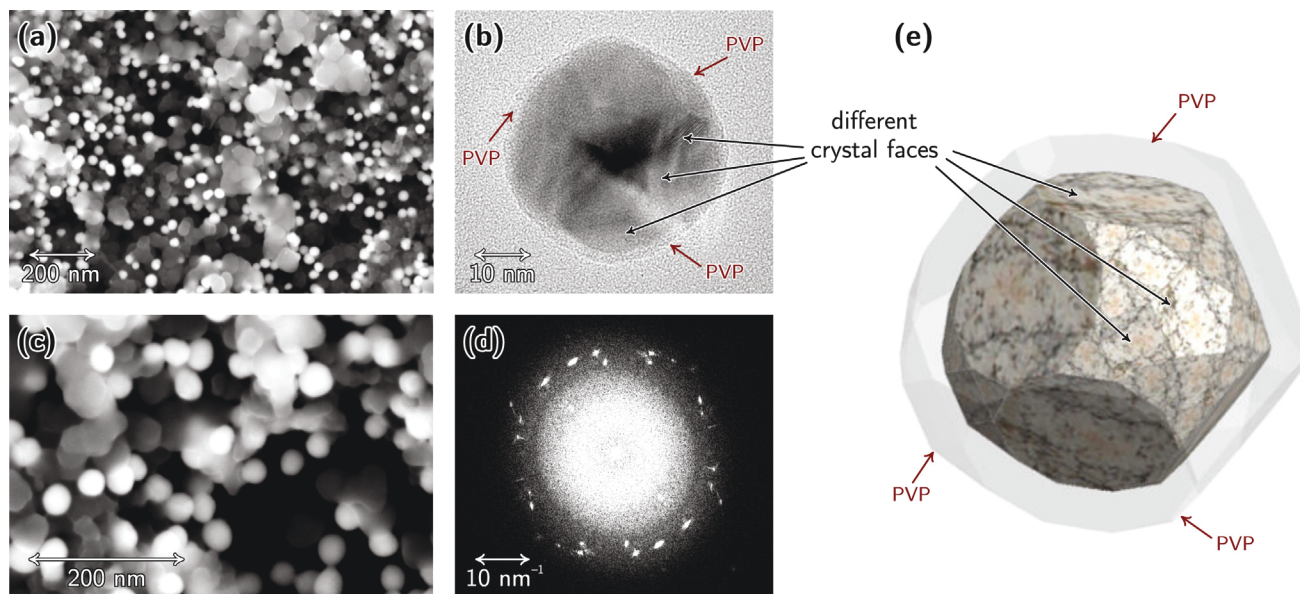
Fig. 3. Representative top-down SEM images (a, c) of PVP-capped Ag NPs dispersed on the carbon microporous layer of the GDE. The HR–TEM image (b) of an individual PVP-capped Ag NP, and its Fourier-transformed representation (d) demonstrate the polycrystalline nature of the nanoparticle, exhibiting different crystalline domains. Schematic drawing of the PVP-capped Ag NP is shown in (e). For a complete (top-down) SEM and TEM view of GDEs prepared by the use of Ag NPs capped with different ligands, see Figure S3 and S4 in the Supporting Information.

of about 37 nm. The HR–TEM image and the corresponding FFT representation of an individual PVP-capped Ag NP, shown in Fig. 3b and d, reveal the polycrystalline nature of the NPs. The drawing in Fig. 3e, inspired by the result of electron micrography, attempts to show a single Ag NP in three dimensions. Similar initial states were found in the case of Ag NPs capped by other ligands (BPEI, PEG and citrate). Independently of the nature of the capping agent used by the provider (NanoComposix) for the synthesis of the studied Ag NPs, we found that all NPs used in this work are of an (almost) spherical shape, as shown in Fig. 3e, and that the NPs exhibit no preferential faceting. The uniformly dispersed particles were isotropic but polycrystalline, and their average size was between 30 and 40 nm in all cases. Corresponding SEM and TEM images of all four types of surfactant-capped Ag NPs are shown in Figures S3 and S4, respectively, of the Supporting Information, where white-light interferometry images (top view of the catalyst layer, Figure S5), as well as cross-sectional (side view) SEM and EDX images (Figure S6) can also be found. The latter show that the majority of Ag NPs does not penetrate the GDE, and remains dispersed on top of the microporous layer.

CO₂RR/HER stressing. In order to study the electrochemical performance of Ag NP GDEs, potentiostatic electrolyses in the configuration shown in Fig. 2 were carried out at three different applied potentials. Keeping comparability in mind, all electrolyses were performed until the same amount of charge (300 C cm⁻², normalized to the geometric surface area of the circular opening of the zero-gap cell) passed through the electrolyser. The product distribution (that is, the partial current densities of CO and H_2 formation, see the dashed lines) were reconstructed on the basis of on-line GC measurements at given fixed time intervals, shown by the dots in Fig. 4.

As the amount of CO and H_2 detected by on-line GC measurements did not account for a 100% Faradaic efficiency, contents of the electrolyte were analysed post-electrolysis by ionic liquid chromatography (IC), which revealed a significant amount of formate production at each setting (see Table S3 in Supporting Information). As no water-soluble products apart from formate were detected after electrolysis by IC, it is safe to assign the missing fraction of the current density (hatched areas in Fig. 4 labelled "rest") to the production of formate [15,24].

Fig. 4 reveals a rather similar behaviour of three out of four studied catalysts. Namely, the PVP-, PEG- and citrate-capped Ag NPs all seem to exhibit a remarkable selectivity towards the production of CO, although especially at larger electrolysing potentials this selectivity, as well as the overall current, significantly decrease with time. That the catalytic performance of these NPs seems not to depend significantly on the nature of the applied capping agents suggests that already at initial stages of the electrolysis at least a partial removal of the capping shell from the surface of the NPs may have occurred, leaving catalytically active sites available to participate in CO_2RR [13,16,21].

As for BPEI-capped Ag NPs, both the overall current and the selectivity of CO production are considerably smaller (essentially at all three applied potentials), and this observation can be explained by the exceptionally strong bonding interactions between the amino groups of BPEI and the Ag NPs. Due to this strong bonding it seems plausible to assume that the BPEI-capped particles remain at least partially inaccessible for the reactants of electrolysis. As a result, the observed performance loss is in turn also smaller compared to the case of NPs capped by other agents (PVP, PEG or citrate).

In case of all four types of NPs, a clear decrease is observed in both the Faradaic efficiencies of CO formation and the current density as a function of time (*i.e.*, charge) at each potential. The performance decay is especially rapid at the electrolysing potential of −2.354 V, where the Faradaic efficiency of CO formation very quickly drops due to intense hydrogen evolution. Although less severe, performance losses can also be observed in the cases of lower electrolysing potentials in Fig. 4. The question whether the observed performance loss has anything to do with the actual morphology changes of the NPs during the electrolysis immediately follows: we found, however, that although by SEM and WAXS investigations significant morphology changes can indeed be monitored, these structural alterations are not the main cause of the performance losses observed in Fig. 4.

The obvious decrease of the overall current density and the relative selectivity of the catalyst NPs to produce CO is rather connected to another phenomenon, namely the formation of a mostly potassium carbonate-based precipitate over the GDE. This
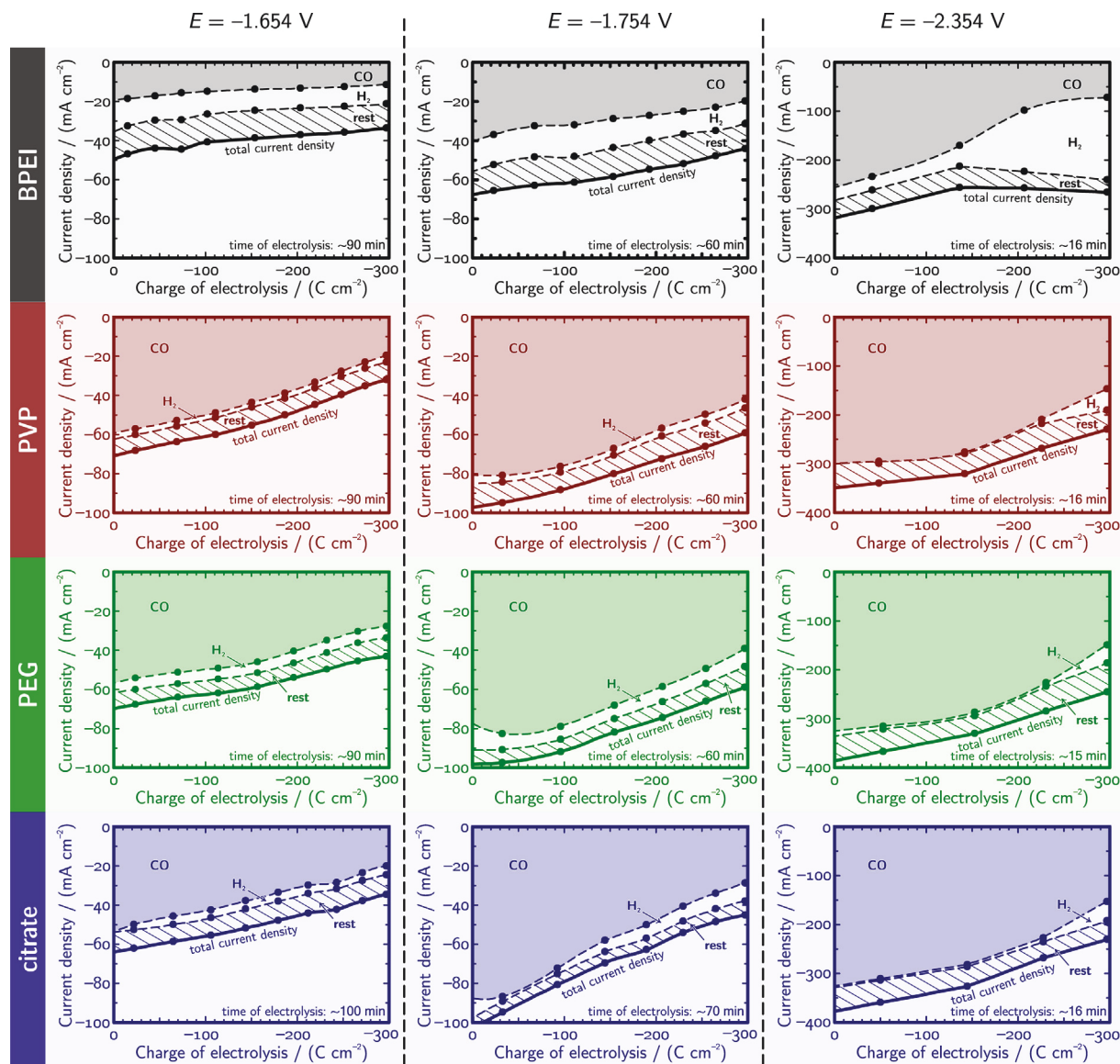
Fig. 4. Total current densities (full thick curves) plotted as a function of the passed charge density at different constant electrolysis potentials (measured vs. Ag/AgCl) for differently capped Ag NP GDEs. Electrolyses were stopped in all cases after the same amount of charge (-300 C cm^{-2}) was passed through the electrode. Shaded areas and dashed curves show the product distribution as reconstructed by GC measurements at different times (indicated by dots). Note that CO and H$_2$ were the only GC-detectable products that however did not account for a 100% of Faradaic efficiency. The "rest" of the current (hatched area in the graphs) can most probably be assigned to formate production (see the text and Tables S2 and S3 in Supporting Information for more details).

serious effect —that however does not hinder the observation of actual morphology changes on the nanoscale— is exemplified in Fig. 5.

As shown in Fig. 5, the pristine GDL we start out from (see Fig. 5a for a photograph) exhibits a clear surface, and the top- and side-view SEM images (Fig. 5b and c) reveal the expected structure of the surface microporous layer and the underlying carbon fibers. The surface of the top microporous layer is hydrophobic, as demonstrated by contact angle measurements on a sessile water drop, Fig. 5d. The EDX mapping analysis (Fig. 5q) reveals only carbon and fluorine signals in the elemental composition (the latter arises due to the PTFE treatment of the GDL applied by the manufacturer).

Fig. 5e shows a photograph of the (PVP-capped) catalyst ink drop-cast on the GDL. The circular area that will serve as the active cathode surface of the electrolyser (this will be in direct contact with the membrane) is shown here by a dashed circle. The catalyst

NPs are clearly visible by SEM (Fig. 5f) and EDX-based elemental mapping (Fig. 5g) confirms that the NPs are clearly composed of Ag. Drop-casting the catalyst ink on the surface does not significantly decrease the hydrophobicity of the GDE (Fig. 5h), while in the EDX spectrum (Fig. 5h) the signal of Ag clearly appears.

When this GDE is subjected to CO$_2$RR/HER stressing, the formation of a potassium carbonate/bicarbonate based precipitate immediately becomes visible also to the bare eye, as shown in the photograph of Fig. 5i. An SEM image of the formed carbonate plaque is shown in Fig. 5j, and the elemental composition map of Fig. 5k reveals K as a major component of this plaque. Due to the formation of the carbonate precipitate the surface of the GDE becomes hydrophilic (Fig. 5l) and the signals of both K and O appear in the EDX spectra of Fig. 5q.

That the formed carbonate plaque is beyond doubt responsible for the performance losses observed before in Fig. 4 can be proven by a set of "recovery" experiments. These show (see Figure S12 in
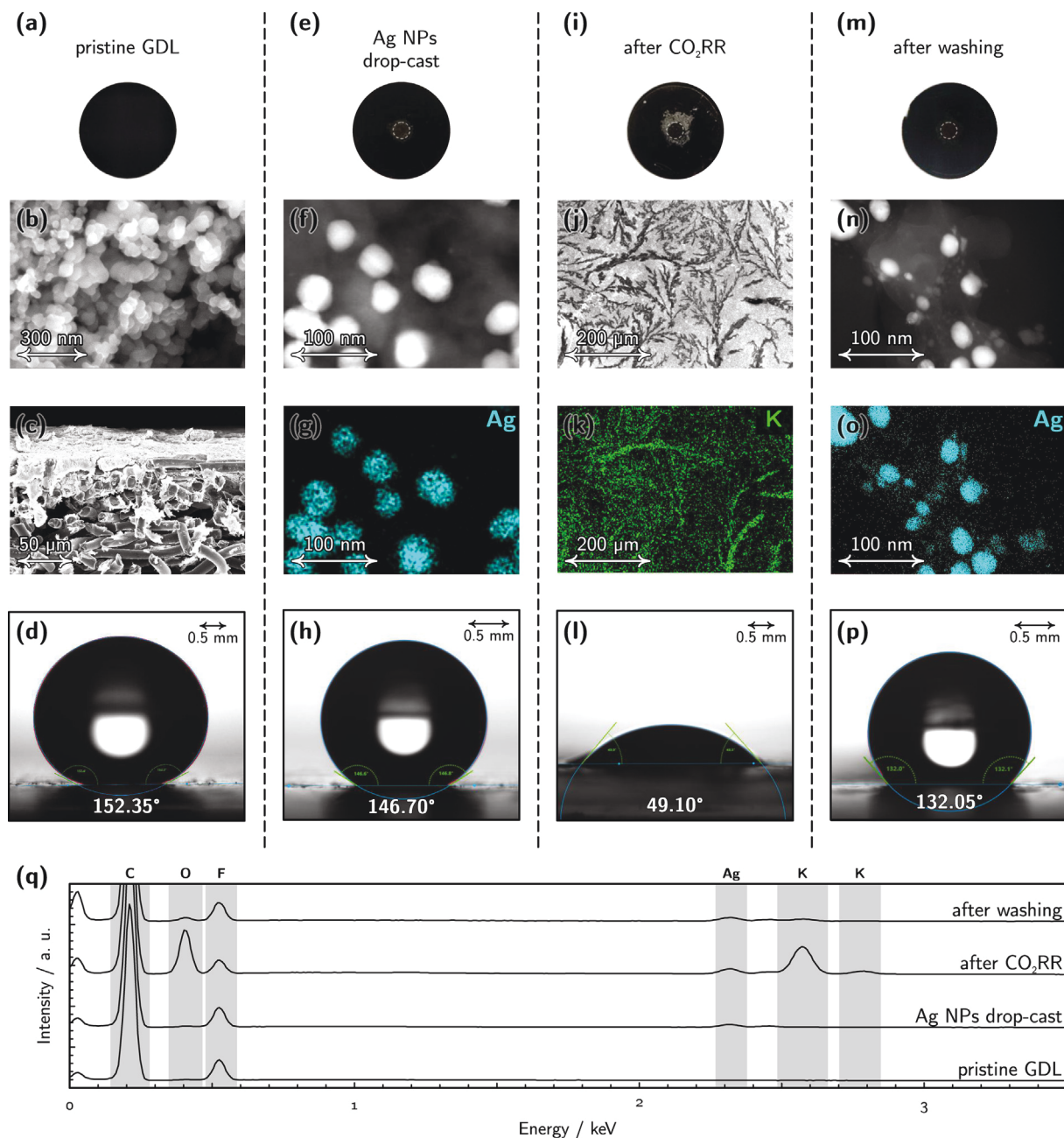
Fig. 5. The characteristic features of a pristine GDL significantly change after surfactant-capped Ag NPs are drop-cast on it, the thus prepared GDE is used for electrolysis, and finally, after the carbonate precipitate formed during CO$_2$RR/HER stressing is washed away. See the text for an exact description of each panel, and Figures S7–S11 of the Supporting Information for more details.

Supporting Information) that following a removal of the carbonate layer by dip-washing, already used GDEs can almost completely regain their efficiency in a subsequent electrolysis.

As the formed carbonate plaque makes us unable to study the degradation of NPs during CO2RR/HER stressing, the carbonate precipitate was removed from the surface following electrolysis by careful dip-washing (see Figure S8 in Supporting Information for details). A photograph of the GDE following the dissolution of the carbonate plaque is shown in Fig. 5m, and the subsequently taken SEM images (Fig. 5n and o) clearly indicate that this cleaning method does leave the actual catalyst NPs intact (compare panels n and o with f and g in Fig. 5). The accuracy of the dip-washing method is also proven by EDX (Fig. 5q) showing that the K and O signals almost fully disappear and the Ag sig-

nal is regained after washing. That the dip-washing technique we used to remove the carbonate plaque from over the catalyst surface did not result in any significant catalyst (Ag) loss was confirmed by ICP–MS analysis (see Table S4 in Supporting Information).

Morphology changes of Ag NPs on GDEs studied by SEM. The reliability of the applied dip-washing method allowed us to apply SEM analysis in order to study the structural changes that the differently capped Ag NPs undergo during extensive CO$_2$RR/HER stressing. Representative SEM images of pre- and post-electrolysis (dip-washed) samples are shown in Fig. 6 for the studied four types of surfactant-capped Ag NP catalysts. The histograms shown in Fig. 7 were prepared by manually processing several micrographs similar to those shown in Fig. 6: the size of each NP, regardless

to form, was determined by measuring its longest dimension as illustrated by Figure S13 in the Supporting Information.

Expectation ranges of the particle sizes (mode±deviation) were determined by making the histograms shown in Fig. 7 subject to probability distribution fitting. Histograms exhibiting a single mode were fitted by log-normal distributions yielding an unsymmetrical (skewed) expectation range, while in case of bimodal distributions the linear combination of two (symmetric) Gaussians were used to describe our datasets. Expectation ranges for the average particle size are specified for all panels of Fig. 7, making it apparent that the morphology of the Ag NPs evolved differently in case of the four different capping agents.

In case of BPEI, the observed particle size distributions are bimodal both before and after electrolyses. Interestingly, the second characteristic particle size (corresponding to a smaller peak) is twice of the first one, which implies, taking into consideration that we used the longest measurable dimension for particle sizing, two-particle aggregates were present at the GDE surface, already before electrolysis. As also shown in Fig. 7, however, no significant change of the characteristic particle sizes are observed when BPEI-capped Ag NPs are exposed to electrolysis stressing at different potentials, and this is in agreement with the results of Fig. 4 that also show a relatively stable catalytic performance of BPEI-capped Ag NPs.

The situation is markedly different in the case of PVP-capped nanoparticles that, as shown in Fig. 7, tend to corrode during elec-

trolysis. Corrosion in case of PVP-capped Ag NPs leads to a significant decrease of the characteristic particle size, as well as to a general broadening and a larger skewness of the distribution.

In the case of PEG, stressing by CO_2RR/HER seems to have rather the opposite effect. While the first characteristic particle size remains essentially unchanged, as a result of electrolysis a second peak becomes visible in the histograms, and the maximum of this peak is approximately twice of that of the first one. This is a clear hint [25] to that in case of PEG, particle coalescence is the most favoured mode of catalyst degradation (see also the micrographs of Fig. 6).

The general increase of particle sizes is also apparent in the case of citrate-capped Ag NPs, as shown in the last row of Fig. 7, although in this case no evolution of further, distinct modes are seen: the histograms, instead, get significantly broadened and skewed as a result of electrolysis. In this particular case we assume that due to the relative instability of the citrate shell at the applied (negative) potentials, the NPs quickly become almost totally unprotected [26]. As a result, their aggregation/coalescence becomes unhindered, and apart from the coalescence of neighbouring particles, also Ostwald ripening (either its two or three-dimensional form) occurs in this case [27,28].

To conclude, the SEM analyses seem to suggest that PVP-capped particles undergo more the corrosion pathway of degradation (Fig. 1), while PEG- and citrate-capped NPs tend more to aggregate, coalesce, and (especially in case of citrate) some form of Ostwald
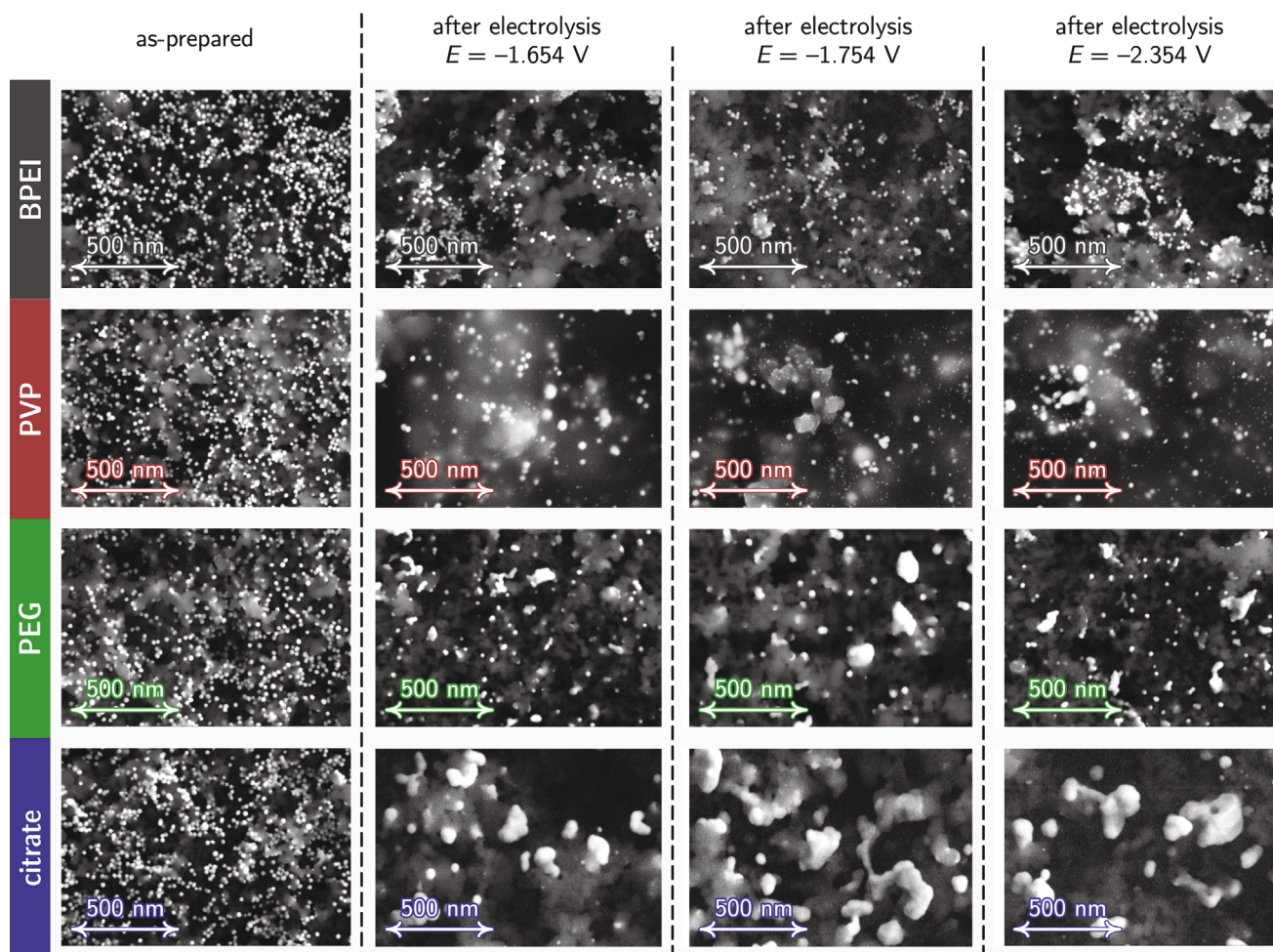

Fig. 6. Representative SEM micrographs of GDEs prepared using Ag NPs stabilized by different capping agents, recorded before ("as-prepared") and after constant charge electrolyses at different potentials (cf. to Fig. 4). These, as well as some other similar SEM images were used to construct the histograms shown in Fig. 7.
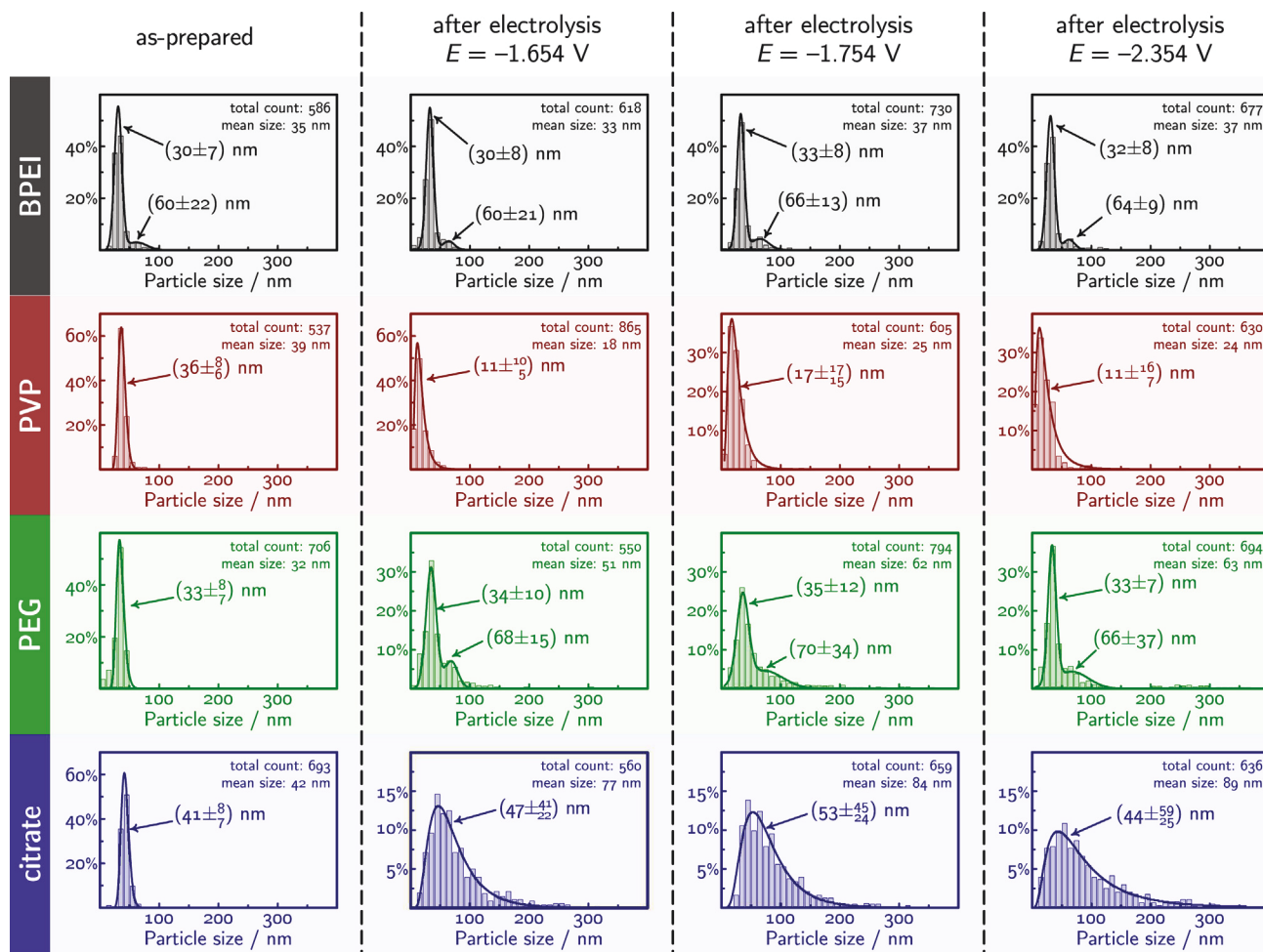
Fig. 7. Histograms showing the particle size distribution of Ag NPs, capped by different ligands, before and after electrolysis at a given potential. Expectation ranges of the particle size are shown for the fitted peak(s).

ripening also seems to take place. Amongst the studied capping agents, BPEI seems to be the most protecting one, as in this case no particular changes of the size distribution was observed when comparing post- to pre-electrolysis SEM images.

Morphology changes of Ag NPs on GDEs studied by WAXS analysis. The above picture can further be nuanced if we also use WAXS measurements to characterize the morphology changes of Ag NP catalysts during electrolysis (Fig. 8). The width of the WAXS peaks have two main contributions —apart from instrumental broadening—, and these are the size of coherently scattering domain (crystallite size) and microstrain (deviation from perfect order). These different characteristic parameters were determined by Rietveld fits of the diffraction pattern. Because the size determined by Rietveld fit maps crystallite sizes rather than full geometrical sizes, direct comparison between the WAXS and SEM-based analysis can reveal new insights about the degradation phenomena. First we note that using only the isotropic size model did not fit the data well. The fits improved significantly only after a size anisotropy had been included, implying that the nanoparticles have preferred growth orientation along the (111) direction (Fig. 8 and Figure S16 in Supporting Information). Along this direction, the crystallite size is about two times longer when compared to the short directions.

In the case of BPEI, the crystallite size is smaller than the particle size determined by the SEM analysis. This hints that the particles are composed from several crystallites, in agreement with the TEM observations. In this case the size does not change signifi-

cantly, supporting the conclusions from the SEM analysis that the particles are stable during electrolysis. The microstrain shows a very low value for as-prepared NPs, but increases significantly for the samples measured after electrolysis. Given that the microstrain is a direct measure of internal disorder of the crystallites, the electrolysis seems to distort the local order which is typically linked to the increase of grain boundaries length. However, as in our case we do not observe any decrease in crystallite dimensions, the increase of microstrain should either be linked to surface phenomena caused by changes in the BPEI surface structure [29], or, alternatively, could be explained by some carbonate precipitates (that were not entirely removed by dip-washing) remaining adherent to the catalyst NPs (cf. to Fig. 5 exhibiting a small K signal even after washing).

The PVP case shows different behaviour. After electrolysis, the crystallite size increases in both directions, independently of the applied current, and the microstrain values increase moderately. This crystallite size increase is apparently opposite to the SEM-derived trend in particle size and the crystallites appear significantly larger than the physical size measured by SEM. This is caused by a broadening of the particle size distribution during electrocatalysis that is due to the formation of some amount of larger NPs while the average size shows a general decrease in the SEM measurements. It is of worth to note that while SEM results a number-weighted distribution, the diffraction amplitude is weighted by the volume of the NPs, therefore the crystallite size
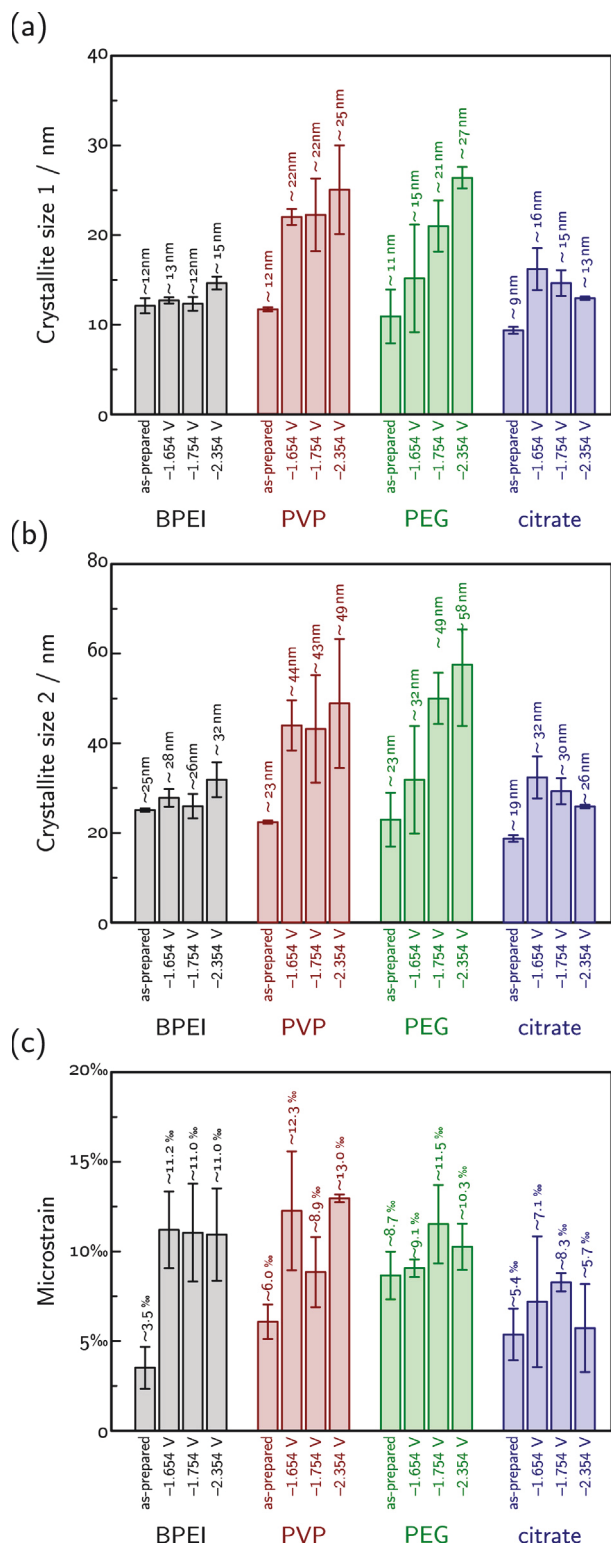
Fig. 8. Crystallite sizes (a, b) and microstrain (c) measured by WAXS of Ag NPs, capped by different ligands, before and after electrolysis at a given potential.

takes place in this case — and this causes both the increase of crystallite sizes (Fig. 8) and the broadening towards bigger sizes of the SEM-based size distribution (Fig. 7).

WAXS measurements on PEG-capped Ag NPs show a similar trend of increasing crystallite size, consistently with the appearance of bimodality in the SEM-based size distribution. PEG-capped NPs are not only aggregated, but the individual crystallites are also fused together through coalescence during electrolysis. The picture is somewhat different for citrate capped NPs that although as evidenced by SEM clearly undergo coalescence to a large extent during electrolysis, at the same time show only a moderate increase of the crystallite size. This is a hint to that the fusion of the NPs does not necessarily involve the merging of crystallites and that the enormously large Ag particles formed from citrate-capped Ag NPs during electrolysis (see, e.g, Fig. 6) can be composed of several distinct crystalline domains. The relatively low changes of microstrain observed in the case of PEG- and citrate-capped NPs are likely linked to the fact that the capping agent is only loosely bound to the surface of these NPs.

Ligand removal and exchange experiments. That in our investigations we saw the most severe degradation taking place in the case of citrate-capped Ag NPs can plausibly be explained by the fact that citrate stabilizes the NPs not by a steric effect as the other three studied ligands do, but by an electrostatic force. It can thus safely be assumed that under the operating conditions of electrolyses — that is, at high cathodic potentials— most of the negatively charged citrate ions will leave not only the surface of the NPs but they would also desorb from the surface of the carbon support. This can enhance the surface mobility of the particles, leading to their more rapid aggregation and then coalescence.

In order to check whether ligand molecules that may have remained adsorbed on the support in the three other (non-citrate) case have any role in determining the degradation pathway of the NPs, we designed a set of ligand exchange/removal experiments. These were based on separating the NPs from their parent dispersion by centrifugation, which left the majority of the capping agents —that would necessarily end up on the support surface during the GDE preparation— in the supernatant (see Table S5 and Figure S14 in Supporting Information). Filtering and re-dispersing the nanoparticles in Milli-Q water after centrifugation (see Section 2 for details) thus allowed us the (at least partial) removal of the carbon substrate-attached ligands or, if re-dispersion took place in the solution of another capping agent, the (again, at least partial) exchange of ligands.

The effect of ligand removal on electrolysis-induced degradation is shown in Fig. 9 for PVP-capped Ag NPs (this time, electrolysis took place at $E = -1.754$ V, see Figure S15a in Supporting Information for more details). We can see a notable difference if we compare this figure to the appropriate panels of Figs. 6 and 7: namely, that while the initial size distribution of the NPs is seemingly unaffected by the removal of excess PVP, the degradation pathway markedly changes. While in the previous case, when excess PVP was adsorbed on the carbon support layer, we primarily observed corrosion (and the change of the average particle size from around 39 to 25 nm), in Fig. 9 we see an increase of the average size (from 42 to 67 nm) and a significant broadening of the distribution. It seems to be a plausible assumption that the apparent coalescence we observe here was in the previous case hindered by support-adsorbed PVP, rendering the degrading NPs immobile. Alternatively, the removal of a significant portion of PVP from the surface of the NPs might have also lead to an increase of the average particle size by allowing quicker Ostwald ripening.

The role of support-adsorbed ligands can further be emphasized if we carry out a ligand exchange (as opposed to removal) experiment with citrate-capped Ag NPs that we in this case after centrifugation re-disperse in a PVP solution. As shown in Fig. 10, this

is much more sensitive to the appearance of larger NPs in the whole ensemble. This can result in crystallite sizes seemingly larger than the size of the NPs as determined by SEM using the distribution maximum. Based on the above observations we can conclude that apart from corrosion, that is a dominant pathway of the degradation of PVP-capped Ag NPs, Ostwald ripening also
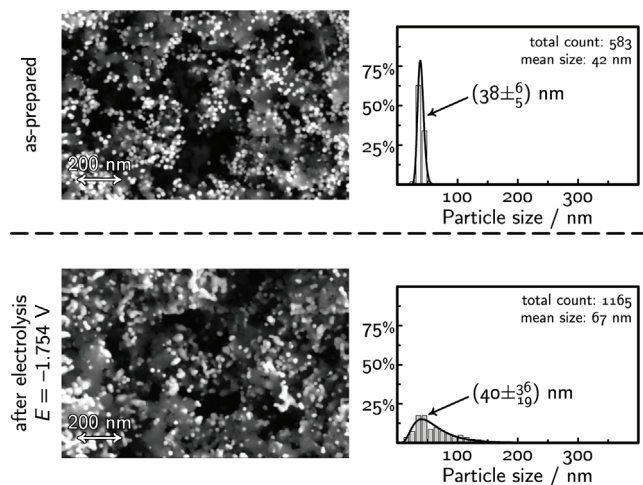
Fig. 9. The partial removal of the excess PVP from the catalyst ink results in less PVP adsorbed on the carbon support, facilitating more the aggregation (rather than the corrosion) of Ag NPs. (Cf. to Figs. 6 and 7).
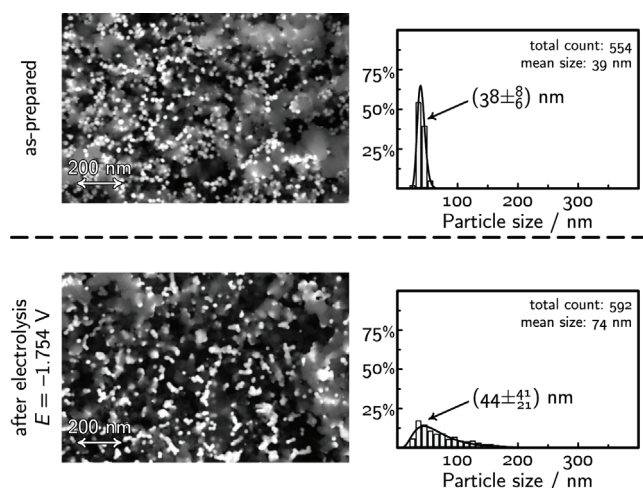

Fig. 10. The partial citrate → PVP ligand exchange in the catalyst ink results in more PVP adsorbed on the carbon support, somewhat hindering the coalescence degradation pathway otherwise observable for citrate-capped NPs. (Cf. to Figs. 6 and 7.).

can milden the coalescence of particles (otherwise characteristic for citrate-capped NPs, see Fig. 6 and 7), and this effect can also be explained by the adsorption of the extra PVP amount on the support surface, hindering the motion of the degrading NPs. (For more details of the electrolysis experiments, see Figure S15b of the Supporting Information.).

4. Conclusion

In this paper we used Ag NPs capped by different stabilizing ligands to prepare gas diffusion electrodes that we applied for CO_2 electroreduction in a zero-gap gas-flow electrolyser. This configuration allowed a high current stressing of the NPs. After careful cleaning of the GDE from the carbonate precipitates formed during electrolysis, we compared SEM images of the catalyst NPs obtained before and after the high current testing, and made these subject to a statistical analysis.

We showed that amongst the studied capping agents, BPEI is the most protective one; in turn, however, it also limits CO formation the most. In case of PVP, mostly corrosion (particle shrinkage)

was observed at practically relevant electrolysing potentials, while the application of PEG and that of citrate lead more to particle coalescence. In parallel with the SEM-based investigations, WAXS analysis was also used to follow the evolution of crystallite size and lattice strain during CO_2RR/HER stressing, and the results were compared to those of SEM mapping.

By studying the effects of capping agent removal and exchange we demonstrated that apart from ligands directly attached to the Ag NPs, also the excess of capping agents (adsorbed on the carbon support surface) plays a decisive role in determining the extent and mode of catalyst degradation.

Declaration of Competing Interest

The authors declare that they have no known competing financial interests or personal relationships that could have appeared to influence the work reported in this paper.

Acknowledgement

Appendix A. Supplementary material

Supplementary data associated with this article can be found, in the online version, at https://doi.org/10.1016/j.jcat.2021.10.016.

References

[1] D.R. Feldman, W.D. Collins, P.J. Gero, M.S. Torn, E.J. Mlawer, T.R. Shippert, Observational determination of surface radiative forcing by CO_2 from 2000 to 2010, Nature 519 (2015) (2000) 339–343, https://doi.org/10.1038/nature14240.

[2] D.T. Whipple, P.J.A. Kenis, Prospects of CO_2 utilization via direct heterogeneous electrochemical reduction, J. Phys. Chem. Lett. 1 (2010) 3451–3458, https://doi.org/10.1021/jz1012627.

[3] H. Coskun, A. Aljabour, P.D. Luna, D. Farka, T. Greunz, D. Stifter, M. Kus, X. Zheng, M. Liu, A.W. Hassel, W. Schöfberger, E.H. Sargent, N.S. Sariciftci, P. Stadler, Biofunctionalized conductive polymers enable efficient CO_2 electroreduction, Sci. Adv. 3 (8) (2017) e1700686, https://doi.org/10.1126/sciadv.1700686.

[4] Y. Hori, Electrochemical CO_2 reduction on metal electrodes, in: C.G. Vayenas, R.E. White, M.E. Gamboa-Aldeco (Eds.), Modern Aspects of Electrochemistry, Vol. 42, Springer, 2008, pp. 89–189.

[5] S. Vesztergom, A. Dutta, M. Rahaman, K. Kiran, I.Z. Montiel, P. Broekmann, Hydrogen bubble templated metal foams as efficient catalysts of CO_2 electroreduction, ChemCatChem 13 (2020) 1039–1058, https://doi.org/10.1002/cctc.202001145.

[6] F. Yu, P. Wei, Y. Yang, Y. Chen, L. Guo, Z. Peng, Material design at nano and atomic scale for electrocatalytic CO_2 reduction, Nano, Mater. Sci. 1 (2019) 60–69, https://doi.org/10.1016/j.nanoms.2019.03.006.

[7] D. Sun, X. Xu, Y. Qin, S.P. Jiang, Z. Shao, Rational design of Ag-based catalysts for the electrochemical CO_2 reduction to CO: A review, ChemSusChem 13 (2019) 39–58, https://doi.org/10.1002/cssc.201902061.

[8] R. Reske, H. Mistry, F. Behafarid, B.R. Cuenya, P. Strasser, Particle size effects in the catalytic electroreduction of CO_2 on Cu nanoparticles, J. Am. Chem. Soc. 136 (19) (2014) 6978–6986, https://doi.org/10.1021/ja500328k.

[9] A. Dutta, A. Kuzume, V. Kaliginedi, M. Rahaman, I. Sinev, M. Ahmadi, B. Roldán Cuenya, S. Vesztergom, P. Broekmann, Probing the chemical state of tin oxide NP catalysts during CO_2 electroreduction: A complementary operando approach, Nano Energy 53 (2018) 828–840, https://doi.org/10.1016/j.nanoen.2018.09.033.

[10] Y. Hou, N. Kovács, H. Xu, C. Sun, R. Erni, M. Gálvez-Vázquez, A. Rieder, H. Hu, Y. Kong, M. Liu, B.J. Wiley, S. Vesztergom, P. Broekmann, Limitations of identical location SEM as a method of degradation studies on surfactant capped nanoparticle electrocatalysts, J. Catal. 394 (2020) 58–66, https://doi.org/10.1016/j.jcat.2020.12.006.

[11] P.C. Okonkwo, O.O. Ige, E.M. Barhoumi, P.C. Uzoma, W. Emori, A. Benamor, A. M. Abdullah, Platinum degradation mechanisms in proton exchange membrane fuel cell (PEMFC) system: A review, Int. J. Hydrog. Energy 46 (29) (2021) 15850–15865, https://doi.org/10.1016/j.ijhydene.2021.02.078.

[12] J. Huang, N. Hörmann, E. Oveisi, A. Loiudice, G.L. De Gregorio, O. Andreussi, N. Marzari, R. Buonsanti, Potential-induced nanoclustering of metallic catalysts during electrochemical CO$_2$ reduction, Nat. Commun. 9 (1) (2018) 3117, https://doi.org/10.1038/s41467-018-05544-3.

[13] J.R. Pankhurst, P. Iyengar, A. Loiudice, M. Mensi, R. Buonsanti, Metal–ligand bond strength determines the fate of organic ligands on the catalyst surface during the electrochemical CO$_2$ reduction reaction, Chem. Sci. 11 (2020) 9296–9302, https://doi.org/10.1039/d0sc03061a.

[14] S. Popović, M. Smiljanić, P. Jovanovič, J. Vavra, R. Buonsanti, N. Hodnik, Stability and degradation mechanisms of copper-based catalysts for electrochemical CO$_2$ reduction, Angew. Chem. 132 (35) (2020) 14844–14854, https://doi.org/10.1002/ange.202000617.

[15] M.de.J. Gálvez-Vázquez, P. Moreno-García, H. Xu, Y. Hou, H. Hu, I. Zelocualtecatl Montiel, A.V. Rudnev, S. Alinejad, V. Grozovski, B.J. Wiley, M. Arenz, P. Broekmann, Environment matters: CO$_2$RR electrocatalyst performance testing in a gas-fed zero-gap electrolyzer, ACS Catal. 10 (21) (2020) 13096–13108, https://doi.org/10.1021/acscatal.0c03609.

[16] H. Hu, M. Liu, Y. Kong, N. Mysuru, C. Sun, M. d. J. Gálvez-Vázquez, U. Müller, R. Erni, V. Grozovski, Y. Hou, P. Broekmann, Activation matters: Hysteresis effects during electrochemical looping of colloidal Ag nanowire catalysts, ACS Catal. 10 (2020) 8503–8514. doi:https://doi.org/10.1021/acscatal.0c02026.

[17] C.-T. Dinh, F.P.G. de Arquer, D. Sinton, E.H. Sargent, High rate, selective, and stable electroreduction of CO$_2$ to CO in basic and neutral media, ACS Energy Lett. 3 (2018) 2835–2840, https://doi.org/10.1021/acsenergylett.8b01734.

[18] T. Haas, R. Krause, R. Weber, M. Demler, G. Schmid, Technical photosynthesis involving CO$_2$ electrolysis and fermentation, Nat. Catal. 1 (2018) 32–39, https://doi.org/10.1038/s41929-017-0005-1.

[19] C.V. Restrepo, C.C. Villa, Synthesis of silver nanoparticles, influence of capping agents, and dependence on size and shape: A review, Environ. Nanotechnol. Monit. Manag. 15 (2021) 100428, https://doi.org/10.1016/j.enmm.2021.100428.

[20] R. Szűcs, D. Balogh-Weiser, E. Sánta-Bell, E. Tóth-Szeles, T. Varga, Z. Kónya, L. Poppe, I. Lagzi, Green synthesis and in situ immobilization of gold nanoparticles and their application for the reduction of p-nitrophenol in continuous-flow mode, RSC Adv. 9 (2019) 9193–9197, https://doi.org/10.1039/c8ra10373a.

[21] M. d. J. Gálvez-Vázquez, H. Xu, P. Moreno-García, Y. Hou, H. Hu, B.J. Wiley, S. Vesztergom, P. Broekmann, Unwrap them first: Operando potential-induced activation is required when using PVP-capped Ag nanocubes as catalysts of CO$_2$ electroreduction, Chimia 75 (2021) 163–168. doi:https://doi.org/10.2533/chimia.2021.163.

[22] J. Kieffer, J.P. Wright, PyFAI: A Python library for high performance azimuthal integration on GPU, Powder Diffr. 28 (2013) S339–S350, https://doi.org/10.1017/s0885715613000924.

[23] B.H. Toby, R.B.V. Dreele, GSAS-II: The genesis of a modern open-source all purpose crystallography software package, J. Appl. Crystallogr. 46 (2013) 544–549, https://doi.org/10.1107/s0021889813003531.

[24] J.S. Yoo, R. Christensen, T. Vegge, J.K. Nørskov, F. Studt, Theoretical insight into the trends that guide the electrochemical reduction of carbon dioxide to formic acid, ChemSusChem 9 (2015) 358–363, https://doi.org/10.1002/cssc.201501197.

[25] C. Spöri, J.T.H. Kwan, A. Bonakdarpour, D.P. Wilkinson, P. Strasser, The stability challenges of oxygen evolving catalysts: Towards a common fundamental understanding and mitigation of catalyst degradation, Angew. Chem. Int. Ed. 56 (2017) 5994–6021, https://doi.org/10.1002/anie.201608601.

[26] I. Schrader, J. Warneke, S. Neumann, S. Grotheer, A.A. Swane, J.J.K. Kirkensgaard, M. Arenz, S. Kunz, Surface chemistry of "unprotected" nanoparticles: A spectroscopic investigation on colloidal particles, J. Phys. Chem. C 119 (31) (2015) 17655–17661, https://doi.org/10.1021/acs.jpcc.5b03863.

[27] J.A.S. Bett, K. Kinoshita, P. Stoneheart, Crystallite growth of platinum dispersed on graphitized carbon black II. Effect of liquid environment, J. Catal. 41 (1976) 124–133, https://doi.org/10.1016/0021-9517(76)90207-4.

[28] P.J. Ferreira, G.J. la O', Y. Shao-Horn, D. Morgan, R. Makharia, S. Kocha, H.A. Gasteiger, Instability of Pt/C electrocatalysts in proton exchange membrane fuel cells, J. Electrochem. Soc. 152 (2005) A2256. doi:https://doi.org/10.1149/1.2050347.

[29] R. Chattot, P. Bordet, I. Martens, J. Drnec, L. Dubau, F. Maillard, Building practical descriptors for defect engineering of electrocatalytic materials, ACS Catal. 10 (2020) 9046–9056, https://doi.org/10.1021/acscatal.0c02144.

5.7. Visualisation and quantification of flooding phenomena in gas diffusion electrodes used for electrochemical CO$_2$ reduction: A combined EDX/ICP-MS approach

Authors: Ying Kong, **Huifang Hu**, Menglong Liu, Yuhui Hou, Viliam Kolivoška, Soma Vesztergom*, and Peter Broekmann*

Highlights: A novel analytic approach, which combines cross-sectional EDX elemental mapping and ICP-MS analysis, was introduced to visualize and quantify the flooding in GDEs. EDX elemental mapping was used to localize the flooding. The mass of flooding based on cations was determined by ICP-MS. Precipitation mapping, which includes the position and amount of flooding, was obtained to integrate these results; this gives a better understanding of electrolyzer malfunctions.

Contributions: I synthesized the Ag NWs and was involved in the scientific discussion of the results.

Visualisation and quantification of flooding phenomena in gas diffusion electrodes used for electrochemical CO_2 reduction: A combined EDX/ICP–MS approach

Ying Kong [a,b], Huifang Hu [a], Menglong Liu [a,b], Yuhui Hou [a,b], Viliam Kolivoška [c], Soma Vesztergom [a,d,*], Peter Broekmann [a,b,*]

[a] University of Bern, Department of Chemistry, Biochemistry and Pharmaceutical Sciences, Freiestrasse 3, 3012 Bern, Switzerland
[b] National Centre of Competence in Research (NCCR) Catalysis, University of Bern, Freiestrasse 3, 3012 Bern, Switzerland
[c] J. Heyrovský Institute of Physical Chemistry of the Czech Academy of Sciences, Dolejškova 2155/3, 18223 Prague, Czech Republic
[d] Eötvös Loránd University, Department of Physical Chemistry, Pázmány Péter sétány 1/A, 1117 Budapest, Hungary

ARTICLE INFO

ABSTRACT

The most promising strategy to scale up the electrochemical CO_2 reduction reaction (ec-CO_2RR) is based on the use of gas diffusion electrodes (GDEs) that allow current densities close to the range of 1 A/cm² to be reached. At such high current densities, however, the flooding of the GDE cathode is often observed in CO_2 electrolysers. Flooding hinders the access of CO_2 to the catalyst, and by thus leaving space for (unwanted) hydrogen evolution, it usually leads to a decrease of the observable Faradaic efficiency of CO_2 reduction products. To avoid flooding as much as possible has thus become one of the most important aims of to-date ec-CO_2RR engineering, and robust analytical methods that can quantitatively assess flooding are now in demand. As flooding is very closely related to the formation of carbonate salts within the GDE structure, in this paper we use alkali (in particular, potassium) carbonates as a tracer of flooding. We present a novel analytical approach —based on the combination of cross-sectional energy-dispersive X-ray (EDX) mapping and inductively coupled plasma mass spectrometry (ICP–MS) analysis— that can not only visualise, but can also quantitatively describe the electrolysis time dependent flooding in GDEs, leading to a better understanding of electrolyser malfunctions.

© 2022 The Authors. Published by Elsevier Inc. This is an open access article under the CC BY-NC-ND license (http://creativecommons.org/licenses/by-nc-nd/4.0/).

1. Introduction

Great progress has recently been made towards the development of new technologies that enable a large-scale reduction of the atmospheric concentration of CO_2, one of the most important contributors of global warming [1]. Among these technologies, electrochemical ones deserve special attention as electrolysers — ideally powered by renewable energy sources— can effectively be used to convert CO_2 into a variety of commodity chemicals and synthetic fuels, such as CO, formic acid, different alcohols and hydrocarbons [2].

In the past few years, the efficiency of newly developed catalysts for the electrochemical CO_2 reduction reaction (ec-CO_2RR) has become so high that under ambient conditions it is not any longer the catalytic activity but rather the limited rate of liquid-phase CO_2 transport that hinders the process [3]. Several attempts have thus been made to boost ec-CO_2RR by increasing the rate of CO_2 transport, and the most promising of these scale-up strategies involve the use of gas diffusion electrodes (GDEs) [4–7].

The use of GDEs enables current densities that are at least one order of magnitude larger than those measurable in standard H-type cells [3,7]. The benefit of achieving high currents comes, however, at the cost of stability issues, and it is primarily the rapid flooding of GDEs that raises most concerns [7–11].

CO_2 electrolysers where the catalyst dispersed over a gas diffusion layer (GDL) contacts the electrolyte solution through a wet membrane —that is, in so-called zero-gap cathode half-cell configurations [7]— flooding usually occurs at high current densities where either the CO_2 reduction reaction itself or its parasitic side-process, hydrogen evolution reaction (HER) cause a significant

near-electrode *p*H increase. The CO_2 supply of the GDE reacts with the electro-generated OH^- ions, which leads to the localised formation of carbonate salts that in turn increases the wettability [8–10] of the GDE and intensifies flooding.

As flooding limits the access of CO_2 to the catalyst, it usually leads to a decrease of the observable Faradaic efficiency of CO_2 reduction products, and leaves space for unwanted hydrogen evolution. To suppress flooding as much as possible, and to understand its mechanism and key factors has thus become one of the most important aims of to-date *ec*-CO_2RR research, and analytical tools that can quantitatively assess the means and extent of flooding are now in demand.

The mechanism of flooding depends on several processes occurring in GDE-based CO_2 electrolysers, and system properties influencing flooding include the wettability of GDEs [12–17] and its dependence on the applied electrode potential (also called electrowetting [18]), the flow-rate [19] and humidity [20,21] of the CO_2 supply, the presence of reaction products [10], and the thickness of the employed membrane [17]. Flooding is very often accompanied by the massive formation of carbonate precipitates on-top, and within deeper layers of the GDE [7–11,18,22–24], and the amount and distribution of carbonates —in case of CO_2 electrolysers operated with a KOH anolyte, these are typically potassium carbonates and bicarbonates— seem to be an important tracer of flooding within the three-dimensional GDE structure.

The aim of this paper is to show that the post-electrolysis analysis of GDE samples by energy-dispersive X-ray (EDX) elemental mapping can easily be used to visualise the electrolysis time dependent penetration of K^+-containing precipitates into the GDE. In order to make the obtained distribution profiles comparable for electrodes that received different electrolysis treatments, it is necessary to convert the relative distribution profiles to absolute concentration *vs.* depth plots that already bear quantitative information. This latter aim can be achieved by an inductively coupled plasma mass spectrometry (ICP–MS)-based determination of the total potassium content of the GDE [25]. The described EDX/ICP–MS combination is a powerful and very robust technique that allows a better understanding of *ec*-CO_2RR electrolyser malfunctions by enabling the accurate visualisation and quantification of flooding phenomena in GDE samples.

2. The method

The scheme of a typical gas-fed CO_2 electrolyser employing a zero-gap cathode half-cell configuration is shown in Fig. 1, with the blown-up section depicting the GDE cathode in direct contact with the anion exchange membrane. The GDE cathode is created by evenly covering the surface of a gas diffusion layer (GDL) with a catalyst ink that can be achieved by using several techniques [3] including drop-casting, airbrushing, vacuum filtering, etc. The uniformity of the catalyst layer thickness depends however not only on the applied technique but also on the imperfections of the gas diffusion layer: especially cracks found on the GDL surface (see, *e.g.*, Fig. 5.b in Section 4) may lead to non-uniform coverage [26–28] and to the burial of some catalyst particles in deeper trenches.

The GDL itself is a bilayer structure that consists of an upper (microporous) and an underlying (fibrous) layer. The microporous layer acts as an electrically conductive mechanical support to the catalyst, holding it in direct contact with the membrane. In many electrolysers, the applied catalyst ink contains silver nanoparticles that direct *ec*-CO_2RR towards the formation of CO as a dominant reaction product [8,11,17,21,24,29]. Note here that CO belongs to the most economically viable *ec*-CO_2RR products [30] and has large

global annual production [3]. The cathode reaction of CO_2-to-CO conversion can be written as

$$CO_2 + H_2O + 2e^- \rightarrow CO + 2OH^-, \tag{1}$$
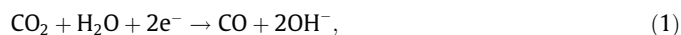
and the operation of the electrolyser should be optimised so that parasitic hydrogen evolution reaction (HER),

$$2H_2O + 2e^- \rightarrow H_2 + 2OH^-, \tag{2}$$
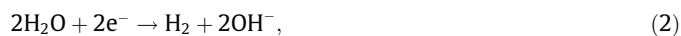
would take place only incidentally.

In the design shown in Fig. 1, a constant (humidified) CO_2 flow penetrates the fibrous part of the GDL, and the CO_2 molecules are transported through the pores of the thin microporous layer to reach the catalyst where they are reduced to CO.

The (essentially wet) membrane has two important roles in the electrolyser: one is that it enables water (a reactant of *ec*-CO_2RR) to access the catalyst, and another is that it allows the passage of the formed OH^- ions (a by-product of CO_2 reduction) from the cathode surface to the anode compartment of the cell. The anode compartment is filled with a solution of KOH, and OH^- ions are oxidised on the Ir anode to form O_2 gas:

$$4OH^- \rightarrow 2H_2O + O_2 + 4e^-. \tag{3}$$

The wettability of the GDL plays a crucial role in determining the cathode performance of gas-fed CO_2 electrolysers. The presence of some amount of water, based on Eq. (1), is essential; however, if too much water enters the GDL structure, it may block the access of CO_2 to the catalyst, shifting the balance of the cathode reaction from the preferred *ec*-CO_2RR towards the parasitic HER [31].

For this reason, GDLs are usually made hydrophobic by the manufacturer (*e.g.*, by a treatment with polytetrafluoroethylene, PTFE) and the conditions of the electrolysis are optimized to uphold hydrophobicity as long as possible. From this point of view, the imperfections of the anion exchange membrane deserve special attention, especially if the membrane allows not only the transfer of OH^- ions, but also the transference of cations. As the real-life behaviour of anion exchange membranes is far from ideal [32], the transference of cations very often occurs, and for example in case of the electrolyser shown by Fig. 1, K^+ ions of the anolyte can thus appear on the cathode side of the cell.

The alkalination of the cathode surface —note that OH^- ions are produced both by Reaction (1) and (2)— clearly acts as a driving force for the transport of K^+ ions from the anode compartment to the cathode, where the alkaline conditions and the presence of CO_2 facilitate the formation of K_2CO_3 or $KHCO_3$ salts. If concentrations are high enough [9], both K_2CO_3 and $KHCO_3$ can form precipitates on-top and within the deeper layers of the GDE. This reduces the hydrophobicity of the GDE and triggers flooding, which ultimately breaks down the overall cell performance.

There seems to be a consensus in literature with regard to that the formation of carbonate precipitates on the cathode side of *ec*-CO_2RR electrolysers is an important indicator of flooding [9–11,20,21,33,34]. In spite of this, scanning electron microscopy (SEM)-based imaging techniques like EDX elemental mapping have only scarcely been used to study the penetration of carbonate precipitates into GDE structures [7,11,34]. The reason behind this is obvious: while EDX elemental (K) mapping, applied in a cross-sectional view to study the penetration of K_2CO_3/$KHCO_3$ precipitates into the GDE structure can give a good qualitative picture about the relative distribution of the formed K^+ salts, the comparison of such elemental maps is by no means straightforward. Such comparisons would require EDX elemental mapping to provide truly quantitative information, which is usually not the case.

Indeed, the quantification of elemental maps is a very demanding task that would not only necessitate the acquisition, storage, and subsequent analysis of entire spectra, pixel-by-pixel [35], but it would also require the in-depth understanding of electron
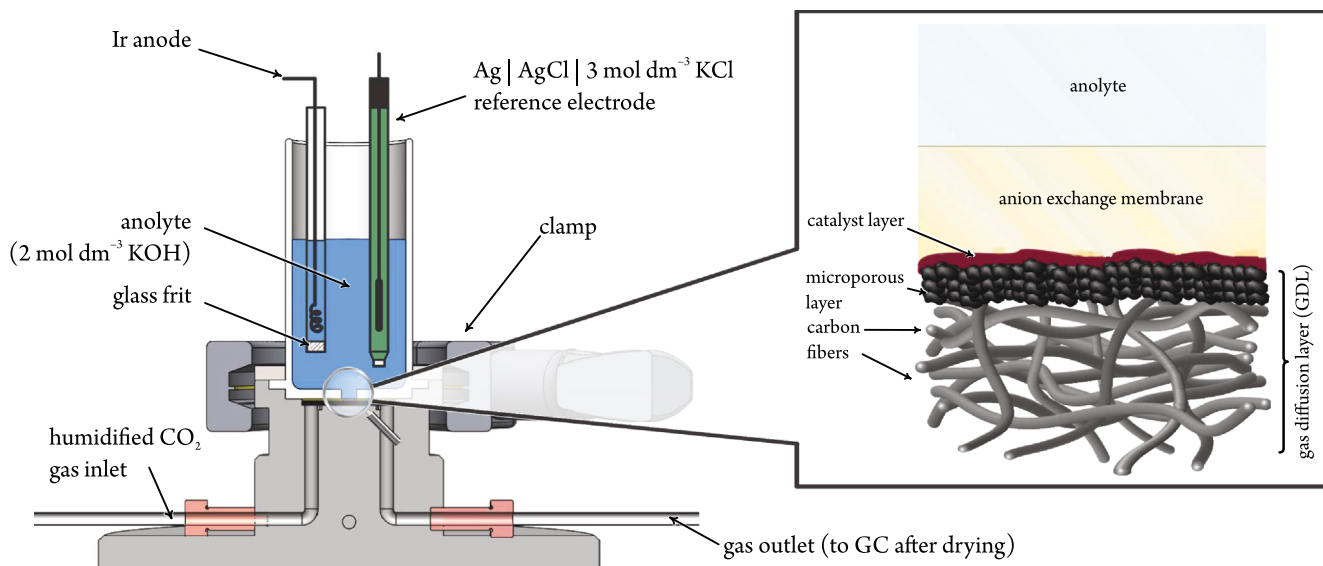
Fig. 1. Scheme of a gas-flow CO_2 electrolyser employing a zero-gap cathode half-cell configuration. The gas diffusion electrode/membrane assembly is shown by the inset at the initial stage of electrolysis.

beam/material interactions, which is particularly challenging when working with heterogeneous and highly porous materials (*e.g.*, GDEs).

X-ray signal intensities are known to depend largely on (amongst other parameters) the applied acceleration voltage [35], and this is exemplarily demonstrated by the cross-sectional EDX elemental (K) maps of Fig. 2. These maps, taken at different applied accelerating voltages, show the same GDE sample that exhibits marks of *ec*-CO_2RR-induced K_2CO_3/$KHCO_3$ precipitation within its structure.

Maps of the top row of Fig. 2 are those shown by the operating software of the SEM instrument. The automatic colouration of these maps is optimised for human perception, and as a result, the maps could lead us to the erroneous conclusion that the potassium concentrations visualised by them are markedly different. As, however, the four maps are made of the very same sample, this is certainly not the case: the maps are differently coloured only because the corresponding K peaks in the EDX spectra become more intense at higher accelerating voltages.

Fortunately, from most SEM operating software, EDX maps can be exported not only in the form of images but also in the form of two-dimensional numerical arrays that represent the (in our case, K) signal intensities over the sampled area. If we create such numerical representations from the four maps shown in the top row of Fig. 2, we get four arrays on which we can perform mathematical operations. We can, for example, normalise the arrays to their (overall) maximum, and we can then convert the arrays back into images. If we use the same colour-code that was applied before, we obtain the images shown by the middle row of Fig. 2. These coloured maps already give a trustworthy representation of intensity ratios; however, at low accelerating voltages, the normalised intensities happen to be so low that we see almost entirely dark fields.

In order to reduce the dependency of intensities on the applied accelerating voltage, we have to normalise each array individually, using their respective maxima as an individual norm. By this approach, we get to the images shown in the bottom row of Fig. 2. These elemental maps, while they all appear a bit dark for the human eye, all look essentially the same. Subtle differences between the images do exist, however, primarily because not only the overall intensity of the spectrum peaks but also the penetration

depth of the electron beam depends on the accelerating voltage [35]. This dependence, while it affects the measured absolute intensities, exerts only a minor effect on the observed relative intensity distributions.

The above two normalisation concepts are illustrated also by the graphs of Fig. 2 that contain sums of intensities for each image row, plotted *vs.* the respective row index. The graphs clearly show that while the recorded K signal intensity does vary greatly with the applied accelerating voltage, and while the exact relationship between local K concentration and intensity may not be known, EDX mapping is still robust enough to deliver a relative distribution of potassium-containing precipitates along the line normal to the GDE surface.

Such relative distributions, obtained from GDEs that had undergone different *ec*-CO_2RR stressing treatment can of course not directly be compared, unless we determine by some other analytical method the total potassium content of the GDE. A variety of elemental analysis methods can be used to achieve this goal; in our practice we favour ICP–MS-based determination.

The essence of the method described here is schematically shown in Fig. 3. On the top surface of GDEs that have previously been used for *ec*-CO_2RR, the appearance of precipitates is usually visible already to the bare eye. The centrally located, salt-covered part (of known geometric area) is removed by a punching blade, and the resulting 'coin' is cut into two by a sharp knife. One part of the coin is briefly sonicated and then left for over-night in a known volume (usually 1 cm^3) of cc. HNO_3, so that its K_2CO_3/$KHCO_3$ content is quantitatively leached. The concentration of the resulting solution is then determined by ICP–MS in known (usually 500 or 1000 times) dilutions: by this method, the total potassium mass that is contained by the given volume of the GDE is calculated and normalised to the base area of the analysed sample. This yields a total surface area-normalised concentration that is usually in the range of a few mg cm^{-2}.

The other half of the coin (Fig. 3) is used for cross-sectional EDX K elemental mapping, without any additional treatment other than drying the sample. In order to improve statistics, usually multiple locations of the same cut are mapped, and sometimes, even additional cuts are made and sampled. The resulting EDX maps are then exported in numerical form, and depth profiles of the relative K distribution are created by row-wise summation. Row indices
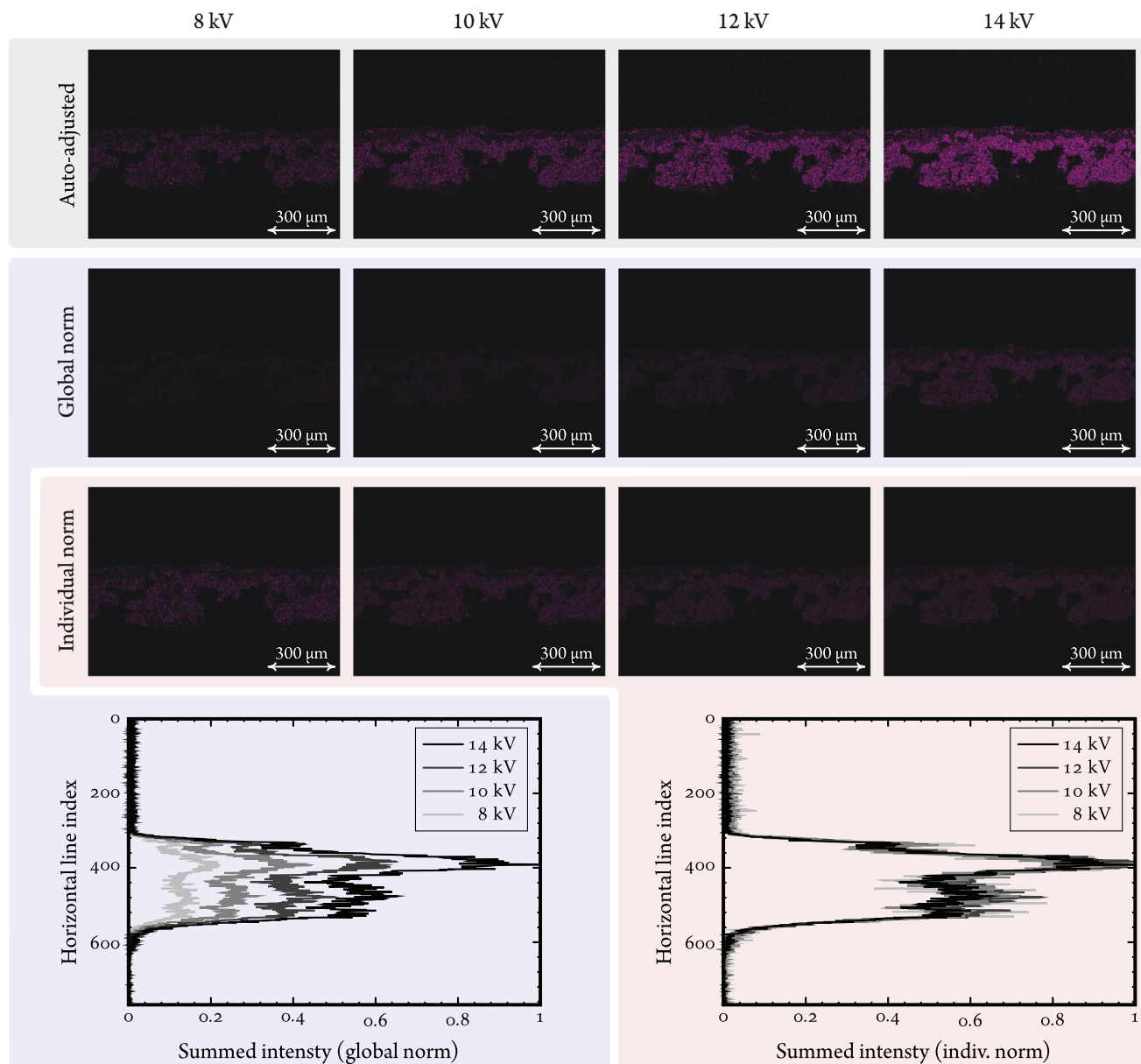
Fig. 2. Electrolysis-induced potassium penetration into a GDE sample visualised by EDX elemental maps (cross-sectional view), recorded using different accelerating voltages as shown. Images of the same column show maps of the exact same intensity dataset, coloured differently. The brightness and the contrast of images in the top row was automatically adjusted for optimal perception by the human eye — this is how most SEM operating software would show these maps. Colour intensities in the middle row were normalised to the largest intensity value detected. In case of the third row, the maps were normalised individually, each to its own maximum intensity. The graphs show the differences of the two normalisation concepts in row-by-row intensity summation. The EDX measurements were made on sample GDE#2, following passage of -1839 C cm^{-2} charge (cf. to Sections 3 and 4, as well as to Fig. 5).

are turned into spatial coordinates knowing the resolution of the map.

The individual relative distributions are aligned on the distance scale by means of (differential) edge detection, and an averaged curve is calculated. The relative distributions are subsequently re-scaled into absolute concentration profiles (usually expressed in units of µg cm^{-3}); the applied scaling factor is chosen so that the full space integral of the averaged absolute concentration profile equals the surface area-normalised concentration determined by ICP–MS.

The described cross-sectional EDX/ICP–MS combination approach yields concentration depth profiles that are comparable for GDE samples that are either of different original structure or that underwent different *ec*-CO$_2$RR stressing treatment (see later

Fig. 5), and can lead to a better understanding of flooding-related phenomena. Note here that in order to obtain statistically reliable data, both the ICP–MS and the EDX mapping measurements are to be repeated several times, using GDE samples that received the very same treatment. As it will be shown later in Fig. 5, this approach helps to identify possible outliers. Also note that ICP–MS measurements may not have to be performed on all (rather just on a few) studied samples, which may reduce the time demand of the analysis.

As the described EDX/ICP–MS combination approach is a post-experimental characterisation technique, it cannot be used for a real-time observation of flooding-related phenomena like it is possible, for example, in *operando* tomographic X-ray absorption spectroscopy [36]. The EDX/ICP–MS combination is, however, a more
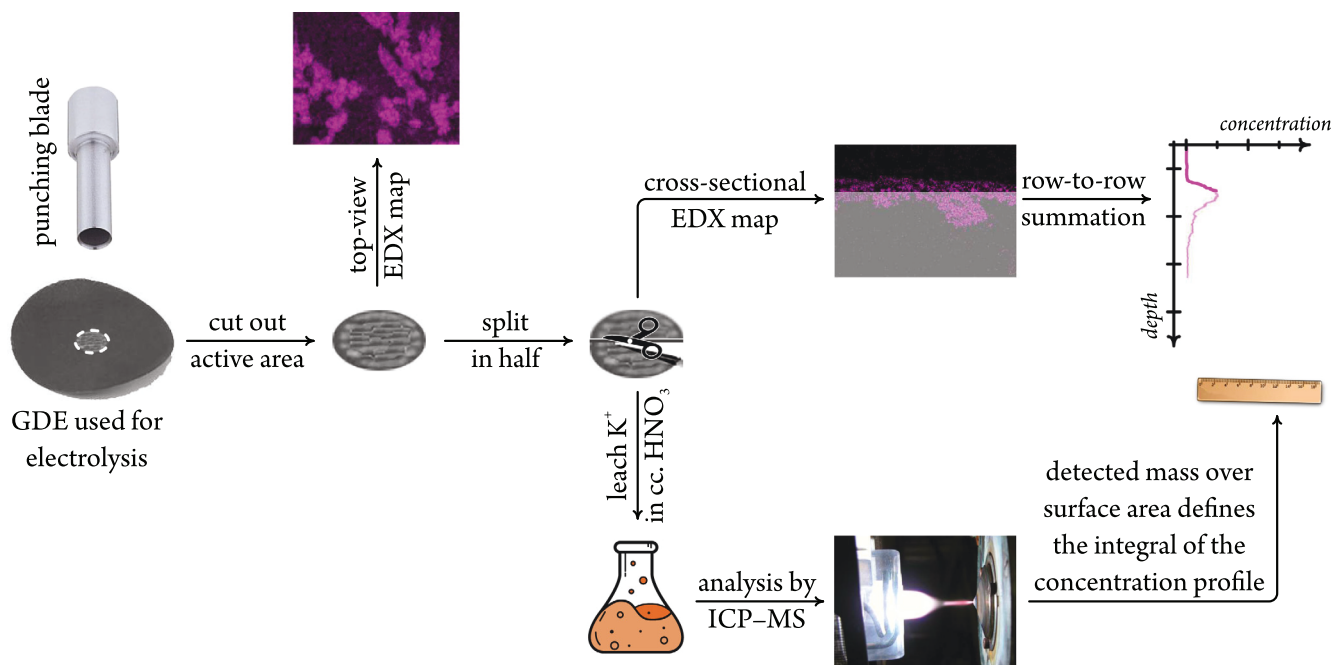
Fig. 3. The strategy to quantitatively assess flooding phenomena in GDEs uses $K_2CO_3/KHCO_3$ precipitates as a tracer of flooding. Following electrolysis, the carbonate precipitates formed over the GDE are visible to the bare eye (and can also be seen by top-down EDX mapping). By cross-sectional EDX, the relative distribution of K can be mapped along the surface normal. Absolute concentration (mass over volume) profiles can be created by applying a scaling factor that sets the integral of the profile equal to the (surface area normalised) K mass determined by ICP–MS analysis.

robust and a considerably cheaper method than X-ray absorption or scattering measurements that require specially designed cells and a significant amount of synchrotron beam-time, and the amount of information gathered from EDX/ICP–MS studies may effectively complement the results of *operando* investigations.

The versatility of the method will be illustrated in Section 4, where we used two different gas diffusion electrodes for CO_2 electrolysis in a gas-fed CO_2 electrolyser employing a zero-gap cathode half-cell configuration, finding that the different structure of the two GDLs result in different $K_2CO_3/KHCO_3$ deposition patterns and, ultimately, different electrolyser stabilities.

3. Experimental

Two commercial gas diffusion layers (Table 1), a Freudenberg H23C8 (GDL#1) and a Sigracet 36BB (GDL#2) paper, were used in this study. The microporous layers of both GDLs contain $\sim 5\%$ PTFE as a water repelling agent.

To prepare a catalyst ink, 4.5 mg of silver nanowires (Ag NWs, prepared as described in [37]) and 0.8 mg of carbon black (VULCAN^{TM} VXC72R, Cabot) were separately dispersed in 20 cm^3 of isopropanol (BASF SE, assay $\geqslant$ 99.0%) by half hour of sonication. Both suspensions were intermixed and sonicated for an additional

Table 1
Parameters of the gas diffusion layers used in this study.

	GDL#1, Freudenberg H23C8	GDL#2, Sigracet 36BB
Microporous layer thickness*	41 μm	97 μm
Fibrous layer thickness*	194 μm	160 μm
Electrical resistivity†	8 mΩ cm^2	9 mΩ cm^2
Area density†	135 g cm^{-2}	105 g cm^{-2}
Air permeability†	90 Gurley s	3 Gurley s

* Average values, determined by cross-sectional SEM.
† Values provided by the manufacturer.

half hour, then dried by a rotary evaporator (Büchi R210, 40 °C, 65 mbar). The resulting mixture was then re-dispersed in 18 cm^3 of isopropanol containing 180 $\mu\ell$ of Nafion 117 solution (Sigma–Aldrich, $\sim$ 5 wt% in a mixture of lower aliphatic alcohols and water) and subjected to 20 min of sonication. Subsequently, the resulting ink was carefully dispersed by using an airbrush pistole (Infinity CR plus) propelled by nitrogen gas (99.999%, Carbagas, Switzerland) onto the GDL substrate.

A CO_2 electrolyser with a zero-gap cathode half-cell configuration (see Fig. 1, details of the electrolyser were described previously in [7,38–41]) was used for the electrochemical reduction of CO_2. The Ag NW-coated GDEs were placed on the stainless steel body, with the Ag NW layer directed upwards. The such formed cathode was then covered by an anion exchange membrane (AEM, X37-50 RT, Dioxide materials), on top of which a PTFE chamber was placed to support the anolyte, a 2.0moldm^{-3} aqueous KOH solution (KOH, analytical grade, was purchased from Sigma Aldrich). A central orifice with a diameter of 3 mm at the bottom of the anode compartment provided contact between the anolyte and the membrane-cathode assembly, and the area of this opening (0.0707 cm^2) was considered the geometric surface area of the cathode, used for the normalization of current to current density. An iridium (Ir) wire (99.9%, MaTeck Material-Technologie & Kristalle GmbH, Germany) separated by a glass frit from the anolyte compartment, and a Ag|AgCl|3moldm^{-3} KCl electrode (double junction design, Metrohm) immersed directly into the anolyte were used as counter and reference electrodes. A humidified CO_2 stream (99.999%, Carbagas, Switzerland) was fed to the fibrous layer of the cathode from the backside of the cell at a constant volumetric flow rate of 18 cm^3 min^{-1}. Electrolyses were carried out using an ECi-200 potentiostat (Nordic Electrochemistry) at a constant current of −20 mA, resulting in a current density of −283 mA cm^{-2}, during which the formed gaseous reaction products were quantified by online gas chromatography (GC, SRI Instruments), as described elsewhere [7].

For the SEM and EDX studies presented in the paper, a Zeiss Gemini 450 SEM was applied, equipped with an InLens secondary electron (SE), a backscatter electron detector (BSD) and a SuperEDX detector.

Contact angle measurements were carried out using a Krüss Advance Drop Shape Analyzer DSA25 (Krüss GmbH, Hamburg, Germany). Electrodes were mounted on a flat stage and water drops (milli-Q water, 1.4 $\mu\ell$) were deposited at room temperature.

Raw data, as well as unprocessed measurement files serving as a basis of this publication can be downloaded from Zenodo [42].

4. Demonstrative experiments

Two gas diffusion electrodes —one supported by a Freudenberg H23C8 paper (GDL#1), and another by a Sigracet 36BB paper (GDL#2)— were created and used in our experiments. The two GDLs, as can be seen in Table 1, are of different structure, and

Fig. 4. The top-down optical microscopy image of the two studied gas diffusion electrodes exhibit a compact microporous layer in case of GDE#1 (a), while the top surface of GDE#2 (b) is laced by small cracks. Both GDEs exhibit severe stability losses (a decrease of the Faradaic efficiency of CO production as a function of the passed charge) when made subject to electrolysis at a constant current density of –283 mA cm^{-2}. While GDE#1 quickly loses stability (c), GDE#2 remains stable for longer time (d). The hydrophobicity of both GDLs decrease heavily during prolonged *ec*-CO$_2$RR stressing (consumed charge: –1839 C cm^{-2}), as revealed by the pre- and post-electrolysis contact angle measurements shown in the insets of (c) and (d). The shift from *ec*-CO$_2$RR to HER is also indicated by changes of the measured electrode potentials shown in panels (e) and (f). That the mentioned hydrophobicity loss is caused by the appearance of K$_2$CO$_3$ or KHCO$_3$ precipitates on-top of both GDEs during electrolysis is clearly shown by the top-down EDX elemental maps of (g) and (h), recorded after the total charge of –1839 C cm^{-2} is passed through the GDEs.

the majority of differences arise from that while the microporous layer of GDL#1 is thinner but more compact (Fig. 4.a), the relatively thick microporous layer of GDL#2 is laced by small cracks that are visible also to the bare eye (Fig. 4.b).

When made subject to constant-current electrolyses experiments (applied current density: –283 mA cm^{-2}), both GDEs initially produce CO at close to 100% Faradaic efficiency. As the electrolysis continues to longer times, the observed Faradaic efficiency however drops down (Fig. 4.c and 4.d), and the observed stability loss commences earlier in case of GDE#1 (with the compact structure) than in case of GDE#2 (having a cracked microporous layer).

The observed efficiency loss is due to the flooding of the GDEs, which can be inferred not only from pre- and post-electrolysis sessile drop goniometry that clearly demonstrates a significant decrease of the surface hydrophobicity during electrolysis (insets of Fig. 4.c and 4.d), but also from top-down EDX elemental mapping that exhibits the formation of massive amounts of K$_2$CO$_3$/KHCO$_3$ precipitates on top of both GDE samples (Fig. 4.e and 4.f).

These top-down EDX elemental maps provide a straightforward explanation of the observed stability differences: while at the end of electrolysis, GDE#1 is more or less uniformly covered by K$_2$CO$_3$/KHCO$_3$ precipitates (and it is safe to assume that this uniform precipitate layer practically blocks all active Ag catalyst sites), we observe a rather non-uniform coverage (and an only partially blocked catalytic activity) in case of GDE#2. As to why the two GDEs are covered differently by the formed carbonate precipitates, top-down EDX mapping provides no answer, however. In order to address this question we have to rely on the combined cross-sectional EDX/ICP–MS method described previously in Section 2.

When GDE samples are made subject to electrolyses consuming different amounts of charge, and the samples are processed as was shown before in Fig. 3, the obtained absolute concentration *vs.* depth profiles are those shown by Fig. 5. Based on these profiles, a very important observation can be made: namely, that the total amount of formed precipitates, as well as the extent to which they penetrate the GDE structure is markedly different on GDE#1 and #2.

On GDE#1 —with the compact surface— K$_2$CO$_3$ and KHCO$_3$ precipitates are mainly formed (and remain) inside the catalyst layer and inside the pores of the microporous layer, and appear only in little amount in the underlying (fibrous) structure. As the microporous layer has a very limited capacity to store the formed carbonates —note that with increasing charge, the concentration profiles seem to saturate—, catalytic sites become blocked, and this results in the quick break-down of the measured Faradaic efficiency (cf. to Fig. 4.c). This saturation effect can well be observed in case of GDE#1, where at charges of −510.0 C cm^{-2} and −1839 C cm^{-2} the K concentration distribution (Fig. 5) within the microporous layer varies only a little, while the Faradaic efficiency of CO production is already significantly lowered at −510.0 C cm^{-2}. In case of GDE#2, the (cracked) microporous layer has a higher capacity to store potassium precipitates, and saturation of the microporous layer (resulting in a significant decrease of the Faradaic efficiency) seems to occur only at −1839 C cm^{-2}.

The higher durability of GDE#2 is probably a result of the presence of cracks in its microporous layer. These cracks allow a direct access of electrolyte solution to the fibrous layer, hence carbonates will also be able to precipitate in deeper parts of the GDE structure. Neither the electrolyte that penetrates the fibrous layer, nor the carbonate crystals which are formed there will block the active catalytic sites on-top of the microporous layer. As a result, the break-down of the Faradaic efficiency of CO production will commence on GDE#2 much later than on GDE#1, since in the (due to the
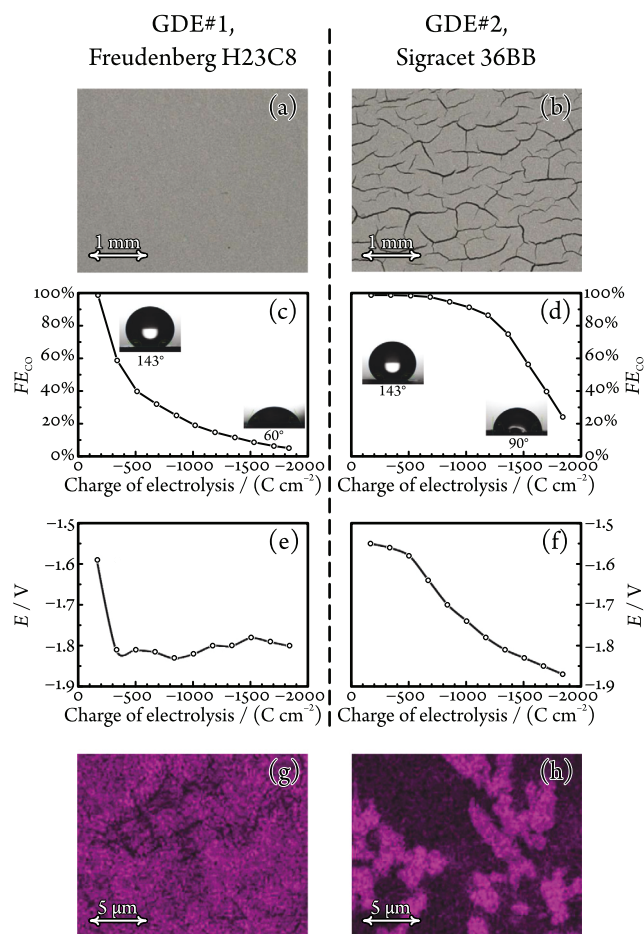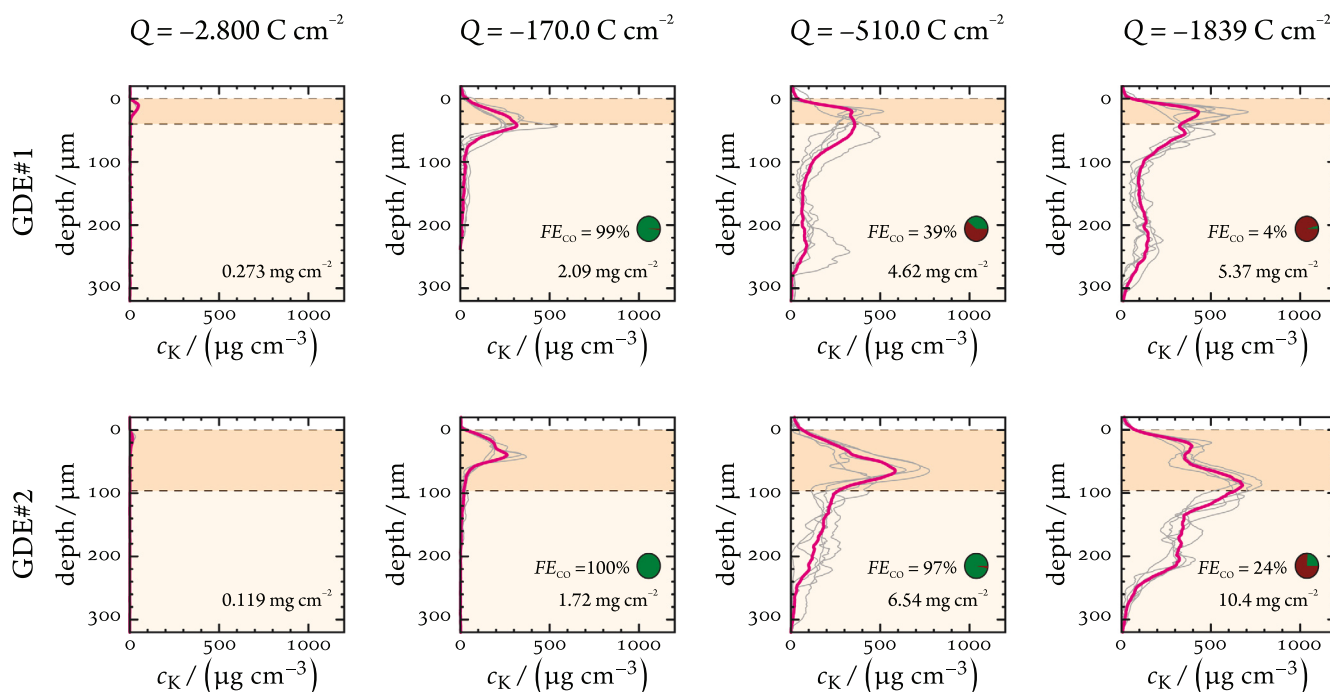
Fig. 5. Depth profiles of the absolute K^+ concentrations in different GDE samples, following electrolyses consuming different charges. The profiles were created by the cross-sectional EDX mapping/ICP–MS combination described in Section 2. (Grey curves show individual, magenta curves the averaged profiles.) The integral of each profile —that is, the total potassium content of the GDE normalised to surface area, determined by ICP–MS—, as well as the Faradaic efficiency of CO production, measured at the moment before the electrolysis was stopped, is given in each panel. The background shading of the panels pictures the GDL as a bi-layer structure (darker shading corresponds to the mic.roporous layer).

cracks, more penetrable) structure of GDE#2 a significantly bigger amount of K^+-containing precipitates has to be formed to effectively block the access of CO_2 to the catalyst layer. In case of GDE#1, blockage to the same effect occurs earlier, as in the absence of eluviation accelerating cracks, the formed precipitates quickly reach a critical concentration in the microporous layer.

Our results thus demonstrate that the crackedness of the GDL surface (maybe, somewhat counter-intuitively) plays a seemingly beneficial role in the water management of the GDE.

5. Conclusion

When *ec*-CO_2RR is carried out in a gas-fed CO_2 electrolyser with a zero-gap cathode half-cell configuration, K_2CO_3/$KHCO_3$ precipitation inside the GDE structure is a sovereign symptom (and probably an important driving force) of flooding. By determining, following electrolysis, the concentration distribution of carbonate salt leftovers within a GDE, we can assess the extent of flooding that occurred during the operation of the electrolyser, and we can better explain any observed stability losses and electrolyser malfunctions.

In this paper, a robust analytical method, based on the combination of cross-sectional EDX elemental mapping and ICP–MS-based analysis, was suggested in order to achieve the above goal. The novelty of this combination is that by ICP–MS measurements we turn EDX elemental —an essentially qualitative technique— into a quantitative characterisation tool that makes the obtained concentration profiles comparable across different GDE samples.

The basic concept and the technical details of the method were accurately described in the paper, and we also presented a short case study that demonstrated the applicability of the method.

We prepared two gas diffusion electrodes (one with a compact, another with a cracked microporous layer support) and made these subject to *ec*-CO_2RR stressing. We found that while the GDE with

the compact surface looses stability (in terms of CO producing efficiency) rather quickly, the one with the cracked surface preserves its stability for a longer time. The newly developed, cross-sectional EDX elemental mapping/ICP–MS-based depth profiling tool provided an insight to the background of these efficiency losses. We found that the fibrous layer of GDEs (provided that it is accessible to water through the cracks of the microporous layer) may act as a reservoir for flooding, and as such, it can prevent (or at least postpone) the flooding-related deactivation of the catalyst layer.

The EDX/ICP–MS-based K precipitation mapping approach described in this paper will in future be used for the creation of statistically meaningful datasets based on which a systematic comparison of various gas diffusion layers and catalyst design concepts can be carried out.

Declaration of Competing Interest

The authors declare that they have no known competing financial interests or personal relationships that could have appeared to influence the work reported in this paper.

Acknowledgement

References

[1] C. Hepburn, E. Adlen, J. Beddington, E.A. Carter, S. Fuss, N.M. Dowell, J.C. Minx, P. Smith, Ch.K. Williams, The technological and economic prospects for CO₂ utilization and removal, Nature 575 (7781) (2019) 87–97, https://doi.org/10.1038/s41586-019-1681-6.

[2] C.A.R. Pappijn, M. Ruitenbeek, M.-F. Reyniers, K.M. Van Geem, Challenges and opportunities of carbon capture and utilization: Electrochemical conversion of CO₂ to ethylene, Front. Energy Res. 8 (2020) 557466, https://doi.org/10.3389/fenrg.2020.557466.

[3] B. Endrődi, G. Bencsik, F. Darvas, R. Jones, K. Rajeshwar, Cs. Janáky, Continuous-flow electroreduction of carbon dioxide, Prog. Energy Combust. Sci. 62 (2017) 133–154, https://doi.org/10.1016/j.pecs.2017.05.005.

[4] J.-B. Vennekoetter, R. Sengpiel, M. Wessling, Beyond the catalyst: How electrode and reactor design determine the product spectrum during electrochemical CO₂ reduction, Chem. Engin. J. 364 (2019) 89–101, https://doi.org/10.1016/j.cej.2019.01.045.

[5] Y. Gu, J. Wei, X. Wu, X. Liu, A study on improving the current density performances of CO₂ electrolysers, Sci. Rep. 11 (2021) 11136, https://doi.org/10.1038/s41598-021-90581-0.

[6] B. Jung, S. Park, C. Lim, W.H. Lee, Y. Lim, J. Na, Ch.-J. Lee, H.-S. Oh, U. Lee, Design methodology for mass transfer-enhanced large-scale electrochemical reactor for CO₂ reduction, Chem. Eng. J. 424 (2021) 130265, https://doi.org/10.1016/j.cej.2021.130265.

[7] M.deJ. Gálvez-Vázquez, P. Moreno-García, H. Xu, Y. Hou, H. Hu, I.Z. Montiel, A. V. Rudnev, Sh. Alinejad, V. Grozovski, B.J. Wiley, M. Arenz, P. Broekmann, Environment matters: CO₂RR electrocatalyst performance testing in a gas-fed zero-gap electrolyzer, ACS Catal. 10 (2020) 13096–13108, https://doi.org/10.1021/acscatal.0c03609.

[8] K. Yang, R. Kas, W.A. Smith, Th. Burdyny, Role of the carbon-based gas diffusion layer on flooding in a gas diffusion electrode cell for electrochemical CO₂ reduction, ACS Energy Lett. 6 (2020) 33–40, https://doi.org/10.1021/acsenergylett.0c02184.

[9] M.E. Leonard, L.E. Clarke, A. Forner-Cuenca, S.M. Brown, F.R. Brushett, Investigating electrode flooding in a flowing electrolyte, gas-fed carbon dioxide electrolyzer, ChemSusChem 13 (2) (2019) 400–411, https://doi.org/10.1002/cssc.201902547.

[10] M.E. Leonard, M.J. Orella, N. Aiello, Y. Román-Leshkov, A. Forner-Cuenca, F.R. Brushett, Flooded by success: On the role of electrode wettability in CO₂ electrolyzers that generate liquid products, J. Electrochem. Soc. 167 (2020) 124521, https://doi.org/10.1149/1945-7111/abaa1a.

[11] B. Endrődi, A. Samu, E. Kecsenovity, T. Halmágyi, D. Sebők, Cs. Janáky, Operando cathode activation with alkali metal cations for high current density operation of water-fed zero-gap carbon dioxide electrolysers, Nature Energy 6 (2021) 439–448, https://doi.org/10.1038/s41560-021-00813-w.

[12] Z. Xing, X. Hu, X. Feng, Tuning the microenvironment in gas-diffusion electrodes enables high-rate CO₂ electrolysis to formate, ACS Energy Lett. 6 (2021) 1694–1702, https://doi.org/10.1021/acsenergylett.1c00612.

[13] Z. Xing, L. Hu, D.S. Ripatti, X. Hu, X. Feng, Enhancing carbon dioxide gas-diffusion electrolysis by creating a hydrophobic catalyst microenvironment, Nature Comm. 12 (2021) 1–11, https://doi.org/10.1038/s41467-020-20397-5.

[14] B. Kim, F. Hillman, M. Ariyoshi, S. Fujikawa, P.J.A. Kenis, Effects of composition of the micro porous layer and the substrate on performance in the electrochemical reduction of CO₂ to CO, J. Power Sources 312 (2016) 192–198, https://doi.org/10.1016/j.jpowsour.2016.02.043.

[15] W.H. Lee, Y.-J. Ko, Y. Choi, S.Y. Lee, C.H. Choi, Y.J. Hwang, B.K. Min, P. Strasser, H.-S. Oh, Highly selective and scalable CO₂ to CO - electrolysis using coral-nanostructured Ag catalysts in zero-gap configuration, Nano Energy 76 (2020) 105030, https://doi.org/10.1016/j.nanoen.2020.105030.

[16] U.O. Nwabara, A.D. Hernandez, D.A. Henckel, X. Chen, E.R. Cofell, M.P. de Heer, S. Verma, A.A. Gewirth, P.J.A. Kenis, Binder-focused approaches to improve the stability of cathodes for CO₂ electroreduction, ACS Appl. Energy Mater. 4 (2021) 5175–5186, https://doi.org/10.1021/acsaem.1c00715.

[17] A. Reyes, R.P. Jansonius, B.A.W. Mowbray, Y. Cao, D.G. Wheeler, J. Chau, D.J. Dvorak, C.P. Berlinguette, Managing hydration at the cathode enables efficient CO₂ electrolysis at commercially relevant current densities, ACS Energy Lett. 5 (2020) 1612–1618, https://doi.org/10.1021/acsenergylett.0c00637.

[18] F. Bienen, J. Hildebrand, D. Kopljar, N. Wagner, E. Klemm, K.A. Friedrich, Importance of time-dependent wetting behavior of gas-diffusion electrodes for reactivity determination, Chem. Ing. Tech. 93 (2021) 1015–1019, https://doi.org/10.1002/cite.202000192.

[19] B. De Mot, J. Hereijgers, M. Duarte, T. Breugelmans, Influence of flow and pressure distribution inside a gas diffusion electrode on the performance of a flow-by CO₂ electrolyzer, Chem. Eng. J. 378 (2019) 122224, https://doi.org/10.1016/j.cej.2019.122224.

[20] B. Endrődi, E. Kecsenovity, A. Samu, F. Darvas, R.V. Jones, V. Török, A. Danyi, Cs. Janáky, Multilayer electrolyzer stack converts carbon dioxide to gas products at high pressure with high efficiency, ACS Energy Lett. 4 (2019) 1770–1777, https://doi.org/10.1021/acsenergylett.9b01142.

[21] D.G. Wheeler, B.A.W. Mowbray, A. Reyes, F. Habibzadeh, J. He, C.P. Berlinguette, Quantification of water transport in a CO₂ electrolyzer, Energy Environ. Sci. 13 (12) (2020) 5126–5134, https://doi.org/10.1039/d0ee02219e.

[22] D. McLaughlin, M. Bierling, R. Moroni, Ch. Vogl, G. Schmid, S. Thiele, Tomographic reconstruction and analysis of a silver CO₂ reduction cathode, Adv. Energy Mater. 10 (19) (2020) 2000488, https://doi.org/10.1002/aenm.202000488.

[23] F. Bienen, D. Kopljar, A. Löwe, S. Geiger, N. Wagner, E. Klemm, K.A. Friedrich, Revealing mechanistic processes in gas-diffusion electrodes during CO₂ reduction via impedance spectroscopy, ACS Sustainable Chem. Eng. 8 (2020) 13759–13768, https://doi.org/10.1021/acssuschemeng.0c04451.

[24] E.R. Cofell, U.O. Nwabara, S.S. Bhargava, D.E. Henckel, P.J.A. Kenis, Investigation of electrolyte-dependent carbonate formation on gas diffusion electrodes for CO₂ electrolysis, ACS Appl. Mater. Interfaces 13 (2021) 15132–15142, https://doi.org/10.1021/acsami.0c21997.

[25] B. De Mot, M. Ramdin, J. Hereijgers, Th.J.H. Vlugt, T. Breugelmans, Direct water injection in catholyte-free zero-gap carbon dioxide electrolyzers, ChemElectroChem 7 (2020) 3839–3843, https://doi.org/10.1002/celc.202000961.

[26] D. Raciti, T. Braun, B.M. Tackett, H. Xu, M. Cruz, B.J. Wiley, Th.P. Moffat, High-aspect-ratio Ag nanowire mat electrodes for electrochemical CO production from CO₂, ACS Catal. 11 (2021) 11945–11959, https://doi.org/10.1021/acscatal.1c02783.

[27] A.J. Welch, A.Q. Fenwick, A. Böhme, H.-Y. Chen, I. Sullivan, X. Li, J.S. DuChene, C. Xiang, H.A. Atwater, Operando local pH measurement within gas diffusion electrodes performing electrochemical carbon dioxide reduction, J. Phys. Chem. C 125 (2021) 20896–20904, https://doi.org/10.1021/acs.jpcc.1c06265.

[28] H.-R. Jhong, F.R. Brushett, P.J.A. Kenis, The effects of catalyst layer deposition methodology on electrode performance, Adv. Energy Mater. 3 (2013) 589–599, https://doi.org/10.1002/aenm.201200759.

[29] H. Haspel, J. Gascon, Is hydroxide just hydroxide? Unidentical CO₂ hydration conditions during hydrogen evolution and carbon dioxide reduction in zero-gap gas diffusion electrode reactors, ACS Appl. Energy Mater. 4 (2021) 8506–8516, https://doi.org/10.1021/acsaem.1c01693.

[30] S. Verma, B. Kim, H.-R. Jhong, S. Ma, P.J.A. Kenis, A gross-margin model for defining technoeconomic benchmarks in the electroreduction of CO₂, ChemSusChem 9 (2016) 1972–1979, https://doi.org/10.1002/cssc.201600394.

[31] N.T. Nesbitt, Th. Burdyny, H. Simonson, D. Salvatore, D. Bohra, R. Kas, W.A. Smith, Liquid–solid boundaries dominate activity of CO₂ reduction on gas-diffusion electrodes, ACS Catal. 10 (2020) 14093–14106, https://doi.org/10.1021/acscatal.0c03319.

[32] T. Luo, S. Abdu, M. Wessling, Selectivity of ion exchange membranes: A review, J. Membr. Sci. 555 (2018) 429–454, https://doi.org/10.1016/j.memsci.2018.03.051.

[33] R. Wang, H. Haspel, A. Pustovarenko, A. Dikhtiarenko, A. Russkikh, G. Shterk, D. Osadchii, S. Ould-Chikh, M. Ma, W.A. Smith, K. Takanabe, F. Kapteijn, J. Gascon, Maximizing Ag utilization in high-rate CO₂ electrochemical reduction with a coordination polymer-mediated gas diffusion electrode, ACS Energy Lett. 4 (2019) 2024–2031, https://doi.org/10.1021/acsenergylett.9b01509.

[34] M. Liu, Y. Kong, H. Hu, N. Kovács, Ch. Sun, I.Z. Montiel, M.deJ. Gálvez Vázquez, Y. Hou, M. Mirolo, I. Martens, J. Drnec, S. Vesztergom, P. Broekmann, The capping agent is the key: Structural alterations of Ag NPs during CO₂ electrolysis probed in a zero-gap gas-flow configuration, J. Catal. 404 (2021) 371–382, https://doi.org/10.1016/j.jcat.2021.10.016.

[35] J.J. Friel, Ch.E. Lyman, Tutorial review: X-ray mapping in electron-beam instruments, Microsc. Microanal. 12 (2006) 2–25, https://doi.org/10.1017/s1431927606060211.

[36] N.J. Firet, Th. Burdyny, N.T. Nesbitt, S. Chandrashekar, A. Longo, W.A. Smith, Copper and silver gas diffusion electrodes performing CO₂ reduction studied through operando X-ray absorption spectroscopy, Catal. Sci. Technol. 10 (2020) 5870–5885, https://doi.org/10.1039/d0cy01267j.

[37] H. Hu, M. Liu, Y. Kong, N. Mysuru, Ch. Sun, M.deJ. Gálvez-Vázquez, U. Müller, R. Erni, V. Grozovski, Y. Hou, P. Broekmann, Activation matters: Hysteresis effects during electrochemical looping of colloidal ag nanowire catalysts, ACS Catal. 10 (2020) 8503–8514, https://doi.org/10.1021/acscatal.0c02026.

[38] M.deJ. Gálvez Vázquez, H. Hu, Y. Hou, P. Moreno-García, A. Zana, G.K.H. Wiberg, P. Broekmann, M. Arenz, Testing a silver nanowire catalyst for the selective CO₂ reduction in a gas diffusion electrode half-cell setup enabling high mass transport conditions, Chimia 73 (2019) 922–927, https://doi.org/10.2533/chimia.2019.922.

[39] Sh. Alinejad, J. Quinson, G.K.H. Wiberg, N. Schlegel, D. Zhang, Y. Li, S. Reichenberger, St. Barcikowski, M. Arenz, Electrochemical reduction of CO₂ on Au electrocatalysts in a zero-gap, half-cell gas diffusion electrode setup: a systematic performance evaluation and comparison to a H-cell setup, in: ChemRxiv, Cambridge Open Engage, 2021. https://doi.org/10.33774/chemrxiv-2021-1t50s-v3.

[40] G.K.H. Wiberg, M. Fleige, M. Arenz, Gas diffusion electrode setup for catalyst testing in concentrated phosphoric acid at elevated temperatures, Rev. Sci. Instrum. 86 (2015) 024102, https://doi.org/10.1063/1.4908169.

[41] M. Inaba, A.W. Jensen, G.W. Sievers, M. Escudero-Escribano, A. Zana, M. Arenz, Benchmarking high surface area electrocatalysts in a gas diffusion electrode: Measurement of oxygen reduction activities under realistic conditions, Energy Environ. Sci. 11 (2018) 988–994, https://doi.org/10.1039/c8ee00019k.

[42] Y. Kong, H. Hu, M. Liu, Y. Hou, V. Kolivoška, S. Vesztergom, P. Broekmann, Raw data for the article Visualisation and quantification of flooding phenomena in gas diffusion electrodes used for electrochemical CO₂ reduction: A combined EDX/ICP–MS approach (2022). https://doi.org/10.5281/ZENODO.6037503.

5.8 Cracks as efficient tools to mitigate flooding in gas diffusion electrodes in electrochemical reduction of carbon dioxide

Authors: Ying Kong, Menglong Liu, **Huifang Hu**, Yuhui Hou, Soma Vesztergom, María de Jesus Gálvez-Vázquez, Iván Zelocualtecatl Montiel, Viliam Kolivoška*, and Peter Broekmann*

Highlights: Commercial GDLs differing in the abundance of cracks in the MPL were selected as catalyst support for electrochemical CO_2RR. The analytic approach combing SEM imaging, EDX elemental mapping, and ICP-MS analysis was applied to obtain the concentration and distribution of precipitation in GDEs. The amount of electrolyte in the perspiration was detected via ICP-MS. The GDEs with numerous cracks display longer sustainable CO_2RR, while the CO_2RR decays in minutes in the GDEs without cracks. Analysis of EDX mapping of precipitation and ICP-MS results reveals that the cracks serve as pathways for the electrolyte transport through the MPL and therefore mitigate the flooding of GDEs. The electrolyte perspiration rate has been demonstrated as an important parameter for the stability of electrolysis system.

Contributions: I synthesized the Ag NWs, conducted some of EDX studies, and participated in the analysis and discussion of results.

Cracks as Efficient Tools to Mitigate Flooding in Gas Diffusion Electrodes Used for the Electrochemical Reduction of Carbon Dioxide

Ying Kong, Menglong Liu, Huifang Hu, Yuhui Hou, Soma Vesztergom, María de Jesus Gálvez-Vázquez, Iván Zelocualtecatl Montiel, Viliam Kolivoška,* and Peter Broekmann*

The advantage of employing gas diffusion electrodes (GDEs) in carbon dioxide reduction electrolyzers is that they allow CO_2 to reach the catalyst in gaseous state, enabling current densities that are orders of magnitude larger than what is achievable in standard H-type cells. The gain in the reaction rate comes, however, at the cost of stability issues related to flooding that occurs when excess electrolyte permeates the micropores of the GDE, effectively blocking the access of CO_2 to the catalyst. For electrolyzers operated with alkaline electrolytes, flooding leaves clear traces within the GDE in the form of precipitated potassium (hydrogen)carbonates. By analyzing the amount and distribution of precipitates, and by quantifying potassium salts transported through the GDE during operation (electrolyte perspiration), important information can be gained with regard to the extent and means of flooding. In this work, a novel combination of energy dispersive X-ray and inductively coupled plasma mass spectrometry based methods is employed to study flooding-related phenomena in GDEs differing in the abundance of cracks in the microporous layer. It is concluded that cracks play an important role in the electrolyte management of CO_2 electrolyzers, and that electrolyte perspiration through cracks is paramount in avoiding flooding-related performance drops.

1. Introduction

Rising levels of atmospheric CO_2 as a dominant greenhouse gas have motivated endeavors to curb carbon emissions and utilize excess CO_2 to produce valuable resources.[1] The electrochemical reduction of CO_2 (denoted hereafter ERCO$_2$) allows not only its conversion to fuels and feedstock chemicals of high added value, but also the simultaneous storage of electrical energy originating from intermittent renewable sources.[2]

ERCO$_2$ operating at commercially relevant reaction rates (current densities) requires efficient and stable catalysts and facile mass transport of reactants and products with minimized energy losses.[3] Gas diffusion electrodes (GDEs) circumvent the problem of limited solubility and slow diffusion of CO_2 in aqueous media by delivering this reactant to the catalyst layer via gas phase.[3–6]

In GDEs, the catalyst layer is located on a supportive gas diffusion layer (GDL) that is composed of a carbon fiber layer (CFL) and a microporous layer (MPL),[4] as shown in **Figure 1**. Besides the reactant delivery, the GDL enables the release of gaseous reaction products, serves as a mechanical support and electrical contact for the catalyst, and plays important role in controlling the amount of electrolyte in the catalyst layer.[4,7,8] GDEs operating in alkaline aqueous electrolytes show highly active and selective ERCO$_2$ toward target products (like CO) due to the combination of reduced ohmic drops,[3,9] favorable electrode kinetics,[3,10–14] and suppression of the electrochemical reduction of water (ERH$_2$O) as a parasitic reaction.[15]

Y. Kong, M. Liu, H. Hu, Y. Hou, S. Vesztergom, M. de J. Gálvez-Vázquez, I. Zelocualtecatl Montiel, P. Broekmann
Department of Chemistry, Biochemistry and Pharmaceutical Sciences
University of Bern
3012 Bern, Switzerland
E-mail: peter.broekmann@unibe.ch

The ORCID identification number(s) for the author(s) of this article can be found under https://doi.org/10.1002/smtd.202200369.

Y. Kong, M. Liu, Y. Hou, P. Broekmann
National Centre of Competence in Research (NCCR) Catalysis
University of Bern
3012 Bern, Switzerland

S. Vesztergom
Department of Physical Chemistry
Eötvös Loránd University
1117 Budapest, Hungary

V. Kolivoška
J. Heyrovský Institute of Physical Chemistry of the Czech Academy of Sciences
18223 Prague, Czech Republic
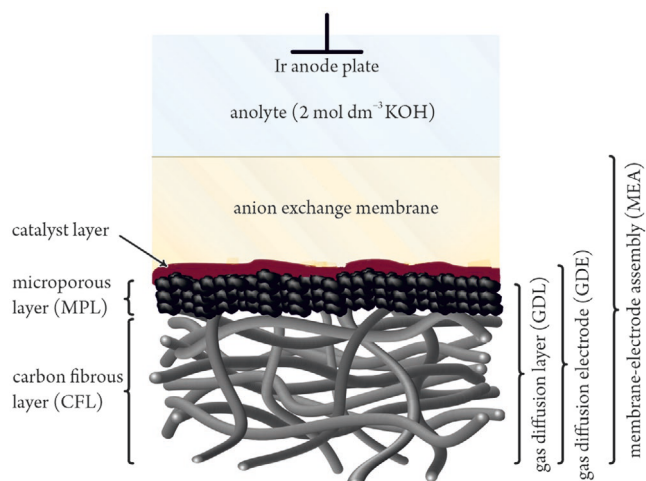E-mail: viliam.kolivoska@jh-inst.cas.cz

Figure 1. Schematic depiction of the zero-gap gas diffusion electrode (ZG GDE).

GDEs interfaced to ion exchange membranes, as shown in Figure 1, constitute membrane-electrode assemblies (MEAs),[16] allowing for decreased ohmic losses,[17] improved catalyst stability, and avoidance of problems due to the formation of gaseous products directly at electrode/electrolyte interfaces.[18]

Reactor arrangements based on MEAs were originally developed in the field of proton exchange membrane fuel cells (PEMFCs).[19] In PEMFCs, both the cathode and the anode are of a GDE structure, and are separated by a thin membrane. ERCO$_2$ electrolyzers often involve a configuration (see Figure 1 for a scheme; Figure S1, Supporting Information for detailed assembly) in which only the cathode is of a MEA structure.[20–22] This configuration is denoted further as a zero-gap GDE (ZG GDE) because the GDE cathode is in a direct contact with the membrane that separates it from the electrolyte solution (the anolyte) that contains the anode.

Despite differences in their mode of operation (electrical-to-chemical vs chemical-to-electrical energy conversion) and in their underlying chemistry, ZG GDE ERCO$_2$ electrolyzers and PEMFCs share several important aspects considering their water (electrolyte) management. In PEMFCs, H$^+$ ions resulting from the anodic oxidation of hydrogen are transported through the membrane to the cathode, where they are combined with electrons and oxygen to form water as the reaction product. In ZG GDE ERCO$_2$ electrolyzers, the membrane has essentially two roles: it controls the amount of water (that acts as a reactant of ERCO$_2$, and the absence of which can cause kinetic limitations[6]) and ensures that gaseous products formed by ERCO$_2$ in the catalyst layer cannot enter the anode compartment.

Insufficient hydration of the membrane can cause, both in PEMFCs and ZG GDE ERCO$_2$ electrolyzers, an increased cell resistance and pronounced energy losses, while excess hydration can lead to the flooding of the GDL and hence compromised transport of gaseous reactants toward the catalyst.[4]

The flooding of GDLs should be understood as a complex phenomenon that depends on diverse physico-chemical processes. System properties influencing flooding include the wettability of GDEs[8,23–29] and its dependence on the applied electrode potential (electrowetting),[30–40] the pH of the electrolyte,[30] the humidity of the reactant gases,[41,42] the presence of reaction intermediates[30] and products,[43] the temperature[30]

and pressure[31,32,37,38] gradients across the cell, as well as the thickness of the employed membranes.[29]

In PEMFC research, the inspection of flooding phenomena has reached a significant degree of maturity.[19,44–47] The distribution of water in the interior of fuel cell structures has been visualized under operando conditions, for example, by optical microscopy (OM), magnetic resonance imaging, neutron imaging, environmental scanning electron microscopy (SEM), X-ray computed tomography, and fluorescence microscopy.[48–50]

Strategies to mitigate flooding in PEMFCs involve the use of MPLs with large voids[51,52] comprising both naturally formed structures (pores[53,54] and cracks[55–58]) and artificially designed architectures (holes[59] and grooves[60]). These bigger voids in the MPLs exhibit a smaller capillary pressure and hydrodynamic resistance compared to that of micropores. Thus, water formed in the cathode catalyst layer can preferentially be drained through the larger voids, reaching the CFL and finally escaping the fuel cell via flow channels and gas outlet. When large voids with appropriate abundance and distribution are present, micropores remain dry and keep their ability to function as efficient transport channels for gaseous reactants.

In the ERCO$_2$ field, flooding has been reported for GDEs either directly interfaced to liquid electrolytes[8,10,11,25,26,28,32–34,36–40,61–70] or blanketed by ion exchange membranes.[22,27,29,41,42,65,71–74] Flooding in ERCO$_2$ electrolyzers was often found to be accompanied by the appearance of precipitated salts inside or on the surface of GDEs.[9,11,22,28,33,34,36,38,39,41,42,61,64–66,68,69,74–76] These salts are either themselves constituents of the electrolyte solution or are formed when such a constituent reacts with CO$_2$. Both flooding and salt precipitation can hinder or even completely block the transport of CO$_2$ to the catalyst. As a result, a transition from ERCO$_2$ to ERH$_2$O is observed, leading to a significant drop of the overall Faradaic efficiency of ERCO$_2$.

In ERCO$_2$ electrolyzers employing alkaline electrolytes, the flooding of GDEs, and the appearance of precipitates within the GDE structure are mutually perpetuating processes. As some of the alkaline electrolyte appears in the GDE, it combines with the CO$_2$ supply gas to form potassium carbonate (or bicarbonate) precipitates. These salt formations decrease the hydrophobicity of the GDE, resulting in the permeation of even more electrolyte to the MPL and the formation of additional amounts of the precipitate.[68]

As a consequence, the appearance of carbonate precipitates within a GDE structure during electrolysis can be regarded as a tracer of flooding. In this vein, several authors have described flooding phenomena by visualizing potassium (as the electrolyte cation) on the surface[22,28,66] or within the interior[34,35,68,69,72,76] of GDEs, by the application of SEM complemented by energy dispersive X-ray (EDX) elemental mapping or by X-ray micro-computed tomography.[66,76] While these SEM-EDX works successfully showed that the appearance of potassium containing precipitates in GDE structures can be interpreted as a sign of flooding, they did not attempt to quantify the distribution of precipitates within the GDE, and to establish a correlation between the latter and the observed performance losses of the electrolyzer. The reason behind this is most likely that EDX is mostly considered a qualitative technique, yielding elemental maps that are not directly (that is, not quantitatively) comparable. This gap can however be bridged by the application of a novel method, based on the combination of cross-sectional EDX measurements

**ADVANCED
SCIENCE NEWS**
www.advancedsciencenews.com

**small
methods**
www.small-methods.com

with an inductively coupled plasma mass spectrometry (ICP-MS) based determination of the total potassium content accumulated within a GDE structure upon the electrolysis.[77]

Note here that from the viewpoint of catalytic performance and stability, not only the total electrolyte content in a GDE but also its spatial distribution may become decisive. While the occurrence of potassium inside the micropores of the MPL can be interpreted as a sign of flooding with high certainty, its appearance in the CFL is not necessarily to be linked to flooding of micropores. In several works, the transport of the liquid electrolyte through the entire GDE (further referred to as electrolyte perspiration) was reported.[37–39,41,66,68,70] It is likely—especially based on what was said above about PEMFCs[51–60]—that the electrolyte perspiration through larger structures in the MPL involving cracks can prevent or at least delay the flooding of the micropores.

In the ERCO$_2$ field, recent works have demonstrated that cracks in the MPL facilitate the reaction due to augmented mass transport of gaseous CO$_2$ to the catalyst[78] and removal of excess electrolyte from the catalyst layer.[37] To the best of our knowledge, however, there is no systematic work studying the impact of MPL cracks on the catalytic activity and water management in ERCO$_2$ electrolyzers, as was carried out for PEMFCs.[55,57] While flooding of GDEs by liquid water formed as the reaction product represents the only barrier for the gas transport in PEMFCs, ERCO$_2$ is further complicated by the intrusion of the electrolyte ions into GDEs, potentially leading to salt precipitation. Exploring the electrolyte transport through MPLs with systematically varied architectures thus becomes the aim of this paper, with the ultimate goal of avoiding electrode flooding and salt precipitation in commercial ERCO$_2$ reactors.

Here we perform a series of galvanostatic experiments in a ZG GDE electrolyzer operated with alkaline anolyte. We employ different GDEs, the MPLs of which exhibit a varied abundance of cracks. To allow for a straightforward monitoring of reaction rates, we employ silver as the ERCO$_2$ catalyst, capable of producing CO with near-unity Faradaic efficiency.[8,10,12–14,16,21,22,27–29,36,38,39,41,42,66,68,70,71,75,76] The evolution of the catalytic performance is inspected by online gas chromatographic monitoring of CO and H$_2$, the latter being the product of ERH$_2$O and hence a fingerprint of electrolyte management deficiencies. Additionally, cell resistance and voltage and surface wettability of GDEs are monitored in the course of the electrolysis. We further utilize potassium as the cation of the employed electrolyte to visualize and quantify flooding and perspiration in the interior of GDEs, based on a recently developed, robust analytical approach that combines cross-sectional EDX elemental mapping and ICP-MS methods.[77] In addition, we monitor the perspiration rate by determining the amount of potassium in the perspirate, employing ICP-MS.

To the best of our knowledge, we perform and present here the first systematic study of flooding phenomena in GDEs at varied stages of the electrolysis, for GDEs with systematically varied microarchitecture. Our results shed light on an important, yet still unaddressed question of ERCO$_2$ engineering, namely, that submillimeter cracks in the MPL of GDEs applied for CO$_2$ electrolysis play a key role in the electrolyte management, and that by providing direct means for electrolyte drainage, cracks can efficiently prevent (or at least delay) the flooding of the catalyst layer.

2. Results and Discussion

The presented work aims at exploring the impact of the MPL structure with the emphasis on naturally occurring cracks on the catalytic activity and electrolyte management in ERCO$_2$ realized in an alkaline ZG GDE-based electrolyzer (full and cross-sectional drawings are shown in Figure S1, Supporting Information).[22,79]

We have selected four commercial GDLs as catalyst supports for our experiments, all of them having a bilayer structure composed of a CFL and an MPL. Three GDLs (36BB, 39BB, and 39BC) contain cracks in their MPLs. The fourth GDL (H23C8) has a crack-free MPL and is utilized as a reference system. For all four GDLs, the CFL is composed of coarse fibers. The surfaces of all GDLs were air-brushed with a catalyst ink containing silver nanowires (see the Experimental Section for details). The use of a catalyst ink based on nanowires was motivated by the assumption that assemblies of these quasi-1D objects form thin layers uniformly covering MPL surfaces and crack walls, without permeating into the interior of micropores.[70] For all four GDEs, the mass loading of silver was constant and equal to ≈40 μg cm^{-2}, as verified by ICP-MS analysis (see the Experimental Section for details). Representative top-down OM images of as-prepared GDEs are shown in **Figure 2**.

The optical micrographs of Figure 2 are very similar to those shown in Figure S2, Supporting Information, taken from bare GDL surfaces unmodified by catalyst ink deposition. This suggests that the air brush deposition leads to uniform catalyst layers without localized accumulation of deposits on the GDL surface or in cracks.

To inspect the structure of the formed catalyst layers in more detail, surfaces of as-prepared GDEs were further imaged by top-down SEM (also shown in Figure 2). For all four GDEs, Ag nanowires are well discerned, appearing as a collection of cylindrical objects with a diameter of ≈100 nm and a length of several micrometers, oriented parallel to the electrode surface. The small spherical features seen in the top-down SEM images of Figure 2 are attributed to the carbon black particles of the catalyst ink. High-resolution cross-sectional focused ion beam SEM images of top parts of MPLs (Figure S3, Supporting Information) demonstrate that the formed catalyst layers are 100 to 300 nm thick and involve one to three layers of Ag nanowires.

To investigate the permeation of the catalyst ink into the interior features of MPLs (micropores and cracks), cross sections of as-prepared GDEs were further inspected by SEM imaging combined with the EDX mapping of silver (Figure 2). For the non-cracked MPL (H23C8), the silver signal is confined to the top part of the MPL, confirming that Ag nanowires do not permeate micropores.

For cracked MPLs (36BB, 39BB, and 39BC) we first focused (in Figure 2) on regions containing cracks appearing as shaded features in the centers of cross-sectional SEM images. The corresponding EDX maps show a strong silver signal in the cracks, confirming that the catalyst ink permeates into the interior of the GDE through the cracks. For all three cracked MPLs, we performed the same analysis for regions with no cracks, with results shown in Figure S3, Supporting Information. In all cases, the silver signal is confined to the top of MPLs, similarly as for the non-cracked MPL (H23C8, Figure 2).
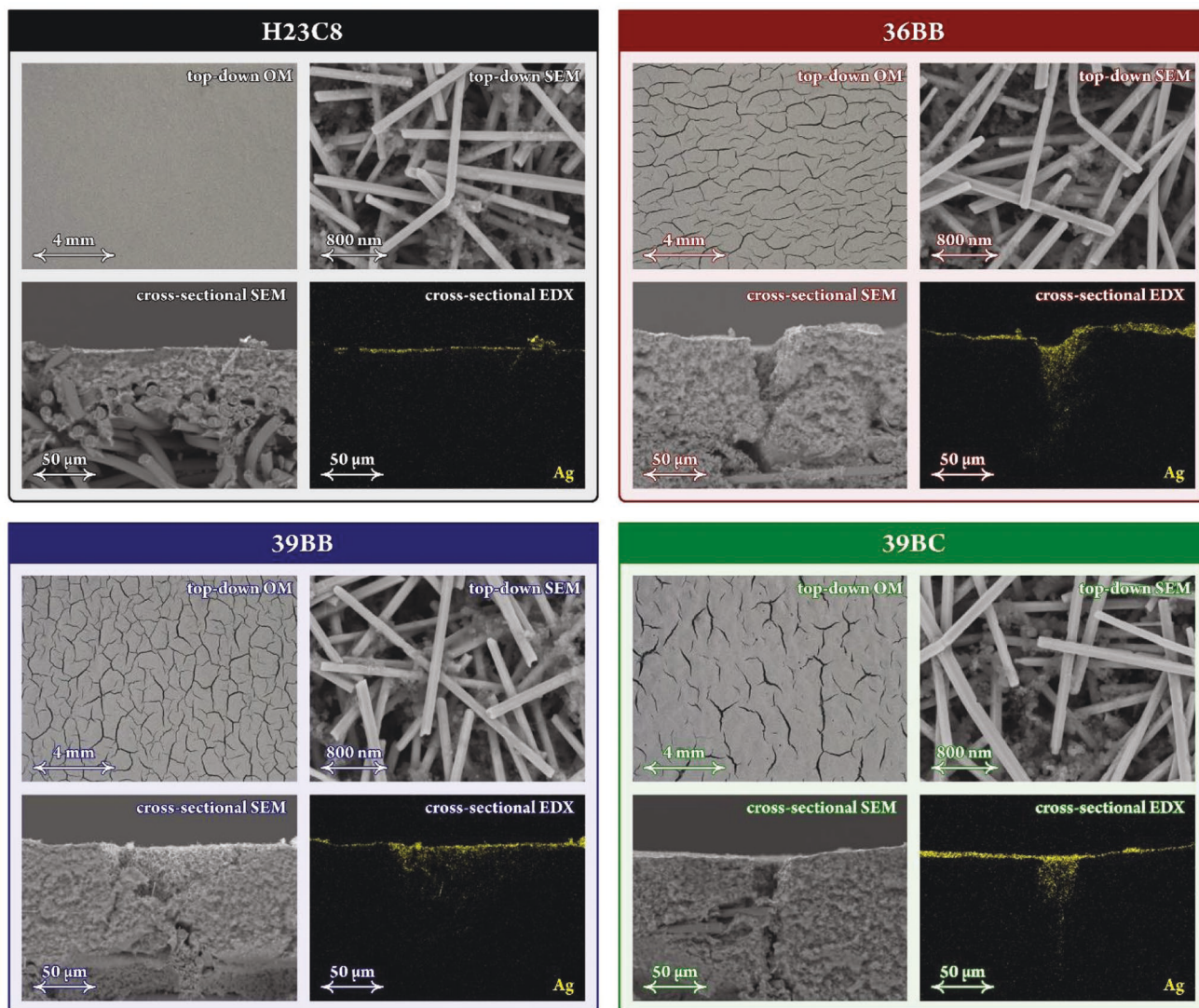
Figure 2. Representative top-down OM and SEM images, and cross-sectional SEM images and silver EDX maps of as-prepared GDEs.

One can conclude that the employed air brush deposition protocol leads to surfaces of MPLs completely covered by a thin catalyst layer that permeates into cracks, but leaves micropores unmodified. Such arrangement of the catalyst layer spatially decouples the target electrochemical process (ERCO$_2$) from the mass transport and charge transport phenomena occurring in the MPL, which is essential for the rigorous interpretation of relationships between the MPL structure, catalytic performance, and electrolyte management characteristics addressed in this work.

With regard to the distribution of cracks (see the optical micrographs of Figure 2 for catalyst ink-covered and Figure S2, Supporting Information for bare GDLs), it can be said that the H23C8 MPL has an almost featureless surface. Surfaces of the other three MPLs contain cracks that appear as distinct, elongated, and dark features. Cracks have no preferential orientation and enclose otherwise flat regions. White-light interferometry images of the pristine GDLs, as well as those of GDLs covered by a catalyst ink (taken before or following electrolysis, Figure S4, Supporting Information) exhibit the same crack distribution that seems undisturbed both by the catalyst ink coating and by subsequent electrolysis.

The pixel-by-pixel analysis of the top-down optical micrographs shown in Figure 2 allowed us to determine the relative occurrence of cracks on the MPL surface, denoted further as the surface crack ratio (CR). Obtained values are listed in **Table 1** and range from 0% to 21%. The characteristic width of cracks ($\approx$100 µm for 36BB and 39BB, 100 to 200 µm for 39BC) is comparable to the thickness of the MPLs (also listed in Table 1), suggesting that most cracks span over the entire MPL depth.

Table 1 also lists void ratio values of entire GDLs, CFLs, and MPLs. These values were determined by densitometry, as described in the Experimental Section. The void ratio values of MPLs (further referred to as VR values) represent the cumulative porosity of MPLs; that is, the porosity that accounts for both cracks and micropores. The structure of micropores is partially resolved in SEM images presented in Figure S2, Supporting Information. As seen in Table 1, VR values scale with CR values, indicating that cracks are significant contributors to the overall porosity of MPLs. However, the differences

Table 1. Physical characteristics of GDLs used in this work. See the Statistical Analysis in the Experimental Section for more information on statistics.

	Entire GDL		CFL		MPL			
	Thickness [µm]	Void ratio [%]	Thickness [µm]	Void ratio [%]	Thickness [µm]	Void ratio (VR) [%]	Crack ratio (CR) [%]	Pores in solid (PS) [%]
H23C8	235 ± 3	60 ± 4	194 ± 5	67 ± 4	41 ± 2	30 ± 8	0 ± 0	30 ± 8
36BB	256 ± 9	70 ± 3	160 ± 20	73 ± 1	97 ± 11	68 ± 4	9 ± 2	64 ± 4
39BB	295 ± 15	81 ± 5	197 ± 22	82 ± 2	98 ± 7	78 ± 8	16 ± 4	74 ± 10
39BC	267 ± 7	72 ± 1	138 ± 21	66 ± 2	129 ± 14	78 ± 4	21 ± 4	72 ± 5

between VR values of cracked MPLs and the one obtained for the non-cracked MPL are more pronounced than the respective CR values, suggesting that cracked MPLs also exhibit a higher microporosity than crack-free MPLs. To quantify this observation, we introduce here a parameter termed the porosity of solid regions (PS) of MPLs, defined as

$$PS = \frac{VR - CR}{1 - CR} \quad (1)$$

Obtained PS values of all applied MPLs are also presented in Table 1. We presume that cracks formed in MPLs result from drying as a part of the manufacturing process of GDLs.[28] The comparison of PS and CR values suggests that the formation of cracks during the drying process is more likely for more porous MPLs. Results of combined OM and SEM imaging (Figure S2, Supporting Information) further show that the characteristic dimensions of cracks and micropores differ by at least two orders of magnitude. This difference has, as will be demonstrated, a huge impact on the capillary phenomena occurring in MPLs, being one of the key factors influencing the electrolyte management and hence catalytic performance of ZG GDEs.

For ERCO$_2$ testing, each GDE prepared and characterized as described above was blanketed by an anion exchange membrane and integrated in the electrolyzer, forming a ZG GDE (see Figure S1, Supporting Information for the arrangement of the electrolyzer and the Experimental Section for details). The electrolysis was performed and monitored under galvanostatic conditions with the GDE being continuously fed by a stream of humidified CO$_2$. **Figure 3** shows the evolution of the Faradaic efficiency (FE) values of CO obtained for all four ZG GDEs, expressed as a function of time as well as normalized charge passed in the electrolysis.

The charge normalization is based on the geometric area of the ZG GDE/anolyte interface, and the presented FE(CO) values were obtained by gas chromatography (GC) monitoring of the formed CO quantity during electrolysis (see the Experimental Section). For all ZG GDEs, CO is initially formed with near-unity FE, confirming that the catalyst shows high activity toward ERCO$_2$.

In the course of the electrolysis, significant differences in the evolution of FE(CO) values are noticed. For the crack-free MPL (H23C8), a fast decline in the CO production rate and a concomitant increase of the H$_2$ production rate are observed. The observed loss of CO production specificity may either be caused by a gradual degradation of the active catalyst sites, or by the retarded mass transport of CO$_2$ toward the catalyst layer.

For GDEs involving cracked MPLs, a markedly different evolution of FE(CO) values is observed. The GDE with the intermediate abundance of cracks (36BB, red) starts losing its catalytic

activity roughly upon one-third of the electrolysis time. GDEs with higher crack abundance (39BB and 39BC, blue and green) continue to generate CO with near-unity FE values till the very end of the electrolysis. To reveal the origin of differences in the catalytic behavior, we performed identical location SEM studies of the catalyst layers deposited on H23C8 and 39BC GDLs (systems showing the smallest and the largest drop in the catalytic activity) before and after the electrolysis. For both systems, the obtained micrographs (Figure S5, Supporting Information) demonstrate that the electrolysis causes no visible changes in the nanomorphology of the catalyst. To exclude the influence of the electron beam used in SEM on the catalytic behavior and subsequent imaging,[80] we have further inspected random
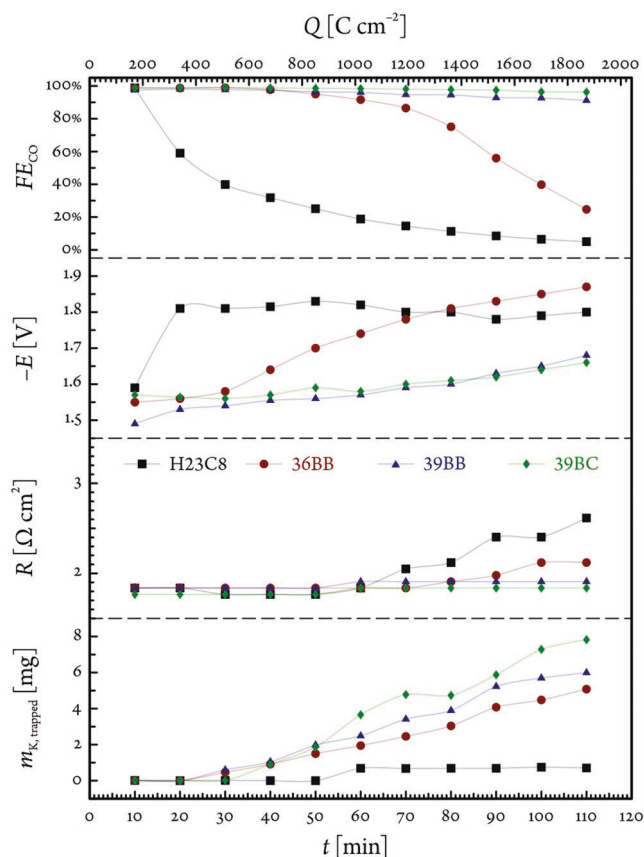
Figure 3. Faradaic efficiency of CO, ohmic drop-corrected cell voltage, normalized cell resistance, and the amount of potassium found by ICP-MS in the outlet trap plotted as a function of time and normalized charge passed in the electrolysis. Experiments were performed in the galvanostatic regime at −283 mA cm^{-2}, employing aqueous 2 M KOH as anolyte. A humidified CO$_2$ stream was fed to the GDE during the experiment at constant flow rate of 18 mL min^{-1}.

**ADVANCED
SCIENCE NEWS**
www.advancedsciencenews.com

**small
methods**
www.small-methods.com

locations of the catalyst layer, not imaged prior to the electrolysis, again showing no signs of degradation (random location SEM micrographs are also shown in Figure S5, Supporting Information). Keeping in mind that catalyst loading and conditions applied in the electrolysis were identical for all four ZG GDEs, this suggests that a decline of the CO production rate observed for H23C8 and 36BB is not caused by the degradation of catalytic sites.

Employing a 36BB GDE selected for the demonstration, we further performed a follow-up electrolysis with a previously once-used electrode, preceded by a rinsing/drying step (see the Experimental Section for details). The catalytic activity of the electrode at the beginning of the follow-up electrolysis was largely restored (Figure S6, Supporting Information). This result not only confirms that the flooded electrolyte may be at least partially removed from the interior of the GDE, but additionally demonstrates that electrodes may be reused. The degradation of the catalyst was further excluded by identical and random location SEM studies performed before the initial and after the follow-up electrolysis (micrographs are also shown in Figure S6, Supporting Information).

The observed differences in the evolution of FE(CO) values among the investigated ZG GDEs are thus clearly attributed to the dissimilar rate of the CO_2 mass transport due to the different structure of MPLs.

It is important to remind that apart from the abundance of cracks (Figure 2; Figure S2, Supporting Information), the investigated MPLs also differ in void structure and, more specifically, in the porosity in solid regions, as documented by the CR, VR, and PS values (see Table 1). To investigate the effect of cracks and micropores on the observed differences in the catalytic behavior, we plotted FE(CO) values found at the end of the electrolysis as a function of the above three structural parameters in Figure S7, Supporting Information. FE(CO) data plotted on the CR basis shows more evident correlation compared to VR and PS parameters, suggesting that the crack abundance is the most important descriptor of differences in the catalytic behavior. Importantly, results of electrolysis experiments combined with the gas chromatographic product analysis suggest that cracks formed in the MPL prevent (39BB and 39BC) or at least delay (36BB) flooding as an adverse phenomenon frequently reported for $ERCO_2$ employing GDEs.

Apart from FE(CO) values, we also monitored the cell resistance as described in the Experimental Section, and plotted it as a function of time (as well as a function of the passed charge) in Figure 3. For MPLs with high crack abundance (39BB and 39BC), almost constant cell resistance values were found after a short initial period, suggesting that the concentration and mobility distribution of ions in these ZG GDEs reach a steady state. For the ZG GDE with lower crack abundance (36BB), a slight increase in resistance values is detected in later stages of the electrolysis, lagging the decrease of FE(CO) values. The resistance increase is either due to decreased electrolyte conductivity upon the reaction between CO_2 and OH^-[3,9] or a decrease of the active electrode area upon flooding or salt precipitation. Resistance values recorded for the non-cracked ZG GDE (H23C8) show an initial, transient decrease (presumably due to the accumulation of electrolyte ions in the catalyst layer and MPL, vide infra), followed by a pronounced increase

toward the end of the electrolysis. The observed time shifts suggest that the cell resistance monitoring can only detect severe flooding events where the concentration and mobility of ions and/or active area of electrodes are affected significantly. The low flooding predicting power of cell resistance measurements is ascribed to significant resistance contributions originating from the anion exchange membrane and the anolyte, which are not affected by flooding of the GDE. The cell resistance thus cannot be used as an early warning signal to detect the onset of flooding.

Figure 3 further shows electrode potential values, mathematically corrected for the ohmic drop based on the measured cell resistance. Values obtained for ZG GDEs with high abundance of cracks (39BB and 39BC) show only subtle (and uniform) shifts, while more pronounced changes are noticed for the crack-free ZG GDE (H23C8) and the ZG GDE with moderate abundance of cracks (36BB). Such changes are probably due to the transition from the $ERCO_2$ to the ERH_2O regime. Importantly, the onset of changes observed in the electrode potential has no lag to the changes noticed in FE(CO) profiles. This suggests that electrode potential monitoring is applicable as an online tool for the detection of flooding of GDEs at commercially relevant current densities.

In experiments performed with all four ZG GDEs, small amounts of liquids and solids were observed at the back of CFLs, that is, in the gas flow channels and in the outlet equipped with a trap (see Experimental Section for details). After making sure that no electrolyte can escape the electrolyzer via leaking due to loosely assembled parts, we arrived at the conclusion that the observed liquids and solids originate from the transport of the electrolyte through ZG GDEs.

In the literature, the appearance of liquid electrolyte at the back of CFLs (termed as electrolyte perspiration) was attributed to the combination of pressure difference between the electrolyte and the gas phase and the electrowetting phenomena in the interior of GDEs.[37,38] For the ZG GDE electrolyzer employed in our study, the former contribution is given by the difference of the hydrostatic pressure acting on the top of the anion exchange membrane and the pressure in the gas flow channel beneath the CFL (see Figure S1, Supporting Information for the electrolyzer design). The magnitude of the hydrostatic pressure was estimated as 2.5 mbar, being much lower than the value needed to trigger electrolyte perspiration through the 39BC based GDE embedded in a flow-by electrolyzer (15 mbar) reported in the work of DeMot et al.[37]

In our study, the stream of gas (humidified CO_2) was fed to the flow channel at atmospheric pressure. Thus, we conclude that a differential pressure of 2.5 mbar (constant for all four ZG GDEs) was applied to the top of the anion exchange membrane. The pressure exerted on the top of GDE may additionally be influenced by the electroosmotic drag[29] resulting from the electric field (formed due to voltage applied across the cell), acting on the electric double layer in the interior of the membrane. The total pressure applied to the top of GDE is opposed by the capillary pressure originating from its hydrophobic interior structures. It is important to note that the ability of GDEs to resist external pressure may be compromised by electrowetting (an increase of wettability upon applying electric voltage between the electrode and the electrolyte).[30–40]

The magnitude of the capillary pressure is inversely proportional to the characteristic dimensions of interior structures. For hydrophobic surfaces, the electrolyte first enters structures with larger dimensions (cracks in this work), while leaving smaller structures (micropores) dry. For hydrophilic surfaces, the order of the electrolyte intrusion is just the opposite.[81] While wettability is not easily measurable in the interior of GDEs, it may be explored on their surfaces by contact angle measurements. In this work, we have monitored values of the contact angle on the surface of GDEs in the course of their preparation and upon subsequent electrolysis[22,26,27,66,70] performed with systematically varied charge consumption (Figures S8,S9, Supporting Information; see also the Statistical Analysis in the Experimental Section).

All four as-purchased (pristine) GDLs have strongly hydrophobic surfaces, with contact angle values obtained for cracked MPLs (164° ± 1°) being slightly lower than that of the crack-free MPL (170°). This is either due to crack walls having higher wettability than solid MPL regions or due to effects of highly curved surfaces. The deposition of the catalyst ink on MPLs leads to the uniform value of 143° ± 1°. This is in line with results of above-presented microscopic observations which demonstrate that the catalyst ink permeates to cracks (Figure 2).

Following electrolysis, the measured contact angle values diverge significantly among the employed electrodes. Values obtained for GDEs with high CR values (39BB and 39BC) are time-independent and equal to 106° ± 2°, indicating that their surfaces retain hydrophobic character. The value obtained for the GDE with the intermediate CR value (36BB) approaches 90°, being at the borderline between hydrophobicity and hydrophilicity. For the crack-free GDE (H23C8), contact angle values fall deep in the hydrophilic region. Washing GDEs with deionized water after completing the electrolysis led to uniform contact angle values of 135° ± 2°, being slightly lower than that obtained for as-prepared GDEs (143° ± 1°). This partial recovery implies that wettability changes observed upon the electrolysis are largely due to electrolyte accumulated in the GDE and not due to the catalyst degradation. This is in accord with results of identical and random location SEM studies of the catalyst layers presented in Figures S5,S6, Supporting Information.

Besides contact angle measurements, we further monitored the rate of electrolyte perspiration in the course of electrolysis by quantifying the amount of potassium in the outlet trap (Figure 3), employing ICP-MS analysis (see Experimental Section for details). For charge below 510 C cm^{-2}, no potassium was found. For non-cracked ZG GDE, the potassium amount remains low till the end of the electrolysis. For cracked ZG GDEs, amounts are significantly higher, scaling with passed charge and abundance of cracks.

As was already outlined above, the presence of cracks in MPLs helps to retain the catalytic activity of GDEs for a longer time (see the end-electrolysis FE(CO) values correlation with the CR parameter in Figure S7, Supporting Information). This is in agreement with the observation that the surface of GDE cathodes constructed of 39BB and 39BC GDLs show less hydrophobicity loss during electrolysis (Figures S8,S9, Supporting Information), because—as will be demonstrated below—of the cracks of these MPL surfaces act as dominant electrolyte transport pathways. For 36BB, the combination of lower CR

value and hydrophobicity loss leads to slower electrolyte perspiration (Figure 3). Low amounts of potassium found for the non-cracked H23C8 suggest that the capacity of micropores to transport the electrolyte is very limited.

Besides the capillary action originating from interfacial forces, one also needs to consider that the flow of liquids through porous media is affected by viscous forces acting in the liquid. For laminar flow of water through pores of cylindrical geometry, Poiseuille law predicts that the flow rate is proportional to the second power of the cross-sectional pore area. This implies that cracks allow the passage of water at faster rate compared to micropores, additionally supporting the dominant role of cracks in the electrolyte transport. In addition to the presented reasoning, the difference in perspiration rates may further be rationalized by unequal rates of water consumption in the ERCO$_2$ and ERH$_2$O reactions. The two reactions proceed according to

$$CO_2 + H_2O + 2e^- \rightarrow CO + 2OH^- \tag{2}$$

and

$$2H_2O + 2e^- \rightarrow H_2 + 2OH^- \tag{3}$$
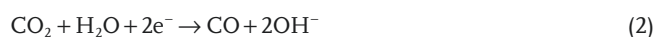
indicating that for ERH$_2$O, the consumption of water per unit passed charge is twice as high as for ERCO$_2$. For the non-cracked ZG GDE, where ERH$_2$O becomes the dominant process soon after the beginning of the electrolysis (Figure 3), higher consumption of water may contribute to the pronounced accumulation of electrolyte ions in the GDE interior, increasing the viscosity and impeding perspiration.

In the following, we further estimate the impact of the electrolyte perspiration on the carbon mass balance in ERCO$_2$, considering the data obtained for ZG GDEs based on 39BB and 39BC as best performing catalytic systems (Figure 3).

As mentioned above, the perspiration results in the accumulation of solids and liquids in gas flow channels and subsequently in the gas outlet equipped with the trap. During the electrolysis, it is not possible to monitor the amount of perspirate in gas flow channels and gas outlet and further analysis is thus restricted to the perspirate found in the trap (see Experimental Section for details). For both ZG GDEs (39BB and 39BC), the amount of potassium found in the trap scales linearly with the consumed charge. For the highest charge (1839 C cm^{-2}), it equals to 6.0 and 7.8 mg, respectively. The electrolyte transported through the GDE is in a permanent contact with gaseous CO$_2$ that is continuously delivered to flow channels. For stoichiometric excess of CO$_2$, we expect that its neutralization proceeds only to the first step, that is, producing HCO$_3^-$ (and not CO$_3^{2-}$). Assuming this stoichiometry, the found mass of potassium corresponds to 1.53 and 1.99 × 10^{-4} mol of CO$_2$. We further discuss these amounts in the relation to the amount of CO$_2$ electrochemically converted to CO (6.74 × 10^{-4} mol) obtained considering FE(CO) of 100% for the sake of simplicity. The obtained CO$_2$ loss due to neutralization amounts to 23% and 30% indicating that the electrolyte perspiration cannot be ignored when drawing the total carbon mass balance of ERCO$_2$. Noteworthy, perspiration-related CO$_2$ losses in the ZG GDE electrolyzer as determined in this work

are significantly lower than those reported for CO_2 neutralization in the interior of GDEs embedded in membrane-based flow-by electrolyzers ($\approx$70%).[82,83]

To provide microscopic insight to the electrolyte intrusion in GDEs, we utilized post-experimental SEM imaging to visualize the surfaces and cross sections of electrodes subjected to the electrolysis (see Experimental Section for details). In all inspections, SEM imaging was complemented by EDX mapping of potassium (shown as purple) utilized in this work as the electrolyte cation, to specifically reveal locations to which the electrolyte has permeated. A collection of top-down and cross-sectional SEM images and EDX-K elemental maps are shown in Figure S10, Supporting Information for four different GDE samples and four different electrolysis treatments.

Here, **Figure 4** shows representative top-down EDX maps obtained for surfaces of GDEs subjected to electrolyzes terminated at the charge consumption of 2.8, 170, 510, and 1839 C cm^{-2}. In these surface maps, the deposited salt appears as fuzzy features, sometimes forming islands that, with on-going electrolysis, tend to cover the catalyst layer. Cross-sectional
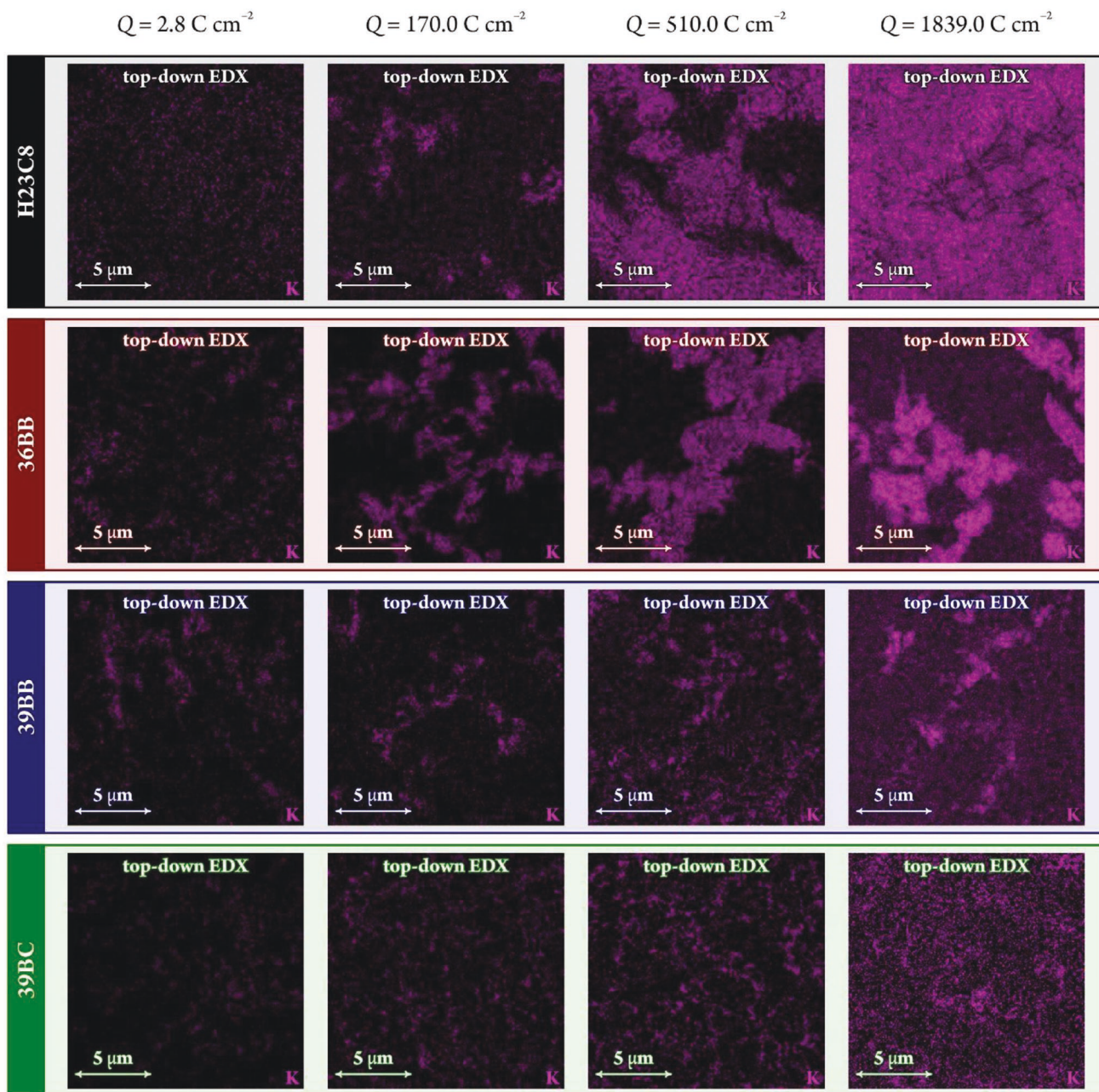

Figure 4. Representative top-down potassium EDX maps obtained for GDEs subjected to electrolyzes performed with varied charge consumption (for a comparison to corresponding top-down SEM images, as well as to cross-sectional SEM images and EDX maps, see Figure S10, Supporting Information).
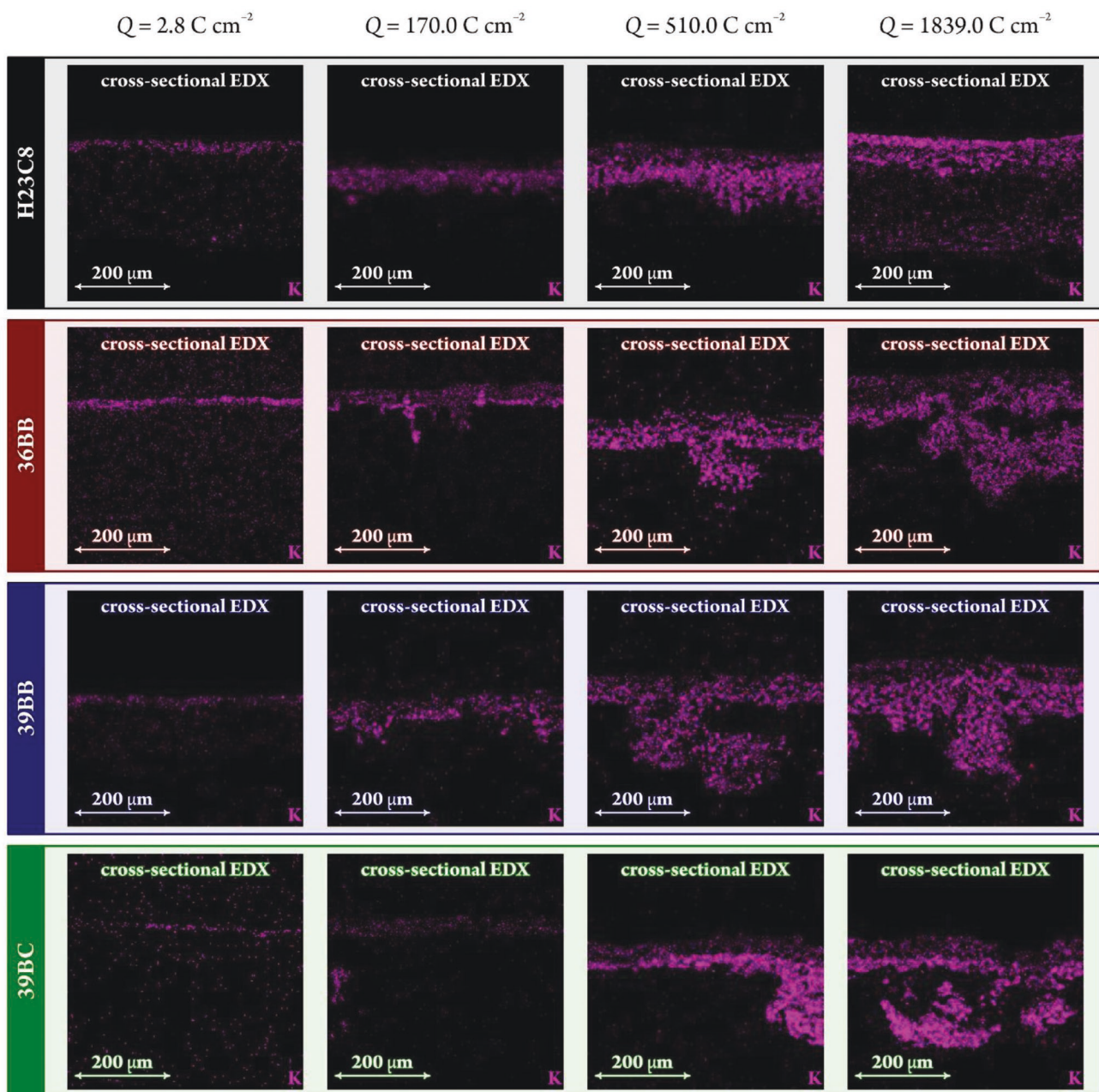
ADVANCED
SCIENCE NEWS
www.advancedsciencenews.com

small
methods
www.small-methods.com

Figure 5. Representative cross-sectional potassium EDX maps obtained for GDEs subjected to electrolyzes performed with varied charge consumption (for a comparison to corresponding cross-sectional SEM images, as well as to top-down SEM images and EDX maps, see Figure S10, Supporting Information).

K EDX maps, shown in **Figure 5**, confirm that salt deposits (these are assumed to be potassium carbonates or hydrocarbonates), while initially formed only on the surface of the MPL, can later penetrate deeper layers of the GDL structure to different extent. Deposits appear already at the early stage of the electrolysis (2.8 C cm^{-2}) on all four GDE types, however they are confined to the surface of GDEs and show sparse coverage. For later stages of the electrolysis (170, 510, and 1839 C cm^{-2}) the amount and the pattern of deposits markedly differ among electrodes.

For the non-cracked GDE (H23C8), the electrolysis ends up with the deposit completely covering the electrode surface

(Figure 4), being largely confined to the MPL (Figure 5). Only a minor amount of the deposit is found at the bottom of the CFL. This observation is in accordance with the low electrolyte perspiration rate found for this system (Figure 3). For the GDE with the intermediate CR value (36BB), the electrolysis leads to patched deposits covering significant portion of the electrode surface (Figure 4) and more pronounced electrolyte intrusion to the interior of the GDL (Figure 5). Higher amounts of the deposit found at the bottom of the CFL are consistent with higher perspiration rate. For GDEs with high CR values (39BB and 39BC), very little amounts of deposits were found at the

electrode surface (Figure 4), with significant intrusion toward the bottom of the CFL (Figure 5), which is in line with the highest electrolyte perspiration rate.

To reveal relationships between the structure of MPLs and patterns of formed deposits, we further performed SEM imaging at higher magnification, together with combined EDX mapping of silver and potassium, with representative results shown in Figure S11, Supporting Information. All inspections were performed on GDEs subjected to electrolyzes terminated after 510 C cm^{-2}. The non-cracked GDE (H23C8) shows that the silver signal is confined to the top of the MPL and the potassium signal is evenly distributed mainly in the MPL, with little intrusion toward the CFL, all being in accord with the above-presented results (Figures 2,4,5). The SEM image obtained for 36BB shows a crack in the middle, with a corresponding region of increased silver signal. The potassium signal is localized mostly beneath this crack. A very similar scenario is observed for 39BB, with the crack, silver signal and potassium signal being in the left part of the inspected region. For 39BC, the SEM image depicts a horizontal rupture in the MPL in the central part of the micrograph with corresponding increase of the silver signal and the potassium signal located mostly below the rupture.

To conclude, high-resolution cross-sectional imaging of GDEs combined with EDX mapping of silver and potassium as signatures of cracks and electrolyte intrusion clearly demonstrate that these features correlate. This unique approach thus provides microscopic evidence that cracks drain excess electrolyte from the MPL, which is macroscopically observed in the form of electrolyte perspiration.

Samples of electrodes subjected to electrolyzes terminated at varied stages were further analyzed by ICP-MS with the goal of determining the total amount of potassium in their interior (see Experimental Section for details). Results are shown as potassium mass normalized to the electrode area (numbers stated in mg cm^{-2} shown in the panels of **Figure 6**). It is worth noting that the ICP-MS technique, while it can provide the absolute amount of potassium in the entire volume of the GDE,[74] lacks information about its spatial distribution. On the contrary, cross-sectional EDX mapping of potassium gives access to the spatial distribution,[34,35,68,69,72,76] but provides no information in terms of the absolute concentration. The two techniques may be combined to provide spatially resolved absolute potassium profiling as demonstrated by our recent contribution.

Following the approach described before,[77] we quantified the potassium distribution in GDEs subjected to electrolysis with the charge consumption varied as described above. Obtained local absolute potassium concentration values were averaged along horizontal lines of EDX maps and plotted as a function of the vertical position (i.e., depth in the GDE), with results depicted as shaded profiles in Figure 6. To provide statistically relevant information, such obtained profiles were further averaged over five individually prepared GDE cross sections, with results shown as thick curves. The concentration scale is established based on the ICP-MS based measurement of the total (surface area normalized) K content of the studied GDE section, providing the integral of the thick curves in Figure 6.

The MPL regions are visualized by shaded bands in Figure 6. The thickness of CFLs as imaged upon the electrolysis was generally found to differ a little from that determined for as-purchased GDLs (see Table 1). We attribute these differences to the swelling of the CFL structure due to electrolyte intrusion.

At early stages of electrolysis (charge consumption of 2.8 C cm^{-2}), little amounts of potassium were observed inside the investigated GDEs (Figure 6), being confined to the top of MPLs. At 170 C cm^{-2}, potassium permeated deeper to the GDE structure, with more pronounced accumulation noticed for systems losing their catalytic activity (H23C8 and 36BB, Figure 3) in top regions of the MPL. Differences among GDEs are most marked at later stages of the electrolysis (510 and 1839 C cm^{-2}). For H23C8, potassium stays localized mostly in the MPL and the top part of the CFL, with very little intrusion found in its bottom part, which is in line with the low perspiration rate observed for this GDE (Figure 3). For 36BB, the intrusion advances deeper to the CFL, being consistent with higher perspiration rate. Among all four GDEs, 36BB shows the highest total potassium content in the GDE presumably due to the combination of highly porous MPL (Table 1), high wettability of the catalyst layer (Figures S8,S9, Supporting Information) and low abundance of cracks as draining features (Table 1, Figure 2; Figure S2, Supporting Information). For 39BB and 39BC, overall lower concentration values in both MPL and CFL are observed, being in accord with the highest perspiration rates and the highest abundance of cracks.

For all four ZG GDEs, the total amount of potassium (numbers in mg cm^{-2} in Figure 6) grows up to 510 C cm^{-2} and converges to a plateau for 1839 C cm^{-2}, suggesting that a steady-state electrolyte intrusion is approached. No distinct correlations were found between the total amount of potassium in GDEs after completing the electrolysis at 1839 C cm^{-2} and the void parameters of MPLs (Figure S7, Supporting Information) suggesting that both cracks and micropores play a role in the accumulation of potassium in MPLs. The highest amount of potassium observed for 36BB presumably reflects a relatively high porosity of its MPL (Table 1) and high wettability of the catalyst layer (Figures S8,S9, Supporting Information), both favoring electrolyte intrusion, combined with low abundance of cracks (Figure 2; Figure S2, Supporting Information) impeding electrolyte perspiration.

For the three cracked GDEs (36BB, 39BB, and 39BC), the amount of potassium found in their interior (Figure 6) is insignificant compared to that determined in the outlet trap (Figure 3). This finding corroborates that cracks function as efficient pathways for the electrolyte transport and indicates that the total amount of CO$_2$ deposited as carbonates in the interior of GDEs can be neglected in the total carbon balance of ERCO$_2$.

We further inspected the back sides of GDEs subjected to the electrolysis by SEM/EDX analysis, finding only little amounts of potassium (Figure S12, Supporting Information). Contact angle measurements performed after the electrolysis with 1839 C cm^{-2} also confirmed that back sides of GDEs largely retained their hydrophobic character (Figure S13, Supporting Information).

To explore the extent of the electrolyte flooding in the absence of CO$_2$, we further carried out an electrolytic experiment employing argon-fed 36BB based ZG GDE selected for the demonstration. The catalytic activity of such treated
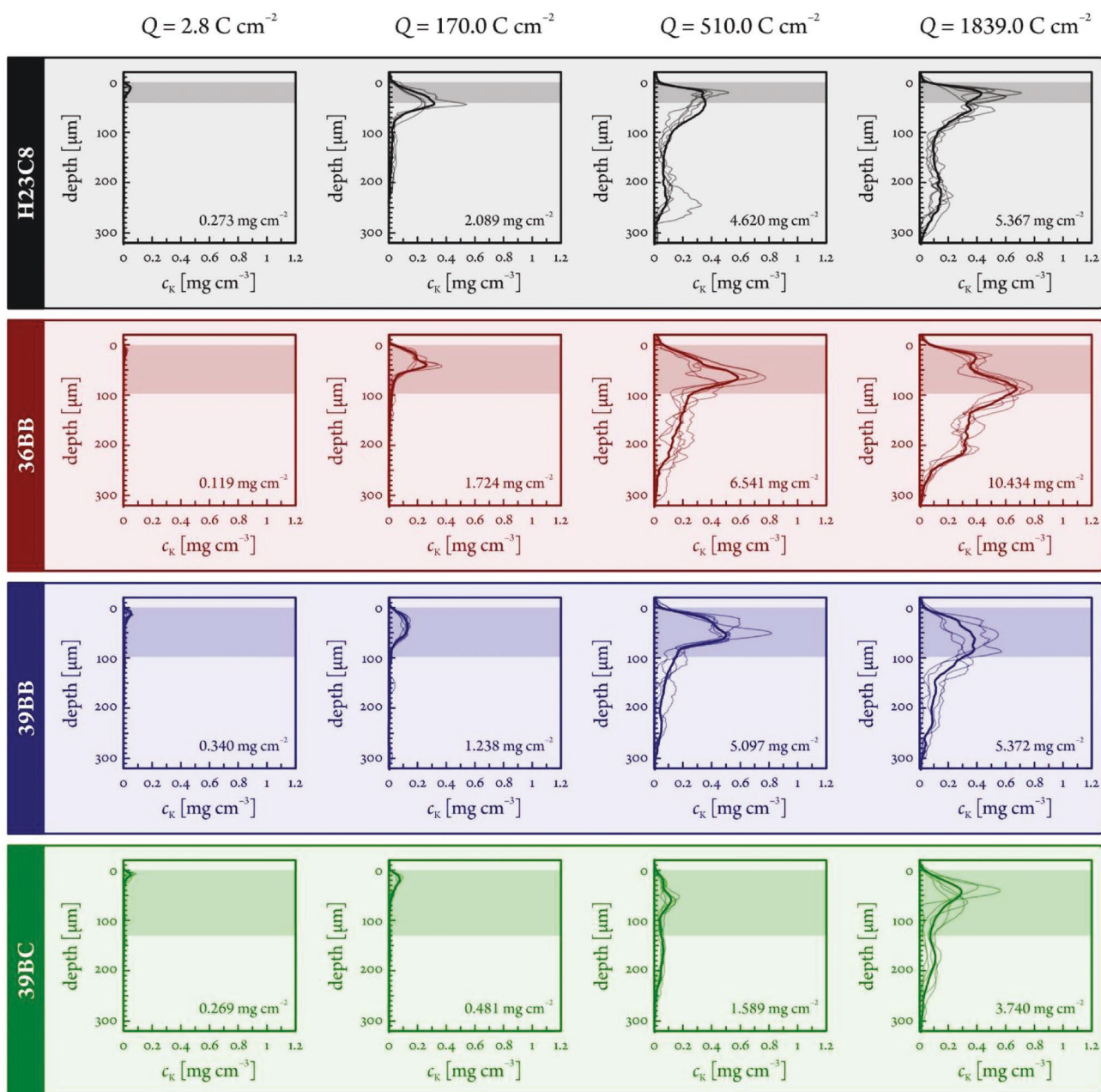
ADVANCED
SCIENCE NEWS
www.advancedsciencenews.com

small
methods
www.small-methods.com

Figure 6. Potassium concentration as a function of depth in cross sections of GDEs subjected to electrolysis performed with varied charge consumption, obtained by combined EDX/ICP-MS approach. Shaded bands indicate MPL regions. The total amount of potassium found in the GDE by ICP-MS, normalized to its surface area, is indicated by numbers. See the Statistical Analysis in the Experimental Section for more information on data processing.

electrode was subsequently inspected in a follow-up electrolysis performed with CO_2. Resulting FE(CO) values (Figure S14, Supporting Information, left panel) were significantly lower compared to those obtained for the as-prepared GDE (Figure 3). This indicates that flooding in the GDE takes place also in the absence of CO_2 and in situ generated (hydrogen)carbonate salts. Nonetheless, when a cleaning/drying step (see the Experimental Section for details) was inserted between the argon-fed and the follow-up CO_2-fed electrolysis, the evolution of the catalytic activity (Figure S14, Supporting Information, right panel) well resembled that obtained for the as-prepared GDE. This demonstrates that flooded electrolyte may be removed from the interior of GDE when flooding has taken place in the absence of CO_2.

Results of the multi-methodological experimental approach presented above have revealed significant differences in the evolution of catalytic activity and the character of the electrolyte intrusion among inspected ZG GDEs due to varied structure of their MPLs. In the following, we aim to find relationships between the MPL structure, electrolyte intrusion pattern, and
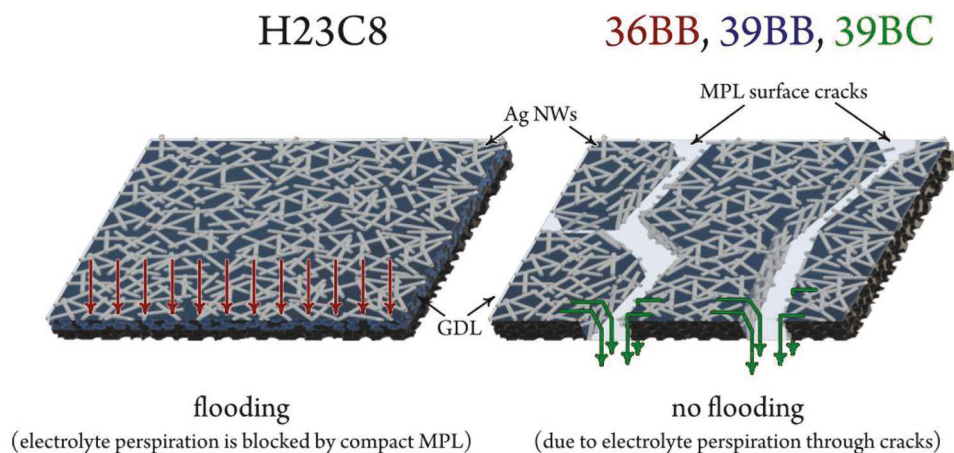
**ADVANCED
SCIENCE NEWS**

www.advancedsciencenews.com

**small
methods**

www.small-methods.com

Figure 7. Schematic depiction of the catalyst layer supported with non-cracked (left) and cracked (right) MPL, visualizing electrode flooding and electrolyte perspiration phenomena.

catalytic activity, and provide mechanistic insights in these phenomena, employing a schematic depiction of the catalyst layers supported by non-cracked and cracked MPLs shown in **Figure 7**.

The MPL of H23C8 contains no cracks (Figure 2; Figure S2, Supporting Information) and shows low internal porosity (Table 1). The electrolysis performed with such ZG GDE leads to an immediate and pronounced decline in FE(CO), significant increase in cell resistance and voltage (Figure 3), loss of hydrophobilicy (Figures S8,S9, Supporting Information) and electrode surface completely covered with potassium (Figure 4) that additionally accumulates in the MPL and top part of CFL (Figures 4,5). All these characteristics are indicative of severe flooding of the MPL (Figure 7, left), with the proposed mechanism presented as follows. The combination of the hydrostatic pressure and electroosmotic drag drives the electrolyte through the anion exchange membrane to the catalyst layer, where water is partially consumed in cathodic processes (first $ERCO_2$, later mainly ERH_2O). In the absence of cracks in the MPL, the excess electrolyte floods its micropores.[81] The presence of the liquid electrolyte in micropores significantly reduces the diffusion coefficient of CO_2.[5] The diffusion rate slows down in the course of the electrolysis as the electrolyte intrudes deeper in the GDL (Figures 4,5). The ERH_2O takes place in the GDL,[70] causing more water to be consumed per unit charge. This accelerates the accumulation of OH^- ions (both originally present in the electrolyte and generated as the by-product of ERH_2O) in the GDL. Increased amounts of OH^- ions are balanced by potassium ions that reach the GDL by ionic migration via the anion exchange membrane that can generally have non-perfect permselectivity.[84] Increased ionic concentration may negatively impact the solubility of gases[85] and reaction kinetics.[3,86] The absence of cracks combined with low internal porosity of the MPL and increased electrolyte viscosity due to accumulated ions leads to low perspiration rate (Figure 3). Furthermore, OH^- ions react with CO_2 dissolved in the electrolyte to form (hydrogen)carbonate anions, reducing the electrolyte conductivity and increasing the risk of the salt precipitation in micropores. The accumulation of ions further leads to loss of hydrophobicity facilitating flooding of micropores.[68]

Based on the results of consecutive electrolytic experiments performed with argon and CO_2 (Figure S14, Supporting Information), we support the view that flooding is not initiated by the carbonate precipitation, being in contradiction to the interpretation presented by Leonard et al.[68] In fact, the intrusion of the electrolyte to micropores may be triggered by electrowetting at extreme cathodic potentials (Figure 3).[30–40] It is important to note that the ex situ SEM/EDX analysis of GDE cross sections, as performed in this work (Figures 4,5), can visualize areas to which the electrolyte has permeated during the electrolysis but cannot distinguish whether solid precipitates are formed during or after the electrolysis.[69]

The MPL of 36BB contains cracks in low abundance (Figure 2; Figure S2, Supporting Information) and has high internal porosity (Table 1). Compared to the crack-free system, this ZG GDE sustains $ERCO_2$ for longer time, shows lower increase in the cell resistance and voltage (Figure 3), less pronounced loss of hydrophobicity (Figures S8,S9, Supporting Information) and lower accumulation of potassium on the electrode surface (Figures 4,5). Compared to micropores, cracks have much greater characteristic dimensions (Figure 2; Figure S2, Supporting Information) and thus constitute preferred pathways for the electrolyte intrusion (Figure 7, right), which was microscopically confirmed by the SEM/EDX analysis (Figure S11, Supporting Information) and macroscopically observed as increased perspiration rate (Figure 3). The perspiration through cracks alleviates the flooding of micropores, enabling them to function as channels for the gas transport.[53,54,56–58] However, the loss of catalytic activity (Figure 3) accompanied by a significant buildup of potassium on the surface (Figure 4) and in the interior (Figure 5) of the GDE observed in later stages of the electrolysis indicate that the crack abundance in 36BB is not sufficient to maintain micropores dry. Values of contact angles found in later stages of the electrolysis are close to 90° (Figures S8,S9, Supporting Information), suggesting that capillary forces have minimal effect on the electrolyte transport through the MPL. In such case, the electrolyte transport rate via cracks and micropores is governed by their hydrodynamic resistance.

MPLs of 39BB and 39BC have high abundance of cracks (Figure 2; Figure S2, Supporting Information) and high

**ADVANCED
SCIENCE NEWS**
www.advancedsciencenews.com

**small
methods**
www.small-methods.com

internal porosity (Table 1). They differ in the architecture of cracks, with 39BB having higher amount of narrow cracks and 39BC having broader cracks with sparser abundance. Both ZG GDEs show near-unity FE(CO) values, no increase in the cell resistance, only subtle cell voltage shifts, high electrolyte perspiration rates (Figure 3), almost no loss of hydrophobicity (Figures S8,S9, Supporting Information) and little accumulation of potassium on the electrode surface (Figure 4) and in its interior (Figures 4,5), with all these characteristics being retained for the entire time span of the electrolysis. This indicates that MPLs of these two electrodes possess sufficient abundance of cracks enabling efficient electrolyte perspiration that prevents the flooding of micropores (Figure 7, right). A desired electrolyte management in the ZG GDE, with the liquid phase being largely confined to the catalyst layer, is thus established.[4] Slightly higher FE(CO) values obtained for the 39BC based system further corroborate that cracks, and not micropores, are the main drainage pathway for the electrolyte perspiration, providing valuable hints for the design of MPLs in future ERCO$_2$ electrolyzers. Near unity FE(CO) values combined with results of cross-sectional EDX mapping of silver indicate that Ag nanowires deposited on crack walls are catalytically active toward ERCO$_2$. In fact, the catalyst located in the interior of cracks may be more active than that deposited on the MPL surface due to facilitated CO$_2$ transport, as recently demonstrated by Welch et al.[78] Nevertheless, it is important to note that the electrolyte perspiration through cracks causes parasitic CO$_2$ losses due to neutralization occurring in gas flow channels, which needs to be accounted for when assessing the overall economic viability of newly designed electrolyzers.

3. Conclusions and Outlook

Cracks as structures naturally occurring in MPLs of GDEs have been reported as beneficial for the water removal in polymer electrolyte membrane fuel cells.

In this work, we have inspected the ability of cracks to improve the electrolyte management and the overall catalytic performance of zero gap GDEs for the electrochemical reduction of carbon dioxide. The employed electrodes contained silver nanowires in a thin catalytic layer and differed in the abundance of cracks in the MPL supporting the catalyst. Utilizing galvanostatic electrolyzes, we demonstrated that electrodes with appropriate abundance of cracks show high and sustained catalytic activity, while a fast transition to parasitic reduction of water was noticed for non-cracked electrodes.

Small amounts of liquids and solids were observed in flow channels and the outlet of the carbon dioxide delivery system indicating that the electrolyte is transported through zero gap GDEs (electrolyte perspiration). For the first time, the amount of the electrolyte in the perspirate was determined, employing ICP-MS, finding that this amount scales with the abundance of cracks.

Cross sections of GDEs subjected to electrolyzes were subsequently inspected by our recently developed analytical approach combining SEM imaging, EDX elemental analysis, and ICP-MS, to obtain absolute concentration profiles of potassium used as the electrolyte intrusion marker. The performed

analysis provided the microscopic evidence that cracks serve as preferential pathways for the electrolyte transport through the MPL. Cracks thus drain excess electrolyte from the catalytic layer, which prevents flooding of micropores and enables them to function as efficient transport channels for gaseous carbon dioxide. In the absence of cracks, the electrolyte was found to flood micropores, reflecting itself as greatly reduced catalytic activity.

Our contribution presents the first study focusing on the effect of cracks on the electrolyte management and catalytic activity in the field of electrochemical CO$_2$ reduction. Besides monitoring the electrolyte intrusion in GDEs as a function of charge consumed in the electrolysis, we found correlations among the catalytic performance, electrochemical characteristics of cells, electrolyte perspiration rates, and surface wettability of electrodes, resolving the influence of cracks and micropores in the electrolyte transport.

While cracks were clearly proven to be beneficial for the electrolyte management, it should not be forgotten that the electrolyte perspiration occurring via these structures leads to non-negligible parasitic losses of carbon dioxide due to its neutralization. Therefore, efforts to optimize the utilization of carbon dioxide in electrolyzers must include searching for conditions under which both electrode flooding and perspiration-related reactant losses are minimized. Following the approaches reported for polymer electrolyte membrane fuel cells, we further aim at manufacturing and inspecting zero gap GDEs based on MPLs modified with artificially created draining elements such as holes or trenches formed by mechanical or laser perforation. The electrolyte perspiration through these structures may be controlled by their dimensions and predicted employing numerical models taking into account the capillary action, hydrodynamic resistance, and electroosmotic drag.

4. Experimental Section

Preparation of Gas Diffusion Electrodes: All experiments performed in this work employed commercial GDLs composed of supporting compressed CFL (carbon without additives) and MPL (carbon black treated with 5% PTFE). MPLs differ in their height, porosity, and abundance of cracks (for details see Results and Discussion). The GDL with crack-free MPL (H23C8) was obtained from Freudenberg, while GDLs involving cracked MPLs (36BB, 39BB, and 39BC) were purchased from Sigracet.

Silver nanowires used in this work as catalysts for ERCO$_2$ were synthesized following the procedure described in the previous work.[87] To prepare the catalyst ink, 4.5 mg of the as-synthesized Ag nanowires and 0.8 mg of carbon black (VULCAN VXC72R, Cabot) were separately dispersed in 20 mL of isopropanol (BASF SE, assay ≥ 99.0%) and sonicated for 30 min. Such prepared dispersions were intermixed, sonicated for 30 min, and dried by a rotary evaporator (Büchi R 210, 40 °C, 65 mbar). The resulting mixture was re-dispersed in 18 mL of isopropanol additionally containing 180 µL of Nafion 117 solution (≈5 wt% in a mixture of lower aliphatic alcohols and water, obtained from Sigma Aldrich) and sonicated for 20 min. The thus prepared catalyst ink was deposited on the MPL surfaces by airbrushing (hand-held Airbrushpistole Infinity CR plus, propelled by nitrogen gas, 99.999%, Carbagas, Switzerland), forming the catalyst layer. Such modified assemblies were dried and used as GDEs in electrolytic experiments performed as follows.

Assembly of the Electrolyzer: All electrochemical experiments performed in this work were realized in the electrolyzer shown in Figure S1,

Supporting Information.[22,79] The electrolyzer was based on ZG GDE arrangement with GDEs prepared as described above, interfaced to the anodic compartment. The assembly of the electrolyzer was carried out as follows. The GDE with the catalyst layer facing upward was placed on a stainless steel support functioning as a current collector and a gas delivery system (it was equipped with flow channels connected to inlet and outlet tubing). The anion exchange membrane (X37-50 RT, Dioxide materials) was subjected to a pre-treatment suggested by the supplier, and gently placed on the top of the GDE. The formed ZG GDE was covered by a Teflon chamber, which was subsequently mounted to the stainless steel support by a clamp. The Teflon chamber was filled with aqueous KOH solution (10 mL, 2 м, pH = 14.3, solid KOH purchased from Sigma Aldrich, prepared employing Milli-Q water) serving as the anolyte. The Teflon chamber contained a central circular orifice (radius of 0.15 cm) in its bottom part defining the geometrical area of the ZG GDE/anolyte interface. Iridium wire (99.9%, MaTeck Material-Technologie & Kristalle GmbH, Germany) separated by glass frit and Ag/AgCl/3 м KCl electrode (double junction design, Metrohm) were immersed in the anolyte and were utilized as the counter electrode and the reference electrode. A flask containing 15 mL of Milli-Q water was placed downstream to the gas outlet and served as a trap to collect the perspirate resulting from the electrolyte transport through the ZG GDE.

Electrochemical Measurements: The catalytic activity of the ZG GDE (set as the working electrode) was inspected by galvanostatic experiments in the electrolyzer assembled as described above, employing an ECi-200 potentiostat (ECi-200, Nordic Electrochemistry). For all four GDEs, the electrolysis was performed at current of −20 mA (corresponding to geometric current density of −283 mA cm^{-2}) for systematically varied time, specifically 10, 600, 1800, and 6500 s. In the Results and Discussion section, the duration of electrolysis is presented as passed charge normalized to the geometrical area of the ZG GDE/anolyte interface (0.0707 cm^2). Unless otherwise specified, a freshly prepared GDE was used in the electrolysis. A humidified gaseous CO$_2$ stream (99.999%, Carbagas, Switzerland) was continuously supplied to the flow channels of the stainless steel support via the inlet at the rate of 18 mL min^{-1} employing a thermal mass flow controller (red-y smart, Vögtlin Instruments). The gaseous mixture leaving the outlet was fed through a drying tube and its composition was analyzed for CO and H$_2$ by online GC (SRI Instruments) in 10 min intervals.[21] The formed CO and H$_2$ quantities, measured during electrolysis, added up to about 100% ± 10% of the quantities that could be expected from the charge of electrolysis. Noting that while the formation of some other products (e.g., that of formate) was possible in very little amount in the studied electrolyzer, it was assumed that the H$_2$:CO formation ratios detectable by GC were, within range of experimental error, correct. Faradaic efficiency values (e.g., those presented in Figure 3) were thus re-scaled so that the measured H$_2$:CO ratios were respected, together accounting for a 100% Faradaic efficiency.

The cell voltage and resistance were monitored in 0.1 s intervals. The cell resistance was obtained by superimposing AC perturbation (5 000 Hz, 50 μA) to the current applied to the cell (20 mA) and monitoring the AC component of the cell voltage.

For the GDE based on 36BB GDL, a follow-up electrolysis experiment was performed with the goal of exploring the possibility of restoring the catalytic activity of once used electrode. First, the GDE was subjected to the electrolysis performed as described above. Afterward, the electrolyzer was disassembled and the GDE was immersed in ≈30 mL of quiescent Milli-Q water for 5 min, the procedure being repeated 7 times. Subsequently, the GDE was dried in a vacuum oven for 2 h at ambient temperature. Such treated GDE was reinstalled into the electrolyzer and its catalytic performance was inspected in a follow-up electrolysis carried out under the same conditions.

Also for the GDE based on 36BB GDL, an additional control electrolytic experiment was performed to inspect the occurrence of flooding in the absence of CO$_2$. First, the GDE was subjected to the electrolysis with humidified CO$_2$ being replaced by humidified argon (99.9999%, Carbagas, Switzerland). Subsequently, the electrolyzer was disassembled and the GDE was either subjected to the cleaning/drying

procedure performed as described above or this step was omitted. Such treated GDE was reinstalled into the electrolyzer and its catalytic performance was inspected in a follow-up electrolysis carried out with humidified CO$_2$.

Characterization of Electrodes: Surfaces of pristine MPLs and as-prepared GDEs were inspected by optical microscopic imaging employing a VHX600 Keyence digital microscopes. The obtained images were utilized to determine the surface CR based on counting pixels corresponding to cracks and solid regions on the MPL surface. The void ratio of CFLs, MPLs, and entire GDLs was obtained by using a pycnometer, employing isopropanol as a liquid that was assumed to completely fill up the internal structures of layers. Surfaces of as-purchased (pristine) MPLs, as-prepared GDEs, and GDEs subjected to the electrolysis were additionally inspected by white light interferometry (Contour GT, Bruker) equipped with Vision64 software (Vision64, Bruker).

A Zeiss Gemini 450 SEM equipped with an EDX spectroscopy instrument (Aztec, Oxford instruments) was used to investigate the structure and content of silver and potassium on surfaces and in the interior of GDEs. Surfaces of GDEs were inspected before and after electrolytic measurements performed as described above. For selected samples, identical location SEM studies were performed. Subsequently, electrodes subjected to the electrolysis were frozen in liquid nitrogen and cut by a sharp blade and such obtained cross sections were examined by SEM/EDX. To obtain statistically significant information, at least five cross sections were prepared and analyzed for each GDE. The cross-sectional imaging was additionally performed for as-purchased GDLs, to determine the thickness of the CFL and the MPL.

The mass loading of silver in the catalyst layer of as-prepared GDEs was determined by means of ICP-MS (NexION 2000 ICP-MS instrument, PerkinElmer). For this purpose, GDEs of circular shape with the radius of 0.1 cm were prepared and examined. GDE samples were introduced to concentrated nitric acid (69.3%, VLSI selectipur, BASF), sonicated for 30 min and left overnight. Additionally, ICP-MS analysis following the same sample treatment was employed to determine the amount of potassium in the interior of GDEs upon the electrolysis. Furthermore, the ICP-MS was employed to determine the amount of potassium in the perspirate resulting from the electrolyte transport through GDEs, found in the trap following the gas outlet.

The wettability of as-purchased GDLs, as prepared GDEs and GDEs subjected to electrolysis performed as described above was assessed by contact angle measurement (Krüss Advance Drop Shape Analyzer DSA25, Krüss GmbH, Hamburg, Germany). Electrodes subjected to the electrolysis were dried for 2 h before actual measurements. All inspected samples were mounted on a flat stage, sessile water drops (Milli-Q water, 1.4 μL) were deposited on their top at room temperature and contact angles were recorded immediately after creating droplets.

Statistical Analysis: For data presented in the form expected value ± error in the paper, the expected value was determined as the arithmetic mean, and the error as the standard deviation of the dataset. Contact angle intervals reported in the text were calculated using values shown in Figure S7, Supporting Information, by averaging over different GDEs that underwent the same electrolysis treatment. The optical micrographs of the as-prepared GDEs (Figure 2) were used for the calculation of surface CRs of the GDEs. The micrographs were utilized to determine the surface CR based on counting pixels corresponding to cracks and solid regions on the MPL surface: the analysis was done by an in-house developed algorithm written in LabVIEW. The void ratios of the carbon fibrous and MPLs of GDLs, as well as the total void ratios of CFLs, MPLs, and entire GDLs, shown in Table 1, were determined by three parallel pycnometer-based densitometry measurements. The vertical depth profiles of K$^+$ concentrations, shown in Figure 6, were created using cross-sectional EDX maps obtained from the respective GDEs following electrolyzes. The total (average) K$^+$ concentrations, corresponding to the integrals of the averaged distribution curves, were determined by a single ICP-MS measurement. In case of each panel of Figure 6, several (five to eight) individual EDX maps were analyzed. These maps were obtained in a numerical format from the Aztec controlling software. Depth profiles were

obtained by a row-to-row summation of the K signal intensity, followed by vertical alignment of the individual distributions. This alignment was based on the assignation of a 0 depth value to the first entry where the detected K intensity reached 3 times the initial noise level. For the alignment, subsequent averaging, and normalization of the distributions, a home-built software (written in LabVIEW) was used; more details of the calculations can be found elsewhere.[77] Raw data serving as a basis for the presented calculations are accessible at Zenodo.[88]

Supporting Information

Supporting Information is available from the Wiley Online Library or from the author.

Conflict of Interest

The authors declare no conflict of interest.

Data Availability Statement

The raw data to this paper are made fully accessible to the public via Zenodo (https://doi.org/10.5281/zenodo.6421142) along with the publication of this manuscript.

[1] I. Ganesh, *Renewable Sustainable Energy Rev.* **2016**, *59*, 1269.
[2] S. Nitopi, E. Bertheussen, S. B. Scott, X. Y. Liu, A. K. Engstfeld, S. Horch, B. Seger, I. E. L. Stephens, K. Chan, C. Hahn, J. K. Norskov, T. F. Jaramillo, I. Chorkendorff, *Chem. Rev.* **2019**, *119*, 7610.
[3] T. Burdyny, W. A. Smith, *Energy Environ. Sci.* **2019**, *12*, 1442.
[4] N. T. Nesbitt, T. Burdyny, H. Simonson, D. Salvatore, D. Bohra, R. Kas, W. A. Smith, *ACS Catal.* **2020**, *10*, 14093.
[5] D. M. Weekes, D. A. Salvatore, A. Reyes, A. X. Huang, C. P. Berlinguette, *Acc. Chem. Res.* **2018**, *51*, 910.
[6] E. W. Lees, B. A. W. Mowbray, F. G. L. Parlane, C. P. Berlinguette, *Nat. Rev. Mater.* **2022**, *7*, 55.
[7] A. Z. Weber, J. Newman, *J. Electrochem. Soc.* **2005**, *152*, A677.
[8] B. Kim, F. Hillman, M. Ariyoshi, S. Fujikawa, P. J. A. Kenis, *J. Power Sources* **2016**, *312*, 192.
[9] E. J. Dufek, T. E. Lister, M. E. McIlwain, *Electrochem. Solid-State Lett.* **2012**, *15*, B48.
[10] S. S. Bhargava, F. Proietto, D. Azmoodeh, E. R. Cofell, D. A. Henckel, S. Verma, C. J. Brooks, A. A. Gewirth, P. J. A. Kenis, *ChemElectroChem* **2020**, *7*, 2001.
[11] S. Verma, Y. Hamasaki, C. Kim, W. X. Huang, S. Lu, H. R. M. Jhong, A. A. Gewirth, T. Fujigaya, N. Nakashima, P. J. A. Kenis, *ACS Energy Lett.* **2018**, *3*, 193.
[12] S. Verma, X. Lu, S. C. Ma, R. I. Masel, P. J. A. Kenis, *Phys. Chem. Chem. Phys.* **2016**, *18*, 7075.
[13] B. Kim, S. Ma, H. R. M. Jhong, P. J. A. Kenis, *Electrochim. Acta* **2015**, *166*, 271.
[14] C. M. Gabardo, A. Seifitokaldani, J. P. Edwards, C. T. Dinh, T. Burdyny, M. G. Kibria, C. P. O'Brien, E. H. Sargent, D. Sinton, *Energy Environ. Sci.* **2018**, *11*, 2531.
[15] V. R. Stamenkovic, D. Strmcnik, P. P. Lopes, N. M. Markovic, *Nat. Mater.* **2017**, *16*, 57.
[16] J. Lee, J. Lim, C. W. Roh, H. S. Whang, H. Lee, *J. CO₂ Util.* **2019**, *31*, 244.
[17] L. C. Weng, A. T. Bell, A. Z. Weber, *Energy Environ. Sci.* **2019**, *12*, 1950.
[18] A. Angulo, P. van der Linde, H. Gardeniers, M. Modestino, D. F. Rivas, *Joule* **2020**, *4*, 555.
[19] L. Cindrella, A. M. Kannan, J. F. Lin, K. Saminathan, Y. Ho, C. W. Lin, J. Wertz, *J. Power Sources* **2009**, *194*, 146.
[20] M. L. Liu, Y. Kong, H. F. Hu, N. Kovacs, C. Z. Sun, I. Z. Montiel, M. D. G. Vazquez, Y. Hou, M. Mirolo, I. Martens, J. Drnec, S. Vesztergom, P. Broekmann, *J. Catal.* **2021**, *404*, 371.
[21] M. D. Galvez-Vazquez, S. Alinejad, H. F. Hu, Y. H. Hou, P. Moreno-Garcia, A. Zana, G. K. H. Wiberg, P. Broekmann, M. Arenz, *Chimia* **2019**, *73*, 922.
[22] M. D. Galvez-Vazquez, P. Moreno-Garcia, H. Xu, Y. H. Hou, H. F. Hu, I. Z. Montiel, A. V. Rudnev, S. Alinejad, V. Grozovski, B. J. Wiley, M. Arenz, P. Broekmann, *ACS Catal.* **2020**, *10*, 13096.
[23] M. Maja, C. Orecchia, M. Strano, P. Tosco, M. Vanni, *Electrochim. Acta* **2000**, *46*, 423.
[24] N. Wagner, M. Schulze, E. Gulzow, *J. Power Sources* **2004**, *127*, 264.
[25] Z. Xing, X. Hu, X. F. Feng, *ACS Energy Lett.* **2021**, *6*, 1694.
[26] Z. Xing, L. Hu, D. S. Ripatti, X. Hu, X. F. Feng, *Nat. Commun.* **2021**, *12*, 136.
[27] W. H. Lee, Y. J. Ko, Y. Choi, S. Y. Lee, C. H. Choi, Y. J. Hwang, B. K. Min, P. Strasser, H. S. Oh, *Nano Energy* **2020**, *76*, 105030.
[28] U. O. Nwabara, A. D. Hernandez, D. A. Henckel, X. Y. Chen, E. R. Cofell, M. P. De-Heer, S. Verma, A. A. Gewirth, P. J. A. Kenis, *ACS Appl. Energy Mater.* **2021**, *4*, 5175.
[29] A. Reyes, R. P. Jansonius, B. A. W. Mowbray, Y. Cao, D. G. Wheeler, J. Chau, D. J. Dvorak, C. P. Berlinguette, *ACS Energy Lett.* **2020**, *5*, 1612.
[30] T. Burchardt, *J. Power Sources* **2004**, *135*, 192.
[31] K. Liu, W. A. Smith, T. Burdyny, *ACS Energy Lett.* **2019**, *4*, 639.
[32] A. Lowe, C. Rieg, T. Hierlemann, N. Salas, D. Kopljar, N. Wagner, E. Klemm, *ChemElectroChem* **2019**, *6*, 4497.
[33] K. J. Puring, D. Siegmund, J. Timm, F. Mollenbruck, S. Schemme, R. Marschall, U. P. Apfel, *Adv. Sustainable Syst.* **2021**, *5*, 2000088.
[34] F. Bienen, A. Lowe, J. Hildebrand, S. Hertle, D. Schonvogel, D. Kopljar, N. Wagner, E. Klemm, K. A. Friedrich, *J. Energy Chem.* **2021**, *62*, 367.
[35] F. Bienen, J. Hildebrand, D. Kopljar, N. Wagner, E. Klemm, K. A. Friedrich, *Chem. Ing. Tech.* **2021**, *93*, 1015.
[36] K. L. Yang, R. Kas, W. A. Smith, T. Burdyny, *ACS Energy Lett.* **2021**, *6*, 33.
[37] B. De Mot, J. Hereijgers, M. Duarte, T. Breugelmans, *Chem. Eng. J.* **2019**, *378*, 122224.
[38] P. Jeanty, C. Scherer, E. Magori, K. Wiesner-Fleischer, O. Hinrichsen, M. Fleischer, *J. CO₂ Util.* **2018**, *24*, 454.
[39] M. Duarte, B. De Mot, J. Hereijgers, T. Breugelmans, *ChemElectroChem* **2019**, *6*, 5596.
[40] S. Sen, S. M. Brown, M. Leonard, F. R. Brushett, *J. Appl. Electrochem.* **2019**, *49*, 917.

[41] D. G. Wheeler, B. A. W. Mowbray, A. Reyes, F. Habibzadeh, J. F. He, C. P. Berlinguette, *Energy Environ. Sci.* **2020**, *13*, 5126.

[42] B. Endrodi, E. Kecsenovity, A. Samu, F. Darvas, R. V. Jones, V. Torok, A. Danyi, C. Janaky, *ACS Energy Lett.* **2019**, *4*, 1770.

[43] M. E. Leonard, M. J. Orella, N. Aiello, Y. Roman-Leshkov, A. Forner-Cuenca, F. R. Brushett, *J. Electrochem. Soc.* **2020**, *167*, 124521.

[44] H. Li, Y. H. Tang, Z. W. Wang, Z. Shi, S. H. Wu, D. T. Song, J. L. Zhang, K. Fatih, J. J. Zhang, H. J. Wang, Z. S. Liu, R. Abouatallah, A. Mazza, *J. Power Sources* **2008**, *178*, 103.

[45] K. Jiao, X. G. Li, *Prog. Energy Combust. Sci.* **2011**, *37*, 221.

[46] N. Yousfi-Steiner, P. Mocoteguy, D. Candusso, D. Hissel, A. Hernandez, A. Aslanides, *J. Power Sources* **2008**, *183*, 260.

[47] P. C. Pei, H. C. Chen, *Appl. Energy* **2014**, *125*, 60.

[48] M. B. Ji, Z. D. Wei, *Energies* **2009**, *2*, 1057.

[49] A. Bazylak, *Int. J. Hydrogen Energy* **2009**, *34*, 3845.

[50] S. Tsushima, S. Hirai, *Prog. Energy Combust. Sci.* **2011**, *37*, 204.

[51] R. Omrani, B. Shabani, *Int. J. Hydrogen Energy* **2017**, *42*, 28515.

[52] S. Tsushima, S. Hirai, *J. Therm. Sci. Technol.* **2015**, *10*, JTST0002.

[53] T. Sasabe, P. Deevanhxay, S. Tsushima, S. Hirai, *Electrochem. Commun.* **2011**, *13*, 638.

[54] E. A. Wargo, V. P. Schulz, A. Cecen, S. R. Kalidindi, E. C. Kumbur, *Electrochim. Acta* **2013**, *87*, 201.

[55] M. P. Manahan, S. Kim, E. C. Kumbur, M. M. Mench, *ECS Trans.* **2009**, *25*, 1745.

[56] H. Markotter, I. Manke, P. Kruger, T. Arlt, J. Haussmann, M. Klages, H. Riesemeier, C. Hartnig, J. Scholta, J. Banhart, *Electrochem. Commun.* **2011**, *13*, 1001.

[57] N. Karst, V. Faucheux, A. Martinent, P. Bouillon, J. P. Simonato, *J. Power Sources* **2010**, *195*, 5228.

[58] J. S. Ma, X. X. Zhang, Z. Y. Jiang, H. Ostadi, K. Jiang, R. Chen, *Fuel* **2014**, *136*, 307.

[59] D. Gerteisen, C. Sadeler, *J. Power Sources* **2010**, *195*, 5252.

[60] K. Nishida, T. Murakami, S. Tsushima, S. Hirai, *J. Power Sources* **2010**, *195*, 3365.

[61] R. L. Cook, R. C. Macduff, A. F. Sammells, *J. Electrochem. Soc.* **1990**, *137*, 607.

[62] G. L. De Gregorio, T. Burdyny, A. Loiudice, P. Iyengar, W. A. Smith, R. Buonsanti, *ACS Catal.* **2020**, *10*, 4854.

[63] M. Jouny, W. Luc, F. Jiao, *Nat. Catal.* **2018**, *1*, 748.

[64] J. J. Lv, M. Jouny, W. Luc, W. L. Zhu, J. J. Zhu, F. Jiao, *Adv. Mater.* **2018**, *30*, 1803111.

[65] C. M. Gabardo, C. P. O'Brien, J. P. Edwards, C. McCallum, Y. Xu, C. T. Dinh, J. Li, E. H. Sargent, D. Sinton, *Joule* **2019**, *3*, 2777.

[66] E. R. Cofell, U. O. Nwabara, S. S. Bhargava, D. E. Henckel, P. J. A. Kenis, *ACS Appl. Mater. Interfaces* **2021**, *13*, 15132.

[67] C. T. Dinh, T. Burdyny, M. G. Kibria, A. Seifitokaldani, C. M. Gabardo, F. P. G. de Arquer, A. Kiani, J. P. Edwards, P. De Luna, O. S. Bushuyev, C. Q. Zou, R. Quintero-Bermudez, Y. J. Pang, D. Sinton, E. H. Sargent, *Science* **2018**, *360*, 783.

[68] M. E. Leonard, L. E. Clarke, A. Forner-Cuenca, S. M. Brown, F. R. Brushett, *ChemSusChem* **2020**, *13*, 400.

[69] D. McLaughlin, M. Bierling, R. Moroni, C. Vogl, G. Schmid, S. Thiele, *Adv. Energy Mater.* **2020**, *10*, 2000488.

[70] D. Raciti, T. Braun, B. M. Tackett, H. Xu, M. Cruz, B. J. Wiley, T. P. Moffat, *ACS Catal.* **2021**, *11*, 11945.

[71] G. O. Larrazabal, P. Strom-Hansen, J. P. Heli, K. Zeiter, K. T. Therldldsen, I. Chorkendorff, B. Seger, *ACS Appl. Mater. Interfaces* **2019**, *11*, 41281.

[72] J. Li, G. X. Chen, Y. Y. Zhu, Z. Liang, A. Pei, C. L. Wu, H. X. Wang, H. R. Lee, K. Liu, S. Chu, Y. Cui, *Nat. Catal.* **2018**, *1*, 592.

[73] A. Patru, T. Binninger, B. Pribyl, T. J. Schmidt, *J. Electrochem. Soc.* **2019**, *166*, F34.

[74] B. De Mot, M. Ramdin, J. Hereijgers, T. J. H. Vlugt, T. Breugelmans, *ChemElectroChem* **2020**, *7*, 3839.

[75] B. Endrodi, E. Kecsenovity, A. Samu, T. Halmagyi, S. Rojas-Carbonell, L. Wang, Y. Yan, C. Janaky, *Energy Environ. Sci.* **2020**, *13*, 4098.

[76] B. Endrodi, A. Samu, E. Kecsenovity, T. Halmagyi, D. Sebok, C. Janaky, *Nat. Energy* **2021**, *6*, 439.

[77] Y. Kong, H. F. Hu, M. L. Liu, Y. Hou, V. Kolivoska, S. Vesztergom, P. Broekmann, *J. Catal.* **2022**, *408*, 1.

[78] A. J. Welch, A. Q. Fenwick, A. Bohme, H. Y. Chen, I. Sullivan, X. Q. Li, J. S. DuChene, C. X. Xiang, H. A. Atwater, *J. Phys. Chem. C* **2021**, *125*, 20896.

[79] G. K. H. Wiberg, M. Fleige, M. Arenz, *Rev. Sci. Instrum.* **2015**, *86*, 024102.

[80] Y. H. Hou, N. Kovacs, H. Xu, C. Z. Sun, R. Erni, M. D. Galvez-Vazquez, A. Rieder, H. F. Hu, Y. Kong, M. L. Liu, B. J. Wiley, S. Vesztergom, P. Broekmann, *J. Catal.* **2021**, *394*, 58.

[81] L. C. Weng, A. T. Bell, A. Z. Weber, *Phys. Chem. Chem. Phys.* **2018**, *20*, 16973.

[82] M. Ma, S. Kim, I. Chorkendorff, B. Seger, *Chem. Sci.* **2020**, *11*, 8854.

[83] M. Ma, E. L. Clark, K. T. Therkildsen, S. Dalsgaard, I. Chorkendorff, B. Seger, *Energy Environ. Sci.* **2020**, *13*, 977.

[84] G. M. Geise, M. A. Hickner, B. E. Logan, *ACS Appl. Mater. Interfaces* **2013**, *5*, 10294.

[85] M. Roehe, A. Botz, D. Franzen, F. Kubannek, B. Ellendorff, D. Oehl, W. Schuhmann, T. Turek, U. Krewer, *ChemElectroChem* **2019**, *6*, 5671.

[86] N. T. Nesbitt, W. A. Smith, *J. Phys. Chem. C* **2021**, *125*, 13085.

[87] H. F. Hu, M. L. Liu, Y. Kong, N. Mysuru, C. Z. Sun, M. D. Galvez-Vazquez, U. Muller, R. Erni, V. Grozovski, Y. H. Hou, P. Broekmann, *ACS Catal.* **2020**, *10*, 8503.

[88] Y. Kong, M. Liu, H. Hu, Y. Hou, S. Vesztergom, M. de J. Gálvez-Vázquez, I. Zelocualtecatl Montiel, V. Kolivoška, P. Broekmann, Raw data for the article "Cracks as efficient tools to mitigate flooding in gas diffusion electrodes used for the electrochemical reduction of carbon dioxide" **2022**, https://doi.org/10.5281/zenodo.6421142.

5.9 Limitations of identical location SEM as a method of degradation studies on surfactant capped nanoparticle electrocatalysts

Authors: Yuhui Hou*, Noémi Kovács, Heng Xu, Changzhe Sun, Rolf Erni, María de Jesús Gálvez-Vázquez, Alain Rieder, **Huifang Hu**, Ying Kong, Menglong Liu, Benjamin J. Wiley, Soma Vesztergom*, and Peter Broekmann

J. Catal., 2021, 394, 58-66. DOI: 10.1016/j.jcat.2020.12.006

Highlights: Ag NC capped by PVP was used as a model catalyst for CO_2RR. The PVP absorbed on the catalyst surface turn into a passive organic contamination layer after explosion of electron beam from SEM, which may decrease some of the activity of catalyst. Therefore, the spot mapped by IL-SEM leads to few or no changes during the electrolysis, though the entire catalyst undergoes degradation. The results suggest that the extreme care should be taken when employing IL-SEM for catalyst degradation studies, especially in the presence of capping agents.

Contributions: I assisted in the electrochemical measurements and helped to prepare the electrodes. Furthermore, I participated in the literature and result discussion during the manuscript writing process.

Limitations of identical location SEM as a method of degradation studies on surfactant capped nanoparticle electrocatalysts

Yuhui Hou [a,1,*], Noémi Kovács [a,b,1], Heng Xu [c], Changzhe Sun [a], Rolf Erni [d], María de Jesús Gálvez-Vázquez [a], Alain Rieder [a], Huifang Hu [a], Ying Kong [a], Menglong Liu [a], Benjamin J. Wiley [c], Soma Vesztergom [a,b,*], Peter Broekmann [a]

[a] *University of Bern, Department of Chemistry and Biochemistry, Freiestrasse 3, 3012 Bern, Switzerland*
[b] *Eötvös Loránd University, Department of Physical Chemistry, Pázmány Péter sétány 1/A, 1117 Budapest, Hungary*
[c] *Duke University, Department of Chemistry, French Family Science Cen 2214, NC–27708 Durham, NC, USA*
[d] *Swiss Federal Laboratories for Materials Science and Technology (EMPA), Electron Microscopy Center, Überlandstrasse 129, CH–8600 Dübendorf, Switzerland*

ARTICLE INFO

ABSTRACT

Identical location scanning electron microscopy (IL–SEM) has become an important tool for electrocatalysis research in the past few years. The method allows for the observation of the same site of an electrode, often down to the same nanoparticle, before and after electrochemical treatment. It is presumed that by IL–SEM, alterations in the surface morphology (the growth, shrinkage, or the disappearance of nanosized features) can be detected, and the thus visualized degradation can be linked to changes of the catalytic performance, observed during prolonged electrolyses. In the rare cases where no degradation is seen, IL–SEM may provide comfort that the studied catalyst is ready for up-scaling and can be moved towards industrial applications. However, although it is usually considered a non-invasive technique, the interpretation of IL–SEM measurements may get more complicated. When, for example, IL–SEM is used to study the degradation of surfactant-capped Ag nanocubes employed as electrocatalysts of CO₂ electroreduction, nanoparticles subjected to the electron beam during pre-electrolysis imaging may lose some of their catalytic activity due to the under-beam formation of a passive organic contamination layer. Although the entirety of the catalyst obviously degrades, the spot mapped by IL–SEM reflects no or little changes during electrolysis. The aim of this paper is to shed light on an important limitation of IL–SEM: extreme care is necessary when applying this method for catalyst degradation studies, especially in case of nanoparticles with surface-adsorbed capping agents.

© 2020 The Author(s). Published by Elsevier Inc. This is an open access article under the CC BY license (http://creativecommons.org/licenses/by/4.0/).

1. Introduction

Due to the ever-increasing consumption of fossil fuels, gigatons of CO₂ are released yearly to the atmosphere, expediting global warming [1]. A possible way of mitigating the effects of atmospheric CO₂ is to reduce it electrochemically. Electrochemical reduction does not only allow CO₂ to be regarded as a valuable raw material instead of an environmentally dangerous waste, but it may also provide a solution for the storage of excess renewable (hydro-, solar or wind) energy [2].

Mostly due to this, electrochemical CO₂ reduction —a process that was first described more than 150 years ago [3]— has recently become the forefront of electrochemical research [4]. Searching for the term "electrochemical CO₂ reduction" on the website of ACS Publications yields 3334 research papers about this topic, only from the past year; Google Scholar, when searched for the same term and for the same period of time, gives > 17000 matches. A majority of these publications are original research papers that describe new catalyst materials, which —somewhat remarkably— all exhibit excellent qualities when applied for CO₂ reduction. This means that by covering electrodes with the newly invented catalysts, and carrying out electrolyses of solutions that contain CO₂ dissolved in some form, high current densities of CO₂ reduction can be achieved at relatively low overpotentials, and the process may in an ideal case yield only one or just a few desired products [4].

* Corresponding authors at: University of Bern, Department of Chemistry and Biochemistry, Freiestrasse 3, 3012 Bern, Switzerland (Y. Hou); Eötvös Loránd University, Department of Physical Chemistry, Pázmány Péter sétány 1/A, 1117 Budapest, Hungary (S. Vesztergom).
E-mail addresses: yuhui.hou@dcb.unibe.ch (Y. Hou), vesztergom@chem.elte.hu (S. Vesztergom), peter.broekmann@dcb.unibe.ch (P. Broekmann).
[1] These authors contributed equally.

Compared to the tremendous amount of research invested in the design of new electrocatalyst materials for CO_2 electroreduction, technologies that operate on an industrial scale are still rare. Undoubtedly, the most important obstacle that hinders the application of newly developed catalysts on an industrial level is an issue of stability: catalysts that may show remarkable features in lab experiments tend to degrade and lose their performance over prolonged use. This may especially be true for catalysts owing their activity to a fine structure, such as colloidally synthesized nanoparticles that are especially prone to degradation over long-time operation. In case of these catalysts, studying (electro-)mechanical degradation and its effects on the catalytic performance has to be the first step of technological up-scaling.

Although many *operando* techniques (*e.g.*, X-ray diffraction, scattering or absorption, as well as Raman spectroscopies [5,6]) can provide an insight to nanoparticle transformations occurring during CO_2 reduction, it is still more common to use *ex situ* electron microscopic (EM) techniques to observe, in particular, the structural changes that electrocatalysts suffer during CO_2 reduction.

In order to apply EM in an electrocatalysis study, the catalyst has to be sampled before and after it is made subject to electrochemical treatment. When comparing images taken before and after electrolysis, we usually work under two implicit assumptions: *(i.)* that the areas scanned before and after the electrolysis are either physically the same, or are both representative of the sample as a whole; and *(ii.)* that any changes we observe are indeed caused by the electrochemical treatment and not by other operations, *e.g.,* the pre-electrolysis scanning of the sample, careless sample transportation, exposition to air or to chemicals, etc.

The former of the above two assumptions can readily be made explicit, for example, if identical location scanning or transmission electron microscopies (IL–SEM or IL–TEM) are employed. IL–TEM was first described by a work of Mayrhofer et al. in 2008 [7], and the first report on the application of IL–SEM by Hodnik et al. [8] followed not much later, in 2012. In early studies, the catalyst material was loaded on a TEM finder grid (made of gold) to facilitate identical location imaging [7]. Later it was found that it is enough to apply a small incision (a cross-like scratch) on other (*e.g.*, graphite) holders to relocate the scanned site after electrolysis, which rendered the use of finder grids unnecessary. Due to the fact that IL–EM is able to visualize changes of a catalyst surface, often down to the details of individual nanoparticles, IL–EM found immediate application in catalyst degradation studies on a variety of target reactions [9,10].

In the field of CO_2 electrolysis, IL–EM became a prominent method of studying catalyst degradation [11–21], mainly because it is considered (and, starting from its discovery, often advertised as) a non-destructive method. It is usually assumed that if a given catalyst preserves good performance characteristics over longer periods of electrolysis, and neither IL–SEM nor IL–TEM reveal any structural degradation, the catalyst is stable and can be considered a potential candidate for up-scaled (*e.g.*, flow cell) studies [15].

Unfortunately, however, the situation is not this simple, especially because, in some cases, the pre-electrolysis EM imaging does affect the future catalytic performance of the sampled catalyst areas. For example, in the literature of IL–TEM studies of electrocatalysts, there are reports on the electron beam induced shrinkage (as well as some ripening) of Pt nanoparticles used in fuel cells [22]. Based on these results, Arenz and Zana strongly recommend that in order to check if the electron beam changes the sample, TEM analysis following the electrochemical measurements should also be performed at pristine locations; *i.e.*, locations which have not been previously exposed to the electron beam [23].

For IL–SEM, probably based on the assumption that the electron dose is much lower than in the case of TEM, no such warning was

given, and it is indeed not likely that the beam used under SEM conditions could induce similar sintering effects observed in TEM. The sintering of nanoparticles may however not be the only way an electron beam can alter a catalyst surface: another, equally important phenomenon —namely, the under-beam formation of a passive layer— should also deserve attention.

That electron bombardment of a conducting sample *in vacuo*, where only slightest traces of organic vapours occur, can result in the coverage of the sample with a non-conducting layer of polymerized carbon compounds was first noticed by Lariviere Stewart [24] in 1934 — that is, four years before von Ardenne built the first SEM [25]. That electron bombardment, especially during focusing, can also cause changes to the surface of a sample inside an SEM was first noticed as early as 1946 by Marton et al. [26]. Recently, two reviews from Postek et al. [27,28] discussed some issues of interpreting SEM images: the second part [28] was entirely devoted to the issue of electron beam-induced specimen contamination.

Postek et al. [28] pointed out that the origin of beam-induced contaminations can both be the sample itself and the vacuum system of the SEM. While the cleanliness of the latter can be significantly improved (for example, by the replacement of diffusion pumps with turbomolecular ones backed by dry backing pumps in modern instruments), the history of the specimen prior to entering the vacuum system still remains important [28]. In case of samples with significant organic content, organic molecules remaining on the sample surface can break, undergo polymerization, and get "pinned" to the sample by the beam during scanning [28]. Depending on the electron dose, the formed carbonaceous layer can grow at a rate of a few nanometers/seconds over the sample surface, even if only low accelerating voltages are used.

It is interesting to note that although under-beam contamination is a well-studied subject in the literature of SEM (see [27,28], as well as the references cited therein), studies on the effect of under-beam contamination/passivation on the future electrochemical behaviour of the sample are scarce, and are mostly focused on corrosion and not on electrocatalytic properties [29]. Yet, as we are going to demonstrate in this paper, under-beam passivation can practically disable the sampled part of a catalyst, especially if it contains organic remnants (capping agents) from the synthesis process. While other parts of the catalyst (not affected by the electron beam before electrolysis) remain active and very often degrade significantly during the catalysed process, the part of the sample affected by pre-electrolysis scanning remains intact, and probably entirely passive, due to the carbonaceous film formed on it under the beam.

Here we demonstrate, by IL–SEM studies on polyvinylpyrrolidone (PVP) functionalized Ag nanocubes used as electrocatalysts for CO_2 reduction, a catalytic activity disabling effect of a passive carbonaceous layer that is known to be formed under the electron beam during pre-electrolysis SEM scans [30]. The aim of this paper is to emphasize the necessity of extreme care being taken not to misinterpret IL–SEM studies that seemingly demonstrate excellent catalyst stability.

2. Experimental

Catalyst preparation. Ag nanocubes (Ag NCs) were prepared by an upscaled synthesis route described elsewhere [31]. As support, a glassy carbon plate (2 mm thickness, Alfa Aesar, type 1) was mirror-polished (0.5 μm alumina suspension, Buehler), was thoroughly rinsed with ultrapure water and ethanol, dried, and masked with an inert PTFE tape to leave an 0.8 cm × 1 cm geometric surface area open for catalyst coating.

In order to form a carbon-supported Ag NC catalyst, 5.6 mg of the as-prepared Ag nanocubes [31] (in the form of powder) was dispersed in 6 cm^3 isopropanol (VLSI Selectipur, BASF) by a 1-hour sonication. 1.5 mg of technical carbon powder (Vulcan XC 72R, Cabot, USA) was also dispersed in 3 cm^3 isopropanol by 1-hour of sonication, and the two suspensions were subsequently mixed by sonicating for 30 min. The resulting suspension was dried overnight under vacuum conditions, yielding a C-supported Ag NC catalyst powder. This powder was re-dispersed in 1.5 cm^3 of isopropanol containing 75 μℓ of a Nafion solution (Aldrich, 5 wt% dissolved in a mixture of lower aliphatic alcohols and water). The obtained dispersion was subjected to sonication for 30 min, and for each electrode, 25 μℓ of the resulted ink was drop-cast onto the glassy carbon plate and dried in a vacuum oven.

An Ag NC catalyst without carbon support was prepared by dispersing 22 mg of the as-prepared Ag NCs in 6 cm^3 isopropanol by 1-hour sonication and spin-coating 75 μℓ of this suspension onto a glassy carbon support in three steps over 1 minute, using 1000 min^{-1} rotation rate on an Ossila spin coater.

Both the C-supported and the unsupported Ag NC catalysts were exposed to a UV-ozone atmosphere (PSD Series, Novascan, operated with air at atmospheric pressure) for 12 min.

For studies on a gas diffusion electrode (GDE, experimental details were described elsewhere [15]) the suspension of carbon-supported Ag NCs was drop-cast on the hydrophobic surface of a Sigracet 39 BC (Fuel Cell Store) GDE, and the nanocubes were percolated through the porous body of the GDE by a vacuum filtration system placed on the rear side of the electrode, followed by air-drying at ambient conditions lasting 30 min. No UV-ozone treatment was applied to the thus prepared, Ag NC-modified GDE. The GDE was used as part of the gas flow cell described in [15], combined with a Sustainion alkaline membrane (X37-50 RT, Dioxide materials) and an anode compartment containing 2 mol dm^{-3} KOH solution.

XPS Characterization. X-ray photoelectron spectroscopy (XPS) studies were carried out using a Thermo ESCALAB 250 XI instrument at a pass energy of 30 eV using monochromated Al K-α line ($h\nu = 1486.7$ eV). Charge correction was based on the position of the C*1s* peak (284.8 eV). The XPS spectra were subjected to a Shirley background subtraction and were analysed using the CasaXPS software.

Electrocatalysis studies. For all electrochemical experiments, a potentiostat/galvanostat (Metrohm Autolab 302N, The Netherlands) was used to control the potential, current density, and transferred charge. The electrolysis experiments were carried out using a custom-built, air-tight, H-type glass cell. Apart from the working electrode that was prepared as described above, the three-electrode arrangement consisted of a "leakless" Ag|AgCl|3 mol dm^{-3}KCl reference (Pine) and a Pt-foil (1.5 cm × 0.5 cm, Goodfellow) counter electrode. For electrolyses, 0.5 mol dm^{-3} KHCO$_3$ (ACS grade, Sigma-Aldrich) electrolyte solutions were prepared with ultrapure water (Milli-Q by Merck Millipore) and were saturated with CO$_2$ (99.999%, Carbagas, Switzerland). During the experiments, continuous gas flow was maintained through the electrolyte solution. To avoid possible fluctuations in CO$_2$ solubility caused by a change in the ambient temperature, all electrochemical experiments were performed at 20 °C, by immersing the H-type cell into a thermostated water bath. Automatic *IR* compensation was applied following the determination of the cell resistance by positive feedback. For the sake of comparability, all potentials given herein were converted to the reversible hydrogen electrode (RHE) scale. The reported current densities were normalized to the geometric surface area.

Gaseous products generated in the cell were detected by connecting the purging gas outlet to a GC analyzer (SRI Instruments

Multigas Analyzer №3). The continuous flow of the carrier CO$_2$ gas through the electrolysis cell carried volatile reaction products from the head-space into the sampling loops of the gas chromatograph. The partial current I_i, corresponding to the formation of a gaseous product i, can be calculated [32] as

$$I_i = x_i n_i F \upsilon_{\mathrm{m}}, \tag{1}$$

where x_i denotes the mole fraction of the products, determined by GC using an independent calibration standard gas (Carbagas); n_i is the number of electrons involved in the reduction reaction to form a particular product ($n = 2$ for both CO and H$_2$ formation); $F = 96485.3$ C mol^{-1} is Faraday's constant; and υ_{m} is the molar CO$_2$ gas flow rate measured by a universal flowmeter (7000 GC flowmeter, Ellutia) at the exit of the electrochemical cell.

The Faradaic efficiency (*FE*) of a given reaction product can be determined by dividing the respective partial current, determined from Eq. (1), by the total current measured electrochemically. A thermal conductivity detector (TCD, for the detection of H$_2$) and a flame ionization detector (FID, for the detection of CO) were applied in our studies. We found that in the studied system H$_2$ and CO are the only two detectable products, accounting for $100\% \pm 5\%$ of the current density that was electrochemically measurable. The electrochemically measured current densities were thus subdivided into partial current densities by taking into account the chromatographically determined concentration ratios, as will be shown later in Fig. 2. During operation, aliquots were analysed in intervals of 20 min during steady state electrolyses.

EM Measurements. EM analysis was conducted with a Zeiss Gemini 450 SEM with an InLens secondary electron (SE) and a backscatter electron detector (BSD). An accelerating voltage of 1.5 kV (probe current of 20 pA) and 5.0 kV (probe current of 120 pA) were applied for SE and BSD imaging, respectively. For high-angle annular dark-field scanning transmission electron microscopy (HAADF–STEM) combined with energy-dispersive X-ray spectroscopy (EDX) and TEM imaging, an FEI Titan Themis (equipped with a SuperEDX detector) was used with an acceleration voltage of 300 kV.

3. Results and discussion

In colloidal nanoparticle synthesis, PVP is a widely applied shape-control agent that promotes the growth of specific crystal faces while hindering others [33,34]. In the synthesis of Ag NCs used in this study, PVP —by strongly binding to the (100) facets of Ag—, facilitated the formation of almost perfect nanocubes of side lengths of about 100 nm, as shown in Fig. 1a. The XPS spectrum (Fig. 1b) of a catalyst prepared without carbon support clearly exhibits a strong Ag3d signal, as well as a small peak that can be assigned to the N*1s* excitation of the PVP molecules adsorbed on the surface of the nanocubes. As shown in Fig. 1b, the applied UV-ozone treatment resulted in a significantly decreased N*1s* peak intensity. The peak has not disappeared, however, which hints that some PVP still remained on the surface despite the UV-ozone treatment.

Although the adsorbed PVP could, in principle, inhibit the catalytic activity of the nanocubes [35,36], the UV-ozone treated, C-supported Ag NCs showed good performance when applied for the electroreduction of CO$_2$. This is demonstrated by Fig. 2a, showing the current density and the product distribution as a function of the applied electrode potential. The current densities shown in Fig. 2a were averaged for 1-hour electrolyses carried out in CO$_2$ saturated 0.5 mol dm^{-3} KHCO$_3$ solutions: for the electrolyses at different potentials, fresh solutions and newly prepared catalysts were applied.
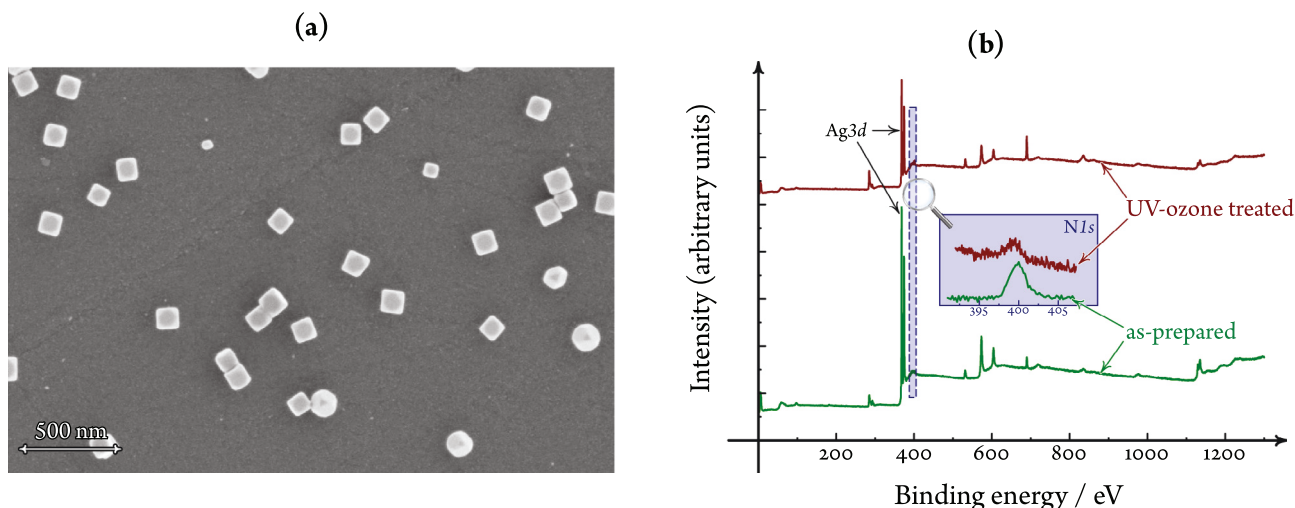
(a)

(b)

Fig. 1. Scanning electron micrograph **(a)** and X-ray photoelectron survey **(b)** of the unsupported Ag NC catalyst. XPS spectra are shown in **(b)** for the as-prepared catalyst (green curve) and for the catalyst made subject to UV-ozone treatment (red curve) as well. (For interpretation of the references to colour in this figure legend, the reader is referred to the web version of this article.)
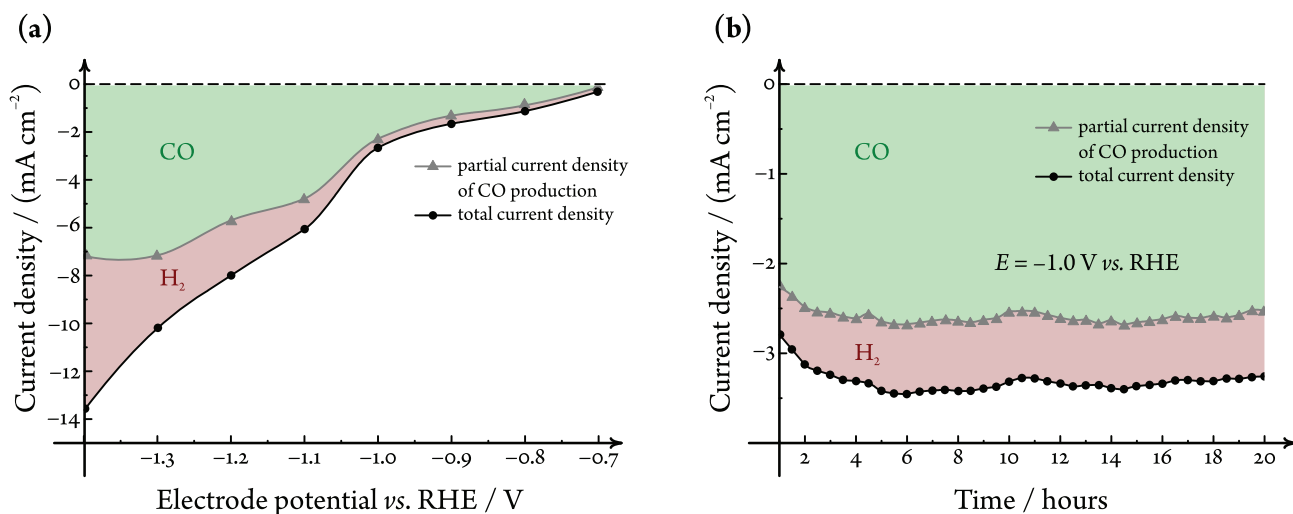
(a)

(b)

Fig. 2. The electrocatalytic performance of carbon-supported Ag nanocubes, used as catalysts of CO_2 electroreduction in a CO_2-saturated 0.5 mol dm^{-3} KHCO$_3$ solution. **(a)** Potential dependence of the current density and the product distribution, as determined by means of online gas chromatography in an H-type cell for 1-hour electrolyses. Each electrolysis (data points) were carried out using a freshly prepared catalyst and a fresh solution. Curves were created by interpolation. **(b)** Time dependence of the catalytic performance, as determined by a single electrolysis experiment lasting 20 hours, with subsequent chromatographic head-space analysis (data points). The curve was created by interpolation.

It is known that on Ag, the primary product of CO_2 reduction is CO [37]. The same is true for the carbon-supported Ag NCs, with the addition that compared to plain silver —*e.g.*, a silver foil [14]— the Ag nanocubes exhibit a broader overpotential range for CO production. That is, only a little amount of H$_2$ is formed at potentials less negative than −1.1 V *vs*. RHE, and CO_2 reduction generally prevails over hydrogen evolution in the entirety of the studied potential range (−1.3 V < E < −0.7 V). This observation is in agreement with other reports on nanoparticulate silver catalysts of CO_2 electroreduction [38].

In order to check the stability of the catalyst, we chose the moderate potential value of −1.0 V *vs*. RHE for a prolonged operation study. As shown in Fig. 2b, the catalyst preserved both its overall activity and its relative selectivity towards the production of CO (the Faradaic efficiency of CO formation was about 80%) for an electrolysis lasting 20 hours.

Nevertheless, since catalysts can maintain their macroscopic activity even as they undergo partial deactivation or decomposi-

tion [39], we carried out IL–SEM investigations of the working electrode surface, which —although the overall activity remained unchanged— indeed revealed some degradation.

In Fig. 3 we compare two scanning electron micrographs of the same spot of a working electrode surface; one recorded before (Fig. 3a) and one after (Fig. 3b) a 20-hours electrolysis treatment at −1.0 V *vs*. RHE, similar to the one used to obtain the data of Fig. 2b. Fig. 3a shows highly isotropic Ag NCs of a side length of about 100 nanometers, distributed evenly on the supporting carbon matrix. As revealed by Fig. 3b, the nanocubes undergo some slight deformation and shrinkage during electrolysis, and, more prominently, some subnanometer sized particles appear on the surface. EDX mapping (Fig. 3c) confirmed that these small particles consist of silver, and are most probably formed as a debris of nanoparticle degradation due to the mechanical impact of gas evolution [16].

In order to get a clearer view of the degradation process of Ag NCs, the above SEM experiment was repeated with a working elec-
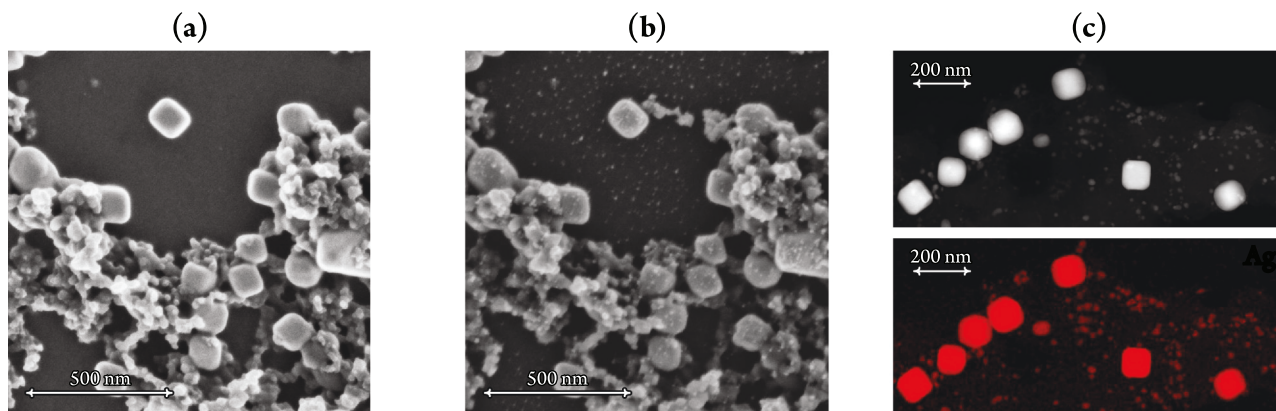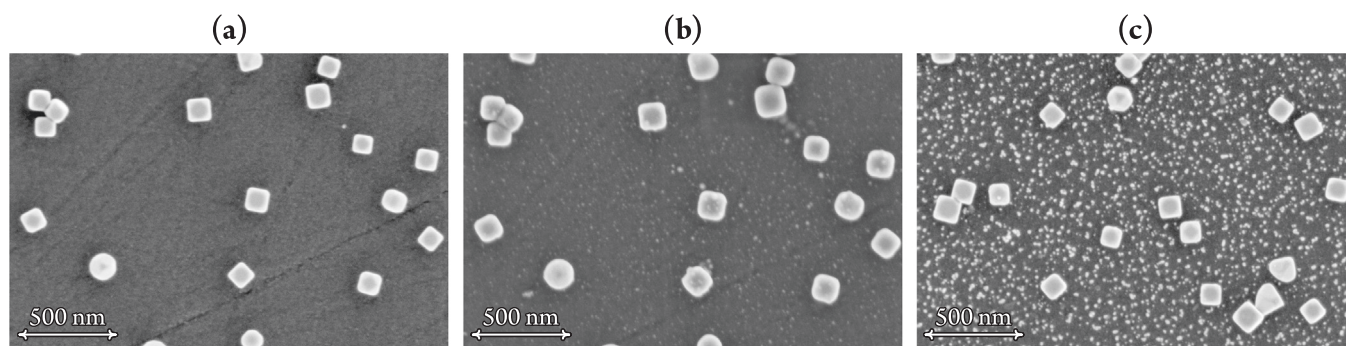
Fig. 3. IL–SEM investigation of the degradation of carbon-supported Ag nanocubes, used as catalysts of CO_2 electroreduction. The same spot of the working electrode surface is shown just before (**a**) and right after (**b**) the electrode was used for a 20-hours electrolysis of a CO_2-saturated 0.5 mol dm^{-3} $KHCO_3$ solution at an electrode potential of -1.0 V *vs.* RHE. The formation of subnanometer sized Ag particles during electrolysis is revealed by the HAADF–STEM (gray-scale) and EDX scans (red-scale) in (**c**), recorded post-electrolysis at a pristine location that has not been subjected to an electron beam before.

Fig. 4. SEM investigation of the degradation of non-supported Ag nanocubes, used as catalysts of CO_2 electroreduction. The same spot of the working electrode surface is shown just before (**a**) and right after (**b**) the electrode was used for a 20-hours electrolysis of a CO_2-saturated 0.5 mol dm^{-3} $KHCO_3$ solution. A different spot of the same sample is shown after electrolysis in (**c**).

trode prepared without the supporting carbon matrix (see the Experimental section for details).

The as-prepared electrode surface is shown in Fig. 4a, exhibiting cubic shaped Ag nanoparticles distributed on the glassy carbon electrode substrate. Somewhat surprisingly, the SEM image of the same spot, recorded after a 20-hours electrolysis, shows practically no degradation and the appearance of just a little amount of the subnanometer sized particles, as shown in Fig. 4b. What is even more surprising is that if we record an SEM micrograph with the same configuration, just of a different spot of the sample —that was not scanned before electrolysis—, the picture gets quite different. Fig. 4c clearly shows slightly deformed Ag nanocubes, along with a significant amount of Ag debris formed during electrolysis.

The micrographs of Fig. 4 very clearly reveal an important pitfall of IL–SEM analysis; namely, that due to electron beam-induced changes of the catalyst surface during the pre-electrolysis scan, the sample may get at least partially deactivated for the catalysed process. Due to its decreased electrocatalytic activity, the pre-scanned area of the sample may show no or little changes during the electrolytic process, while other spots (that were not affected by pre-electrolysis SEM scanning) preserve their activity and, in turn, exhibit significant degradation. In other words, the often advertised nondestructiveness of IL–SEM [8,9] should not be taken as granted — at least, not for all catalyst types.

That the effect shown in Fig. 4 can indeed be explained by pre-electrolysis electron beam–sample interactions is further demon-

strated by Fig. 5, showing an SEM micrograph of a working electrode surface obtained after electrolysis. Only a part (a rectangular segment) of this sample was scanned by SEM before electrolysis took place, and despite that the sample was exposed

Fig. 5. SEM micrograph of a sample of non-supported Ag NC catalyst taken after a 40-hours electrolysis at -1 V *vs.* RHE in a CO_2-saturated 0.5 mol dm^{-3} $KHCO_3$ solution. A rectangular segment of the sample —shown in the image by its corners— was also scanned before electrolysis. This pre-scanned area exhibits different degradation features compared to the rest of the surface.
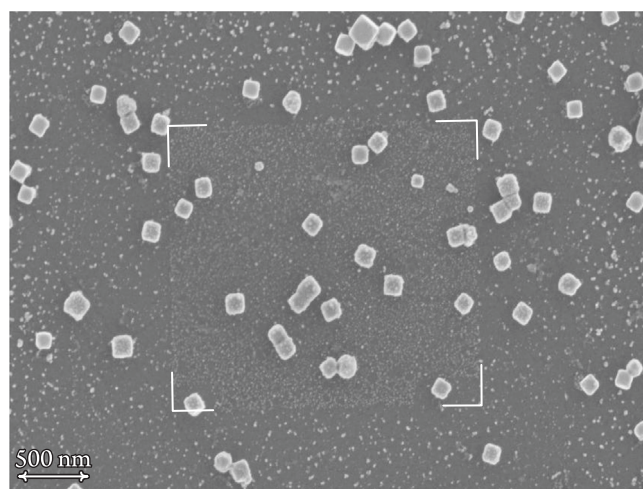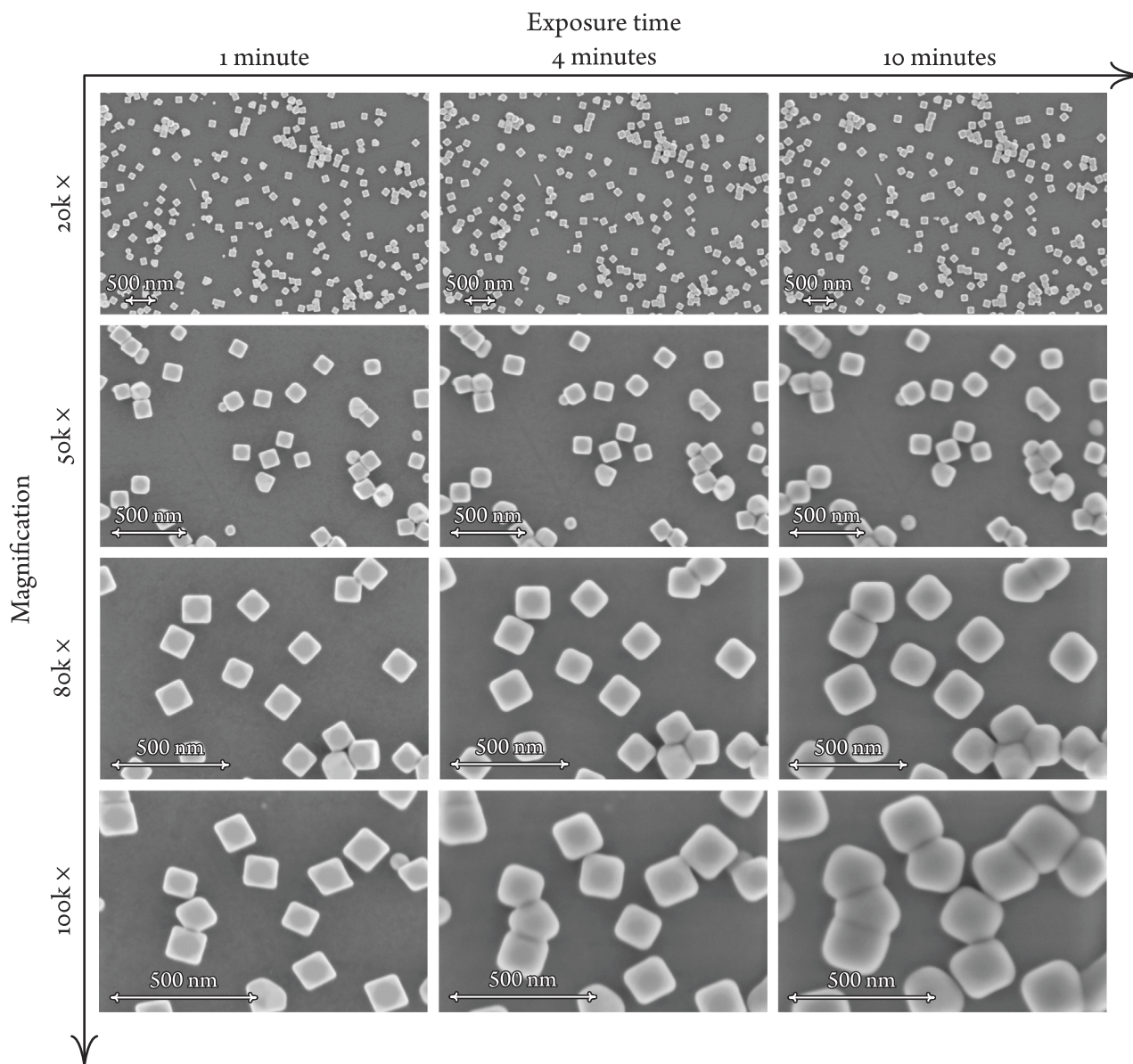
Exposure time

Fig. 6. SEM micrographs of a catalyst surface, obtained using different magnifications and after different scanning times. The applied accelerating voltage was 1.5 kV.
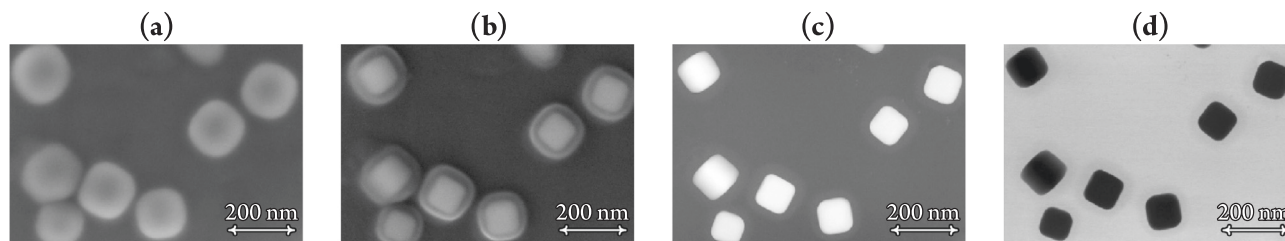

Fig. 7. Electron microscopic images of Ag NCs after electron beam irradiation was carried out for 10 min with a scanning electron beam of 1.5 kV accelerating voltage. **(a)** Secondary electron SEM image taken at 1.5 kV acceleration voltage. **(b)** Secondary electron SEM image obtained at 20 kV. **(c)** HAADF–STEM image taken at 300 kV. **(d)** TEM bright field image taken at 300 kV.

to the electron beam only for a short time, a marked difference can be observed between the degradation features of the pre-scanned segment and the rest of the surface area. Most notably, the coverage of the pre-scanned area with the subnanometer sized Ag particles is less pronounced, compared to other sites. This hints that

the electron beam exerts an effect not only on the Ag nanoparticles but also on the underlying glassy carbon substrate.

Note that provided we refrain from long-time exposure of the sample to the electron beam, the above-described electron beam irradiation effect is hardly noticeable *per se*. Yet, as shown by Fig. 5, even the irradiation damages that remained undetected dur-
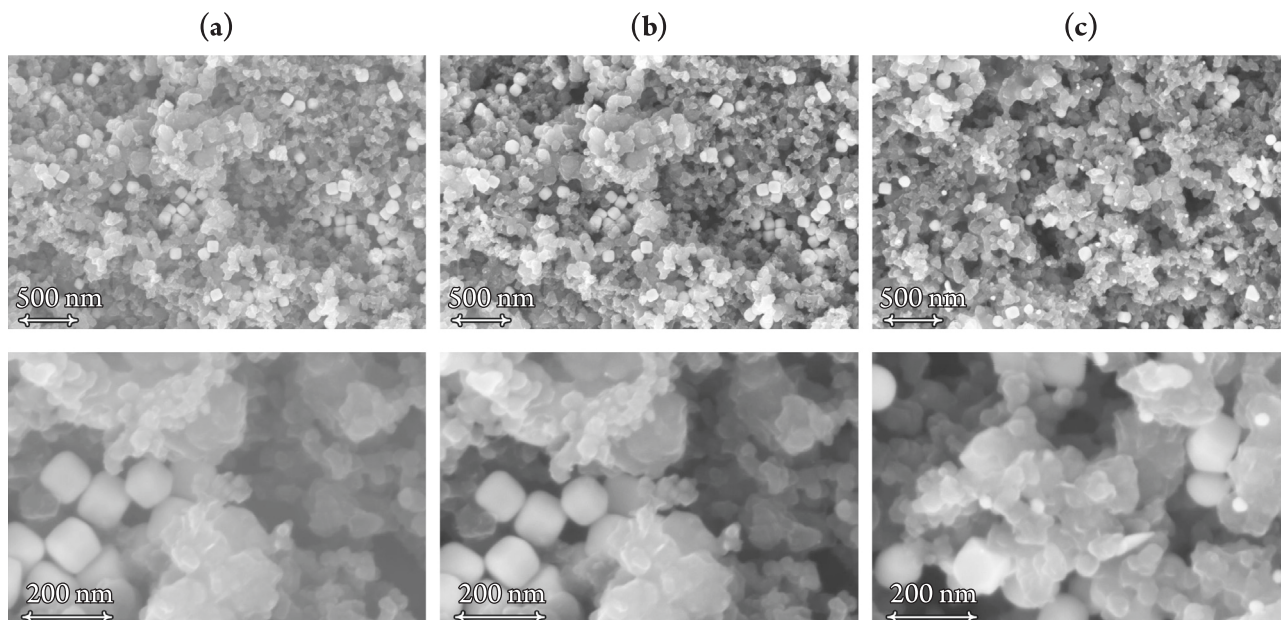
Fig. 8. SEM micrographs of different magnification of a GDE modified by Ag NCs. Identical locations are shown prior to **(a)** and after **(b)** a potentiostatic electrolysis at −2.0 V *vs.* an Ag | AgCl | 3 mol dm^{-3} KCl(aq) reference electrode consuming 1600 C cm^{-2}. A different location is shown after the electrolysis in **(c)**.

ing pre-electrolysis EM scanning can prove significant when the sample is used for electrolysis and scanned afterwards.

To demonstrate the irradiation effect in itself, we carried out prolonged SEM scans on one of our catalyst samples. As revealed by Fig. 6, the effect of contamination (as visualized by the growth and even the apparent merging of the nanocubes) is more pronounced when larger magnifications are applied (*i.e.*, when the beam is more focused) or when the sample is scanned for longer times.

At first glance, the growing and subsequently merging nanocubes shown in Fig. 6 may resemble the coalescence of Pt nanoparticles observed by Chorkendorff et al. under *in situ* TEM conditions [22]. Note, however, that under TEM conditions, the accelerating voltage and the electron dose are both much higher than in SEM. Accordingly, the main feature that Chorkendorff et al. described in their study was a shrinkage (and not a growth) of most nanoparticles, with only a few of these displaying actual coalescence [22]. Shrinkage in this study was shown to be an effect of both the high electron dose and the oxidizing atmosphere. None of these are characteristic of our SEM measurements; thus in our case, it seems more straightforward to presume that the beam has little effect on the nanocubes themselves, and it is rather the under-beam formation of a carbonaceous passive layer what is seen in Fig. 6.

Although the SEM images recorded at an accelerating voltage of 1.5 kV may not allow a clear distinction between the core of the nanoparticles and the contamination layer formed around them (Figs. 6 and 7a), the contamination layer can be visualized by EM scans at higher (20 kV) accelerating voltage (Fig. 7b). That under the formed carbonaceous contamination layer the Ag nanocubes preserve their original shape can be confirmed by the HAADF–STEM and the TEM bright field images shown in Figs. 7c and d, respectively.

It is of worth noting that the contamination layer is most probably formed by the PVP capping agent, remnants of which remain adsorbed on the Ag nanocubes despite the applied UV–ozone treatment, and then get polymerized and pinned to the electrode surface by the electron beam [28]. Based on the electrocatalytic degradation pattern shown by Fig. 5, we can assume that some PVP may also remain on the substrate, forming there a carbona-

ceous shell that is however presumed to be not as thick as on the surfaces of the nanocubes, where PVP is primarily adsorbed.

The under-beam formation of the passive layer on the surface of nanoparticulate catalysts seems to block the pre-scanned surface even if entirely different settings, and much harsher electrolysis conditions, compared to what was described before, are applied. This is demonstrated by Fig. 8, where we modified a gas diffusion electrode (GDE) with carbon-supported Ag NCs (this time, without the application of UV-ozone treatment), and performed electrolysis by applying a potential of −1.4 V *vs.* RHE, thus passing through a total charge amount of 1600 C cm^{-2}. While the identical location SEM images of Fig. 8a and b show no trace of degradation, particle deformation and the appearance of newly formed, small particles is clearly shown by the SEM micrograph of Fig. 8c, recorded at a random spot after the electrolysis. Although as pointed out in [40], in fact any organic contaminations of a catalyst sample may act as source of material for the formation of passive carbonaceous crust layers, the prominent role of PVP in this process is further supported by our numerous IL–SEM studies on PVP-free catalysts, where no such contamination effects were ever seen [11–20].

4. Concluding remarks

No effort has so far been made to demonstrate the effect of capping-agent related under-beam passive layer formation on the catalytic behaviour of nanoparticle type electrocatalysts. This is considered worrying, particularly because of the emerging popularity of IL–SEM-based stability studies where the pre-electrolysis scanning can contaminate (and consequently disable) the catalyst sample in a way that the post-electrolysis scan would deceivingly show no degradation.

Using PVP-functionalised Ag nanocubes as model catalysts of CO$_2$ reduction, we demonstrated how under-beam contamination (a carbonaceous, passive crust formed over the catalyst particles) might account for artefacts in IL–SEM studies in such a way that the experimenter is provided with false comfort with regard to the stability of the catalyst. This paper was written with the aim to direct attention to this possible pitfall of IL–SEM studies, which

may especially emerge when IL–SEM is applied on electrocatalysts prepared by a synthesis route involving capping agents.

Apart from the issues that PVP remnants can cause in the interpretation of IL–SEM experiments, it should also be emphasized that shape-forming surfactants may exert further unwanted effects also on the essential catalytic properties. *E.g.*, in case of the system studied here we have to note that if no action (in our case, UV-ozone treatment) is taken to remove (at least most of) the adhering PVP remnants, this will negatively affect both the selectivity and the stability of the catalyst. In our case omission of the UV-ozone treatment resulted, for example, in the overall Faradaic efficiency (toward CO production) dropping from $\sim 80\%$ to $\sim 65\%$, and a further dropping to below 50% over 2 hours of electrolysis (under conditions similar to those applying for Fig. 2b). The removal of capping agents may be based on plasma/thermal annealing [41] (note that the UV-ozone treatment we applied here proved to be far from ideal), or it may even rely on mere electrochemical methods. Namely, it was recently shown in two independent studies (by our group [42] and by Pankhurst et al. [43]) that capping agent remnants may effectively be removed by the harsh cathodic potentials applied during CO_2 electrolysis. Needless to say, the latter "*operando* activation" method [42] does not work for capping agents baked to the catalyst surface by the electron beam in an IL–SEM scenario.

Declaration of Competing Interest

The authors declare that they have no known competing financial interests or personal relationships that could have appeared to influence the work reported in this paper.

Acknowledgement

References

[1] D.R. Feldman, W.D. Collins, P.J. Gero, M.S. Torn, E.J. Mlawer, T.R. Shippert, Observational determination of surface radiative forcing by CO2 from 2000 to 2010, Nature 519 (7543) (2015) 339–343, https://doi.org/10.1038/nature14240.

[2] S. Nitopi, E. Bertheussen, S.B. Scott, X. Liu, A.K. Engstfeld, S. Horch, B. Seger, I.E.L. Stephens, K. Chan, C. Hahn, J.K. Nørskov, T.F. Jaramillo, I. Chorkendorff, Progress and perspectives of electrochemical CO2 reduction on copper in aqueous electrolyte, Chem. Rev. 119 (12) (2019) 7610–7672, https://doi.org/10.1021/acs.chemrev.8b00705.

[3] E. Royer, Réduction de l'acide carbonique en acide formique, Compt. Rend. Hebd. Séances Acad. Sci. 70 (1870) 731–732.

[4] H.-R.M. Jhong, S. Ma, P.J.A. Kenis, Electrochemical conversion of CO2 to useful chemicals: Current status, remaining challenges, and future opportunities, Curr. Opin. Chem. Eng. 2 (2) (2013) 191–199, https://doi.org/10.1016/j.coche.2013.03.005.

[5] A.D. Handoko, F. Wei, Jenndy, B.S. Yeo, Z.W. Seh, Understanding heterogeneous electrocatalytic carbon dioxide reduction through operando techniques, Nature Catal. 1 (12) (2018) 922–934, https://doi.org/10.1038/s41929-018-0182-6.

[6] A. Bergmann, B. Roldán Cuenya, Operando insights into nanoparticle transformations during catalysis, ACS Catal. 9 (11) (2019) 10020–10043, https://doi.org/10.1021/acscatal.9b01831.

[7] K.J.J. Mayrhofer, J.C. Meier, S.J. Ashton, G.K.H. Wiberg, F. Kraus, M. Hanzlik, M. Arenz, Fuel cell catalyst degradation on the nanoscale, Electrochem. Commun. 10 (8) (2008) 1144–1147, https://doi.org/10.1016/j.elecom.2008.05.032.

[8] N. Hodnik, M. Zorko, M. Bele, S. Hočevar, M. Gaberšček, Identical location scanning electron microscopy: A case study of electrochemical degradation of PtNi nanoparticles using a new nondestructive method, J. Phys. Chem. C 116 (40) (2012) 21326–21333, https://doi.org/10.1021/jp303831c.

[9] N. Hodnik, S. Cherevko, Spot the difference at the nanoscale: Identical location electron microscopy in electrocatalysis, Curr. Opin. Electrochem. 15 (2019) 73–82, https://doi.org/10.1016/j.coelec.2019.03.007.

[10] J.C. Meier, I. Katsounaros, C. Galeano, H.J. Bongard, A.A. Topalov, A. Kostka, A. Karschin, F. Schüth, K.J.J. Mayrhofer, Stability investigations of electrocatalysts on the nanoscale, Energy Environ. Sci. 5 (11) (2012) 9319, https://doi.org/10.1039/c2ee22550f.

[11] M. Rahaman, A. Dutta, A. Zanetti, P. Broekmann, Electrochemical reduction of CO2 into multicarbon alcohols on activated Cu mesh catalysts: An identical location (IL) study, ACS Catal. 7 (11) (2017) 7946–7956, https://doi.org/10.1021/acscatal.7b02234.

[12] A. Dutta, M. Rahaman, M. Mohos, A. Zanetti, P. Broekmann, Electrochemical CO2 conversion using skeleton (sponge) type of Cu catalysts, ACS Catal. 7 (8) (2017) 5431–5437, https://doi.org/10.1021/acscatal.7b01548.

[13] P. Moreno-García, N. Schlegel, A. Zanetti, A. Cedeño López, M.deJ. Gálvez-Vázquez, A. Dutta, M. Rahaman, P. Broekmann, Selective electrochemical reduction of CO2 to CO on Zn-based foams produced by Cu²⁺ and template-assisted electrodeposition, ACS Appl. Mater. Interfaces 10 (37) (2018) 31355–31365, https://doi.org/10.1021/acsami.8b0989.

[14] A. Dutta, C.E. Morstein, M. Rahaman, A. Cedeño López, P. Broekmann, Beyond copper in CO_2 electrolysis: Effective hydrocarbon production on silver-nanofoam catalysts, ACS Catal. 8 (9) (2018) 8357–8368, https://doi.org/10.1021/acscatal.8b01738.

[15] M.deJ. Gálvez-Vázquez, S. Alinejad, H. Hu, Y. Hou, P. Moreno-García, A. Zana, G.K.H. Wiberg, P. Broekmann, M. Arenz, Testing a silver nanowire catalyst for the selective CO2 reduction in a gas diffusion electrode half-cell setup enabling high mass transport conditions, CHIMIA Int. J. Chem. 73 (11) (2019) 922–927, https://doi.org/10.2533/chimia.2019.92.

[16] Y. Hou, S. Bolat, A. Bornet, Y.E. Romanyuk, H. Guo, P. Moreno-García, I.Z. Montiel, Z. Lai, U. Müller, V. Grozovski, P. Broekmann, Photonic curing: Activation and stabilization of metal membrane catalysts (MMCs) for the electrochemical reduction of CO2, ACS Catal. 9 (10) (2019) 9518–9529, https://doi.org/10.1021/acscatal.9b03664.

[17] Y. Hou, R. Erni, R. Widmer, M. Rahaman, H. Guo, R. Fasel, P. Moreno-García, Y. Zhang, P. Broekmann, Synthesis and characterization of degradation-resistant Cu@CuPd nanowire catalysts for the efficient production of formate and CO from CO2, ChemElectroChem 6 (12) (2019) 3189–3198, https://doi.org/10.1002/celc.201900752.

[18] M.deJ. Gálvez-Vázquez, P. Moreno-García, H. Guo, Y. Hou, A. Dutta, S.R. Waldvogel, P. Broekmann, Leaded bronze alloy as a catalyst for the electroreduction of CO2, ChemElectroChem 6 (8) (2019) 2324–2330, https://doi.org/10.1002/celc.201900537.

[19] A.V. Rudnev, K. Kiran, A. Cedeño López, A. Dutta, I. Gjuroski, J. Furrer, P. Broekmann, Enhanced electrocatalytic CO formation from CO_2 on nanostructured silver foam electrodes in ionic liquid/water mixtures, Electrochim. Acta 306 (2019) 245–253, https://doi.org/10.1016/j.electacta.2019.03.102.

[20] A. Dutta, I.Z. Montiel, R. Erni, K. Kiran, M. Rahaman, J. Drnec, P. Broekmann, Activation of bimetallic AgCu foam electrocatalysts for ethanol formation from CO2 by selective Cu oxidation/reduction, Nano Energy 68 (2020) 104331, https://doi.org/10.1016/j.nanoen.2019.104331.

[21] W.T. Osowiecki, J.J. Nussbaum, G.A. Kamat, G. Katsoukis, M. Ledendecker, H. Frei, A.T. Bell, A.P. Alivisatos, Factors and dynamics of Cu nanocrystal reconstruction under CO2 reduction, ACS Appl. Energy Mater. 2 (11) (2019) 7744–7749, https://doi.org/10.1021/acsaem.9b01714.

[22] S.B. Simonsen, I. Chorkendorff, S. Dahl, M. Skoglundh, J. Sehested, S. Helveg, Direct observations of oxygen-induced platinum nanoparticle ripening studied by in situ TEM, J. Am. Chem. Soc. 132 (23) (2010) 7968–7975, https://doi.org/10.1021/ja910094r.

[23] M. Arenz, A. Zana, Fuel cell catalyst degradation: Identical location electron microscopy and related methods, Nano Energy 29 (2016) 299–313, https://doi.org/10.1016/j.nanoen.2016.04.027.

[24] R. Lariviere Stewart, Insulating films formed under electron and ion bombardment, Phys. Rev. 45 (7) (1934) 488–490, https://doi.org/10.1103/physrev.45.488.

[25] M. von Ardenne, Das elektronen-rastermikroskop, Z. Phys. 109 (9–10) (1938) 553–572, https://doi.org/10.1007/bf01341584.

[26] L. Marton, N.N. Das Gupta, C. Marton, Modifications of specimens in electron microscopy, Science 104 (2689) (1946) 35–36, https://doi.org/10.1126/science.104.2689.35.

[27] M.T. Postek, A.E. Vladár, Does your SEM really tell the truth?—How would you know? Part 1, Scanning 35 (6) (2013) 355–361, https://doi.org/10.1002/sca.21075.

[28] M.T. Postek, A.E. Vladár, K.P. Purushotham, Does your SEM really tell the truth?—How would you know? Part 2, Scanning 36 (3) (2013) 347–355, https://doi.org/10.1002/sca.21124.

[29] B. Luo, Y. Fang, J. Li, Z. Huang, B. Hu, J. Zhou, Improved stability of metal nanowires via electron beam irradiation induced surface passivation, ACS Appl. Mater. Interfaces 11 (13) (2019) 12195–12201, https://doi.org/10.1021/acsami.9b00875.

[30] S.F. Tan, M. Bosman, C.A. Nijhuis, Molecular coatings for stabilizing silver and gold nanocubes under electron beam irradiation, Langmuir 33 (5) (2017) 1189–1196, https://doi.org/10.1021/acs.langmuir.6b03721.

[31] S.H. Im, Y.T. Lee, B. Wiley, Y. Xia, Large-scale synthesis of silver nanocubes: The role of HCl in promoting cube perfection and monodispersity, Angew. Chem. 117 (14) (2005) 2192–2195, https://doi.org/10.1002/ange.200462208.

[32] A.V. Rudnev, Online chromatographic detection, in: K. Wandelt (Ed.), Encyclopedia of Interfacial Chemistry, Elsevier, Amsterdam, 2018, pp. 321–325, https://doi.org/10.1016/b978-0-12-409547-2.13564-4.

[33] J. Zhang, Q. Wang, X. Zhang, J. Wang, M. Guo, B.J. Wiley, C. Li, C. Hu, Carbamide promoted polyol synthesis and transmittance properties of silver nanocubes, Inorg. Chem. Front. 3 (4) (2016) 547–555, https://doi.org/10.1039/c5qi00256g.

[34] K.M. Koczkur, S. Mourdikoudis, L. Polavarapu, S.E. Skrabalak, Polyvinylpyrrolidone (PVP) in nanoparticle synthesis, Dalton Trans. 44 (41) (2015) 17883–17905, https://doi.org/10.1039/c5dt02964c.

[35] N. Naresh, F.G.S. Wasim, B.P. Ladewig, M. Neergat, Removal of surfactant and capping agent from Pd nanocubes (Pd-NCs) using tert-butylamine: Its effect on electrochemical characteristics, J. Mater. Chem. A 1 (30) (2013) 8553, https://doi.org/10.1039/c3ta11183k.

[36] D. Ung, B.M. Cossairt, Effect of surface ligands on CoP for the hydrogen evolution reaction, ACS Appl. Energy Mater. 2 (3) (2019) 1642–1645, https://doi.org/10.1021/acsaem.9b00240.

[37] Y. Hori, Electrochemical CO_2 reduction on metal electrodes, in: C.G. Vayenas, R.E. White, M.E. Gamboa-Aldeco (Eds.), Modern Aspects of Electrochemistry, Vol. 42, Springer, New York, 2008, pp. 89–189, https://doi.org/10.1007/978-0-387-49489-0.

[38] D. Sun, X. Xu, Y. Qin, S.P. Jiang, Z. Shao, Rational design of Ag-based catalysts for the electrochemical CO2 reduction to CO: A review, ChemSusChem 13 (2019) 39–58, https://doi.org/10.1002/cssc.201902061.

[39] A. Moysiadou, X. Hu, Stability profiles of transition metal oxides in the oxygen evolution reaction in alkaline medium, J. Mater. Chem. A 7 (45) (2019) 25865–25877, https://doi.org/10.1039/c9ta10308b.

[40] M. Zorko, B. Jozinović, M. Bele, N. Hodnik, M. Gaberšček, SEM method for direct visual tracking of nanoscale morphological changes of platinum based electrocatalysts on fixed locations upon electrochemical or thermal treatments, Ultramicroscopy 140 (2014) 44–50, https://doi.org/10.1016/j.ultramic.2014.02.006.

[41] I. Puspitasari, E. Skupien, F. Kapteijn, P. Kooyman, Au capping agent removal using plasma at mild temperature, Catalysts 6 (2016) 179, https://doi.org/10.3390/catal6110179.

[42] H. Hu, M. Liu, Y. Kong, N. Mysuru, C. Sun, M. d. J. Gálvez-Vázquez, U. Müller, R. Erni, V. Grozovski, Y. Hou, P. Broekmann, Activation matters: Hysteresis effects during electrochemical looping of colloidal Ag nanowire catalysts, ACS Catal. 10 (2020) 8503–8514. https://doi.org/10.1021/acscatal.0c02026.

[43] J.R. Pankhurst, P. Iyengar, A. Loiudice, M. Mensi, R. Buonsanti, Metal–ligand bond strength determines the fate of organic ligands on the catalyst surface during the electrochemical CO2 reduction reaction, Chem. Sci. 11 (2020) 9296–9302, https://doi.org/10.1039/d0sc03061a.

5.10 Unwrap them first: Operando potential-induced activation is required when using PVP-capped Ag nanocubes as catalysts of CO$_2$ electroreduction

Authors: María de Jesús Gálvez-Vázquez, Heng Xu, Pavel Moreno-García, Yuhui Hou, **Huifang Hu**, Benjamin J. Wiley, Soma Vesztergom* and Peter Broekmann*

Highlights: Operando potential-induced activation was applied on PVP-capped Ag NC catalysts for CO$_2$ electroreduction. Higher activity and selectivity are achieved at mild potentials after polarizing to harsh negative potentials. Activation processes cause little degradation on the catalysts surface from the SEM studies of pre- and post-electrolysis. Furthermore, the activation method can be tuned through the electrolyte compositions.

Contributions: I was involved in the scientific discussion of the results.

Unwrap Them First: *Operando* Potential-induced Activation Is Required when Using PVP-Capped Ag Nanocubes as Catalysts of CO₂ Electroreduction

María de Jesús Gálvez-Vázquez[a], Heng Xu[b], Pavel Moreno-García[a], Yuhui Hou[a], Huifang Hu[a], Benjamin J. Wiley[b], Soma Vesztergom*[c], and Peter Broekmann*[a]

Abstract: Metallic nanoparticles of different shape can be used as efficient electrocatalysts for many technologically and environmentally relevant processes, like the electroreduction of CO₂. Intense research is thus targeted at finding the morphology of nanosized features that best suits catalytic needs. In order to control the shape and size distribution of the designed nanoobjects, and to prevent their aggregation, synthesis routes often rely on the use of organic capping agents (surfactants). It is known, however, that these agents tend to remain adsorbed on the surface of the synthesized nanoparticles and may significantly impair their catalytic performance, both in terms of overall yield and of product selectivity. It thus became a standard procedure to apply certain methods (*e.g.* involving UV-ozone or plasma treatments) for the removal of capping agents from the surface of nanoparticles, before they are used as catalysts. Proper design of the operating procedure of the electrocatalysis process may, however, render such cleaning steps unnecessary. In this paper we use poly-vinylpyrrolidone (PVP) capped Ag nanocubes to demonstrate a mere electrochemical, *operando* activation method. The proposed method is based on an observed hysteresis of the catalytic yield of CO (the desired product of CO₂ electroreduction) as a function of the applied potential. When as-synthesized nanocubes were directly used for CO₂ electroreduction, the CO yield was rather low at moderate overpotentials. However, following a potential excursion to more negative potentials, most of the (blocking) PVP was irreversibly removed from the catalyst surface, allowing a significantly higher catalytic yield even under less harsh operating conditions. The described hysteresis of the product distribution is shown to be of transient nature, and following *operando* activation by a single 'break-in' cycle, a truly efficient catalyst was obtained that retained its stability during long hours of operation.

Keywords: Catalyst activation · CO₂ reduction · Electrocatalysis · Nanoparticles · Polyvinylpyrrolidone (PVP)

María de Jesús Gálvez-Vázquez studied chemistry and received her MSc specialization in materials science at the Benemérita Universidad Autónoma de Puebla in Mexico. In 2017 she started her PhD project in the group of Prof. Dr. Peter Broekmann at the University of Bern. Her main focus is the study of different catalyst materials applied for the electrochemical reduction of carbon dioxide under controlled mass transport conditions.

Heng Xu is a PhD student in the Department of Chemistry at Duke University. He received his BSc in chemistry from Jilin University in 2018 and then joined Prof. Dr. Benjamin J. Wiley's group in the same year. His research interests include the shape-controlled synthesis of metal nanocrystals and understanding of the anisotropic growth of metal nanocrystals with electrochemistry.

Dr. Pavel Moreno-García obtained a PhD in chemistry and molecular science at the University of Bern in 2013, under supervision of Prof. Dr. Thomas Wandlowski. At that time, his work was devoted to the study of electronic transport through nanoobjects at electrified interfaces by *in situ* STM. In 2013, he joined the group of Prof. Dr. Peter Broekmann, where he is involved in electrocatalysis research on the direct electrochemical conversion of carbon dioxide to more valuable products, instrumental development, and studies using laser ablation/ ionization mass spectrometry.

Dr. Yuhui Hou received her PhD in physical chemistry from Xiamen University, China in 2015. Before joining Prof. Dr. Peter Broekmann's group at the University of Bern, she worked as a post-doctoral fellow in Hokkaido University (Japan), where she mainly focused on methane conversion. Her current research interest is to develop

*Correspondence: Prof. Dr. P. Broekmann[a], E-mail: peter.broekmann@dcb.unibe.ch; Dr. S. Vesztergom[c], E-mail: vesztergom@chem.elte.hu

[a]University of Bern, Department of Chemistry, Biochemistry and Pharmaceutical Sciences; [b]Duke University, Department of Chemistry, USA ;[c]Eötvös Loránd University, Department of Physical Chemistry, H-1107 Budapest, Pázmány Péter sétány 1/A, Hungary

electrocatalysts *via* colloidal synthesis for electrochemical CO_2 reduction. She is also interested in investigating catalyst degradation under electrochemical CO_2 reduction conditions by identical-location scanning electron microscopy.
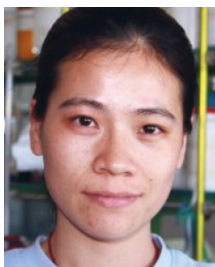
Huifang Hu obtained her MSc in materials science and engineering from Fuzhou University (China). After a short experience in technical college, she joined the Interfacial Electrochemistry Group of Prof. Dr. Peter Broekmann as a PhD student in 2019. Her PhD project focuses on the electrochemical conversion of CO_2 into value-added products.

Prof. Dr. Benjamin J. Wiley is a professor in the Department of Chemistry at Duke University. He received his BSc in chemical engineering from the University of Minnesota in 2003, and his PhD in chemical engineering from the University of Washington, Seattle in 2007. Prof. Dr. Wiley is the recipient of the Beilby Medal from the Royal Society of Chemistry and has been recognized as a Highly Cited Researcher by Thomson Reuters in 2014 and 2018. His current research focuses on understanding the processes that drive anisotropic growth of nanostructures and understanding the structure–property relationship of nanostructures and for applications in electronics, medicine, and electrochemistry.

Dr. Soma Vesztergom obtained his MSc (2010) and PhD (2014) degrees in chemistry, working with Prof. Dr. Győző G. Láng at Eötvös Loránd University, Hungary. He was a post-doctoral researcher in Prof. Dr. Peter Broekmann's group at the University of Bern for a year (2014) and is a regular collaborator of this group since then. His research primarily focuses on instrumental developments in electrochemistry and on the modelling of electrocatalytic processes. Currently, he is an assistant professor at Eötvös Loránd University in Budapest.

Prof. Dr. Peter Broekmann obtained his MSc in chemistry (1998) and a PhD (2000) from the University of Bonn. After a postdoctoral stay at the University of Twente (The Netherlands) in 2001, he became project leader at the Institute of Physical Chemistry in Bonn. Since 2008 he holds a lecturer position for electrochemistry at the University of Bern. His research focuses on metal deposition processes for semiconductor and electrocatalysis applications.

1. Introduction

As a result of the ever-increasing consumption of fossil fuels, gigatons of CO_2 are released to the atmosphere every year, expediting global warming.[1] A possible way of mitigating the effects of rising CO_2 concentrations in the atmosphere is to reduce it electrochemically. This approach does not only allow CO_2 to be regarded as a valuable raw material instead of an environmentally dangerous waste, but it may also provide a solution for the storage of excess renewable (hydro-, solar or wind) energy.[1] It

is probably for this reason that the topic of electrochemical CO_2 reduction – an otherwise more than 150 years old idea[2] – has recently become the forefront of electrochemical research.[3] Today, a tremendous amount of research is invested in the design of new electrocatalyst materials for CO_2 electroreduction, and researchers seem to agree that apart from their chemical composition it is the nanoscale structure of electrocatalysts that mostly affect their performance.[4,5]

In order to create nanosized catalyst particles with a well-defined size and structure distribution, and to avoid the agglomeration of such particles, the synthesis route of colloidal catalyst nanoparticles (NPs) very often involves the use of surfactants (capping agents). When the aim is to synthesize metallic (*e.g.* Ag[6,7]) NPs, a very often used agent is poly-(vinylpyrrolidone), PVP. PVP owes its popularity to a four-fold synergistic effect, *i.e.* depending on the conditions of synthesis, it may act as a stabilizer, a shape control, a dispersant and/or a reducing agent.[8] Although PVP can be used for the design of a variety of Ag nanostructures (such as nanocubes[6,9] or nanowires[10]), the application of such agents has one significant drawback. That is, surfactants used for the synthesis tend to remain adsorbed on the surface of the nanoparticles, hindering or even impairing their catalytic activity.

As a result, capping agent removal steps must be applied before the NPs can effectively be used as catalysts in a CO_2 electroreduction process. Removal steps often imply the use of additional solvents,[11] or they rely on high temperature plasma[12] or UV–ozone treatments.[13] These require precise optimization in order to remove most of the capping agents while keeping effects detrimental to the catalyst structure at a minimum. Of course, in order to keep the catalyst particles as intact as possible, evading any forms of thermal treatments would be highly desirable, and in this respect the application of electrochemical activation methods seem to provide a viable alternative. That the application of harsh reductive potentials in an electrochemical cell can successfully activate a catalyst (that may afterwards be used more effectively, even under milder conditions) was recently shown by our group for Ag nanowires,[10] and by the group of Buonsanti[14] for Cu nanocrystal catalysts.

In this short communication we aim to investigate this effect further, and show that by applying PVP-capped (untreated) Ag nanocubes for the electroreduction of CO_2, a positive hysteresis effect can be observed when determining the catalytic selectivity towards CO formation as a function of the applied (cathodic) potential. Based on these findings we infer that instead of using thermal methods, surface-pinned capping agents could also be removed and metallic NP catalysts can be activated *operando*, by the application of a 'break-in' cycle in the electrolysis cell.

Effective 'break in', in the case of PVP-capped Ag nanocubes (Ag NCs) applied for the electroreduction of CO_2, requires the setting of harsh cathodic potentials. Under such conditions, although the $CO:H_2$ yield ratio is far from ideal, most of the capping agents are irreversibly desorbed from the surface of the NCs. While during the time of 'break-in', some catalyst degradation does occur, at the end we obtain a catalyst that works better even under normal (not so harsh) operating conditions. Improvement can be seen both in the achievable current and in the higher selectivity for CO production.

2. Experimental

2.1 *Synthesis of Ag NCs*

Ag NCs were synthesized using a previously reported method with minor modification.[6] 5 cm³ of ethylene glycol (J. T. Baker) was added to a 250 cm³ two-neck flask preheated to 160 °C. A light N_2 flow was introduced just above the ethylene glycol for the first 10 min, followed by heating the solvent for another 50 min. Next, 3 cm³ ethylene glycol solution of AgNO₃ (94 mmol

dm⁻³) and 3 cm³ ethylene glycol solution containing polyvinylpyrrolidone (M_w = 55000 g mol⁻¹, 144 mmol dm⁻³) and NaCl (0.22 mmol dm⁻³) were simultaneously injected into the flask at a rate of 45 cm³ h⁻¹, with the solution observed to turn yellow during this process. Under continuous stirring at 160 °C, the solution exhibited a color transition series from yellow to clear yellow, brown, greenish, and finally ochre and opaque. The whole process required 16 to 24 h for completion. After the solution had turned opaque, the reaction was quenched by adding 22 cm³ acetone to the hot solution, followed by cooling in an ice-water bath. To purify the NCs, the solution was first centrifuged at 2000 *g* for 30 min, then the precipitate was dispersed and centrifuged, three times, in 10 cm³ of deionized water at 9000 *g* for 10 min per run.[15]

2.2 Preparation of Ag NCs catalyst ink

For the preparation of the carbon-supported Ag NCs ink, 1.5 mg of the Ag NCs and 0.26 mg of carbon black (Vulcan XC 72R, Cabot) were separately dispersed in 10 cm³ of isopropanol (VLSI Selectipur, BASF) by 1 h sonication. Both suspensions were intermixed, sonicated for 1 h and dried using a rotary evaporator. The obtained carbon-supported Ag NCs were then re-dispersed in 1 cm³ of isopropanol containing 50 µl of Nafion (5 wt.%, 15–20% water, Sigma-Aldrich). The resulting suspension was subjected to sonication for 1 h, yielding a homogeneous catalyst ink (85% Ag NCs and 15% carbon black).

2.3 Preparation of the Gas Diffusion Electrodes

Ag NCs containing gas diffusion electrodes (Ag NC GDEs) for all electrochemical and characterization experiments were prepared as follows: a 0.8 cm × 3 cm carbon paper (Sigracet 39 BC, Fuel Cell Store) was cut and placed over a nylon membrane filter (pore size 0.22 µm, Fischerbrand) on top of the funnel of a vacuum filtrating system. The GDE was then covered by a rectangular mask, leaving 0.2 cm² uncovered and 141.5 µl of the carbon supported Ag NCs ink was drop-cast on top of it. The resulting Ag NC GDEs were dried at ambient conditions for at least 30 min and then their backside and edges were masked with Teflon tape, to leave only the Ag NCs ink-modified surface uncovered (0.2 cm²). Analysis by inductively coupled plasma-mass spectrometry (ICP–MS) of the freshly prepared samples was used to determine the catalyst mass loading, which amounted to ~71 µg cm⁻² Ag.

2.4 Electrochemical Measurements and Product Analysis

Electrochemical experiments were performed using a PGSTAT128N potentiostat/galvanostat (Metrohm Autolab) and a custom-made, airtight H-type cell with a Nafion membrane (Nafion 117, Sigma Aldrich) separating the cathode and anode compartments. The three-electrode arrangement consisted of the Ag-NC-GDE working, a Pt foil (1 cm × 1 cm) counter and a single junction (Pine Research) Ag | AgCl | KCl (sat.) reference electrode. Reported current densities were obtained by normalizing the current to the geometric surface area of the working electrode, 0.2 cm². Prior to the electrolysis experiments, both cell compartments were filled with 32 cm³ of either 0.5 mol dm⁻³ or 2 mol dm⁻³ KHCO₃ solution (ACS grade, Sigma-Aldrich) and then saturated by CO₂ gas (99.999%, Carbagas, Switzerland) for at least 30 min. For the sake of comparability, electrode potentials in the paper are referred to the reversible hydrogen electrode (RHE), calculated as:

$$E_{vs.\ RHE} = E_{vs.\ Ag\,|\,AgCl} + 210\ mV + 59\ mV \cdot pH \tag{1}$$

For all potentiostatic experiments, the measured electrode potential was *IR*-corrected post-experimentally, for which the solu-tion resistance was determined impedimetrically at the beginning of electrolysis. The *p*H values of the CO₂-saturated 0.5 mol dm⁻³ and 2 mol dm⁻³ KHCO₃ solutions were 7.4 and 7.9, respectively. Electrolyses were run for 60 min and online gas chromatography was applied (every 20 min) to quantify the formed products.

Gaseous products generated in the cell were detected by connecting the purging gas outlet to a GC analyzer (SRI Instruments Multigas Analyzer). The continuous flow of the carrier CO₂ gas through the electrolysis cell carried volatile reaction products from the head-space into the sampling loops of the gas chromatograph. The partial current I_i, corresponding to the formation of a gaseous product *i*, can be calculated[16] as

$$I_i = x_i\ n_i\ F\ v_m, \tag{2}$$

where x_i denotes the mole fraction of the products, determined by GC using an independent calibration standard gas (Carbagas); n_i is the number of electrons involved in the reduction reaction to form a particular product (*n* = 2 for both CO and H₂ formation); F = 96485.3 C mol⁻¹ is Faraday's constant; and v_m is the molar CO₂ gas flow rate measured by a universal flowmeter (7000 GC flowmeter, Ellutia) at the exit of the electrochemical cell. The Faradaic efficiency (FE) of a given reaction product can be determined by dividing the respective partial current, determined from Eqn. (2), by the total current measured electrochemically. A thermal conductivity detector (TCD, for the detection of H₂) and a flame ionization detector (FID, for the detection of CO) were equipped to our gas chromatograph.

The electrolyte was analyzed after the electrolysis experiment to quantify the amount of formate produced by means of ion exchange chromatography (Metrohm Ltd., Switzerland). This chromatograph was coupled to an L–7100 pump, a separation and an ion exclusion column (Metrosep A Supp 7-250) and a conductivity detector.

2.5 Scanning Electron Microscopy (SEM) and Energy-dispersive X-ray Spectroscopy (EDX) Characterization

The morphological characterization of the prepared Ag NC GDEs by SEM imaging experiments was performed before (for the as-prepared electrodes) and after electrochemical treatment. Analysis was conducted using a Zeiss Gemini 450 SEM equipped with an InLens secondary electron and a back-scattered electron detector. An accelerating voltage of 5 kV and a beam current of 200 pA were applied at a working distance of 4.5 mm. The AZtec 4.2 software (Oxford Instruments) was used to acquire EDX surface mappings of selected Ag NC GDEs. An acceleration voltage of 10 kV and a beam current of 1.2 nA were applied at a working distance of 8.5 mm.

2.6 Determination of Catalyst Loading by Inductively Coupled Plasma-Mass Spectrometry (ICP–MS)

Freshly prepared Ag NC GDEs were immersed in 3 cm³ of concentrated HNO₃ (BASF) to dissolve the Ag NCs embedded on their surfaces for 24 h. The resulting solutions were diluted with 3% HNO₃ solution by a factor of 500 and were then fed into a NExION 2000 ICP–MS instrument (Perkin Elmer) to obtain the Ag mass loading of the electrodes.

3. Results and Discussion

A peculiar hysteresis effect (Fig. 1) was observed when conducting electrolysis experiments coupled to chromatographic product detection using PVP-capped Ag NCs in a CO₂-saturated, 2.0 mol dm⁻³ KHCO₃ solution. Here we carried out potentiostatic electrolyses, all lasting for one hour, and record-ed a relatively stationary current that was later averaged and

compared to the amounts of CO and H_2, determined by gas chromatography. It is important to note that the determined total amounts of CO and H_2 did not account for a 100% of Faradaic efficiency, and some 5% of formate ($HCOO^-$) was found in the solution by post-electrolysis liquid chromatography analysis after each electrolysis, practically independently from the applied potential.

The first electrolysis experiment was carried out at an applied potential of −0.75 V *vs*. RHE, where the Faradaic efficiency of CO production was relatively low, ~55%. By gradually stepping the potential in the cathodic direction, the FE of CO production first increased, reaching a maximum of ~82% at around −0.9 V, as shown in Fig. 1(a). At potentials even more negative, CO_2 reduction (CO production) became disfavored compared to the competing hydrogen evolution reaction (HER).

In our experiments, −1.1 V was the most extreme potential reached, following which we began to gradually apply lower voltages. As shown in Fig. 1(a), after a first excursion to −1.1 V, the measured FE of CO production remained higher even at

potentials just mildly cathodic, and the FE of CO production did not drop below 70% at potentials as positive as −0.6 V *vs*. RHE.

It is interesting to note in Fig. 1(b), showing plots of partial current densities of CO and H_2 formation as a function of potential, that the partial current of HER follows – within range of error – the same track during the negative and the positive going scans of the potential excursion. For CO, however, a significant enhancement of currents can be observed during the latter, positive going scan, which allows us to conclude that the first potential excursion to extremely negative potentials indeed served as a 'break-in' of the catalyst. Although it is obvious that −1.1 V, in the current system, is not an ideal operating potential, it seems that applying this value for a short time allows the catalyst to be operated, later on, at milder potentials, where it can then still produce CO with a good yield.

The described activation method has its origins in the potential-induced removal of PVP from the surface of the Ag NCs, occurring at negative potentials that can overcome the
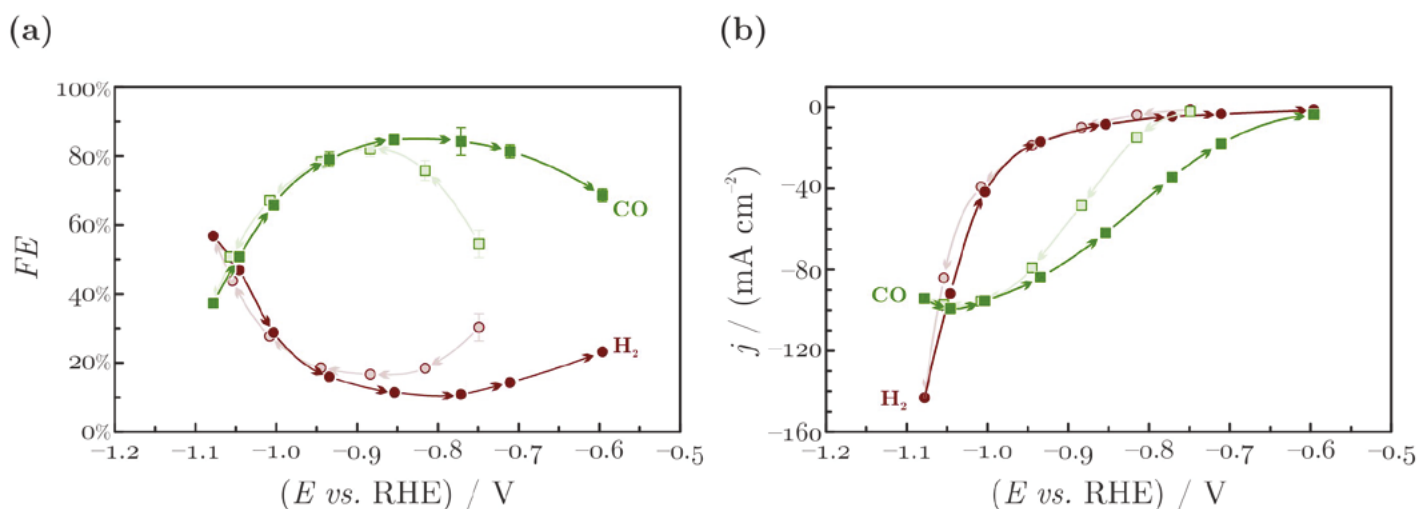

(a)

(b)

Fig. 1. Potentiostatic electrolyses were carried out using PVP-coated Ag NCs dropcast on a GDE, used as electrocatalysts of CO_2-reduction in a CO_2-saturated 2.0 mol dm⁻³ $KHCO_3$ solution. Faradaic efficiencies (a) and partial current densities (b) of CO (green) and H_2 (red) are shown as a function of the *IR*-drop corrected electrode potential. Data (dots) were recorded by gas chromatography; trends (curves) were created by spline interpolation. Arrows show the direction of the potential excursion.
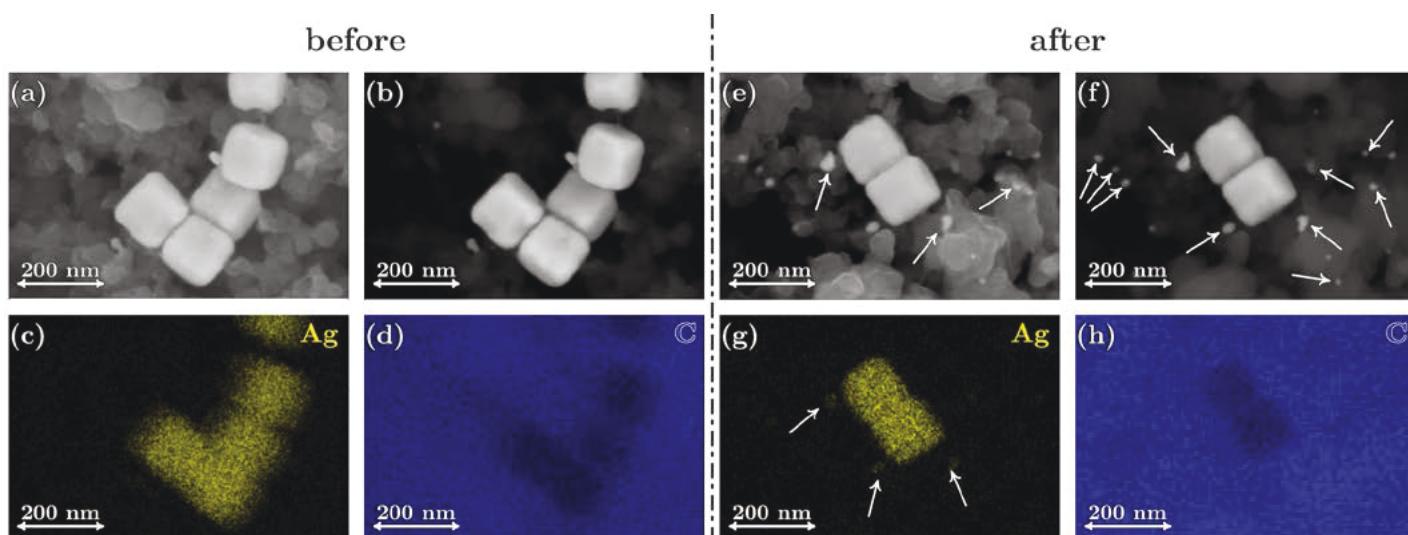

Fig. 2. Ag NCs drop-cast on a GDE, as observed before and after applying the electrochemical treatment shown in Fig. 1, in a CO_2-saturated 2.0 mol dm⁻³ $KHCO_3$ solution. Panels (a) and (e) show the secondary electron, (b) and (f) the back-scattered electron images of the NCs, with a side length of ~100 nm. Elemental composition maps, recorded by EDX, are shown in panels (c) and (g) for silver and in panels (d) and (h) for carbon. The arrows point to smaller Ag particles, formed by the degradation of the NCs during the potential-induced activation.

binding strength between the Ag NCs and their PVP coating. [14] The method can be called *operando*, since it can directly be realized within an electrochemical cell, rendering the use of other (solvent[11] or thermal annealing-based[12,13]) capping agent removal techniques unnecessary.

In order to apply *operando* activation, only a single 'break-in' electrolysis cycle (at suitably negative potentials) is required to gain a catalyst that can later work stably and highly active, even at less reductive potentials. The increase of activity is, as seen in Fig. 1, very significant, and following *operando* activation the catalyst does not lose its activity for hours of electrolyses.

The method has only one, minor flaw: that is, as seen in Fig. 2, during the initial activation step the Ag NCs tend to degrade. As a result, some newly formed, small Ag particles appear on the catalyst surface. These, however, seem not to disturb the electrocatalysis process, and when the electrolysis is continued at milder potentials, degradation stops and no such particles will further be formed.

The degradation effects described above can be sufficiently overcome if we make sure that during the 'break-in' cycle only lower currents (creating less mechanical strain) flow through the catalyst. This can be achieved by supplying less reactants to the surface; *e.g.* by lowering the concentration of the $KHCO_3$ electrolyte from 2 to 0.5 mol dm^{-3}. By conducting electrolyses in such a system, we observe a hysteresis (Fig. 3) that is similar to the one seen in the previous case, although the measured partial currents (both for CO and for H_2) are significantly lower. Yet, this does not seem change the PVP-to-metal binding strength and the value of the cathodic potential that has to be reached in order to break these bonds. Thus the activity increases observed in Fig. 3 compare well with those seen in Fig. 1, while significantly less degradation is observed (compare Figs 4 and 2).

4. Conclusion

Silver nanoparticles with well-defined shapes can be fabricated by a variety of synthesis methods, and the thus prepared particles can potentially be used as efficient catalysts in CO_2
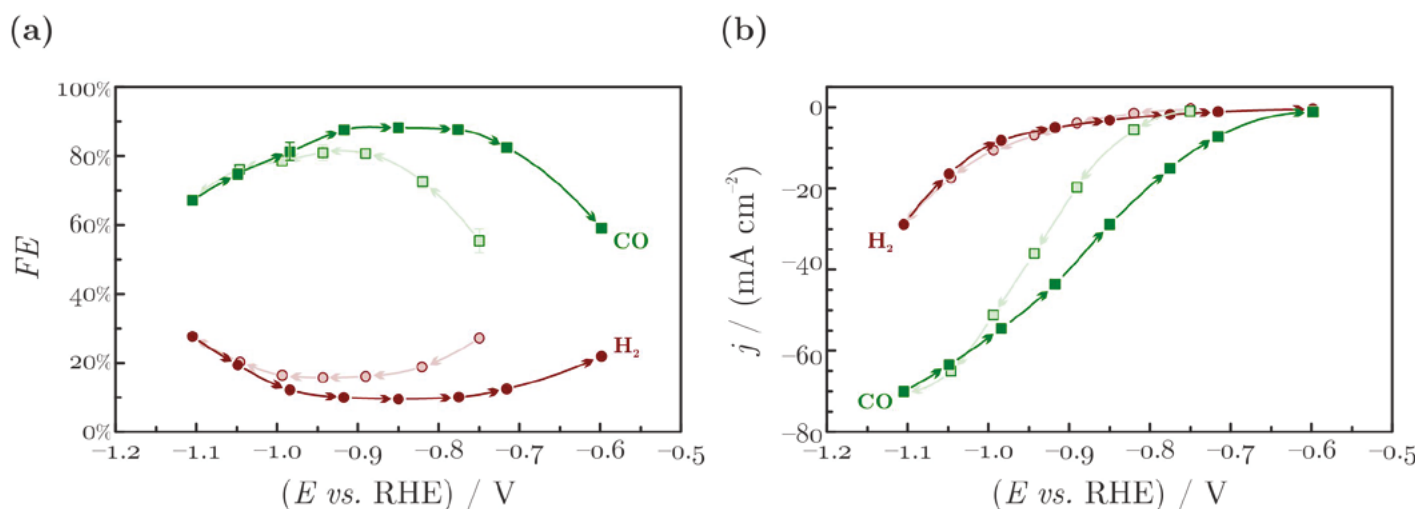

Fig. 3. Potentiostatic electrolyses were carried out using PVP-coated Ag NCs dropcast on a GDE, used as electrocatalysts of CO_2-reduction in a CO_2-saturated 0.5 mol dm^{-3} $KHCO_3$ solution. Faradaic efficiencies (a) and partial current densities (b) of CO (green) and H_2 (red) are shown as a function of the *IR*-drop corrected electrode potential. Data (dots) were recorded by gas chromatography; trends (curves) were created by spline interpolation. Arrows show the direction of the potential excursion.
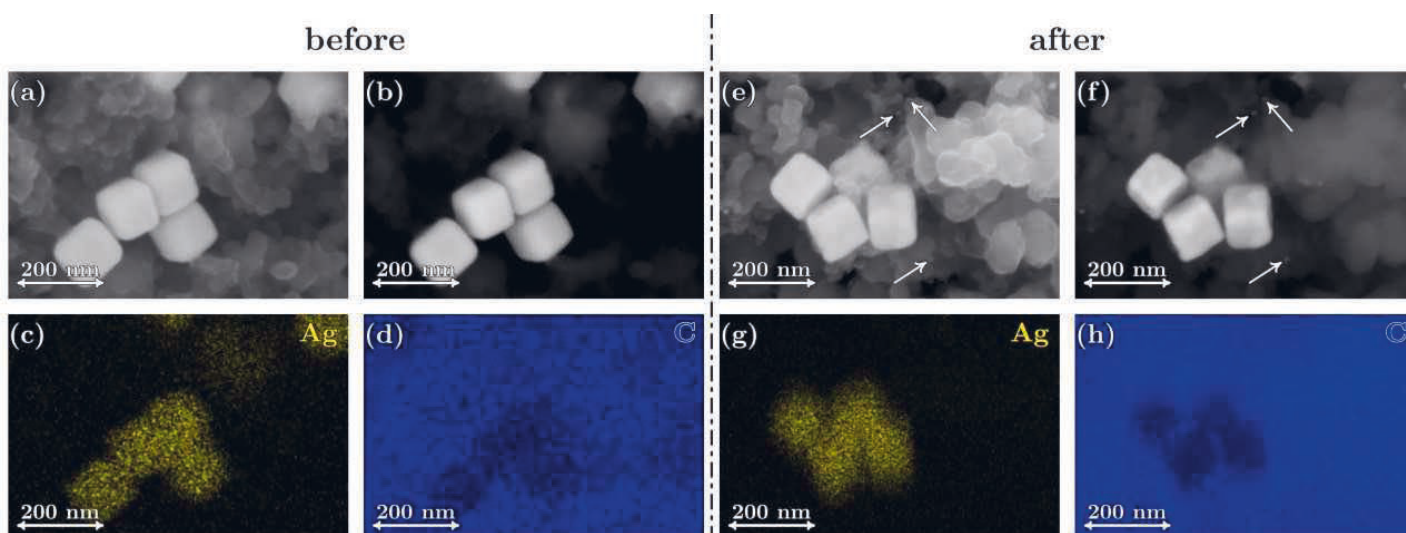

Fig. 4. Ag NCs drop-cast on a GDE, as observed before and after applying the electrochemical treatment shown in Fig. 3, in a CO_2-saturated 0.5 mol dm^{-3} $KHCO_3$ solution. Panels (a) and (e) show the secondary electron, (b) and (f) the back-scattered electron images of the NCs, with a side length of ~100 nm. Elemental composition maps, recorded by EDX, are shown in panels (c) and (g) for silver and in panels (d) and (h) for carbon. The arrows point to smaller Ag particles, formed by the degradation of the NCs during the potential-induced activation.

electroreduction. It is a major problem of catalyst design, however, that PVP – a capping agent used for the shape control of the catalyst particles – can remain adsorbed on the surface of the nanostructures, significantly decreasing the catalytic activity. Although some methods (solvent or thermal annealing based ones) are available for PVP removal, these can potentially damage the catalyst by exhibiting it to contaminations or to thermal shock.

In this short communication we described an alternative, potential-induced activation method that can be used to effectively remove PVP from the surface of Ag nanocubes. The method works *operando* in the electrochemical cell, and requires that before use, the working electrode is polarized to harsh negative potentials. By applying a single 'break-in' cycle, we gain a catalyst that shows higher activity and good stability during subsequent normal operation at mild (not so negative) electrode potentials. The described activation method, as was studied by pre- and post-electrolysis SEM imaging, causes only little degradation to the catalyst surface, and the method can be fine-tuned by selecting proper electrolyte compositions.

[1] D. R. Feldman, W. D. Collins, P. J. Gero, M. S. Torn, E. J. Mlawer, T. R. Shippert, *Nature* **2015**, *519*, 339, https://doi.org/10.1038/nature14240
[2] E. Royer, *Compt. Rend. Hebd. Séances Acad. Sci.* **1870**, *70*, 731.
[3] H.-R. M. Jhong, S. Ma, P. J. A. Kenis, *Curr. Opin. Chem. Eng.* **2013**, *2*, 191, https://doi.org/10.1016/j.coche.2013.03.005
[4] F. Yu, P. Wei, Y. Yang, Y. Chen, L. Guo, Z. Peng, *Nano Mater. Sci.* **2019**, *1*, 60, https://doi.org/10.1016/j.nanoms.2019.03.006
[5] D. Sun, X. Xu, Y. Qin, S. P. Jiang, Z. Shao, *ChemSusChem* **2019**, *13*, 39, https://doi.org/10.1002/cssc.201902061
[6] S. H. Im, Y. T. Lee, B. Wiley, Y. Xia, *Angew. Chem.* **2005**, *117*, 2192, https://doi.org/10.1002/anie.200462208
[7] J. Zhang, Q. Wang, X. Zhang, J. Wang, M. Guo, B. J. Wiley, C. Li, C. Hu, *Inorg. Chem. Front.* **2016**, *3*, 547, https://doi.org/10.1039/C5QI00256G
[8] K. M. Koczkur, S. Mourdikoudis, L. Polavarapu, S. E. Skrabalak, *Dalton Trans.* **2015**, *44*, 17883, https://doi.org/10.1039/C5DT02964C
[9] Y. Hou, N. Kovács, H. Xu, C. Sun, R. Erni, M. d. J. Gálvez-Vázquez, A. Rieder, H. Hu, Y. Kong, M. Liu, B. J. Wiley, S. Vesztergom, P. Broekmann, *J. Catal.* **2020**, *394*, 58, https://doi.org/10.1016/j.jcat.2020.12.006
[10] H. Hu, M. Liu, Y. Kong, N. Mysuru, C. Sun, M. d. J. Gálvez-Vázquez, U. Müller, R. Erni, V. Grozovski, Y. Hou, P. Broekmann, *ACS Catal.* **2020**, *10*, 8503, https://doi.org/10.1021/acscatal.0c02026
[11] N. Naresh, F. G. S. Wasim, B. P. Ladewig, M. Neergat, *J. Mater. Chem. A* **2013**, *1*, 8553, https://doi.org/10.1039/C3TA11183K
[12] I. Puspitasari, E. Skupien, F. Kapteijn, P. Kooyman, *Catalysts* **2016**, *6*, 179, https://doi.org/10.3390/catal6110179
[13] Z. Niu, Y. Li, *Chem. Mater.* **2014**, *26*, 72, https://doi.org/10.1021/cm4022479
[14] J. R. Pankhurst, P. Iyengar, A. Loiudice, M. Mensi, R. Buonsanti, *Chem. Sci.* **2020**, *11*, 9296, https://doi.org/10.1039/D0SC03061A
[15] S. E. Skrabalak, L. Au, X. Li, Y. Xia, *Nat. Protoc.* **2007**, *2*, 2182, https://doi.org/10.1038/nprot.2007.326
[16] A. V. Rudnev, in 'Encyclopedia of Interfacial Chemistry', Ed.: K. Wandelt, Elsevier, Amsterdam, **2018**, pp. 321–325.

6. Appendix

6.1 List of publications from this work

1. **H. Hu**, M. Liu, Y. Kong, N. Mysuru, C. Sun, M. D. J. Gálvez-Vázquez, U. Müller, R. Erni, V. Grozovski, Y. Hou, and P. Broekmann, Activation matters: hysteresis effects during electrochemical looping of colloidal Ag nanowire catalysts. *ACS Catal.*, 2020, 10 (15), 8503-8514.

2. **H. Hu**, M. Liu, Y. Kong, I. Z. Montiel, Y. Hou, A. V. Rudnev, and P. Broekmann, Size-dependent structural alterations in Ag nanoparticles during CO_2 Electrolysis in a gas-fed zero-gap electrolyzer. *ChemElectroChem*, 2022, 9 (17), e202200615.

3. **H. Hu**, Y. Kong, M. Liu, V. Kolivoška, A. V. Rudnev, Y. Hou, R. Erni, S. Vesztergom, and P. Broekmann, Effective perspiration is essential to uphold the stability of zero-gap MEA-based cathodes used in CO_2 electrolysers. *J. Mater. Chem. A*, 2023, 11, 5083-5094.

4. M. J. Galvez-Vazquez, S. Alinejad, **H. Hu**, Y. Hou, P. Moreno-Garcia, A. Zana, G. K. H. Wiberg, P. Broekmann, and M. Arenz, Testing a silver nanowire catalyst for the selective CO_2 reduction in a gas diffusion electrode half-cell setup enabling high mass transport conditions. *Chimia*, 2019, 73 (11), 922-927.

5. M. De Jesus Gálvez-Vázquez, P. Moreno-García, H. Xu, Y. Hou, **H. Hu**, I. Z. Montiel, A. V. Rudnev, S. Alinejad, V. Grozovski, B. J. Wiley, M. Arenz, and P. Broekmann, Environment matters: CO₂RR electrocatalyst performance testing in a gas-fed zero-gap electrolyzer. *ACS Catal.*, 2020, 10 (21), 13096-13108.

6. M. Liu, Y. Kong, **H. Hu**, N. Kovács, C. Sun, I. Zelocualtecatl Montiel, M. D. J. Gálvez Vázquez, Y. Hou, M. Mirolo, I. Martens, J. Drnec, S. Vesztergom, and P. Broekmann, The capping agent is the key: Structural alterations of Ag NPs during CO_2 electrolysis probed in a zero-gap gas-flow configuration. *J. Catal.*, 2021, 404, 371-382.

7. Y. Kong, **H. Hu**, M. Liu, Y. Hou, V. Kolivoška, S. Vesztergom, and P. Broekmann, Visualisation and quantification of flooding phenomena in gas diffusion electrodes used for electrochemical CO_2 reduction: a combined EDX/ICP–MS approach. *J. Catal.*, 2022, 408, 1-8.

8. Y. Kong, M. Liu, **H. Hu**, Y. Hou, S. Vesztergom, M. J. Galvez-Vazquez, I. Zelocualtecatl Montiel, V. Kolivoska, and P. Broekmann, Cracks as efficient tools to mitigate flooding in gas diffusion electrodes used for the electrochemical reduction of carbon dioxide. *Small Methods*, 2022, e2200369.

9. Y. Hou, N. Kovács, H. Xu, C. Sun, R. Erni, M. D. J. Gálvez-Vázquez, A. Rieder, **H. Hu**, Y. Kong, M. Liu, B. J. Wiley, S. Vesztergom, and P. Broekmann, Limitations of identical location SEM as a method of degradation studies on surfactant capped nanoparticle electrocatalysts. *J. Catal.*, 2021, 394, 58-66.

10. M. J. Galvez-Vazquez, H. Xu, P. Moreno-Garcia, Y. Hou, **H. Hu**, B. J. Wiley, S. Vesztergom, and P. Broekmann, Unwrap them first: operando potential-induced activation is required when using PVP-capped Ag nanocubes as catalysts of CO_2 electroreduction. *Chimia*, 2021, 75 (3), 163-168.

6.2 Conferences and presentation

1. SwissCat Symposium 2022, Annual Meeting of the SCS Section Catalysis, Bern, Switzerland, June 30, 2022, participation

2. 15th International Fischer Symposium a meeting on nanoscale electrochemistry, Kloster Seeon, Germany, June 12-16, 2022, poster presentation titled "Hysteresis Effects during Electrochemical Looping of Colloidal Ag Nanowire Catalysts"

3. 8th symposium of the SCCER "Heat and Electricity Storage", EMPA, Switzerland, November 5, 2019, participation

6.3 Acknowledgement

Here, I would like to convey my heartfelt gratitude to all the people who I met and worked with me. First, I am thankful to my supervisor, Prof. Dr. Peter Broekmann, for giving me the opportunity to work in his group, giving me the valuable feedback on my work, and showing me his genuine support during the whole period of my PhD program.

I am very grateful to Prof. Dr. Wenjing Hong (Xiamen University), Dr. Soma Vesztergom (Eötvös Loránd University), and Prof. Dr. Matthias Arenz (University of Bern) for their kind acceptance of invitation to act as referee of my PhD work. Furthermore, I acknowledge Prof. Dr. Matthias Arenz for recommending me to Prof. Dr. Peter Broekmann four years ago, providing the zero-gap gas-fed electrolyzer, and granting me access to his labs.

A special thanks to Dr. Chaoqi Zhang (University of Barcelona) and Prof. Dr. Hongbing Zhan (Fuzhou University, my master's supervisor), who inspired me to complete a PhD abroad. I also thanks Prof. Dr. Qijin Chi (Technical University of Denmark) and Prof. Dr. Jens Ulstrup (Technical University of Denmark), who assisted me apply the scholarship.

I acknowledge the financial support from China Scholarship Council (CSC) to provide me the opportunity to study in Switzerland. It was wonderful to broaden my horizons and experience different customs.

This project began on 4th March 2019 under the guidance of Dr. Yühui Hou. Dr. Yühui Hou introduced me to CO_2RR, the synthesis of colloidal catalysts, and the use of devices in the lab. The most important things that I learned from her were optimism and the flexibility to find a way to solve the problems. Even after leaving our group to the company in July 2021, she still provides the support to me. For the first project, I came across the problems of reproducing the catalysts. I appreciate the suggestions from Heng Xu (Duke University) and Qi Kang (Shanghai Jiao Tong University) to prepare the catalysts. After I went home in January 2020, my colleagues Ying Kong, Menglong Liu, and Dr. Yühui Hou helped me finish some of the experiments for this project. Master student Nisarga Mysuru carried out some of the electrolysis measurements in the first project as well.

The second project based on inverted rotating disc electrode started in September 2020, which has not done owing to some technical issues yet. Dr. Pavel Moreno-Garcia, Dr. Noémi Kovacs (Eötvös Loránd University), and Dr. Soma Vesztergom informed me on how to use the setup and analyze the results. When I began the studies of the flow cell, Dr. María de Jesús Gálvez-Vázquez

offered assistance with assembling the configurations and preparing the GDEs. The scientific discussions with Ying Kong and Menglong Liu were very helpful for the work. It was great to work with Dr. Alexander Rudnev (Russian Academy of Sciences) on his high efficiency in the Ag NPs degradation project in the flow cell. Dr. Viliam Kolivoška (Czech Academy of Sciences) and Dr. Soma Vesztergom gave deeper knowledge and detailed advice for the research of the capping agents influence on the stability of the flow cell. Dr. Ivan Zelocualtecatl Montiel helped me do a large amount of ICP-MS analysis before Nicola Lüdi taught me how to use ICP-MS instrument and provided me a lot of important information and suggestions for writing this thesis.

I also thanks to my other colleagues: Dr. Abhijit Dutta, Dr. Vitali Grozovski, Dr. Kiran, Dr. Yuzhen Wang, Alain Rieder, Anna Iarchuk, Liliana Gálvez Vázquez, Dr. Alena Cedeño López, and Changzhe Sun; our technicians: René Bühler, Dennis Tsubasa Flury, Lorine Gaudin, Levi Widmer, Mike Liechiti, Sven Hadorn, Elea Karst, Rafael, and Jasmin, who are creating a friendly and healthy working environment and gave the support to my work.

I highly appreciate Prof. Dr. Rolf Erni (Empa) for support of transmission electron microscopy, Dr. Ulrich Müller (Empa) for XPS analysis, and Prof. Dr. Martin Albrecht (University of Bern) for providing the hood and the rotary evaporator. I express my gratitude to Ms. Beatrice Frey, who taught me how to use the SEM and was accessible to support us in SEM analysis. I thank Dr. Nicolas Dolder for instruction of ultracentrifugation. I give my sincere thanks to all the members of the mechanical workshop, Human Resources (Ms. Beatrice Thönen, Ms. Beatrice Niederhauser, Ms. Sigrid Zimmermann, and Mr. Stefan Lisiecki), IT support team, Ausgabe, and other departmental staff (Ms. Sandra Zbinden, and PD Dr. Karl Krämer).

I want to thank my friends in Switzerland: Jia Du, Qi Huang, Zhiqiang Lai, Damin Zhang, Heng Liu, Tao Wan, Sinan Li, and Hang Chen. I am very grateful for having you by my side all this time. The time we spent together will be always be a precious memory for me. I highly appreciate my babies (August and 66) and the cats around the DCBP (Little Yellow, Little Black, Gustav, Statue, and Cat Boss) who gave me a lot of fun and made me relax after the work.

Finally and most importantly, I would like to express my deepest gratitude to my family and boyfriend, whose unconditional love, support, and encouragement make me who I am today. I am and will forever be indebted to them.

6.4 Declaration of consent

Declaration of consent

on the basis of Article 18 of the PromR Phil.-nat. 19

Name/First Name: Huifang Hu

Registration Number: 18-136-887

Study program: Chemistry and Molecular Sciences

Bachelor ☐ Master ☐ Dissertation ☑

Title of the thesis: Activity, Selectivity and Stability of Colloidal Silver Catalysts for Electrochemical CO2 Reduction Reaction

Supervisor: Prof. Dr. Peter Broekmann

I declare herewith that this thesis is my own work and that I have not used any sources other than those stated. I have indicated the adoption of quotations as well as thoughts taken from other authors as such in the thesis. I am aware that the Senate pursuant to Article 36 paragraph 1 litera r of the University Act of September 5th, 1996 and Article 69 of the University Statute of June 7th, 2011 is authorized to revoke the doctoral degree awarded on the basis of this thesis.

For the purposes of evaluation and verification of compliance with the declaration of originality and the regulations governing plagiarism, I hereby grant the University of Bern the right to process my personal data and to perform the acts of use this requires, in particular, to reproduce the written thesis and to store it permanently in a database, and to use said database, or to make said database available, to enable comparison with theses submitted by others.

Bern, November 16th, 2022

Place/Date

Huifang Hu (胡慧芳)

Signature